

THERMAL STRUCTURE, COMPENSATION MECHANISMS, AND TECTONICS
OF ACTIVELY-DEFORMING CONTINENTS: BAIKAL RIFT ZONE AND
LARGE-SCALE OVERTHRUST AND EXTENSIONAL TERRAINS

BY

CAROLYN DENISE RUPPEL

B.S., MASSACHUSETTS INSTITUTE OF TECHNOLOGY (1986)
M.S., MASSACHUSETTS INSTITUTE OF TECHNOLOGY (1986)

SUBMITTED TO THE DEPARTMENT OF EARTH, ATMOSPHERIC, AND
PLANETARY SCIENCES IN PARTIAL FULFILLMENT OF THE REQUIREMENTS
FOR THE DEGREE OF

DOCTOR OF PHILOSOPHY

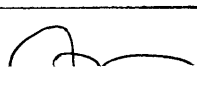
AT THE

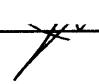
MASSACHUSETTS INSTITUTE OF TECHNOLOGY

FEBRUARY, 1992

© MASSACHUSETTS INSTITUTE OF TECHNOLOGY

SIGNATURE OF AUTHOR _____
DEPARTMENT OF EARTH, ATMOSPHERIC, AND PLANETARY SCIENCES
JANUARY, 1992

CERTIFIED BY _____
 MARCIA K. MCNUTT
THESIS SUPERVISOR

ACCEPTED BY _____
 THOMAS H. JORDAN
DEPARTMENT HEAD

WITHDRAWN
FROM
MIT LIBRARIES
JAN 16 1992

THERMAL STRUCTURE, COMPENSATION MECHANISMS, AND TECTONICS OF
ACTIVELY-DEFORMING CONTINENTS: BAIKAL RIFT ZONE AND
LARGE-SCALE OVERTHRUST AND EXTENSIONAL TERRAINS

BY

CAROLYN DENISE RUPPEL

SUBMITTED TO THE DEPARTMENT OF EARTH, ATMOSPHERIC, AND PLANETARY
SCIENCES ON 10 JANUARY, 1992, IN PARTIAL FULFILLMENT OF THE REQUIREMENTS
FOR THE DEGREE OF DOCTOR OF PHILOSOPHY IN GEOPHYSICS AND GEOLOGY

ABSTRACT

Active deformation at and near the surface of continents represents a manifestation of processes operating at depth and provides information on the underlying thermal, mechanical, and dynamic structure of the continental lithosphere. The four studies included here focus on characterizing various aspects of continental thermal structure in three settings: the extensional setting of the Baikal Rift zone (BRZ), a generalized compressional setting analogous to the Himalayas, and a generalized extensional setting including pure shear, simple shear, and modified pure shear components. For each study, the approach involves incorporating both geological and geophysical data to understand the first-order problem of how the crust and mantle lithosphere respond thermally and mechanically to deformation. A variety of approaches are suitable to the examination of this problem, including simple analysis of geophysical data, the development of forward and inverse models, and the study of active surface tectonics.

The Baikal Rift Zone (BRZ) of eastern Siberia represents the cold, discrete endmember in the class of active intracontinental rift systems, and a variety of geological and geophysical data constrain its thermal and mechanical structure at depth and its mode of shallow compensation. The onset of rifting in a narrow, sinistral zone at the edge of the Siberian platform and Aldan shield was marked by a sudden change in the character of sedimentation and tectonism at approximately 4 Ma, and lateral variations in the lithosphere's response to rifting led to the evolution of four distinct tectonic provinces. Topography, seismic, heat flow, and gravity data also indicate significant lateral heterogeneity along the BRZ and quantitatively constrain temperatures at depth. Bouguer gravity data over the BRZ are dominated by the short-wavelength low associated with sedimentary fill in Lake Baikal, but longer-wavelength features can be explained by regional compensation via flexural support of the topographic load by an elastic plate with

rigidity 7×10^{22} to 6×10^{23} Nm. Spectral analysis of the gravity data yields some scant evidence for dynamic compensation at the longest wavelengths and for thinning of the elastic plate towards the axis of the rift zone. The long-wavelength Bouguer low over the rift zone can be explained by the presence of only 2 to 4 km of partially molten material with density 200 kg/m^3 and 400 kg/m^3 less than surrounding rock (respectively). The reduction of P-wave velocities between the platform and the rift axis by up to 0.3 km/sec may imply the presence of a thermal anomaly on the order of 150°C beneath Lake Baikal, but observed strain rates, earthquake focal depths, and experimentally determined crustal rheology combine to constrain the crustal thermal gradient to less than approximately 20°C/km .

Analysis of Landsat photos, measurement of observed fault offsets, and synthesis of data on the rift's morphology, age, thickness of basin sediments, amount of extension, and seismicity patterns show that much of the opening along the axis of the BRZ may be the result of displacements along large-scale left-lateral strike-slip faults and of the consequent development of pull-apart basins. The predominance of strike-slip faulting over normal faulting has not previously been recognized in any presently existing intracontinental rift system and implies that the future evolution of the BRZ may follow the pattern of the strike-slip Dead Sea rift system. Strike-slip displacements in the BRZ are interpreted both as the cause of the discrete, brittle, and avolcanic nature of the rift and as an effect of "passive" plate-boundary forces that drive internal deformation of the Asian continent thousands of kilometers from the Himalayan collisional front. Published "passive" models which predict strike-slip faulting, but not extension, near the site of the BRZ are consistent with the interpretation presented here. Furthermore, the geophysical and geological data are not consistent with a more "active" thermal mechanism for rifting; this conclusion is based on: (1) the paucity of rift-related volcanic rocks, (2) the thick elastic plate required by the gravity data, (3) the absence of a well-defined heat flow anomaly, (4) significant lateral variations in crustal thickness (not expected if the lower crust is ductile enough to flow), (5) the presence of earthquakes to deep crustal levels, (6) high seismicity, and (7) no pronounced reduction in P-wave velocities beneath the rift's axis.

The thermal structure of actively deforming continents is also considered from the standpoint of the temperature evolution of the crust in compressional and extensional settings and the degree to which geological data represent the true thermal state of the lithosphere during orogenesis. Two-dimensional thermal models of time-transitive crustal thickening and subsequent unroofing in large-scale overthrust terrains generate pressure-temperature-time (PTt) paths that lack the large temperature inversions of two-dimensional models. Burial rate (proportional to dP/dt), not thrust fault geometry (dip angle), controls the topology of synthrusting PT paths and plays a minor role in determining the maximum temperature rocks attain later in their thermal histories during unroofing. Nearly all of the models produce PT paths with the usual sense (clockwise on conventional PT diagrams; counterclockwise here), and the amount of heating and duration of heating following the end of thrusting are a function of the rate of unroofing ($-dP/dt$) during this period. The results obtained here show that the initial thermal state of the lithosphere prior to thrusting has a profound effect on PT path morphologies and on the peak metamorphic conditions attained by samples. For excess heat distributed across the entire lithosphere (*e.g.*, due to increased mantle heat flow), a plot of peak temperatures experienced by metamorphic rocks *versus* structural depth (TMAX plot) closely represents the initial geotherm. Excess heat confined to the crust (*e.g.*, increased radioactive heating in a layer) yields a TMAX plot

which corresponds to the initial geotherm only near the top of the hanging wall. TMAX plots for both of these cases show no temperature inversion which exceeds the nominal uncertainties ($\pm 50\text{K}$) for geothermometric data. Shear heating can lead to significant temperature inversions at the fault zone if the frictional coefficient μ is 0.6 or greater.

For extensional terrains, theoretical pressure-temperature-time (PTt) paths of rocks uplifted from deep and intermediate crustal levels during extensional episodes are used to compare the effects of extension via ductile stretching of the entire lithosphere ("pure shear") and thinning that results from movement of crustal blocks along rooted large-scale low-angle normal faults ("simple shear"; terminology of *Wernicke* [1985]). Our results indicate that the temperature-time paths of rocks uplifted by "pure shear" and "simple shear" thinning of the lithosphere have similar morphologies and differ primarily in the amount of cooling that accompanies extension. The pressure-temperature paths are characterized by fairly constant cooling with moderate dP/dT for the "simple shear" case, but a short interval of isothermal uplift followed by high dP/dT for the "pure shear" case. Thinning of the lithosphere with a modified "pure shear" mechanism that includes a zone of decoupling in the lower crust to mimic the effects of the introduction of heat into the lower lithosphere produces PTt paths whose forms depend strongly on the amount of heating in the lower lithosphere. The form of PTt paths for rocks in normal-fault (*i.e.* "simple shear") settings are strongly dependent on unroofing rate (displacement rate multiplied by fault dip), but essentially independent of detachment geometry.

We conclude that forward models are generally inappropriate for reconstructing metamorphic thermal histories from actual petrologic and geochronologic data. For example, given current levels of uncertainty in the techniques used to reconstruct PTt paths for metamorphic terranes, it is probably generally impossible to distinguish between "pure shear" and "simple shear" mechanisms strictly on the basis of petrologic or geochronologic data. For compressional terrains in particular, inverse models that use a postthrusting thermal regime consistent with two-dimensional forward models and that integrate values of dP/dt , dT/dt , and radioactive heating rates extracted from suites of metamorphic rocks provide the best hope for furthering our understanding of the thermal evolution of metamorphic terrains.

Thesis supervisor: Marcia K. McNutt
Title: Griswold Professor of Geophysics

ПОСВЯЩЕНИЕ

Посвящается молодым русским учёным

DEDICATION

Dedicated to the young Russian scientists

ACKNOWLEDGEMENTS

When the former Soviet Union—a place where I have spent some strange and wonderful times the past few summers—is changing so rapidly, it seems ridiculous to speak about “life in graduate school” on these pages. As I sit here comfortably, wondering whether I and my peers will ever land the sorts of jobs for which we have trained, my friends and colleagues in Moscow and Irkutsk, not yet accustomed to calling themselves “Russians” instead of “Soviets”, must worry about more fundamental questions: whether science has any future in their country and whether they will even be able to find food next week. Although I see my young Russian friends only once a year, they are perhaps more deserving of my gratitude than almost anyone else: To Misha Karpychev, Zhenya Burov, Tamara Gudkova, Lana Panasyuk, Tanya Perepelova, and their families and friends, I say a hearty “spasibo” for providing many wonderful hours of conversation and for showing me the true meaning of hospitality. If they have not succeeded in improving my Russian language abilities, they have at least taught me to be more patient and more thankful for the undeserved advantages I enjoy due to an accident of birth.

During my years at MIT, there have always been faculty members who were not my formal advisors, but who spent time helping me anyway. Foremost among these people is Kip Hodges, who is a coauthor of Chapters 4 and 5 of this thesis. Kip read papers promptly, took my ideas seriously, shared his sarcasm, political ideas, and musings on the future of science, provided an endless and approachable source of calm in my sea of panic, taught me a lot about tolerance, and, most importantly, helped me find a small bit of self-confidence. It is thanks to Kip and his seemingly infinite reserves of patience that I finish graduate school a much better geologist than when I started. Wiki Royden, a co-author of Chapter 5, has contributed in some way to every chapter of this thesis, and she has provided a wonderful role model for the sort of geologist's geophysicist and geophysicist's geologist that I hope I can be. Peter Molnar deserves thanks for having allowed me to take up his time during his very infrequent stopovers in Boston and for providing such a good model (a word I'm not supposed to use) for how to be an honest scientist. If Peter were not so humble about his achievements, I may have been scared away from the study of Asian tectonics early on. Clark Burchfiel allowed this geophysicist to sit in on years' worth of regional tectonics seminars, and I thank him for letting me be so obstreperous in my skepticism. Finally, I thank Marcia McNutt for taking the risk of admitting me to graduate school and for providing me with the freedom to do fieldwork all over the world and projects in other parts of the department.

A handful of other scientists has helped me at various stages in my work. Debbie Hutchinson stands out from the rest in her willingness to keep the politics out of science and to preserve the tradition of open exchange of ideas to which I still idealistically cling with youthful abandon. I also acknowledge the help of Kathy Crane, Paul Davis, Paul Hearn, and Bob Meyer at various stages of my studies. Among the Russian scientists who merit special mention are Misha Kogan, who originated the Baikal project and arranged several of my trips to the now-defunct USSR, and Academician Logatchev, who has sponsored my visits to the rift zone. Kiril Levy, Zoltan Balla, Yuli Zorin, and Lev Zonenshain contributed to my understanding of the Baikal rift zone and of the realities of working there.

Graduate students come and go, and those who surround one during the last throes of his thesis often get all the credit for having been supportive. To prevent making this mistake, I first acknowledge the now-graduated friends—Anne Sheehan, Randy Mackie,

Joanne Fredrich, Steve Hickman, Geoff Abers, and especially Sarah Kruse—for answering lots of my stupid questions over the years. Sarah has been a particular source of moral support since the very first days of graduate school and has helped me face up to real life in ways that no one else has. Gail Christeson (my e-mail penpal), Cecily Wolfe, Paula Waschbusch, Mike Bergman, Andrew Gunstensen, Peter Puster, Steve Shapiro, and Pete Kaufmann have played an important role in my life over the years, sometimes just by being the friendly face on a particularly bad day. I will never forget the stoicism and good humor with which Paula, Gail, and Cec have endured my mood swings over the past six months. D'Arcy Straub and Helen Webb have graciously allowed me to create a Ted Madden-esque mess in the office. Finally, I thank Peter Burkholder, a non-MIT graduate student I came to know under rather bad circumstances during my last summer in Siberia. Peter's inquisitiveness about Baikal provided a major impetus for me to continue thinking about the rift at a time when I was particularly discouraged, and his unflagging enthusiasm forced me to face that fact that, despite my grumbling, I do love my work with a passion.

Over the past few years, Jon "Jape" How has shared his life and family with me. Most of all, I owe him a debt of time for all the plans we cancelled so that I could work more or travel longer. Jon has been on the frontline of this thesis-writing business and has endured my worst moods and supported me during one of the most confidence-shaking and personally disappointing times of my life. His most important contribution, though, was in not letting me quit. Without the stability and support he has provided, I think I probably would have given up several months ago.

TABLE OF CONTENTS

Abstract.....	2
Dedication.....	5
Acknowledgements.....	6
Table of Contents.....	8
CHAPTER 1. INTRODUCTION.....	10
CHAPTER 2. THE BAIKAL RIFT ZONE: TECTONICS, COMPENSATION, AND CONSTRAINTS ON DRIVING MECHANISMS FOR RIFTING.....	15
Introduction.....	15
Geologic setting.....	17
Archaen through Mesozoic history.....	17
Mesozoic deformation.....	19
Cenozoic rifting.....	19
Tectonic provinces of the BRZ.....	21
Rift axis and Lake Baikal basins.....	22
Sediments in Lake Baikal basins.....	25
Sayan Region.....	27
Barguzin Area and the accomodation zone.....	30
Udokan Region.....	31
Data.....	32
Topography.....	32
Seismicity.....	33
Seismic refraction data.....	38
Heat flow data.....	40
Gravity anomaly lack of data.....	42
Compensation of short-wavelength features.....	44
Previous work.....	44
Admittance.....	45
Coherence analyses.....	48
Conventional forward modeling techniques.....	50
Sediment corrections.....	52
Profile I.....	54
Profile II.....	55
Profile III.....	58
Profile IV.....	60
Crustal thickness variations and isostatic equilibrium.....	61
Thermal Anomalies beneath the BRZ.....	63
Qualitative constraints on driving forces for BRZ rifting.....	67
Conclusions.....	72
Acknowledgements.....	73
Appendix: Earthquake Epicenters.....	74
Tables.....	83
Figures.....	94
CHAPTER 3. STRIKE-SLIP FAULTING AND THE ORIGIN OF THE BAIKAL RIFT ZONE....	129
Introduction.....	129
Tectonic framework.....	130
Strike-slip displacements and rift development.....	134
Discussion.....	137
Conclusions.....	140
Acknowledgements.....	140

Figures.....	142
CHAPTER 4. PRESSURE-TEMPERATURE-TIME PATHS FROM 2D THERMAL MODELS: PROGRADE, RETROGRADE, AND INVERTED METAMORPHISM.....	153
Introduction.....	153
The two-dimensional model.....	154
Geological relevance.....	157
Comparison with one-dimensional models.....	163
Two-dimensional models: effect of position in the thickening lithosphere.....	167
Simple shear (thrust faulting) vs. pure shear thickening.....	168
The burial path.....	171
Fault dip.....	172
Burial rate.....	174
The unroofing path.....	175
Unroofing mechanism: pure shear, simple shear, and erosion.....	175
Denudation rate.....	178
Importance of initial thermal structure.....	179
Increased mantle heat flow.....	180
Radioactive heat production.....	182
Shear heating.....	184
Simultaneous thrusting and erosion.....	187
Inverted post-thrusting geotherms vs. TMAX.....	189
Discussion.....	190
Pressure-temperature paths from natural samples.....	191
Time-temperature paths from natural samples.....	193
The importance of integrative PTt studies and inverse modeling.....	193
Conclusions.....	195
Acknowledgements.....	197
Figures.....	199
CHAPTER 5. THERMAL MODELING OF EXTENSIONAL TECTONICS: APPLICATION TO PRESSURE-TEMPERATURE-TIME PATHS OF METAMORPHIC ROCKS.....	234
Introduction.....	234
Methods and models.....	236
Geologic relevance.....	239
Pure shear versus simple shear.....	240
Modified pure shear.....	244
Simple shear models.....	246
Discussion.....	248
Conclusions.....	250
Acknowledgements.....	252
Figures.....	253
CHAPTER 6. CONCLUSIONS.....	268
Summary.....	268
Oceanic analogs to continental features.....	271
Suggestions for Future Research.....	273
REFERENCES.....	277

Chapter 1

Introduction

The advancement of the theory of plate-tectonics in the late 1960s led to fundamental changes in scientists' most basic assumptions about the Earth and to an immediate revolution in marine geology and geophysics. Suddenly, with a single theory, marine geophysicists could explain decades' worth of observations from the world's oceans and the spatial distribution of earthquakes and volcanoes and ponder possible connections between motions in the mantle and deformation at the surface. However, among students of continental tectonics, the plate-tectonic revolution did not take hold as quickly. Without a well-distributed pattern of ridges, trenches, and transform faults to guide these workers, the preconception that the continents were passively rafted on oceanic plates was difficult to overcome and the connection between large-scale horizontal motion of plates and deformation at the margins of continents or in their interiors hard to make. Not until the pioneering studies of *Dewey and Bird* [1970] and *Atwater* [1970] was plate-tectonics inexorably linked to geological and geophysical observations on the continents, and the subsequent years marked an explosion in our understanding of continental deformation in the context of plate-tectonics.

The amount of accumulated data from both active and stable regions on the continents has recently increased to the point that it is possible to formulate coherent geologic histories for tectonic events at the scale of entire orogenies (*e.g.*, *Sengör* [1984]). The next important step for students of continental tectonics will bring us back full circle to

the marine roots of the plate-tectonic revolution, towards a synthetic approach which interprets surface deformation not in the context of continental vs. oceanic settings but in terms of fundamental Earth processes. This new focus of continental tectonics is the driving force behind the studies which comprise this thesis. Through the complete integration of geological and geophysical data, the application of the methods of marine geophysics to zones of active continental deformation, and the analysis of the deep structure of continental features which have close oceanic analogs, these studies seek to bridge the gap not only between geology and geophysics but also between the often diverging fields of continental and marine geophysics.

A major focus of this thesis is rifts, features which are common to both oceans and continents and which serve as windows into the thermal, mechanical, and dynamic structure of the underlying mantle lithosphere. Rift zones represent areas where the Earth has effectively split apart, either at oceanic and continental plate boundaries or at points of extensional failure in the crust. At rifts, magma chemistry provides clues about the source of melt, domal topography reflects the role of thermal and dynamic uplift, and other geophysical and geochemical observations may constrain temperatures in the lithosphere. Rifts thus provide a natural laboratory for study of the deep thermal, mechanical, and dynamic structure of the continents and for drawing connections between oceanic and continental processes. A primary focus of this study is therefore to analyze the implications of rift observations for the deep structure of the continents and to use geological and geophysical data to examine how the temperature variations within the crust, mantle lithosphere, or at even deeper levels affect surface deformation and the evolution of tectonic provinces.

Another motivating force for the studies in this thesis is our poor understanding of thermal aspects of continental tectonism. The ability to draw valid comparisons between continents and oceans has been hampered by the absence of simple accretionary

mehcanisms for continental crust and a lack of firm knowledge about the nature of the lithosphere beneath continents. The studies presented here seek to characterize not only the deep thermal and dynamic structure beneath certain tectonically-active areas, but also the time-dependent thermal evolution of shallow continental horizons. These sorts of analyses serve to connect the physics of tectonic processes to geological observations at the Earth's surface.

OVERVIEW

The first two chapters of this thesis focus on the Baikal Rift zone of eastern Siberia, a young intracontinental rift which has only recently become the focus of active research among many Western scientists. The Baikal Rift zone, the deepest and most discrete of the Earth's active intracontinental rifts, is located 2000 km from any active plate boundaries, deep within the 11000 km wide expanse of the Eurasian continent. The geology and geophysics of the Baikal Rift zone provide important clues not only about the evolution of this rift system, but also about the role of pre-existing crustal weaknesses in localizing intraplate extension, the role of far-field forces in driving extension, and the nature of the deep lithosphere beneath a continental region more isolated from the oceans than any other on Earth. In Chapter 2, we describe the geological setting and geophysical characteristics of the Baikal Rift zone, constrain its mode of shallow compensation, and qualitatively describe the thermal and chemical characteristics of the deep lithosphere. In particular, we emphasize the similarities and differences between surface geology and structure on one hand and patterns of seismicity, crustal thickness variations, heat flow, magnetic anomalies, and basin gravity anomalies on the other. Among the important aspects of this chapter is a discussion of the existing models for the evolution of the Baikal Rift zone and how these models generally fail to explain some of the geological and geophysical observations.

Chapter 3 also pertains to the Baikal Rift zone, but narrowly focuses on its evolution and the role of strike-slip motions in opening the rift's deep axial basin at the site of Lake Baikal. Analysis of the structural style of the Baikal Rift zone using Landsat photos and other geological data reveals that strike-slip movements along major left-lateral faults and shear zones may control the rift's present-day morphology, explain the presence of sediments in excess of 7 km thick in parts of the axial basins, and account for much of the opening of the rift since Pliocene time. In this chapter, we draw analogies with the Dead Sea Rift, for which Baikal may serve as an example of a proto-rift, and underscore the geological and geophysical aspects of the Baikal Rift zone which distinguish it as an endmember in the class of continental extensional rift structures.

Chapter 4 shifts the emphasis from extensional to compressional tectonism, focusing on aspects of the thermal evolution of large-scale overthrust terrains. Specifically, we seek to understand how time-transitive processes (*e.g.*, thrusting, erosion, and conduction of heat both laterally and vertically) operative in compressional settings affect temperatures in the crust and the pressure-temperature-time paths (PTt) recorded by metamorphic rocks. PTt paths provide one of the few direct measures of the thermal conditions in the lithosphere before, during, and after orogenic events, but they are frequently misinterpreted or over-interpreted. By examining the effects of variations in such factors as radiogenic heating, thrust and erosion rate, unroofing and burial mechanisms, frictional heating, and heat flow into the base of the crust, we highlight the nonunique nature of most PTt paths and underscore the problems inherent in the continued application of one-dimensional instantaneous thermal models to the interpretation of PTt data.

Chapter 5 switches the emphasis back to extensional terrains, but concentrates on their generalized thermal evolution instead of the processes associated with the development of specific extensional features like rifts or normal faults. Using two-dimensional thermal

models, we track the cooling paths of rocks at intermediate and deep crustal levels as they are carried closer to the surface by movement along normal faults or by pure shear thinning of the crust or entire lithosphere. Analysis of the PT and Tt paths associated with movement of deep or intermediate level rocks to near-surface crustal horizons permits an evaluation of the relative importance of such factors as fault geometry and unroofing rate in controlling the morphology of extensional terrain cooling paths. Once again, we focus on the nonunique nature of PT and Tt paths produced by varying fault-related factors and extensional mechanisms and note that uncertainties—both in the empirically-determined geothermometers and geobarometers and in the analyses of field samples—render it nearly impossible to distinguish between pure shear and simple shear extensional mechanisms based on PT and Tt data alone.

Finally, Chapter 6 summarizes some of the principal results of this study and outlines important areas of future research. The studies which comprise this thesis focus on processes in the crust and mantle beneath regions of active tectonism on the continents. The approach taken here depends on complete integration of geophysical data and surface geology in the analysis of compensation mechanisms, deep thermal structure, and driving forces for extension in settings like the Baikal Rift zone. Alternate approaches include forward modeling of surface deformation and the development of tectonic provinces based on analytic or numerical calculations of the thermal, mechanical, and dynamic response of the lithosphere to deep-seated processes and characterization of the deep structure of active areas using magnetotelluric or seismic data. In this chapter, we briefly explore how the results of different approaches to studying the deep structure of the continents may relate to the work presented here and describe how the different approaches may be integrated in the future.

Chapter 2

The Baikal Rift Zone: Tectonics, Compensation, and Constraints on Driving Mechanisms for Rifting

INTRODUCTION

Among the Earth's large-scale and active continental rift systems, the Baikal Rift zone (BRZ) of eastern Siberia and the relatively inaccessible West Antarctica Rift (*e.g.*, *Behrendt et al.* [1991]) remain the only ones whose geological and geophysical characteristics remain poorly understood. The BRZ is perhaps unique among continental rifts in that nearly every theory of riftogenesis has been applied to it. The BRZ has alternately been interpreted as hot [*Lubimova*, 1969] and cold [*Lysak*, 1978], passive [*Tapponnier and Molnar*, 1979] and active [*Zorin*, 1977], thinned-skinned [*Pleshonov and Romazina*, 1981; *Balla et al.*, 1991] and thick-skinned (*e.g.*, *Artemjev and Artyushkov* [1971]; *Zorin and Rogozhina* [1978]), and of Pliocene (4 Ma; *e.g.*, *Nikolayev et al.* [1985]; *Artyushkov et al.* [1990]) and Eocene to Miocene age [*Logatchev and Florensov*, 1978]. Over the past few years, the increased availability of geophysical data for the BRZ has provided an opportunity to resolve many of the remaining questions about the rift's initiation and development and forms a basis for comparisons between the BRZ and other continental rift systems. This paper seeks to fill the gap left by other studies of the BRZ by first presenting an integrated analysis of the geological data and old and new geophysical observations and by subsequently applying the results to the

problems of shallow compensation beneath the rift and characterization of the thermal anomalies at depth.

The first researchers to place the BRZ in the context of intraAsian deformation and plate-tectonic interactions were *Molnar and Tapponnier* [1975], who attributed the development of the BRZ to forces associated with the Eocene collision of India and Asia. In this interpretation, the BRZ represents the zone of greatest penetration of the Himalayan orogeny within the Asian continent. Regardless of whether the BRZ did or did not develop in response to the application of far-field forces, Molnar and Tapponnier's work represented the important first step in trying to explain profound extensional deformation at a site 2000 km from any active plate boundary and near the center of the largest expanse of continental crust on present-day Earth. Subsequent interpretations have attributed extensional deformation at the site of the Baikal rift to processes ranging from large-scale convective thinning of the lithosphere [*Artemjev and Artyushkov*, 1971] to heating above a thermal plume or the intrusion of a single large dike directly beneath the rift's axis [*Zorin et al.*, 1979; *Zorin*, 1981].

Although this paper cannot fully resolve all of the issues associated with the evolution of the BRZ, the data we present here should serve as a starting point for distinguishing between different rift mechanisms. We first provide a brief overview of the geologic setting, plate-tectonic evolution, and tectonic provinces of the BRZ. Such summaries have generally been inaccessible to Western scientists, and the inclusion of this overview, which includes new interpretations of the overall structural setting of the rift zone, provides a foundation for synthesis of the geological and geophysical data. The second part of this paper describes the geophysical datasets assembled in the course of this study and synthesizes these new data with older information to provide a coherent framework for the geophysical setting of the BRZ. We focus here on describing data assembled from primary sources since much of the literature on the BRZ presently includes

only interpretations of the data and not the data themselves. Finally, we explore the shallow compensation of the BRZ and roughly constrain its deep thermal structure based on simple physical considerations and an analysis of the geological and geophysical data.

GEOLOGIC SETTING

The BRZ is bounded by the irregular edge of the Siberian platform on the west and the Sayan-Baikal folded zone on the east. Although development of the platform and the folded zone predate rift-related deformation by at least 50 my, the older features influence the location of the young rift system [Zamarayev and Ruzhich, 1978]. It is thus important to examine the entire geologic history of the region in order to understand the evolution of young rift features. This section briefly describes the geology of the BRZ, summarized in Figure 2.1, and the relationship between tectonic events and sediment deposition and magma generation (Fig. 3.1). Geologic data are taken from Soviet maps at scales of 1:1,000,000 [Khrenov *et al.*, 1983] and 1:1,500,000 [Yanshin *et al.*, 1980].

ARCHAEN THROUGH MESOZOIC HISTORY

The oldest rocks in the BRZ area lie in the core of the folded zone and comprise the Archaen and Lower Proterozoic crystalline basement complex. These basement rocks crop out west of the lake in the shear zone of the Main Sayan fault, east of the lake in the Lesser Khamar-Daban and Zagan Mountains, and to the north at the end of the Udokan shear zone. Unconformably overlying the Lower Proterozoic basement rocks are the weakly metamorphosed clastics and calcsilicates of Upper Proterozoic age. Outcrops of Upper Proterozoic rocks, including intrusives, occur south of the Main Sayan fault and in its shear zone, particularly in northern Mongolia and along the southern shore of Lake Baikal. However, the most important exposures of Upper Proterozoic rocks in the BRZ area are

those that define the edge of the Siberian platform. These rocks form a continuous belt over 800km long which begins near the mouth of the Angara River, runs along the lake's western shore, and then swings due north away from the lake into a broad region of exposures bounded on the north by arcuate faults along the edge of the platform. Although Upper Proterozoic rocks are primarily confined to the areas west and south of the lake, the continuous exposures at the edge of the platform to the north may imply the onset of suturing in this area before the end of Upper Proterozoic time.

The distribution of Paleozoic rocks in the Baikal region reflects the separate histories of the platform and folded zone prior to suturing. In the interior of the Siberian platform, Paleozoic rocks consist primarily of Cambrian to Ordovician clastic rocks, but calcsilicates predominate in the Cambrian section close to the lake. Cambrian sedimentary rocks also crop out in a broad region of northern Mongolia and in small isolated pockets within the folded zone. Generally, however, the Paleozoic section in the folded zone consists almost exclusively of intrusive rocks emplaced during the Baikalian orogeny in early Paleozoic time. Intrusive batholiths lie within 20 km east of Lake Baikal everywhere north of the Selenga delta and make up most of the mountain ranges east of the lake. The notable absence of Paleozoic intrusive rocks west of Lake Baikal implies that processes responsible for crustal melting in the folded zone acted prior to the accretion of this continental microplate to the edge of the Siberian platform. Paleozoic intrusive rocks also do not occur north of the Main Sayan fault; thus, like the central part of the Baikal suture zone, the Main Sayan fault serves as a fundamental boundary between undisturbed platform and deformed continental crust.

MESOZOIC DEFORMATION

Mesozoic time was a period of relative quiet in the BRZ area. Mesozoic rocks are not widespread in the BRZ area and consist primarily of Jurassic sediments deposited directly on Cambrian rocks near the mouth of the Angara River and in a 75 km wide belt stretching away from the lake to the northwest, parallel to the Main Sayan fault. Shales and other fine-grained clastics comprise the Jurassic section, and the pattern of Jurassic outcrops implies that sediments pooled around the Cambrian core of the Siberian platform, which may have been a topographic high during Jurassic time. Alternately, post-Mesozoic (during Cretaceous to Neogene time; *Logatchev and Florensov [1978]*) doming of platform rocks may have caused Jurassic sedimentary rocks to be completely stripped from the top of the Lena-Angara steppe. Isolated pockets of Cretaceous and Jurassic sedimentary rocks also crop out south of the Main Sayan fault and in the southern part of the folded zone. The nature and distribution of Mesozoic volcanic and plutonic rocks are more poorly known: Soviet geological maps refer to Triassic and Jurassic andesite, basalt, and tuff fields east of Lake Baikal, but the proximity of these rocks to Neogene volcanics and known disparities between dates obtained by various workers for Baikal area volcanic rocks make it possible that these rocks are actually much younger than Mesozoic age.

CENOZOIC RIFTING

The BRZ area experienced a second major phase of tectonism during Cenozoic time, but the precise timing of the onset of rifting remains unknown. *Logatchev and Florensov [1978]* and *Logatchev and Zorin [1987]* describe the evolution of the BRZ as the consequence of two stages of extensional deformation, one from Eocene to Early Pliocene time and another between Middle Pliocene time and the present. Their analysis is

based primarily on interpretations of the sedimentary record, which, for the initial stage of rifting, lacks the coarse lithologies associated with rapid tectonic movement and high relief. They conclude that the basins of Lake Baikal opened in Eocene to early Miocene time while the outermost rift basins to both east and west were formed during the second stage of rifting, probably in Pliocene to Quaternary time. In recent years, the two-phase interpretation of Baikal rifting has been challenged by workers who recognize a widespread change in the nature of sediments at 4 Ma (*e.g.*, *Nikolayev et al* [1985]). The sudden onset of coarse sedimentation at this time, coupled with merging of the South and Central basins and the beginning of rapid subsidence in the North basin, indicate that many of the observed features of the BRZ may be a result of deformation in the past few millions of years. For some workers, this interpretation is difficult to reconcile with evidence for the evolution of unique taxa in Lake Baikal, which may require the existence of a lake for more than 4 or 5 my. However, even if rifting in the BRZ dates only to Pliocene time, this does not preclude the presence of a proto-Lake Baikal along the Paleozoic suture zone prior to the onset of extensional deformation.

At present, the lack of age constraints on sediments and volcanic rocks makes the elimination of either the two-phase or one-phase rifting scenarios impossible. The Cenozoic and Quaternary sedimentary section in the BRZ is limited to sediments which fill rift basins and river valleys, and drilling and seismic methods are only beginning to provide clues about the composition and thickness of sedimentary units. In the rift basins outside of Lake Baikal, sediments consist primarily of coarse alluvium near active range-bounding fault structures and along mountain fronts and sands, clays, and possibly some interbedded basalt flows within the valley floors. Within Lake Baikal, the base of the sedimentary column is made up clastic rocks at the base which give way to deep-water lacustrine sediments near the top.

The nature of young volcanic rocks is even more poorly understood than the character of young sediments. According to Soviet maps, young (Neogene) volcanic rocks occur only in the Vitim plateau east of the Barguzin basin and south and west of Lake Baikal near the Mongolian border. Cinder cones occur both south of the Main Sayan fault and south of the Chara rift basin, far to the rift's northeast. In the Tunka basin, cinder cones sit directly in the valley floor, implying that basaltic flows probably form part of the basin fill. A key question remaining about the BRZ is why the rift is so "dry" or avolcanic compared to other continental rift systems. As some volcanic rocks mapped as Tertiary age are reclassified as Quaternary and as more information about ash content is gleaned from examination of Baikal sediment cores, we may learn that rifting in the BRZ was accompanied by more volcanism than previously thought.

TECTONIC PROVINCES OF THE BRZ

Four distinct tectonic provinces comprise the BRZ: the rift axis, the Sayan and Udokan regions, and the Barguzin accommodation zone. Within the overall evolutionary and tectonic framework of the BRZ, each of these provinces has a unique history and is associated with specific fault systems, shown in detail in Figure 2.2. The basins of Lake Baikal and the flanking mountains and plateaus make up the axial part of the BRZ, and this axis serves as the link between the Sayan region to the west of the lake's southern tip and the Udokan area to the east of the lake's northern tip, giving the rift its characteristic S-shaped morphology. The Barguzin accommodation zone, which lies just east of the North Basin, probably serves as the locus of the extension along the northern part of the rift's axis and also acts as a link between the deformation occurring in the Central Basin of the axial zone and to the north in the Udokan shear zone. The major structural features discussed below have been described in greater detail by *Sherman et al.* [1973] and *Sherman* [1978].

RIFT AXIS AND LAKE BAIKAL BASINS

The axis of the BRZ closely follows the edge of the Siberian platform and consists of a broad domal feature west of the lake, the deep and narrow basins of Lake Baikal, and the rugged mountains which form the shoulders of the rift on both the east and west. The morphology of each of these elements provides important clues about the fault structures which control their development, and topographic maps and Landsat photos clarify the relationships between the rift basins and the flanking topographic highs.

The axial part of the BRZ is characterized by heterogeneity both along strike and perpendicular to strike. In general, the most gentle topography on the rift flanks is associated with the broad Lena-Angara Steppe west of the central part of the rift's axis and the much smaller Olkhon Plateau, which fills a roughly triangular region between the Sayan tectonic province and the mouth of the Angara River. Average elevations in these areas is 700-900m, but maximum elevations increase eastward towards the lake and particularly northward along the axes of the Primorye and Baikal ranges. The Primorye Range closely follows the lake's western shore from the Angara River in the south to the latitude of Olkhon Island in the north, where it becomes the Baikal Range. This range is more heterogeneous than the Primorye Range and follows the lake's shoreline only as far north as the Bolsodey inlet, where it abruptly swings to the north, away from the lake, and becomes much wider. The Primorye Range and the southern part of the Baikal range probably represent the uplifted edge of the block that forms the footwall of the eastward-dipping basin-bounding Obruchev normal fault. The steady increase in elevation from 900m at the southern end of the Primorye Range to over 2000 m in the central Baikal Range may indicate that the footwall block is tilted or, alternately, that other faults, particularly the oblique-slip Academician Ridge structure, cut the Obruchev fault, resulting

in differential uplift of the Primorye and Baikal Range segments of the footwall block. This interpretation is also supported by the sudden change in strike of the Baikal Range.

Average elevations in the folded zone east of the lake are 1200 to 1400 m, significantly higher than to the west of the lake. However, the relationship between high topography and rift-related faulting is not clear. Whereas the highest peaks in the Primorye and Baikal Ranges lie close to Lake Baikal on the west, the axes of the ranges which bound the lake's basins on the east lie 50 or more km away. Thus, along much of the lake's eastern shore, distinguishing clear rift shoulders is not possible. Northeast-striking ranges define the overall fabric of this area, and it is likely that this orientation of ranges, like the orientation of the rift's axis itself, is an effect of orogenesis which predates rifting. Along some parts of the rift's axis, the topographic highs within the Khamar-Daban, Golonbin, and Barguzin Ranges may represent rift flank uplifts in the footwall of a lake-bounding westward-dipping normal fault and imply a two-sided graben structure for the Baikal basins. Other features of these ranges probably are produced by faulting on eastwardly dipping surfaces in the hanging wall of the Obruchev complex (half-graben structure) or by transpression along strike-slip and normal faults with rapidly changing orientations. A clear example of the latter case occurs along the eastern side of the Central Baikal basin where a system of overlapping normal(?) fault segments appears to step repeatedly towards and away from the lake, creating shoreline segments characterized by high peaks alternating with shallow basins.

Three basins comprise Lake Baikal, which fills the axial part of the rift zone. The North Basin is the shallowest, with a maximum water depth of about 900m (450m below sea level) and shows the characteristic asymmetry of the Baikal basins, with the deepest point occurring close to the steep fault scarp on the western side. The basin trends N55°E at its southern end but curves to about N35°E to the north, where it separates the Baikal Range on the west from the Barguzin Range on the east. The northern end of the North

Baikal Basin slopes gradually into the linear shoreline and a fault dipping at 45-60° towards the lake [Nikolayev *et al.*, 1985], while the southern end of the basin abuts an oblique-slip structure along the line connecting Olkhon Island and the shallow submarine Academy Ridge horst. This transfer fault may cut the Obruchev normal fault, leading to the en echelon arrangement of the Central and Northern Basins.

Of the lake's three basins, the central one is the deepest (water depth 1625m; 1175m below sea level) and most strongly asymmetric. The Central basin has linear sides striking at about N55°E, and the deepest point occurs close to the steep, linear northern edge, which parallels the transfer fault and is nearly perpendicular to the basin's sides. The western side of the basin is bounded by the Obruchev Fault as far north as the northern tip of Olkhon Island. Movement along the Academy Ridge oblique-slip structure has dragged Olkhon Island and the segment of the Obruchev Fault along the island's eastern edge away from the lake's shoreline towards the northeast. To the south, the Central Basin narrows from over 40 km width to less than 10 km, and the primary depocenter is pushed close to the lake's western shore by the massive deltaic sediments at the mouth of the Selenga River. The delta impinges on the lake at the position of the Bugul'deyka submarine ridge, a horst structure separating the Central and South Basins. These two basins were apparently linked until the end of Pliocene time, and the Bugul'deyka horst is therefore a fairly young structure.

The Selenga Delta and Bugul'deyka horst also have a significant effect on the morphology of the South Baikal Basin, whose narrow northern extension resembles the southern part of the Central Baikal basin, consisting of a narrow trough proximal to the western shore. The South Basin is the smallest of the Baikal basins and strikes across the region's general northeasterly oriented fabric at N85°E. The major difference in strike between the South Basin and the North and Central Basins is closely related to the complicated tectonic framework in which the South basin has evolved. Like the Central

Basin, to which the South Basin was probably linked prior to the beginning of Neogene time [Nikolayev *et al.*, 1985], the southern basin is deep (water depth 1420m; 963m below sea level) and strongly asymmetric. However, although the Obruchev normal fault or some extension of it clearly bounds the very steep western edge of the Southern Basin, no clear rift shoulders are present in this area and the basin-bounding Primorye Range does not extend this far south. The lateral heterogeneity of the geological features from the southern tip of the Primorye Range to the southernmost tip of the lake may explain the lack of high peaks on the rift shoulders in this region. In contrast to the area to the north, where Proterozoic metasedimentary rocks lie along most of the lake's western shore, the geology along the western side of the Southern basin is complicated by the presence of Jurassic rocks in the Angara River valley and Paleozoic intrusive rocks along the edge of the Sayan tectonic province, in the shear zone of the Main Sayan fault.

Sediments in Lake Baikal basins. The thickness of sediments within Lake Baikal remains unknown, but most published estimates lie in the range of 6-7 km, a value based primarily on interpretations of gravity and deep seismic sounding data (*e.g.*, Zorin [1977]). Nikolayev *et al.* [1985] report maximum sediment thicknesses of 2.5-3 km in the central and southern basins and 1.5-2 km in the northern basin based on an analysis of continuous seismic profiles and imply that many researchers have misinterpreted Jurassic platform sediments beneath the lake as part of the synrift sedimentary sequence. More recent analyses of multichannel seismic data by Hutchinson *et al* [1991 and pers. comm.] have led to revised estimates of 4-7 km of sediments in some parts of the lake, and a sediment thickness map based on their MCS results is shown in Fig. 2.3. The thickest sediments are concentrated along the western edge of the South and Central Basins where the Obruchev normal fault enters pre-rifting basement. The sedimentary pile thins from greater than 7 km at places along this edge to about 1 km close to the eastern shore. In the North Basin,

preliminary data show that the sediments reach thicknesses of greater than 4 km and thin towards the east over a much smaller distance than in the South and Central basins.

The age of sediments in Lake Baikal has also been the subject of much debate. The Southern basin, recognized as the oldest axial basin in the BRZ system on the basis of its morphology, structure, and depth, may have sediments as old as Late Cretaceous to Middle Miocene age [Logatchev and Florensov, 1977] or be floored by sediments of only Paleogene to Early Miocene age [Nikolayev *et al.*, 1985]. In their interpretation, the base of the Baikal sedimentary complex is correlative with the Miocene to Early Pliocene Tankhoy formation, consisting of siliciclastic rocks interbedded with coal-bearing layers and clays. An angular unconformity, which marks the beginning of rifting in this interpretation, separates the Tankhoy formation from the overlying Middle and Upper Pliocene poorly-cemented siliclastic rocks correlative with the Anosova Formation. A small unconformity at the top of the Anosova sediments marks the onset of deep-water sedimentation during Lower Pleistocene time. These deep water sediments consist of interbedded lacustrine sands and clays and may be confined primarily to the North Basin.

Although the new sediment thickness estimates of Hutchinson *et al.* [1991] probably supersede those of Nikolayev *et al.* [1985], many of their observations regarding the distribution, relative thicknesses, and features of sedimentary rocks still provide useful information about the relationships between faulting and basin and rift evolution. For example, they recognize truncated sediment beds along faults on the northwestern side of the lake in the South and Central basins and the lack of pre-Pleistocene sediments more than a few tens of kilometers north of the Academician Ridge transfer structure. These observations imply synchronous sedimentation and tectonism with the Baikal basins and indicate that the Academician Ridge is a long-lived structure which has controlled sedimentation patterns for at least several millions of years. The estimates Nikolayev *et al.* [1985] give for relative thicknesses of parts of the sedimentary pile within each of the three

Baikal basin may indicate that subsidence in the South and Central basins proceeded steadily from Miocene through Lower Pleistocene time while the North Basin has subsided only since the beginning of Pleistocene time.

Present rates of sedimentation reported by Karabanov (pers. comm.) and Sandimirov, Pampura, and Kuptsov (pers. comm.) for a small number of sites are 0.65 mm/yr in the South Basin, 0.95-1.2 mm/yr [Edgington *et al.*, 1990] for the Selenga Delta area, 0.46 mm/yr in the Central Basin, and 0.34 to 0.67 mm/yr in the North Basin. The factors which control sedimentation rate include climate, uplift rate, susceptibility of rocks to erosion, distance of basins from source rocks, various kinds of tectonic activity, and proximity to rivers. Thus, we exercise caution in assuming that the present sedimentation rates reflect the long-term history of Lake Baikal or that these rates even apply outside the local area in which they were measured. However, if these rates were constant with time, the 4-6 km section in most of Lake Baikal could be deposited within 6-10 my. Multichannel seismic profiles indicating widening of the rift's axis with time may imply that the basins of Lake Baikal have entered the thermal phase of subsidence, and the sedimentation rates measured at present likely underestimate the average rate since rift initiation.

SAYAN REGION

Due west of the southern end of Lake Baikal lies the East Sayan region. Major tectonic elements in this area include the Main Sayan fault, the associated East Sayan Range, and five rift basins: the east-west striking Tunka and Khoitogol-Mondy depressions and the north-south striking Khubsugul, Darkhat, and Busingol-Belin basins. Movement along the Tunka fault, which forms a major west-trending splay of the older Main Sayan fault, controls rift-related deformation in the Sayan area and perhaps throughout the whole southern end of the BRZ. However, much of the Sayan province

overlaps with the area of intense intraplate deformation in Mongolia and therefore serves as a transition zone between the discrete basins of the axial part of the BRZ and the strike-slip zones of Mongolia.

The Main Sayan fault, is among the major Asian strike-slip faults recognized by *Tapponnier and Molnar* [1979] and can be traced at least 600 km west-northwest from the southern tip of Lake Baikal on satellite photos. Landsat images reveal a well-developed discrete fault scarp entering Lake Baikal's southwestern tip and possibly emerging from its southeasternmost point for a distance of less than 10 km, implying that the part of Main Sayan fault forms the southern edge of the South Baikal basin. *Balla et al.* [1990] also argue that the Tunka Basin fault bounds the South Baikal basin. Satellite photos [Chapter 3] show that the active Tunka fault is merely a large splay of the mostly inactive Main Sayan fault although the Main Sayan fault may change from predominantly strike-slip to predominantly dip-slip within a few kilometers of the lake where the Tunka fault intersects the main scarp. Initial deformation along the entire length of the Main Sayan fault may have begun in Archaen or Early Proterozoic time when right-lateral thrusting apparently predominated. Cenozoic reactivation of the fault led to a change in its polarity from thrust to normal and right-lateral to left-lateral and probably a switch in the locus of displacement from the Main Sayan fault proper to the more southerly Tunka splay. Tight constraints for the duration and amount of Cenozoic displacements along the Tunka splay of the Main Sayan fault are lacking, but the fault zone has many of the classic features of mature strike-slip systems, including secondary extensional fractures and Riedel shears and areas of transpression and transtension related to slight changes in fault orientation. Seismicity patterns, crustal thickness data, and surface geology show that deformation along the active portion Main Sayan fault has been predominantly thick-skinned. Thus, the Main Sayan fault probably serves as a fundamental boundary between the Siberian platform and the more deformed and deformable crust of the Mongolian microplate while the Tunka fault

forms a major splay of the Main Sayan fault and separates the older Sayan mountains from the younger rift basins of northern Mongolia.

The five extensional basins of the East Sayan region lie south of the Main Sayan fault in Mongolia and near the southern border of the Soviet Union. From west to east, the Busingol-Belin, Darkhat, and Khubsugul (Hövsgöl in *Tapponnier and Molnar's* [1979] terminology) basins represent the westernmost extension of the BRZ, and *Logatchev and Florensov* [1978] argue that these three meridionally-oriented basins are among the youngest in the region, having been initiated only since the beginning of Pliocene time. Soviet geological maps imply that these basins form as two-sided grabens between paired normal faults bounding their western and eastern sides. Alternately, the basins may be pull-apart structures between two large-scale subparallel predominantly strike-slip faults. The Tunka basin bounding fault, which has both left-lateral and dip-slip components, runs close to the northern edge of the three meridionally-oriented Mongolian basins, and *Tapponnier and Molnar* [1979] recognize the east-west striking left-lateral Hangayn fault and possibly other left-lateral faults within 100km south of the basins. Additional evidence for the role of strike-slip displacement in the evolution of the easternmost of the three north-south basins, the Khubsugul, is provided by the distribution of young basalts south of the Lake Baikal and east of Khubsugul basin. These basalts outline nearly a perfect rhomboid over 100 km long on each side and may therefore mark the highly extended edges of a pull-apart type structure.

Closer to the Main Sayan fault lie the east-west oriented Tunka Basin and the smaller Khoitogol-Mondy (KM) Basin. The Tunka basin forms a latitudinally-elongated rhomb with pronounced south-directed asymmetry while the KM basin has a more symmetric form. The major structural feature associated with the Tunka basin is the Tunka fault, a 200km long left-lateral normal fault which runs from the Main Sayan fault scarp on the east, along the northern edge of the Tunka Basin, and finally out of the basin to the

west and south. On the north side of the Tunka Basin, the high mountains of the Tunka Alps lie in the footwall of the normal fault, and evidence for the presence of a pervasive foliation with the same orientation on both sides of the basin indicate that the Tunka fault may be a feature of regional-scale importance. The pronounced lateral heterogeneity of the Tunka Alps, including elevations which decrease from over 3000m to 2100m from west to east and a change in strike from ENE to WNW, may be associated with one or more transfer structures that pierce the Tunka fault at a high angle and divide the floor of the Tunka basin into several depocenters. In situ cinder cones, ash-laden detrital material and basaltic flows within one of the uplifted horst structures along the transfer faults, and hot springs with temperatures in excess of 45°C imply the presence of hot crust beneath the Tunka basin.

BARGUZIN AREA AND THE ACCOMODATION ZONE

The Barguzin Basin, the largest BRZ basin not contained within Lake Baikal, measures 150 km from southwest to northeast and lies east of Lake Baikal, striking slightly oblique to the North Baikal basin. The high Barguzin range (2500m) separates the North Baikal basin on the west from the Barguzin basin on the east and widens to the north where the Barguzin Basin and Tsipi-Bount Basin bend into the left-lateral Udokan shear zone. Marshes abut the Barguzin Range along the western side of the Barguzin basin while on the east well-developed alluvial fans comprised of older Quaternary sediments occur at the base of the low (1500m) Ikat Range. The Barguzin basin thus displays the same westward-directed asymmetry as is observed in the Baikal basins.

Many features of the Barguzin basin province imply that this area serves as an accomodation zone between the southern and northern parts of the BRZ. The Barguzin-Tsipi-Bount basin system is roughly bounded on the south by the Academician

Ridge oblique-slip structure and on the north by the Udokan shear zone, and the orientation of principal structures within the Barguzin zone is consistent with the sense of shear displacement between these two features. Differential motion between the Udokan and Academician Ridge systems may contribute to compression in the wide northern part of the Barguzin Range, southward tilting and narrowing of the Barguzin Basin floor, and the observed sense of basin asymmetry. The Barguzin basin contains 2 km or more of predominantly Miocene and Pliocene sediments while the sedimentary fill of the North Basin dates only to early Pleistocene time. Thus, the Barguzin basin may have been the primary site of extension and sedimentation in the northern part of the rift zone prior to the Pleistocene onset of rapid subsidence in the North Baikal basin. However, the high seismicity of the Barguzin basin compared to the nearly complete lack of seismic events within the North Baikal basin indicates that the Barguzin accommodation zone continues to play an active role in axial rift zone processes. Coupled with multichannel seismic data of *Hutchinson et al.* [1991] which show North Basin sediments to be flat-lying and undisturbed by faults, the geophysical data support the interpretation that the Barguzin Basin, not the North Basin, represents the active northern part of the rift's axial zone.

UDOKAN REGION

The fourth tectonic province in the BRZ is the 800km long Udokan left-lateral shear zone, which extends ENE from the northern end of Lake Baikal. This area is characterized by high average elevations and pronounced along-strike heterogeneity. Close to Lake Baikal lie the en echelon Lower and Upper Angara Basins. These basins have nearly perfectly rhombohedral forms and are bounded by left-lateral strike-slip faults running roughly NNW and range-front normal faults subparallel to the overall strike of the shear zone. In the Upper Angara basin, the outcrop patterns of old and young Quaternary

sediments imply pronounced north-directed asymmetry, and sediment thickness has been estimated at only 1 to 1.2 km from seismic reflection data. Further to the east, roughly at the intersection of the Barguzin accommodation zone and the Udokan shear zone, lies the Muya Basin, the most irregularly shaped of all the BRZ basins. The morphology of the Muya Basin is apparently controlled not only by the Udokan shear zone and Barguzin accommodation zone but also by the presence of a geologically complicated Aldan shield block along its northern side. East of the Muya basin, the Udokan shear zone turns abruptly to the NE along the edge of the Aldan shield. The outermost BRZ basins, the Chara and Tokka Basins, lie in the northeastern extension of the Udokan shear zone and are apparently not connected to each other or to the Muya basin by any simple structures. Although the morphology, structures, and geology associated with these outermost basins clearly distinguishes them from the Baikal basins, an important shared characteristic is the overall tectonic setting of the Chara and Tokka Basins and those that form the rift's axis: All develop along the edge of the Siberian platform or Aldan shield, which apparently serves as the single most important tectonic element within the BRZ.

DATA

TOPOGRAPHY

In the absence of field-based observational data, topographic and bathymetric maps provide important clues about the active fault structures and neotectonic features of the BRZ. The map shown in Fig. 2.4a was compiled from digitized topographic and bathymetric contour maps at scales of 1:500,000 and 1:1,000,000 respectively. This map clearly delineates fault scarps, asymmetric rift basins, and the complicated patterns of

compression and extension associated with strike-slip and normal sense displacements.

Topographic domes often characterize continental and oceanic rift systems, and 2000-km long topographic profiles perpendicular to Lake Baikal (Fig. 2.4b) indicate that a domal feature of approximately 400m amplitude is also present in the BRZ. The relationship between this topographic dome and rift-related deformation is unclear however: Siberian platform sediments thicken eastward towards the suture zone at the site of Lake Baikal, and much of the high topography in the folded zone east of the lake is probably a remnant of older compressional deformation. Data on the distribution, lithology, and age of sediments provide the most important constraint on how much of the observed doming is spatially and temporally related to rifting processes, but such an analysis has not yet been undertaken in the BRZ. Regionally compensated crustal thickness variations of 0 to 4 km could produce nearly all of the domal topography.

The long topographic profiles also highlight the morphology of the rift axis and rift flank uplifts. The rift axis occurs off the center of the dome towards the northwest and displays considerable along-strike heterogeneity in its degree of asymmetry and depth of basins. Rift flanks display similar variation both along strike and from west to east across the lake. Although the wavelength of rift flank uplifts remains relatively constant at approximately 150 km along the length of the rift, the amplitude of these features increases from south to north. North and west of the rift axis, the rift flanks rise sharply out of the gentle domal topography, but, to the east, no pronounced topographic break between the folded belt and rift shoulders is evident at some positions along the rift.

SEISMICITY

The BRZ and the nearby Mongolian region to the southwest and Udokan region to the northeast are among the most seismically active regions within the Asian continent and

have been the site of many events of magnitude 4.5 or greater in the last quarter century. Figure 2.5a and the appendix provide a compilation of over 450 epicentral locations for earthquakes between 1814 and 1990. Soviet catalogs [*Atlas of Russian Earthquakes*, 1962; Kogan, pers. comm.] provide approximate epicentral locations for 6 events between 1814 and 1903, 40 events between 1903 and 1951, and over 100 events between 1952 and 1981. Comparison of the epicentral locations given by the ISC for post-1964 events and those provided by Soviet catalogs yield differences less than one-tenth of a degree in most cases, but we use ISC, not Soviet, epicenters for the 1964-1989 events listed in both catalogs. *Doser* [1991a, b] recently relocated over 60 events of magnitude 4.5 to 5 between 1950 and 1989, and her epicentral locations are assumed to supersede those provided by both the ISC and Soviet catalogs for these events.

In order to characterize the nature of seismicity in the BRZ on a large scale, we compile focal mechanism data for 52 events between 1950 and 1989. These focal mechanisms, shown in Fig. 2.5b and listed in Table 2.I, are taken from solutions by *Misharina* [1972], *Das and Filson* [1975], *Solonenko* [1977], *Misharina et al.* [1985], *Solonenko and Solonenko* [1987], and *Doser* [1991a,b] (all compiled by *Doser* [1991a,b], and Harvard CMT and represent only those earthquakes for which the distribution of first-motion data were sufficient to constrain the orientation of nodal planes closely. In choosing well-constrained events, we require at least 3 arrivals per quadrant and/or a subjectively non-ambiguous fit of the nodal planes to the first-arrivals. Some of the events for which *Doser* [1991a, b] provides solutions are therefore not shown here. In general, *Doser's* solutions differ significantly from those given by Harvard CMT, but appear to be much more consistent with first-motion data she presents.

Many researchers (*e.g.*, *Solonenko* [1978]) have noted the general trends of BRZ seismicity. The most striking feature is the aseismicity of the Siberian platform, even along edges bounded by major fault systems (*i.e.*, Main Sayan and Obruchev systems). Within

the tectonically complicated region southwest of the lake, seismicity is diffuse and spatially linked to a number of different faults. The northern edge of this diffuse zone closely follows the trace of one of the active Tunka splay of the Main Sayan fault, and focal mechanisms along the fault provide evidence for predominantly left-lateral strike-slip motion. None of the focal mechanisms in the entire East Sayan region and northern Mongolia have any significant normal fault component, supporting the interpretation that the rift basins of this region are primarily formed by coseismic displacement of strike-slip faults.

Seismicity in the axial region of the BRZ is concentrated in the South and Central Baikal basins. Poor station coverage makes precise determination of hypocentral depths difficult, and it is therefore impossible to constrain the deep geometry of the normal faults beneath the basins as suggested by *Jackson* [1987]. However, most events in the South and Central basins occur between 20 kilometers east of the lake's southeastern shore and 20 kilometers west of the northwestern shore. This distribution of events may represent the effects of systematic error in the location of epicenters or may result from the basin's asymmetry at depth. Earthquakes probably occur in bedrock far below the thick column of sediments accumulated on the northwestern sides of the basin along the Obruchev fault system and are therefore located tens of kilometers away from shore in this area. On the eastern side of the lake, earthquakes are likely associated with back-faulting of blocks within the hanging wall of the Obruchev fault and the distribution of epicenters may indicate gradual migration of the normal faulting regime into the mountains along the southeastern shore. This interpretation is consistent with the asymmetry of the rift zone, the lack of well-developed alluvial fans along the southeastern shore, and the relatively low topography on the rift's southeastern flank along the South and Central basins. Within the South Baikal basin, the Selenga delta and nearby Bugul'deyka horst have been highly seismogenic in recent times, and focal mechanisms in this area are consistent with normal

and strike-slip displacements on steeply-dipping faults striking parallel to the basins' sides [Doser, 1991a]. It should be noted that few seismic events occur near the Main Sayan fault along the southern edge of Lake Baikal despite evidence from stream offsets that this part of the fault has been recently active and serves as a major structural break between the platform and deformed areas. The high seismicity within the lake may therefore represent the delayed release of strain energy caused by aseismic displacement along the Main Sayan fault.

The pattern of BRZ seismicity changes abruptly across the Academician ridge transfer structure which separates the Central and North Baikal basins. The Central Basin and even the transfer feature itself are the sites of many small events, but, north of the Academician ridge, the main part of the North Basin is nearly aseismic as far south of the Baikal Range. The differences between the amount and pattern of seismicity in the South and Central Basins relative to the North Basin offer more evidence for the unique tectonic setting and evolutionary history of the North Basin within the BRZ framework. The few focal mechanism solutions for events near the Academician ridge and within the North basin reflect a varied pattern of faulting: The focal mechanism for an earthquake at the southern end of Olkhon Island, near the inferred position of the oblique-slip Academician ridge fault, is consistent with nearly pure strike-slip movement along a left-lateral fault oriented parallel to the submarine ridge. Just north of Svyatnoy Nos, a 1981 earthquake had both a thrust and left-lateral component consistent with the sense of offset observed in the island's ridge from Landsat photos [Chapter 3]. Even further north, along the eastern shore of the lake, the single available focal mechanism is consistent with displacement on a high-angle normal fault dipping toward the axis of the basin.

In contrast to the nearly aseismic North Basin, the nearby Barguzin Basin and accommodation zone have been the site of many events of magnitude greater than 4.5 since 1964. These events are generally characterized by normal sense displacement along faults

oriented subparallel to the axis of the basin, and the principal extension direction is therefore subperpendicular to the basin and oblique to the strike of the lake. The level of seismicity in the Barguzin Basin contrasts sharply not only with the North Basin to its west but also with the area of the folded zone to its east. Clearly, the Barguzin area is the major locus of coseismic deformation in this part of the rift system, and the rotation of principal extension axes [*Misharina and Solonenko, 1972*] from azimuths of approximately 140° in the Barguzin basin area to approximately 300° in the Udokan shear zone are consistent with the region's interpretation as an accommodation zone.

The Udokan zone north and east of Lake Baikal is well-defined by seismic events occurring within and between major rift basins along a line trending nearly due east. Within 200 km of the lake, seismicity is fairly diffuse, but, further to the east, earthquakes are confined to a narrower zone. Focal mechanisms in this region are consistent with movement along large-scale basin-bounding normal faults oriented both parallel to and oblique to the strike of the shear zone, but strike-slip displacements dominate for many earthquakes, particularly those associated with deformation in the outermost Chara and Tokka rift basins. *Golenetsky and Misharina [1978]* and *Doser [1991a,b]* interpret focal mechanism solutions to imply that tensional axes are oriented subperpendicular to the easterly trend of the chain of basins.

The vertical distribution of earthquakes in many tectonically active areas delineates seismic and aseismic zones which may correspond to regions of brittle and plastic deformation respectively [*Chen and Molnar, 1983*]. Figure 2.6 shows the depths of ISC earthquakes from 1964 to 1986 and depths for some events between 1917 and 1989 determined by *Doser [1991a,b]* using waveform modeling. ISC events for which fewer than 5 stations reported P-arrivals or those for which the source depth was arbitrarily assigned as the surface or the Moho are ignored. Hypocenter depths determined from data collected at stations more distant from the epicenter than the approximate depth to the

source are notoriously unreliable, and the ISC data in Fig. 2.6 therefore represent only the general vertical distribution of large earthquakes. Most events are confined to the upper and middle crust in the range of 0 to 20 km depth, while the lower 20 km of the crust, between depths of 20 and approximately 40 km, is nearly aseismic. These data loosely imply that brittle failure is the predominant deformation mechanism to 20 km depth and possibly deeper beneath the rift zone. However, recent studies by *Déverchère et al.* [1991] using data collected by the local Baikal seismic network indicate that up to 10% of all BRZ earthquakes may occur in the lower crust or upper mantle.

SEISMIC REFRACTION DATA

Seismic refraction data from the BRZ provide an important constraint on crustal thickness variations and the presence of possible density or thermal anomalies at crustal levels. Figure 2.7 shows Moho depths and upper mantle P-wave velocities determined by *Puzirev* [1981] and *Vinnik* [pers. comm.] from seismic refraction data. *Vinnik's* values represent a re-interpretation of existing refraction profiles (most likely those discussed by *Puzirev*) and should probably be considered average values. On the other hand, the results shown in *Puzirev* [1981], derived from both reflected and refracted arrivals, provide more complete coverage along the profiles, but may represent an over-interpretation of the data. For the data shown in Fig. 2.7, we arbitrarily assign errors in excess of ± 1 km for Moho depths and ± 0.1 km/sec for P-wave velocities. Actual errors may be significantly greater, particularly for crustal thickness data.

The Moho map in Fig. 2.7a highlights the localized nature of the rift: Although the Moho lies at depths of 35-45 km beneath Lake Baikal, the thickness of the crust both to the west and east of the rift axis lies in the 38-40 km range. The thinnest crust in the BRZ is 35 to 38 km thick and occurs beneath the Central basin, the Selenga delta, and the western

part of the Ulan-Burgasky Range. The region of thin crust, coincident with the position of the arched uplift of the surface described by *Logatchev and Florensov* [1978] and others, is displaced southeast relative to the rift axis, and, to both the southeast and northwest of this feature, the crust thickens to 39-40 km. The northern edge of the Moho upwarp is bounded by the Academician Ridge, and the crust thickens from an average of 36-37 km in the Central basin to 43 km along the Academician transfer fault. Still further north, crustal thickness varies between 43 km along the eastern edge of the North basin to 41 km along its axis.

The active rift basins due east of the northern tip of Lake Baikal show a wide variability in crustal thickness. No clear trend of crustal thickening or thinning is evident along the zone, and crustal thickness varies between 36 and 46 km with most values clustering in the 41-44 km range. At the southern tip of Lake Baikal, the tectonically active region near the Main Sayan fault also displays wide variability in crustal thickness (41-53 km), but there a clear trend emerges from the data: Crust in this area thickens from an average of 41-43 km just north of the fault to 47-53 km south of the fault, and the break between relatively thin and thick crust is best defined at the extreme tip of the lake where the crust thickens by 5-7 km at the position of the southern shoreline. Finally, crustal thickness data also provide important constraints on deformation within the Barguzin basin, one of the most active elements within the BRZ. Data along the axis of this basin show deepening of the Moho from 41 km at near its center to 47 km beneath the mountains which bound its southern end near Lake Baikal.

P-wave velocities beneath the BRZ range from 7.3 to 8.1 km/sec, but lie in the much narrower range of 7.7 to 8.1 km/sec close to the rift axis. Beneath the platform region west of the lake, P-wave velocities are 8.0 to 8.1 km/sec, normal for fairly cold lithosphere. A refraction profile along the axes of the North and Central basins consistently yields an upper mantle P-wave velocity of 7.7 km/sec. Just to the southeast of this

along-axis profile, a parallel survey along the eastern shore of the lake produced P-wave velocities of 7.8 km/sec. No data are available for most of the South Basin, but P-wave velocities at the basin's southern terminus and in the Sayan area cover nearly the entire range, from 7.5 km/sec at 50 km south of the fault in the Tunka basin and 7.8 km/sec just south of the fault trace to 8.0 km/sec immediately to its north.

The most significant local scale variations in upper mantle P-wave velocities occur in the non-riftogenic basins along the upper Selenga River and in the zone of active rifting due east of the northern tip of the lake. In the non-riftogenic basins, P-wave velocities are consistently 8.1 km/sec but drop to 7.9-8.0 km/sec to the east. Within and between the rift basins in the Udokan region, P-wave velocities are generally 7.7 km/sec, but locally are as high as 8.1 km/sec and as low as 7.3 km/sec. To the north, south, and west of the 7.7 km/sec zone, upper mantle P-wave velocities rise to 7.8 km/sec. The high variability of P-wave velocities within the Udokan region may reflect misinterpretations of the refraction data or, alternately, the presence of significant local variations in crustal lithology. It should be noted that the largest local P-wave velocity variations are spatially linked to the anomalous Muya basin and may therefore hold an important key to understanding the connection between evolution of this basin and the rest of the rift zone.

HEAT FLOW DATA

Figure 2.8 shows heat flow values measured between 1966 and 1984 [*Dushkov, 1985*]. Terrestrial heat flow measurements were carried out at depths of several hundred meters to more than 3000m in boreholes, while marine heat probes penetrating 1 to 2 m into bottom sediments were used for measurements in Lake Baikal. Some of the original data were corrected for climatic, topographic, and other factors, and Fig. 2.9a shows heat flow as a function of topography in the BRZ for both corrected and uncorrected data. Error

bars correspond to 7.5%, 15%, and 25% uncertainty in heat flow values based on the reliability value assigned to each measurement by the original researchers. Uncorrected data for Lake Baikal and BRZ basins and mountains are generally less than 75 mW/m^2 , while the corrected data range from 20 mW/m^2 to greater than 400 mW/m^2 . The highest heat flow values generally occur in the lake, between 250 m above sea level and 400 m below sea level, and recent measurements push the maximum heat flow value for Lake Baikal even higher than 400 mW/m^2 to greater than 1200 mW/m^2 [Crane *et al.*, 1991].

Figure 2.9b shows composite heat flow profiles across the North and South Baikal basins. Due to the difficulty of obtaining terrestrial heat flow measurements, the area off the axis of the rift (outside Lake Baikal) is poorly sampled. However, the few measurements west of the lake in the platform region allow us to establish an average background heat flow value of $45 \pm 10 \text{ mW/m}^2$, well within the range of values expected for old continental crust [Sclater *et al.*, 1980]. Major deviations from this background value occur only in young sediments of the Khanda river valley, where heat flow rises to nearly 100 mW/m^2 , and in the sediments of the Selenga delta, which are characterized by heat flow of $30\text{-}120 \text{ mW/m}^2$. Thermal conductivity at the sampled terrestrial sites averages approximately 3 W/m-K , corresponding to a thermal gradient of approximately 15°C/km in the upper crust beneath regions with heat flow equal to the background value.

Figure 2.9 also highlights differences between the heat flow patterns in the North and South Basins and the high variability of measured heat flow within the axial zone of the rift. On average, heat flow across the North Basin is higher than heat flow in the South basin, although these variations may not be significant in light of the large uncertainties in the measurements. Among the explanations for this difference are the presence of an anomalous heat source beneath the North Basin, more active hydrothermal circulation in fault zones, or thinner sediments and thus less sediment blanketing. The high variability of heat flow measurements within the lake (rift axis) has been explained by Crane *et al* [1991]

as an effect of meteoric water circulation along active fault zones beneath and around the lake and report the presence of hydrothermal vents similar to those found at mid-ocean ridges in the North Basin. The pattern of observed variations in heat flow values may also provide an important clue to the position of faults beneath the lake, as noted by *Crane and O'Connell* [1983] in lakes of the East African Rift system. As suggested by Crane [pers. comm.], connecting the sites of high ($>100\text{mW/m}^2$) and low ($<75\text{ mW/m}^2$) heat flow between adjacent profiles perpendicular to the lake's shores produces lines of constant heat flow trending subparallel to the basin-bounding normal faults (Fig. 2.9c) and may confirm the interpretation that heat flow within the lake is controlled by the circulation of water through fault zones. Hot springs (see Fig. 2.1) in the BRZ also are spatially linked with known faults and may be an effect of a similar water circulation process.

GRAVITY ANOMALY DATA

The available sources of gravity data for the BRZ include satellite measurements of the long-wavelength field, published profiles without scales (*e.g.*, *Zorin et al.* [1986]), the 100km by 100km free-air dataset used by *Kogan and McNutt* [1987], and five short (250-500 km long) Bouguer gravity anomaly profiles subperpendicular to the rift axis. Figure 2.10 shows long-wavelength free-air gravity anomalies in the BRZ area after removal of the Gem9 field up to degree and order 10. Free-air gravity anomalies range from less than -40 mgal over Lake Baikal to greater than +20 mgal over the folded zone and arched uplift region. At the wavelengths represented here, the free-air anomalies are closely correlated with topography only over the Sayan region and Lake Baikal. For example, the high topography of the Baikal Range is associated with a free-air low, whereas the basins of the Udokan shear zone and low-lying platform areas in the northwest corner of Fig. 2.10 correspond to free-air highs. This lack of correlation between free-air anomalies and

topography may imply that the gravity field shown here reflects the importance of subsurface density variations in much of the BRZ.

The long-wavelength simple Bouguer anomalies calculated from free-air measurements over the BRZ are dominated by a broad low of relative amplitude -80 to -100 mgal trending parallel to the rift axis. Just as the rift axis occurs off the center of the BRZ topographic dome towards the northwest, the axis also lies to the northwest of the center of the Bouguer anomaly low. As expected, the pattern of the simple Bouguer anomalies shows good correlation with topography: The folded zone and the area south of the Main Sayan fault are characterized by Bouguer anomaly lows, implying the presence of a compensating root beneath the high topography in these regions, while relative gravity lows and highs occur over the lake and platform regions respectively. The correlation between Bouguer anomalies and topography does not hold for the entire BRZ however. Perhaps one of the most significant features of the Bouguer field is the lack of evidence for root zones beneath high rift flanks. Although the bounding topographic highs along the rift axis generally have half-wavelengths less than 100 km, flexural support of these features should cause reduction of the Bouguer anomaly over a much wider area. The absence of certain predicted features in the Bouguer field may therefore provide further evidence that subcrustal processes (*e.g.*, small scale convection) may be involved in producing some features of the BRZ.

Figure 2.11 shows four Bouguer gravity profiles across the rift zone and the corresponding topographic profiles. These data were obtained from a Soviet map contoured at 10 mgal intervals based on measurements taken with a Soviet-built GAK-3M gravimeter during the 1950s. The original data were reduced using a crustal density of 2300 kg/m³; we have recalculated the simple Bouguer anomaly using the topographic dataset of Fig. 2.4a and crustal density of 2670 kg/m³ and removed the Gem9 field up to degree and order 15. The original data include terrain corrections whose magnitudes are

not provided, and our inability to recalculate these corrections using the preferred higher crustal density should have the effect of causing our final Bouguer values to be too low by approximately 1/6th the magnitude of the terrain corrections. Although these terrain corrections probably average under 20 mgal in most cases, we account for all of the possible errors in the data (including meter drift, subjective contouring of the original map, incorrect terrain corrections, elevation errors) by conservatively estimating error bars of ± 10 mgal for these data.

The primary features of the Bouguer gravity profiles are a short-wavelength minimum of 60 to 120 mgal amplitude at the position of Lake Baikal, short-wavelength highs up to 0 to 60 mgal amplitude on the rift shoulders, and a total signal of only 20-60 mgal on the rift flanks. Bouguer anomalies are generally constant at about -80 mgal in the area northwest of the rift axis and decrease steadily southeast of Lake Baikal. The southeasterly slope of the Bouguer profiles appears to steepen from south to north, from approximately 0.03 mgal/km in Profile II to greater than 0.1 mgal/km in Profile IV.

COMPENSATION OF SHORT-WAVELENGTH FEATURES

The depth of compensation beneath the BRZ provides a first order constraint on whether the processes responsible for the evolution and maintenance of the rift's features are confined primarily to the crust, mantle lithosphere, or underlying upper mantle. The primary techniques used to constrain the depth of compensation are forward modeling of gravity and crustal thickness data and admittance and coherence calculations.

PREVIOUS WORK

Previous efforts to constrain the depth of compensation in the BRZ include coherence analyses of long-wavelength gravity anomalies [*Diament and Kogan, 1990*] and

local studies of the short-wavelength low over the rift axis [Zorin, 1966]. Using the 100km by 100km free-air dataset of Kogan and McNutt [1987], Diament and Kogan [1990] calculate the Bouguer anomalies in a region 1600 km square over the BRZ and examine the coherence between the Bouguer signal and the topographic load. Their results are consistent with regional compensation of the rift by flexure of a 30 km thick elastic plate, lithospheric stretching by a factor of 1.2 to 1.5, and elevation of the 600°C isotherm to near the base of the 40 km thick crust. These results contrast with those of Zorin *et al.* [1986], who argues that the strong local minimum associated with the axial part of the rift zone can be explained by almost complete removal of upper mantle material beneath Lake Baikal (infinite stretching) and the impingement of asthenospheric material on the base of the crust. Zorin [1966, 1981] argue that this "great dike" hypothesis can explain the Bouguer anomaly low and long-wavelength domal uplift in the BRZ and elevated heat flow in the lake.

ADMITTANCE

One measure of the depth of compensation is the spectral admittance Q (*e.g.*, Dorman and Lewis [1970]), the isotropic isostatic response function calculated from averages of the Fourier transforms of topography $h(x)$ and Bouguer anomaly data $b(x)$ in discrete wavenumber bands, denoted here by angle brackets. Observed admittance $Q(k)$ is given by:

$$Q(k) = \frac{\langle B(k) H^*(k) \rangle}{\langle H(k) H^*(k) \rangle} \quad (2.1),$$

where $B(k)$ and $H(k)$ represent the Fourier transforms of Bouguer anomaly and topography data respectively, the asterisk denotes the complex conjugate, and k is the one or

two-dimensional wavenumber, $k=2\pi/\lambda=(k_x^2+k_y^2)^{1/2}$. To find the best-fitting elastic plate thickness, the observed admittance $Q(k)$ is compared to theoretical admittance Q given by:

$$\hat{Q} = -2\pi\rho_c G e^{-kz} \left[\frac{(\phi H_b^2 + H_t^2/\xi)}{H_b^2 + H_t^2} \right] \quad (2.2),$$

where z_m is the depth to the compensating interface, assumed here to be at the Moho, and constants have the meaning described in Table 2.II. In applying (2), we use the formulation of *Forsyth* [1985] and calculate \hat{Q} assuming various ratios f of bottom to top loading. H_b and H_t , the Fourier transforms of the amplitudes of the loads on the bottom and top of the crustal layer, are related by $|H_b| = f\rho_c |H_t| / \xi \Delta\rho$. Physically, the constants ϕ and ξ respectively represent the degree of regional compensation of bottom loads by flexure at the top of the crust ($\phi = 1 + Dk^4/\rho_c g$) and of top loads by flexure at the base of the crust ($\xi = 1 + Dk^4/\Delta\rho g$), where D is the flexural rigidity and g is the gravitational acceleration. For perfect local compensation of loading at a given wavelength, $\phi = \xi = 1$, while values of ϕ and ξ greater than 1 indicate regional compensation. To facilitate comparison between results obtained from examining various kinds of geophysical data, the depth of compensation calculations are presented in terms of elastic plate thickness T_e instead of flexural rigidity D . These parameters are related by $D = ET_e^3/12(1-\nu^2)$, where E and ν are Young's modulus and Poisson's ratio, taken as 100GPa and 0.25 respectively.

Figure 2.12a shows Q as a function of wavelength for box corresponding to the 12° by 14° region shown in Fig. 2.4a.. Bouguer gravity anomalies were calculated from the 100km x 100km free-air dataset of *Kogan and McNutt* [1987] with the Gem9 field up to degree and order 15 removed, and topography is taken as the weighted average topography in a 1° square areas centered on the gravity datapoints. For $\rho_c = 2670 \text{ kg/m}^3$, admittance Q ranges from approximately -0.105 mgal/m at 2500 km wavelength to -0.015 mgal/m at 150 km wavelength. Due to the wide spacing of the data however, only wavelengths greater

than approximately 400km are adequately sampled, and we therefore consider the results for the two smallest wavelength bands unreliable. For longer wavelengths, particularly those in annuli centered on 850km and 2500km, admittance Q plots above theoretical \hat{Q} curves for no bottom loading ($f=0$) and all elastic plate thicknesses T_e .

Explanations for overly negative observed admittance at intermediate and long wavelengths include a) use of incorrect ρ_c in conversion of free-air to Bouguer anomalies and thus calculation of Q , b) overcompensation of long wavelength loads, c) the presence of a long-wavelength Bouguer gravity anomaly gradient not correlated with topography, and d) dynamic compensation at long wavelengths. Recalculation of Bouguer anomalies, Q , and \hat{Q} using crustal densities both lower and higher than 2670 kg/m^3 results in a slightly closer correlation between theoretical and observed values for $\rho_c = 2500 \text{ kg/m}^3$ and slightly worse correlation for $\rho_c = 2800 \text{ kg/m}^3$. No reasonable value of crustal density brings Q at the longest wavelengths significantly closer to \hat{Q} however. Q values that are too negative at the longest wavelength sampled may also indicate “overcompensation” of topographic loads, defined as flexure of an elastic plate beyond the amount predicted by local compensation mechanisms ($D=0$; Airy isostasy). The failure of the elastic plate model at these wavelengths may therefore be more consistent with Pratt-type compensation of surface loads.

The data shown in Fig. 2.11 indicate that an appreciable regional gradient remains in the Bouguer gravity anomaly profiles at some positions along the rift, even after the removal of the long-wavelength satellite-derived gravity field. The presence of a long-wavelength Bouguer anomaly gradient not correlated with topography could cause Q to be more negative at long wavelengths and may lead to the observed pattern of admittance values. Finally, in studies of the East Africa Rift, *Ebinger et al.* [1989] have proposed that admittance values more negative than \hat{Q} at long wavelengths may indicate the presence of a dynamic compensation component. The gravity data for the BRZ are too poor to support

this contention only on the basis of the admittance results, but the pattern of observed Q values is qualitatively consistent with the some dynamic compensation of long wavelengths.

Based only on the admittance results in Fig. 2.12a, it is not possible to constrain the mode or depth of compensation in the BRZ. When uncertainties are taken into account, the Q values could imply overcompensation of long-wavelength features and failure of the elastic plate model. If the 850 km wavelength point reliably represents the data, then an elastic plate with significant flexural rigidity ($T_e = 40-60$ km) loaded from below ($f=1-5$) could be responsible for the observed pattern of Q values. Finally, the overly negative admittance at the longest wavelength may provide more information about the role of dynamic compensation than about the level of compensation within the crust or upper mantle.

COHERENCE ANALYSES

Coherence techniques measure the correlation between Bouguer gravity anomalies and topography and are not subject to many of the problems inherent in admittance calculations. The poor admittance results obtained above may reflect the presence of loads within the crust or mantle, instead of at the compensating interfaces, the combination of tectonic provinces with different thermal and mechanical properties, and bias towards low rigidities introduced by the weighting of Bouguer anomalies proportional to the square of topography. As demonstrated by *Forsyth* [1985], the coherence technique effectively avoids some of these difficulties. Observed coherence γ^2 is given by:

$$\gamma^2 = \frac{\langle B(k) H^*(k) \rangle^2}{\langle H(k) H^*(k) \rangle \langle B(k) B^*(k) \rangle} \quad (2.3),$$

where the notation is the same as in (1). Theoretical coherence γ_0^2 is calculated from:

$$\gamma_0^2 = \frac{\langle H_t W_t + H_b W_b \rangle^2}{\langle H_t^2 + H_b^2 \rangle \langle W_t^2 + W_b^2 \rangle} \quad (2.4),$$

where $H(k)$ and $W(k)$ represent the Fourier transforms of loads and corresponding deflections as a function of wavenumber and the subscripts t and b refer to loading and deflection at the top and bottom of the crust respectively.

Figure 2.12b shows coherence results obtained for one-dimensional Bouguer anomaly profiles shown in Fig. 2.11 and for two-dimensional Bouguer anomalies calculated on the 100km by 100km grid covering a 10° by 10° area from 50 to 60°N and 100 to 110°E. The two-dimensional region we use for spectral analyses is smaller than the area used by *Diament and Kogan* [1990] and should therefore more accurately represent the mode of compensation of the BRZ itself, instead of the average compensation mechanism for a greater part of the Asian continent. At long wavelengths in the two-dimensional dataset, coherence is nearly 1, implying local compensation of such features as the topographic swell. Coherence falls off in the wavelength annulus centered on 850 km wavelength and reaches 0.5 at approximately 300 km wavelength. This pattern of coherence corresponds to flexural rigidity D of 7×10^{22} Nm to 6×10^{23} Nm ($T_e = 20$ -40km), close to the 2.8×10^{23} Nm value of *Diament and Kogan* [1990]. The similarity between their results and those obtained here indicate that the region close to the BRZ is compensated by the same average mechanism as the larger area which surrounds it. Processes contributing to the development of the BRZ may control the flexural rigidity of the entire region or, alternately, the BRZ may be such a localized feature that the widely-spaced data used in this analysis do not adequately represent its mode of compensation.

To test these hypotheses, we calculate coherence for the one-dimensional Bouguer profiles in Fig. 2.11, taking into account the effects of water and sediment loads in Lake Baikal. The coherence results, denoted by symbols other than filled circles in Fig. 2.12b, indicate high coherence to short wavelengths and are generally consistent with support of the BRZ by a weak plate with rigidity of 1.5×10^{20} Nm to 9×10^{21} Nm, corresponding to T_e values of 2.5 to 10 km. The disparity between the T_e values obtained using the two-dimensional data and the one-dimensional profiles may imply weakening of the crust close to the axial part of the BRZ. However, highly correlated Bouguer gravity and topography signals like those in the profiles used here results in relatively high coherence values at short wavelengths and thus underestimation of T_e .

CONVENTIONAL FORWARD MODELING TECHNIQUES

Calculations of theoretical gravity and deflection based on the flexure of thin elastic plates assume that topographic loads are compensated by the density contrast at the Moho. Failure to duplicate observed gravity and crustal thickness variations with simple elastic plate models may therefore provide information about the relative depth of compensation for various topographic loads or may merely indicate the presence of anomalous masses within the crust or mantle lithosphere. In the absence of complete two-dimensional gravity data over the BRZ, the only constraints on these sorts of calculations are the one-dimensional gravity profiles and crustal thicknesses obtained from the analysis of seismic refraction data. In the Fourier wavenumber domain, the transforms of deflection $w(x,y)$ and topography $h(x,y)$, denoted by $W(k)$ and $H(k)$ respectively, are related by:

$$W(k) = \frac{\rho}{(\rho_m - \rho)(1 + \alpha k^4)} H(k) e^{-kz_m} \quad (2.5),$$

where α is the flexural parameter, given by:

$$\alpha = \sqrt[4]{\frac{D}{\Delta\rho g}} \quad (2.6).$$

Equation 2.5 represents the isostatic response of lithosphere with flexural rigidity D to loading at various wavelengths k . The Fourier transform $B(k)$ of theoretical Bouguer gravity anomalies $b(x,y)$ can be calculated from deflection using the relation [Parker, 1973]:

$$B(k) = -2\pi G \Delta\rho e^{-2\pi k z_m} \sum_{n=1}^{\infty} \frac{(2\pi k)^{n-1}}{n!} W(k)^n \quad (2.7).$$

In practice, $W(k)$ is calculated such that average deflection about an interface at a depth of w' from z_m is 0. The value of w' is given by Equation 2.5 for $k=0$, and Bouguer gravity $b(x,y)$ calculated from Equation 2.7 is adjusted by a factor of $-2\pi G \Delta\rho w'$, equivalent to applying a uniform DC shift to the theoretical gravity field. This method of calculating theoretical deflection and Bouguer gravity anomalies assumes that topographic loads are compensated only by flexure at the Moho interface and that the supporting elastic plate is continuous and has constant flexural rigidity.

Using the topographic dataset of Fig. 2.4a, we calculate theoretical deflection and Bouguer gravity anomalies in two dimensions by summing the contributions of the topography and water above a datum at 0m (sea level) and the contribution of water and sediments below 0 m. Synthetic gravity and deflection data were then compared to observed Bouguer anomalies and crustal thickness variations along Profiles I-IV. For all of the profiles discussed here, the negative load associated with the basin produces a compensating upwarp of the Moho. Filling the basin with water causes a downward depression of the Moho and leads to the superposition of a short-wavelength negative anomaly on the longer wavelength positive anomaly caused by the Moho upwarp beneath the basin. When the wavelengths of the gravity anomalies due to the two opposing basin

signatures differ by a large amount, as is the case for thin elastic plates, the total gravity anomaly may be positive over the rift flanks.

Sediment corrections

The Bouguer gravity profiles are dominated by large amplitude short-wavelength negative anomalies over Lake Baikal, features which cannot be fit without the inclusion of the negative load of thick sedimentary sequences in the axial basins. Traditionally, the negative relative gravity anomaly caused by the juxtaposition of sediments against denser crustal rocks is calculated assuming constant density throughout the sedimentary column. As demonstrated by *Cowie and Karner* [1990], this simplification usually results in overestimation of the magnitude of the negative gravity anomaly over basins. They instead propose the use of a Fourier-domain scheme for calculating the gravity anomaly due to a column of sediments whose density varies with depth according to exponential compaction curves. The density-depth function for exponentially compacting sediments is given by:

$$\Delta\rho(z)=(\rho_c-\rho_w) \Phi_0 e^{-k_p(H-z)} \quad (2.8),$$

where Φ_0 is porosity at the top of the sedimentary column, H is the depth at which all material has density ρ_c , k_p is a constant wavenumber describing the e-folding depth of the porosity function, and other constants are given in Table 2.II. The Fourier transform of the gravity anomaly due to these sediments of density $\Delta\rho(z)$ filling a basin in crust of density ρ_c is given by:

$$\Delta G(k) = -2\pi G e^{-kH} \sum_{n=0}^{\infty} \frac{k^n}{n!} \mathcal{F} \left\{ \int_{H-s}^H u^n \Delta\rho(u) du \right\} \quad (2.9),$$

where k is the two-dimensional horizontal wavenumber, \mathcal{F} denotes the Fourier transform, $s(x,y)$ is thickness of sediments, the integration variable u equals $H-z$, and constants are as given in Table 2.II.

If ρ_c and ρ_w are assumed constant at 2670 kg/m^3 and 1000 kg/m^3 respectively, the gravity anomaly calculated from Equation 2.9 is dependent on the choice of Φ_0 , k_p , and H in Equation 2.8. The sediment density relationship is least sensitive to choice of H , the most well-constrained of the three variables. Since the maximum thickness of sediments in Lake Baikal is greater than 7 km, we choose H to be 8 km. In order to estimate k_p , we assume a nearly linear relationship between porosity and compressional wave velocity [Wyllie *et al.*, 1956] and use velocity-depth curves derived from multichannel seismic studies of Lake Baikal sediments [Hutchinson, pers. comm.] to determine an e-folding depth of approximately 2.5 km for porosity. Combined with observations which constrain Φ_0 to be equal to approximately 0.6 [Karabanov, pers. comm.], Equation 2.8 describes density-depth function C in Fig. 2.13. Since sediment density is most sensitive to variations in Φ_0 and since this parameter is probably the least well-constrained in Equation 2.8, we also test $\Phi_0 = 0.2, 0.4, \text{ and } 0.8$, which correspond to density-depth Curves A, B, and D (respectively) in Fig. 2.13. The average density of sediments in Lake Baikal ranges from approximately 2000 kg/m^3 for Curve D ($\Phi_0 = 0.8$) to 2100, 2300, and 2500 kg/m^3 for $\Phi_0 = 0.6, 0.4, \text{ and } 0.2$ respectively (Curves B-D).

In calculating the theoretical Bouguer gravity profiles, we simultaneously vary two parameters: (1) the thickness of the elastic plate (0, 10, and 30 km; $D = 0 \text{ Nm}$ (local Airy compensation), $8.9 \times 10^{21} \text{ Nm}$, and $2.4 \times 10^{23} \text{ Nm}$ respectively) which flexes in response to the applied topographic load and (2) the form of the density-depth function for sediments in Lake Baikal. Thus, sediment corrections are applied to the model in order to reproduce the observed data; we do not simply subtract an estimate of the gravity contribution of sediments from the data. Sediment thicknesses within the lake are determined by interpolation and gridding of an incomplete map compiled from MCS data by *Hutchinson et al.* [1991] and reproduced in Fig. 2.3. We note particularly that the large degree of lateral heterogeneity in the distribution and thickness of sediments means that shifting

Profiles I and III (refer to Fig. 2.11a) by less than 10 km south or north (respectively) significantly affects the magnitude of the theoretical gravity anomaly low due to sediments.

Profile I

Profile I, whose location is shown in Fig. 2.11a, crosses the southern part of the BRZ at the Selenga delta, a complicated region near the junction of the South and Central Baikal basins. Figure 2.14a presents a summary of all geophysical data along Profile I. Rift flanks in this part of the BRZ rise 450m above the lake's surface on the west and 650m on the east, and the bathymetric profile shows even more pronounced westward-directed asymmetry within the lake, where the deepest point occurs close to the northwestern shore against the scarp of the Obruchev fault system. Heat flow data along the profile range between 35 and 90 mW/m², and no clear trend emerges except along the steep northwestern side of the basin, where heat flow decreases rapidly from the basin's edge towards the deepest part of the lake. The Bouguer gravity anomaly along the profile slopes constantly at approximately -0.15 mgal/km towards the basin from the northwestern side, and no deviations from this constant slope are spatially correlated with the rift flank uplift. The axial Bouguer low has amplitude of approximately -90mgal and a wavelength shorter than the entire basin and delta region but longer than the principal bathymetric deep. A short-wavelength positive anomaly of relative amplitude 20mgal occurs 40 km basinward of the rift's southeastern flank, but data do not extend far enough eastward to constrain the relationship between the flank uplift and the rift.

Predicted Bouguer anomalies calculated using elastic plates of thickness 0, 10, and 30 km and the preferred density-depth function (Curve C in Fig. 2.13) do not match any of the features of the observed Bouguer profile (Fig. 2.14a). Most importantly, the calculations do not predict the observed slope of the western side of the profile, the flat Bouguer anomaly on the rift shoulders, or the implied positive step of approximately 20

mgal between the observed Bouguer values on the west and east sides of the basin. Furthermore, not only does the magnitude of the basin gravity low misfit the observations by at least 40 mgal, but the narrow width of the deepest part of the basin relative to the width of the observed Bouguer anomaly means that any theoretical gravity low over the basin will have too short a wavelength to match the observations in this part of the profile. Much of the misfit can probably be attributed to the presence of sediments of unknown thickness in the Selenga Delta, which forms the eastern part of the Baikal basin in this profile. This possibility is further supported by crustal thickness data which indicate that the Moho shoals from approximately 39 km under the northwestern rift flank to approximately 36-37 km under the basin and Selenga delta. This lateral variation in crustal thickness is roughly consistent with local Airy compensation under the rift's axis. If sediments replace some of the denser crustal material beneath the Selenga delta creating an upwarp of the Moho in this area, the agreement between the theoretical and observed deflections for the Airy model should be even better.

Figure 2.14b shows a comparison between observed and theoretical Bouguer gravity anomalies calculated using elastic plates of 0, 10, and 30 km thickness and sediment density-depth functions corresponding to Curves A-D in Fig. 2.13. For the water-sediment-basin profile shown at the bottom of Fig. 2.14b, even the combination of the stiffest elastic plate and the lowest average sediment densities ($\Phi_0=0.8$)—a combination which should produce the maximum Bouguer low over the basin—cannot reproduce the observed magnitude of the basin Bouguer anomaly.

Profile II

Profile II (location shown in Fig. 2.11a) crosses the axis of the rift zone at the southern tip of Olkhon Island where the oblique-slip Academician ridge structure and the basin-bounding normal fault intersect. Geophysical data for Profile II are summarized

in Figure 2.15a. Heat flow data along Profile II range from 40-100 mW/m² and rise less rapidly towards the center of the basin from the northwestern edge than from the southeastern edge. The observed Bouguer profile is characterized by a regional slope of approximately -0.03 mgal/km, a negative anomaly of amplitude -90 mgal over the lake, and a 60km wide +40 mgal signal over the rift's northwestern flank. The local positive Bouguer anomaly on this side of the basin is spatially correlated with the steep scarp which forms the basin's northwestern edge and an associated rift flank uplift of approximately 400m amplitude.

Theoretical Bouguer anomalies calculated assuming compensation of the topographic load by the flexure of elastic plates of 0 and 10 km thickness and a sediment density-depth profile corresponding to $\Phi_0=0.6$ predict flanking Bouguer anomaly highs northwest and southeast of the rift axis and lows of approximately -50 and -70 mgal amplitude (respectively) over the lake. While the general morphology of the theoretical Bouguer gravity curves is similar to the observed Bouguer profile, the observed data are characterized by a Bouguer high only on the northwest rift flank and a basin low 40 or more milligals more negative than the theoretical values. Aside from the general wavelength and amplitude similarities between the theoretical and observed Bouguer anomalies, the calculation indicates only flexure of a thin (0-10 km) elastic plate produces gravity anomalies which more closely match the data along the non-basin portions of the profile. The close agreement between the observed and theoretical Bouguer values over the lake for the stiffer plate ($T_e=30$ km) is merely a consequence of superimposing the large low due to sediments on the small relative positive anomaly created by the gentle long-wavelength upwarp of the Moho beneath the relatively negative water and sediment load.

Crustal thickness data along Profile II are poorly distributed, but are loosely consistent with shoaling of the Moho toward's the center of the basin and deepening of the

Moho by up to 5 km just southeast of the rift axis. None of the theoretical deflection curves closely match the observed crustal thickness data along this profile although the form of the Moho is most consistent with Airy compensation of surface features coupled with the presence of subsurface loads of low relative density.

Figure 2.15b shows a comparison between observed Bouguer anomalies and those calculated assuming all possible combinations of the three elastic plate thicknesses (0, 10, and 30 km) and the four density-depth profiles for the sedimentary column ($\Phi_0=0.2, 0.4, 0.6,$ and 0.8). Airy compensation ($T_e=0$ km) of topographic and sediment and water loads produces the best overall fit to the observed Bouguer data, but even sediments with the lowest average density ($\Phi_0=0.8$) cannot fit the magnitude of the observed Bouguer low over the basin. Furthermore, while the wavelength and relative amplitudes of anomalies west of the lake are closely matched by the Airy model, the observed Bouguer values 50 to 150 km west of the rift's axis are more positive than the calculated values by approximately 10 mgal; anomalies within 50 km of the axis on the rift flanks are more negative than the calculated Bouguer anomalies by at least the same amount. East of the lake, an Airy mechanism predicts Bouguer values in close agreement with the observations except right at the lake's edge. At this position, the observed anomalies trace no local Bouguer high whereas the Airy model predicts the presence of such a rift-flanking high. Flexure of the stiff elastic plate ($T_e=30$ km) can reproduce the observed flat Bouguer profile close to the lake's eastern edge, match the anomalies at a distance of 50-150 km west of the lake, and reproduce the observed low over the lake for sediments of $\Phi_0=0.6-0.8$. However, the gravity anomalies due to flexure of the stiff plate do not match the wavelength or amplitude of the observations on the western rift flank and particularly cannot reproduce the local high on the lake's western shore.

Profile III

Profile III runs through one of the most tectonically-complicated parts of the BRZ axis (Fig. 2.11a), crossing into the axial part of the rift zone over the Baikal range and the basin-bounding normal fault along the western edge of the North Basin. The southeastern part of the profile passes close to the inferred intersection of the Academician ridge transfer fault and the eastern shore of the lake and eastward over the Barguzin range and into the southern end of the Barguzin basin. Heat flow data, shown with other geophysical data in Figure 2.16a, are clustered primarily in the 40 to 120 mW/m² range, but values as high as 400 mW/m² are recorded near the deepest point at the base of the lake's steep northwestern edge. The observed Bouguer gravity anomalies, plotted with a regional slope of 0.05 mgal/km removed, lack a significant rift-flanking high and are characterized by a basin minimum of only -75 mgal amplitude and a pronounced low to the southeast over the Ikat Range. The topographic profile coincident with the reported position of Profile III is shown in Fig. 2.11c. Rift flank uplifts northwest and southeast of Lake Baikal on the coincident profile have wavelengths and amplitudes of 100 km and 800 m and 30 km and 600 m respectively.

Based on the disparity between the magnitude of the observed gravity low over the basin and the thickness of sediments in Lake Baikal along the coincident topographic profile, we infer that the reported latitude coordinates of the profile may be imprecise by up to one-tenth of a degree. Sediment thicknesses 8-10 km to the south of the reported location of the profile are much greater than along the coincident profile, but the profile no longer crosses a peak in the Baikal Range on the westward flank of the rift. The calculation of theoretical Bouguer gravity anomalies is completed in the two-dimensional Fourier domain, and the profiles are then pulled out of the two-dimensional grid. Thus, the lack of a clear rift flank uplift along the shifted topographic profile does not greatly affect the

calculated gravity signal for compensation of topographic loads by flexure of elastic plates of non-zero thickness.

Theoretical Bouguer gravity anomaly curves calculated for 0, 10, and 30 km thick elastic plates each fit some features of the observed Bouguer signal. For example, the 0 km thick plate produces a gravity signal of the same form as the observed anomalies on the western flank of the rift, but the theoretical values are too negative by approximately 10 mgal. Over the basin, the best fit to the magnitude of the observed Bouguer anomalies is obtained using the stiffest (30 km thick) elastic plate for the preferred $\Phi_0=0.6$ value chosen here. However, a stiff plate cannot produce the local Bouguer highs which flank the basin on both the northwest and southeast. Finally, flexure of a 10 km thick elastic plate provides the best fit to both the wavelength and amplitude of the observed Bouguer anomalies southeast of the lake over the Barguzin basin and folded zone.

Figure 2.16b shows observed Bouguer anomalies plotted with calculated Bouguer profiles for all combinations of the three elastic plate thicknesses (0, 10, and 30 km) and four density-depth sediment curves ($\Phi_0=0.2, 0.4, 0.6,$ and 0.8). The best overall fit to the observed Bouguer anomalies is obtained for an elastic plate of 10 km thickness assuming sediments with $\Phi_0=0.8$ km. For this case, the observed and theoretical Bouguer anomalies differ by greater than 10 mgal only at distances greater than 100 km west of Lake Baikal. This mismatch is similar to that observed in the same region for Profile II and may indicate the presence of denser than average crustal material beneath some parts of the platform region, systematic deepening of the Moho towards the west, or possibly even some difference between mantle beneath the rift axis and folded zone and beneath the platform region away from the zone of active rift deformation.

Profile IV

Profile IV crosses the North Baikal basin and the Barguzin basin well north of the Academician Ridge transfer structure as shown in Fig. 2.11a. Heat flow, illustrated with other geophysical data in Fig. 2.17a, ranges from 40 to 160mW/m² (not including uncertainties) along this profile and is highest along the edges of the basin, near the inferred positions of the basin-bounding normal faults. These data display the same sense of asymmetry as the bathymetric profile, with the most rapid decrease in heat flow associated with the steeper northwestern slope of the basin. Distinct 50 km wide rift flank uplifts occur on the northwestern and southeastern sides of both the Lake Baikal basin and the Barguzin basin, and, in both instances, these uplifts have higher elevations on the southeastern sides of the basins. The observed Bouguer gravity anomalies are flat northwest of the rift axis, and no significant anomaly is associated with the pronounced relief of the rift flank. The short-wavelength basin low has relative amplitude of -115 mgal, the largest of any of the profiles, and a narrow 20 mgal high occurs at the position of the southeastern rift flank.

The theoretical Bouguer gravity anomalies calculated assuming $\Phi_0=0.6$ for the sedimentary fill and flexural support of topography by elastic plates of 0, 10, and 30 km thickness are plotted in Fig. 2.16a with observed data from which a regional slope of 0.1 mgal/km has been removed. Generally, the theoretical Bouguer curves reproduce only the relatively flat observed Bouguer field northwest of Lake Baikal. To the southeast, the theoretical Bouguer anomalies match neither the wavelength nor the amplitude of the observed Bouguer profile, and the misfit over the lake is in excess of 50 mgal even for the stiffest (30 km thick) plate.

Figure 2.17 shows the sediment thickness data for Profile IV and theoretical Bouguer gravity anomalies for all combinations of elastic plate thicknesses ($T_e=0, 10,$ and 30 km) and surface porosity of sediments ($\Phi_0=0.2, 0.4, 0.6,$ and 0.8) plotted with the

observed Bouguer signal. The best fit to the Bouguer anomalies west of the lake is obtained by assuming Airy compensation of the topographic load. Over the lake, however, even sediments with the lowest average density ($\Phi_0=0.8$) loading the stiffest plate do not produce a negative anomaly large enough to match the observations. The misfit is particularly large along the western side of the basin where the sediment thicknesses reported by *Hutchinson et al.* [1991] were interpolated due to lack of sufficient MCS data. The gravity data indicate that the sediment thicknesses along the western flank of the basin may be underestimated or that the sediments in the North Basin differ from those in the South and Central Basins. For example, if the sediments in the North Basin are overpressured or simply even less consolidated, the calculated magnitude of the low over the basin would be much greater and produce values in closer agreement with the observations. The unique role of the North Basin as a passive graben which has subsided rapidly only since the beginning of Pleistocene time renders it likely that the sediments vary significantly from those in the other basins. Furthermore, *Hutchinson et al.* [1991] note that the basement beneath the North Basin has different acoustic characteristics than the basement underlying the South and Central Basins, perhaps a further indication that the large negative gravity anomaly over the North Basin carries some hidden significance.

CRUSTAL THICKNESS VARIATIONS AND ISOSTATIC EQUILIBRIUM

Comparisons between observed and predicted crustal thicknesses may also provide a loose constraint on the depth of compensation in parts of the BRZ if the theoretical deflections predicted from regional compensation models can be shown to match crustal thickness variations. The crustal thickness profiles used for this comparison are those of *Puzirev* [1981] and are denoted by letters A-D in Fig. 2.7. Profile A runs subperpendicular to the axis of the rift just south of Bouguer anomaly Profile I and crosses

Lake Baikal where the basin is nearly symmetric and pronounced rift shoulders absent, while Profile B lies almost entirely within the older folded zone at distances greater than 200 km from the rift axis. Profile C samples the folded Baikal mountains northwest of the lake and the rift basins of the Udokan shear zone, and Profile D runs along the eastern side of Lake Baikal and axis of the Barguzin basin, roughly bounding the Barguzin accommodation zone on the southeast.

Theoretical Moho deflections along these profiles are calculated from Equation 2.5 for 0 km thick plate (Airy compensation) loaded by the topography shown in Fig. 2.4a. The assumption of Airy compensation causes the calculated deflections to be maximized. Thus, any crustal thickness variations in excess of the theoretical deflections must represent a departure from the simple crustal compensation mechanisms discussed here. Theoretical and observed crustal thickness variations for the Profiles A-D are shown in Fig. 2.18. In light of probable uncertainties in excess of 1 km for the crustal thickness data, Profiles A and B show generally good agreement between local compensation models and observed Moho depths. In Profile C, the misfit between theoretical and observed crustal thickness values is associated with thin crust beneath the Baikal Mountains. Thin crust west of the lake in this area offers further evidence for the existence of a Moho step across the suture zone and may indicate compensation of the Baikal Mountains by a thick elastic plate which does not flex significantly in response to the topographic load. In Profile D, the main region of mismatch occurs along the axis of the Tsipi-Bount basin at the edge of the Barguzin accommodation zone, but no obvious explanation exists for the presence of overthickened crust in this area.

THERMAL ANOMALIES BENEATH THE BRZ

An integrated analysis of the many kinds of geophysical and geological data presented here may provide information about whether a thermal anomaly exists beneath the BRZ and, if so, what the magnitude, form, and cause of the thermal anomaly may be. Heat flow data represent the most direct means of measuring the temperatures beneath the rift zone, but P-wave velocities, earthquake depths, and absolute gravity values also provide important means of describing the thermal structure of Baikal crust. Finally, interpretation of raw geophysical data yields information about elastic plate thickness, depth of compensation, Curie isotherm depth, and position of low-velocity zones, results which can be used to characterize any possible thermal anomaly indirectly. In the discussion here, we limit ourselves to a consideration of crustal and upper mantle thermal anomalies.

Heat flow values in the BRZ fall into two groups: Measurements outside the lake lie with the normal range for old continental lithosphere while data within the lake vary widely between 20 mW/m^2 and over 1200 mW/m^2 . The presence of a sedimentary column 4-6 km thick would reduce the background heat flow of 48 mW/m^2 by 0 to 30%, depending on the age of the sediments and their thermal conductivity structure and rate of internal heat generation. More precise calculation of the thermal blanketing effects of Lake Baikal sediments is presently not possible given the large number of unknown parameters, but even simple calculations underscore that heat flow should be reduced, not elevated, within the lake unless some process contributes to the presence of excess heat there. Neglecting the effects of fluid circulation in active fault zones at the bottom of the lake and advection of pore fluid within the sedimentary column for the sake of simplicity, one possible explanation for high average heat flow confined primarily to the lake and nearby basins would be an upper crustal thermal anomaly (*e.g.*, intrusion) directly beneath parts of the rift's axis. Any thermal anomaly at levels deeper than the upper crust would be

expected to produce elevated heat flow over a broader area than the lake alone and would thus be inconsistent with the heat flow observations.

P-wave velocities may also be used to characterize the thermal structure of the BRZ. P-wave velocities are markedly lower than the Siberian platform value of 8.0 to 8.1 km/sec only along the axis of Lake Baikal and in some parts of the Udokan shear zone. An estimate of the magnitude of the temperature increase ΔT necessary to produce the observed 0.3 km/sec reduction in P-wave velocities Δv_p beneath the rift axis can be made by applying the approximate relation $\Delta T = 0.5^\circ\text{C/m/sec} * \Delta v_p$ [Fischer *et al.*, 1988]. This calculation yields $\Delta T = 150^\circ\text{C}$ between the lower crust beneath the rift axis and beneath the platform and folded regions. While estimates of temperatures based on seismic velocities suffer from many complications, the calculated temperature difference would be consistent with the presence of a localized disturbance of the lower crust beneath the region of maximum extension at the rift axis. If an average crustal thermal gradient in the Baikal area is approximately 15°C/km , then the temperature at the base of the 40-km thick crust would be approximately 600°C , a value in agreement with the results of *Diament and Kogan* [1990]. The region of low P-wave velocities could therefore be associated with lower crustal temperatures of approximately 750°C , too cold for significant amounts of partial melt to be present. The increased thermal gradient due to such higher temperatures would not raise surface heat flow by an amount exceeding the large uncertainties associated with the heat flow measurements, even if we assume maximum crustal thickness differences of 5 km between the rift axis and the platform or folded zone. An approximate relation between P-wave velocity v_p and heat flow q is given by:

$$q = \frac{-K(T_0 + 0.5\Delta v_p)}{z_m} \quad (2.11),$$

where T_0 is the “normal” temperature at the base of the crust at depth z_m and Δv_p is measured relative to the P-velocity of “normal” crust. Figure 2.19 shows the theoretical

correlation between q and v_p plotted with observed BRZ data assuming $T_0=600^\circ\text{C}$ and 1000°C and v_p of “normal” crust equal to 7.8 km/sec or 8.0 km/sec. The lack of correlation between heat flow and lower crustal velocity may be an effect of the unreliability of heat flow measurements or of lateral variations in the magnitude of the radiogenic contribution to the observed heat flow. On the other hand, the results shown in Fig. 2.19 may indicate that upper crustal processes (*e.g.*, hydrothermal circulation in deep fault zones), not large-scale mid- or lower crustal thermal anomalies, exercise the primary control over surface heat flow measurements.

The distribution of seismicity beneath the rift zone also constrains the thermal structure at depth. The BRZ is more seismogenic than the Rio Grande, East African, Red Sea, Dead Sea, and Rhine Graben rift systems and is also characterized by earthquakes which occur to greater depths. For example, earthquakes in the hot Rio Grande rift occur primarily in the upper 12 km of the crust [*Rinehart et al.*, 1979; *Sanford et al.*, 1979], while the highly seismogenic layer of the crust is up to 20 km thick beneath the BRZ. Thus, the brittle-plastic transition, marked by the boundary between seismogenic and non-seismogenic crust [*Chen and Molnar*, 1983; *Meissner and Strehlau*, 1982], may occur at depths two times greater in the BRZ than in the some other rift zones. This observation, coupled with the prevalence of lower crustal and upper mantle earthquakes, implies that the BRZ is relatively cold at depth. For maximum extension of 30 km across a zone 200 km wide in a minimum of 4 my, the calculated strain rate in the BRZ is approximately $10^{-15}/\text{sec}$. Using this extensional strain rate and the estimated $15^\circ\text{C}/\text{km}$ temperature gradient and assuming a state of hydrostatic pore pressure, *Brace and Kohlstedt* [1980] conclude that brittle failure is the predominant mode of failure to a depth of approximately 17 km. Figure 2.20 shows yield strength envelopes calculated for a range of temperature gradients ($15\text{-}25^\circ\text{C}$) and average strain rates ($10^{-15}/\text{sec}$ to $10^{-16}/\text{sec}$) reported for the BRZ in the literature. We use the quartz flow law given by *Buck* [in press]

and assume that water content decreases exponentially from the surface to 10 km depth based on evidence for circulation of water through pervasively faulted BRZ crust. These calculations show that, for earthquakes to occur at crustal depths in excess of 20 km, temperature gradients in the BRZ probably cannot exceed 20°/km, corresponding to surface heat flow of 60 mW/m².

The absolute level of Bouguer gravity anomalies may also constrain the presence of thermal anomalies at depth. Typical approaches to forward-modeling of gravity data seek to duplicate the relative amplitudes of various features in the observed data, and thus calculated theoretical gravity profiles are often simply shifted by some number of milligals until they match the baseline of the observed data. In the analysis of the short Bouguer profiles above, the theoretical gravity anomalies produced by forward techniques were shifted by -10 to -30 mgal to fit the baseline level of the observed data, even after known long-wavelength fields had been removed. Lack of high-quality data over a broad region of the BRZ makes it impossible to determine how the short Bouguer profiles fit into the larger scale regional field, but some evidence suggests that these short profiles may lie almost entirely within a regional long-wavelength low. The shift applied to the theoretical gravity curves may therefore carry great significance in this case since it may reflect the presence of a thermal or dynamic anomaly responsible for the long-wavelength Bouguer low over the region. Figure 2.21 shows the residual Bouguer gravity low calculated by subtracting the Bouguer anomalies along 2000 km profiles perpendicular to the rift from the theoretical Bouguer anomalies due to Airy compensation of topography. Use of an Airy compensation mechanism is justified in this case since the long-wavelengths represented here should be supported locally. By integrating the isostatic anomalies (Δg_{iso}) shown in Fig. 2.21, we can estimate the mass deficit M of the anomalous low-density material beneath the rift zone of width l from:

$$M = \frac{1}{2\pi G} \int_{-l/2}^{l/2} \Delta g_{iso} dx \quad (2.12).$$

This calculation yields an average mass deficit of 4×10^5 kg/m for the long profiles and as large as 7 to 10×10^5 kg/m for the area of width 600 km centered on the rift's axis. Although a unique explanation for the gravity low is not possible, the amplitude and wavelength of the signal loosely constrain it to be caused by low density lower crustal material beneath the entire rift zone or low density material in the upper mantle beneath the center of the rift zone. Low density masses with these forms and distribution could result from partial melt in the lower crust and a more plume-like intrusion or passive upwelling beneath the rift zone respectively. For anomalous densities of $\Delta\rho = -100$ and -200 kg/m³, molten layers of 4 and 2 km thickness could respectively explain the average mass deficit over the long profile. Even thicker bodies of low density material are required to explain the mass deficits over the rift's axis.

QUALITATIVE CONSTRAINTS ON DRIVING FORCES FOR BRZ RIFTING

A principal debate about continental rift zones centers on whether they are primarily active or passive features (*e.g.*, Logatchev *et al.* [1983]). This terminology, wrought with difficulties, is widely employed in the literature, and will be used here in the following sense: A passive mechanism refers to rifting in response to the application of far-field stresses, while an active mechanism requires excess heat or active convection beneath the rift to drive the emplacement of a thermal plume, large scale thinning, or merely convective upwelling which weakens the lithosphere. Based on the data presented in this study, we cannot yet conclude whether an active or passive mechanism is primarily responsible for rifting in the BRZ. However, some simple physical considerations may narrow the range of possible explanations for the evolution of the BRZ.

Those who advocate a passive rifting mechanism for the BRZ typically attribute the far-field forces which drive extension to lithospheric stresses associated with the India-Asia collision zone 2000 km to the southwest [Tapponnier and Molnar, 1979]. The geometry of this scenario is illustrated in Fig. 2.22. In the absence of geological indicators of long-term strain or in-situ measurements, earthquake data provide the only means of describing the state of stress in the lithosphere. Based on focal mechanism analyses, maximum compressive stress σ_1 at the India-Asia intracontinental subduction zone is oriented at roughly north-south, subperpendicular to the Greater Himalayan front, while maximum extensional stress σ_3 in the BRZ has an orientation of approximately 100-130° east of north [Misharina, 1972]. Thus, if the forces driving collision along the northern edge of India and extension at the Paleozoic suture along the margin of the Siberian platform are the same, σ_1 must rotate from horizontal to vertical and σ_3 from vertical to horizontal across the tectonically-active region which separates the BRZ and the Himalayas. Royden and Burchfiel [1987] show that such shifts in the direction of σ_1 and σ_3 can occur over distances as short as the width of the Tibetan plateau (500-700 km) under certain conditions, thus rendering plausible the possibility that the stresses in the BRZ and along the Himalayan front may arise from the same tectonic event. The applicability of these results to larger-scale settings without the particular characteristics of the Tibetan plateau is probably limited however. In addition, their results probably have relevance only for the state of stress in the upper crust, not for that in the entire lithosphere. Numerical [England and McKenzie, 1982, 1983] and laboratory [Tapponnier et al., 1982] models of deformation of the Asian plate in response to the encroachment of an indenter (India) fail to produce extension at the site of the BRZ, a result widely interpreted as casting doubt on the passive model for BRZ development.

Also important to the evaluation of the passive rifting model for the BRZ is the critical question of whether forces can be transmitted laterally through large lithospheric

blocks in general and, more specifically, across the Tibetan plateau. Using simple energy arguments, *Molnar and Lyon-Caen* [1988] demonstrate that the compressive stresses characteristic of large-scale overthrust terranes can be transmitted through the zone of active deformation and into blocks adjacent to the Tibetan plateau. However, recent surface wave analyses imply the existence of a low-velocity zone at crustal levels beneath Tibet [*Molnar*, 1988], and S-wave delays may be loosely consistent with dynamic uplift of the plateau due to small-scale convection at relatively shallow depths [*Molnar*, 1990]. Furthermore, preliminary analysis of new Bouguer anomaly data yield an estimate of 40 km for the elastic plate thickness beneath Tibet, a value much less than the observed 60-70 km crustal thickness [*Molnar*, 1988]. Thus, geophysical data support the contention that the lower crust and upper mantle beneath Tibet may be too weak to transmit stresses related to collision into the tectonically-active Tarim basin, Mongolian strike-slip belt, and thence into the BRZ. On the other hand, intraAsian deformation occurs within microplates which jostle against each other, producing surface features and possibly affecting the structure of the region at depth. The contention that the Tibetan plateau must be strong enough to transmit *all* of the collisional stresses is somewhat specious since motions between the Asian microplates, coupled with brittle and plastic deformation within microplate interiors, may also generate enough stress to drive “passive” tectonism in susceptible areas (*e.g.*, at pre-existing crustal weaknesses). Published plate motion models [*Minster and Jordan*, 1978; *DeMets et al.*, 1990] treat the entire Asian plate as a single unit and do not permit internal deformation; thus, there exists no reliable means of assessing whether a discrepancy in the plate motion vectors may result from a combination of N-S compression in the Himalayas and Tibet, E-W and SE-NW extension in the high Tibetan plateau and the BRZ (respectively), and large-scale strike-slip faulting in Mongolia and parts of China.

Many of the published models for the evolution of the BRZ might loosely be interpreted as describing active driving forces for rifting. For example, the hypothesis that

the asthenosphere impinges directly on the base of the crust beneath the axial part of the BRZ [Zorin *et al.*, 1986] implies that small-scale convection and associated thermal erosion of the lithosphere may play a role in this setting. At the opposite extreme is a more classically thermal mechanism like the “great dike” hypothesis for the emplacement of a thermal plume below Lake Baikal [Zorin, 1966]. As demonstrated above, surface geophysical observations probably do not strongly support the presence of a thermal anomaly at depth beneath the rift zone although some data are consistent with a slightly elevated temperatures in the crust. Preliminary results of Slack (pers. comm.) for one teleseismic event indicate that PKP delays beneath the BRZ are only one-quarter as large as those beneath the East African Rift zone, implying relatively cold lithosphere beneath Baikal, and the paucity of rift-related volcanic rocks and the lack of evidence for large-scale extension or ductile deformation also indicate that thermal mechanisms may not be operative beneath the BRZ. On the other hand, interpretations of deep-seismic sounding results lead some workers to postulate the the presence of a low-velocity body (magma chamber or asthenospheric upwelling) at depths of 40-80 km beneath the southern part of the rift [Puzyrev and Krylov, 1977], and both seismic and electrical data image an upper crustal low-velocity/high conductivity [Gornostayev *et al.*, 1970; Krylov *et al.*, 1975] layer between approximately 12 and 20 km depth. Conductive heating associated with emplacement of a thermal plume at the base of the 45 km thick crust would cause a 10% temperature change in near surface rocks after approximately 10 my, while the thermal diffusion time for the entire crust exceeds 60 my. If the plume were allowed to cool with time after emplacement, instead of being maintained at a constant temperature, propagation of the thermal perturbation to near-surface rocks may require even longer or may result in little net heating. Thus, data which sample deep levels within the crust and upper mantle provide the best possibility for constraining the existence of a thermal disturbance and thermal driving mechanism in the BRZ.

Closely related to thermal mechanisms are dynamic mechanisms for rifting of the lithosphere. Although the relationship between active continental extension and the transmission of stresses in the viscous convecting layer to the overlying lithospheric lid has been explored in only a preliminary fashion [*Fleitout and Froidevaux*, 1982], small-scale convection can qualitatively reproduce some of the surface observations in rift settings (*e.g.*, rift flank uplifts [*Buck*, 1986] and rift swells [*Yuen and Fleitout*, 1985]). As demonstrated by *Fleitout and Froidevaux* [1982], tractions associated with convection beneath the lithosphere can also cause the development of extensional stress fields in the rigid layer. In addition, doming over convective upwellings eventually leads to extensional failure of the crust when potential energy reaches a critical level [*England and Houseman*, 1988], and convective erosion at the base of the lithosphere provides a mechanism for elevating the lithospheric thermal gradient and generating deep melts. It should be noted that, just as dynamic and thermal mechanisms are not completely independent, neither are passive and dynamic driving mechanisms: In some settings, passive thinning has been linked to the onset of small-scale convection (*e.g.*, *Buck* [1986]). Thus, surface observations that support the presence of dynamic upwellings at depth beneath some rifts do not necessarily imply that dynamic mechanisms drive extension since, in many cases, small-scale convection may be an effect, not a cause, of rift initiation. At some point, however, dynamic effects may play as an important a role in driving continuing deformation as the passive process.

Physical arguments presented by *Neugebauer* [1983] lead him to conclude that “mantle diapirism”, not thermal or passive mechanisms, is the only viable mechanism for continental rifting in many settings. In the BRZ, however, the role of dynamic mechanisms is nearly impossible to constrain without geophysical data that sample the lower lithosphere and underlying mantle. Surface wave dispersion studies of the Siberian platform, adjacent to the BRZ on the west, reveal low-velocity zones at depths of 95 to 140

km and 200 to 240 km in the upper mantle [Kozhevnikov, 1987], but extrapolation of these results across the suture and into the actively deforming microplate comprising the Baikal region is probably not valid. Tomographic inversions for deep seismic velocity structure and analysis of S-wave delays provide the best hope for delineating large scale thermal perturbations consistent with convective thinning of the lithosphere or low-viscosity zones where small-scale convection might occur.

CONCLUSIONS

The Baikal Rift zone is a young, active rift system characterized by significant lateral heterogeneity in both its geological and geophysical features. Major tectonic provinces within the BRZ include the Sayan region—whose deformation is controlled by the left-lateral Main Sayan fault, the axial zone occupied by Lake Baikal, the Barguzin accommodation zone, and the left-lateral Udokan diffuse shear zone. Seismic, heat flow, magnetic, and gravity data generally indicate that no large thermal anomaly is required to explain the geophysical observations in the BRZ, and analysis of shallow compensation using a variety of techniques implies that most of the features of the short-wavelength potential field data can be explained by flexure of the lithosphere, sediment-loading in deep basins, and crustal or possibly upper mantle mass deficits, particularly beneath the rift's axis. Our results show that the BRZ lithosphere has significant flexural strength ($D=7 \times 10^{22}$ Nm to 6×10^{23} Nm) although there is some evidence for thinning of the elastic plate towards the axis of the rift. Coupled with (1) the paucity of young volcanic rocks, (2) the occurrence of earthquakes to deep levels in the crust, (3) the lack of a well-defined heat flow anomaly separable from hydrothermal effects, and (4) preliminary results which show only a 1 sec delay in PKP arrivals in the BRZ area [Slack, pers. comm.], the elastic plate

thickness result may confirm that BRZ lithosphere is colder than that in other rift zones or, alternately, that the BRZ is simply younger.

The driving forces for extension in the BRZ are difficult to constrain with the existing datasets. Because we find no strong evidence for the existence of a large thermal anomaly beneath the BRZ, we attribute the present state of extension to the effects of a passive rifting process. Transmission and re-orientation of compressional stresses arising at the Indian-Asian collision zone may provide the passive driving forces for rifting, or these forces could arise secondarily as microplates jostle in response to collision [*Zonenshain and Savostin, 1981*]. Inability to document the precise source of passive driving forces for BRZ rifting does not invalidate the passive interpretation however.

ACKNOWLEDGEMENTS

We thank P. Cowie and G. Karner, D. Edginton, and especially D. Hutchinson for providing preprints of their work. S. Lysak, Yu. Zorin, N. Melnikov, and L. Vinnik respectively supplied an exhaustive heat flow catalog, magnetic anomaly maps, geologic maps, and refraction results. Discussions with K. Crane, P. Molnar, D. Hutchinson, P. Burkholder, L. Royden, K. Hodges, V. Golubev, Yu. Zorin, S. Sherman, P. Davis, and C. Wolfe are gratefully acknowledged. This work was supported by NASA grant NAG5-1084 to M. K. McNutt.

APPENDIX: EARTHQUAKE EPICENTERS

Epicenters for 597 BRZ earthquakes between 1814 and 1989 from historical Russian compilations [Kogan, pers. comm. (His II); *Atlas of Russian Earthquakes*, 1962 (His I)], the ISC, Harvard CMT, and *Doser* [1991a,b]. When more than one source provides an epicentral location, the more current sources are presumed to supersede all prior ones. Both *Doser*'s relocations and Harvard CMT and ISC epicenters are given for a few of the events to permit comparison of the precision of the locations.

<u>Year</u>	<u>Month</u>	<u>Day</u>	<u>Latitude (°E)</u>	<u>Long.(°N)</u>	<u>Reference</u>	<u>Year</u>	<u>Month</u>	<u>Day</u>	<u>Latitude (°E)</u>	<u>Long.(°N)</u>	<u>Reference</u>
1862	1	12	52.30	106.70	His I	1939	5	26	53.50	108.30	His I
1869	11	1	53.50	109.20	His I		5	19	52.20	99.50	His I
1871	3	4	52.30	106.50	His I	1940	1	2	52.90	106.70	His I
1902	4	12	51.50	104.70	His I	1940	7	3	52.20	106.60	His I
1903	11	26	52.20	106.80	His I		9	23	56.00	111.00	His I
1912	4	12	51.80	104.30	His I	1941	7	1	52.60	106.80	His I
1912	5	22	51.70	103.80	His I	1949	4	10	51.60	104.60	His I
1912	7	15	51.90	105.80	His I		5	6	53.50	109.90	His I
1917	4	29	56.00	115.00	His I	1950	4	4	51.78	101.36	Doser
1924	3	16	52.20	105.80	His I		4	4	51.70	101.00	His I
1925	4	23	51.80	105.90	His I		9	8	51.70	100.90	His I
1925	6	24	54.60	109.40	His I	1951	11	6	52.40	106.40	His I
	10	9	51.90	105.20	His I	1952	3	1	53.10	106.80	His I
	11	19	51.90	105.70	His I		3	8	53.10	106.80	His I
1926	1	7	52.00	105.30	His I		7	16	52.50	106.80	His I
	2	4	51.30	102.30	His I		8	19	52.50	101.50	His I
	4	12	51.90	102.40	His I		11	6	51.90	100.50	His I
	5	7	52.00	101.60	His I		11	7	54.10	108.00	His I
	6	18	52.20	102.00	His I		11	14	53.30	107.00	His I
	6	21	52.40	106.60	His I		11	25	52.70	106.80	His I
1927	4	10	51.80	105.20	His I		12	1	51.80	105.60	His I
	7	14	51.80	105.00	His I		12	8	51.80	105.20	His I
1928	12	18	52.00	101.60	His I	1953	2	3	51.40	100.70	His I
1929	5	10	50.20	106.30	His I		3	5	51.90	105.90	His I
1930	4	3	51.60	101.50	His I		3	15	52.00	106.30	His I
	4	15	51.80	105.00	His I		4	14	51.80	105.20	His I
	4	21	52.00	105.60	His I		4	19	51.80	105.20	His I
1931	5	6	53.60	107.20	His I		5	13	52.30	106.50	His I
	8	6	55.00	108.90	His I		5	15	51.70	105.20	His I
1932	4	21	52.20	106.20	His I		5	29	52.40	106.70	His I
	8	14	52.20	101.70	His I		6	18	52.50	101.40	His I
1934	7	6	52.20	106.30	His I		8	3	52.70	110.50	His I
1936	3	11	56.50	112.50	His I		8	4	53.20	107.10	His I
1937	7	25	56.00	111.00	His I		8	11	53.30	107.20	His I

<u>Year</u>	<u>Month</u>	<u>Day</u>	<u>Latitude (°E)</u>	<u>Long.(°N)</u>	<u>Reference</u>	<u>Year</u>	<u>Month</u>	<u>Day</u>	<u>Latitude (°E)</u>	<u>Long.(°N)</u>	<u>Reference</u>
1953	10	20	53.20	107.50	His I	1955	6	29	52.50	106.70	His I
	11	12	52.30	106.50	His I		7	18	51.30	101.60	His I
	12	17	50.00	111.00	His I		7	21	52.10	106.40	His I
1954	1	24	53.30	108.50	His I		8	23	52.50	106.50	His I
	2	4	52.50	99.00	His I		8	27	50.10	107.70	His I
	2	15	53.10	107.00	His I		9	5	52.00	102.00	His I
1954	2	23	51.30	102.60	His I		9	20	52.80	106.80	His I
	3	5	51.80	101.50	His I		10	16	52.50	106.10	His I
	3	7	50.20	103.20	His I		10	18	52.30	106.50	His I
	3	15	51.90	106.50	His I		12	9	51.70	105.40	His I
	3	21	51.40	102.10	His I	1956	1	10	51.70	101.90	His I
	4	23	52.80	107.50	His I		3	8	54.00	109.00	His I
	5	1	51.00	101.00	His I		3	21	52.20	106.40	His I
	5	20	53.30	107.70	His I		4	3	52.30	106.30	His I
	6	12	52.20	106.40	His I		4	9	52.30	106.40	His I
	6	25	52.10	106.40	His I		4	29	51.90	105.50	His I
	6	26	51.10	105.00	His I		5	21	51.60	105.80	His I
	6	27	53.00	108.00	His I		5	27	51.60	102.40	His I
	7	3	52.30	106.30	His I		6	14	55.00	110.00	His I
	7	20	51.70	105.80	His I		6	16	55.00	110.00	His I
	7	20	52.40	106.80	His I		7	10	52.90	107.90	His I
	9	2	52.20	106.30	His I		7	17	54.30	110.70	His I
	9	20	51.00	101.00	His I		7	22	51.30	105.30	His I
	10	5	54.50	109.50	His I		7	24	51.70	106.60	His I
	10	13	52.00	105.90	His I		7	26	51.60	106.70	His I
	11	4	51.00	104.20	His I		8	16	52.80	106.60	His I
	11	29	53.00	109.00	His I		8	17	52.60	106.50	His I
1955	1	17	51.60	105.10	His I		9	17	52.10	106.20	His I
	2	22	52.50	106.40	His I		9	22	52.80	106.90	His I
	3	10	52.70	106.60	His I		9	27	54.80	110.20	His I
	4	3	51.50	101.50	His I		10	5	53.10	108.10	His I
	5	6	51.00	100.00	His I		10	10	54.20	110.30	His I
	6	20	51.90	105.00	His I		10	13	50.30	112.70	His I
	6	26	51.50	101.50	His I		10	15	52.10	105.80	His I

<u>Year</u>	<u>Month</u>	<u>Day</u>	<u>Latitude (°E)</u>	<u>Long.(°N)</u>	<u>Reference</u>	<u>Year</u>	<u>Month</u>	<u>Day</u>	<u>Latitude (°E)</u>	<u>Long.(°N)</u>	<u>Reference</u>
1956	10	15	54.50	110.90	His I	1961	7	27	54.13	110.00	Doser
	10	19	52.60	107.10	His I		11	20	50.80	92.30	His II
	11	3	51.70	99.50	His I		11	23	55.85	110.15	Doser
	12	8	52.60	106.80	His I	1962	4	13	49.10	87.20	His II
	12	17	51.60	103.50	His I		11	11	55.84	113.22	Doser
1957	2	6	50.12	105.32	Doser		12	14	50.40	90.60	His II
	2	7	50.00	105.50	His I	1963	1	9	54.68	111.77	Doser
	2	8	50.00	105.50	His I		2	10	52.56	106.85	His II
	3	3	56.00	111.00	His I		2	15	55.20	111.00	Doser
	3	29	51.70	106.00	His I		4	23	46.70	103.50	His II
	4	18	51.80	105.30	His I		6	1	49.70	109.70	His II
	6	27	56.20	116.54	Doser		6	21	47.80	130.50	His II
1957	6	29	56.25	116.93	Doser	1963	6	22	53.10	121.10	His II
	7	19	51.80	105.40	His I		7	5	50.40	90.60	His II
	8	23	52.50	107.30	His I		12	1	56.02	111.95	Doser
	8	26	52.00	105.50	His I	1964	2	29	53.50	90.90	His II
	9	17	56.50	113.00	His I		9	24	53.00	121.50	ISC
1958	1	5	56.51	121.11	Doser		10	17	52.30	106.50	ISC
	9	14	56.61	121.00	Doser		10	23	56.60	124.50	ISC
1959	8	29	52.64	106.90	Doser		11	2	51.40	102.00	ISC
1960	2	15	52.50	107.00	His II		12	11	52.40	106.30	ISC
	3	12	52.00	106.00	His II	1965	2	11	48.50	93.30	His II
	4	12	46.50	96.00	His II		3	29	56.30	126.30	His II
	4	23	45.00	98.00	His II		10	6	49.90	102.50	ISC
	4	27	53.00	97.00	His II		11	9	49.60	111.80	ISC
	6	25	47.00	94.50	His II		11	14	52.73	106.61	ISC
	6	28	46.00	94.50	His II		11	17	50.70	91.10	His II
	7	18	56.00	111.00	His II		11	21	50.52	111.92	Doser
	9	15	46.40	93.90	His II		12	11	50.60	112.10	ISC
	9	20	50.10	88.40	His II		12	26	53.90	113.10	ISC
	9	22	52.50	107.00	His II	1966	5	10	51.79	98.93	Doser
	10	6	52.20	107.20	His II		6	10	45.20	99.70	His II
	5	21	48.00	86.40	His II		6	19	44.80	99.60	His II
	6	25	52.40	106.50	His II		8	30	51.66	104.61	His II

<u>Year</u>	<u>Month</u>	<u>Day</u>	<u>Latitude (°E)</u>	<u>Long.(°N)</u>	<u>Reference</u>
1966	10	2	43.70	125.10	His II
	10	28	44.60	101.70	His II
	12	31	56.00	118.00	ISC
	12	31	55.55	110.80	ISC
	12	31	55.20	110.90	ISC
1967	1	5	49.00	105.00	ISC
	1	5	49.00	103.00	ISC
	1	5	48.16	102.93	ISC
	1	5	48.31	102.87	ISC
	1	5	50.00	108.00	ISC
	1	5	48.22	102.90	ISC
	1	5	48.43	103.00	ISC
	1	6	48.50	102.80	ISC
	1	7	48.25	102.80	ISC
	1	7	48.17	103.01	ISC
	1	9	53.00	111.00	ISC
	1	15	55.57	110.81	Doser
	1	18	56.54	120.93	Doser
	1	18	48.10	102.96	ISC
	1	20	48.05	103.09	ISC
	1	20	48.80	102.51	ISC
	1	20	48.08	103.02	ISC
	1	21	48.17	103.06	ISC
	1	22	48.19	102.95	ISC
	1	22	48.04	103.10	ISC
	1	29	48.02	103.03	His II
	1	31	48.02	103.04	ISC
	2	11	52.09	106.46	His II
	2	11	52.09	106.46	Doser
	2	27	51.10	89.91	His II
	6	7	49.44	97.15	ISC
	6	7	49.47	97.08	ISC
	6	10	49.50	97.24	ISC
	6	21	48.89	122.20	ISC

<u>Year</u>	<u>Month</u>	<u>Day</u>	<u>Latitude (°E)</u>	<u>Long.(°N)</u>	<u>Reference</u>
1967	8	22	56.31	112.66	ISC
	9	11	45.00	99.30	His II
	9	20	48.21	102.97	ISC
	9	25	49.00	102.00	ISC
1968	1	5	48.00	102.00	ISC
	3	13	53.70	109.50	ISC
	4	25	50.60	103.70	ISC
	6	13	48.08	102.92	ISC
	6	27	54.70	111.10	ISC
1969	1	21	53.30	112.00	ISC
	4	6	50.32	91.22	His II
	9	20	55.00	116.00	ISC
	10	30	52.35	95.73	ISC
1970	1	27	45.78	94.20	His II
	3	24	52.40	107.10	ISC
	3	28	52.16	105.92	His II
	3	29	52.90	105.70	ISC
	4	3	45.13	99.25	His II
	5	14	47.42	89.26	His II
	5	15	50.17	91.25	His II
	5	15	50.25	91.34	His II
	5	15	50.18	91.34	His II
	5	15	50.22	91.26	His II
	5	15	56.79	117.90	Doser
	5	15	50.29	91.19	His II
	5	16	54.40	117.50	ISC
	5	17	50.19	91.26	His II
	5	18	50.26	91.30	His II
	5	18	56.82	117.85	Doser
	5	19	52.70	116.80	ISC
	5	23	50.06	91.63	His II
	8	13	51.84	105.64	His II
	9	3	49.30	113.60	ISC
	9	8	53.49	108.47	ISC

<u>Year</u>	<u>Month</u>	<u>Day</u>	<u>Latitude (°E)</u>	<u>Long.(°N)</u>	<u>Reference</u>	<u>Year</u>	<u>Month</u>	<u>Day</u>	<u>Latitude (°E)</u>	<u>Long.(°N)</u>	<u>Reference</u>
1970	9	19	48.36	89.30	His II	1973	8	18	50.15	91.27	His II
	10	17	57.90	111.50	ISC		8	27	53.50	108.50	ISC
	10	14	40.93	89.43	His II		10	2	44.43	102.62	His II
1971	1	11	50.13	90.93	His II		10	14	53.73	109.46	ISC
	1	11	50.11	91.01	His II		11	2	54.12	125.84	His II
	1	27	56.05	113.34	ISC	1974	1	22	54.90	112.64	ISC
	2	25	53.26	108.40	ISC		2	19	55.61	113.40	ISC
	2	26	55.42	109.87	ISC		3	22	49.90	90.81	His II
	3	27	48.20	98.60	ISC		4	9	56.00	110.85	ISC
	5	31	52.46	107.13	ISC		4	13	55.59	111.16	ISC
	6	14	56.10	123.60	Doser		6	16	56.48	112.39	ISC
	8	24	52.21	91.43	His II		7	1	56.09	113.81	Doser
	9	6	48.60	112.10	ISC		7	4	45.48	93.68	His II
	9	23	54.68	110.55	ISC		7	4	45.14	94.03	His II
	10	7	51.22	104.99	ISC		7	4	45.08	93.93	His II
	12	18	56.85	113.73	Doser		7	6	45.12	94.09	His II
1972	1	4	55.71	110.57	ISC		9	5	50.97	89.39	His II
	2	4	53.05	107.84	ISC		9	5	50.96	89.53	His II
	2	26	50.45	97.15	Doser		10	8	60.59	118.15	His II
	3	20	52.15	107.61	ISC		10	10	53.87	109.18	ISC
	3	25	45.35	100.81	His II		11	29	51.77	98.73	ISC
	5	8	55.48	111.33	ISC		12	16	56.32	116.65	ISC
	6	13	54.92	126.38	His II		12	18	48.35	103.29	ISC
	8	9	52.81	107.74	His II	1975	2	6	56.29	118.08	Doser
	8	9	56.83	127.16	His II		2	2	50.47	90.94	His II
	8	11	44.74	102.04	His II		3	28	46.49	91.79	His II
	8	31	52.27	95.34	Doser		3	31	46.71	91.29	His II
	9	28	52.41	95.98	ISC		9	12	48.96	103.95	ISC
	9	29	52.47	95.13	ISC		9	24	53.65	109.40	ISC
	11	25	56.19	123.56	Doser		9	25	49.61	98.46	ISC
1973	1	25	51.68	104.19	ISC		10	4	53.65	109.49	ISC
	4	30	50.99	89.73	His II		10	22	45.06	100.14	His II
	5	22	53.65	107.71	ISC		10	27	48.22	102.69	His II
	6	16	54.80	112.69	Doser		10	27	48.05	102.88	ISC

<u>Year</u>	<u>Month</u>	<u>Day</u>	<u>Latitude (°E)</u>	<u>Long.(°N)</u>	<u>Reference</u>	<u>Year</u>	<u>Month</u>	<u>Day</u>	<u>Latitude (°E)</u>	<u>Long.(°N)</u>	<u>Reference</u>
1975	11	9	47.97	102.97	His II	1978	10	7	61.52	112.88	His II
	11	27	45.10	99.92	His II		10	16	45.23	93.68	His II
	12	1	50.48	91.70	His II		11	30	52.83	107.23	ISC
1976	1	17	52.56	107.38	ISC	1979	1	10	55.27	111.48	Doser
	4	1	51.06	98.03	Doser		1	10	55.41	111.28	Doser
	4	1	50.82	100.29	ISC		1	17	55.76	110.64	ISC
	5	19	52.34	106.50	ISC		1	19	55.43	111.38	ISC
	6	17	51.32	98.01	ISC		1	29	52.45	97.91	ISC
	9	7	48.36	123.05	ISC		2	6	51.93	106.67	ISC
	9	25	55.87	110.53	ISC		2	6	49.04	116.54	ISC
	9	28	55.85	110.57	ISC		2	10	55.54	111.36	ISC
	10	14	45.24	93.94	His II		4	15	56.26	113.37	ISC
	11	2	56.11	111.57	Doser		4	27	56.71	129.80	His II
	11	5	61.53	112.71	His II		7	11	48.01	103.33	His II
1977	1	21	52.59	109.18	ISC		8	12	61.87	122.18	His II
	1	27	55.03	111.11	ISC		10	7	61.85	113.09	His II
	4	4	47.93	95.18	His II		10	10	53.06	108.48	ISC
	6	4	56.20	111.62	Doser		11	26	56.48	113.68	ISC
	7	15	48.56	86.81	His II		12	5	55.55	111.36	Doser
	8	10	50.77	110.76	Doser	1980	2	6	51.54	105.34	His II
	8	16	53.95	128.74	His II		2	8	56.01	113.49	ISC
	8	20	64.22	99.58	His II		2	10	48.99	121.87	ISC
	9	7	52.35	106.64	ISC		4	4	55.27	109.61	ISC
	9	10	57.29	106.23	ISC		5	23	51.69	100.79	ISC
1978	3	31	53.45	108.41	ISC		7	23	52.42	102.70	ISC
	6	20	56.26	112.70	ISC		7	27	55.95	111.17	ISC
	8	3	52.07	96.92	Doser		7	30	52.67	107.01	ISC
	8	9	52.14	96.99	ISC		7	30	52.75	107.09	ISC
	8	9	63.71	125.32	His II		9	23	52.41	98.55	ISC
	8	9	45.80	94.18	His II		9	26	51.92	105.49	ISC
	8	19	44.62	95.91	His II		9	26	51.89	105.53	ISC
	8	31	50.96	98.53	ISC	1979	9	26	51.88	105.44	ISC
	8	31	51.13	98.39	His II		10	2	51.43	108.24	His II
	10	1	57.33	122.25	ISC	1980	11	1	60.82	97.57	His II

<u>Year</u>	<u>Month</u>	<u>Day</u>	<u>Latitude (°E)</u>	<u>Long.(°N)</u>	<u>Reference</u>	<u>Year</u>	<u>Month</u>	<u>Day</u>	<u>Latitude (°E)</u>	<u>Long.(°N)</u>	<u>Reference</u>
1980	11	2	50.17	91.09	His II	1982	10	3	56.11	111.04	ISC
	12	15	45.92	90.28	His II		10	8	56.12	111.03	ISC
	12	15	45.99	90.38	His II		11	13	52.76	107.39	ISC
1981	1	5	53.04	107.56	ISC		11	16	52.44	107.57	ISC
	1	23	56.60	118.08	ISC		12	3	51.74	101.39	ISC
	2	10	43.77	86.60	His II		12	4	51.55	101.52	ISC
	2	19	53.02	107.71	ISC		12	5	51.49	101.40	ISC
	2	20	48.84	104.05	ISC	1983	11	20	51.29	98.39	ISC
	2	25	56.70	111.33	ISC		11	24	53.10	107.14	ISC
	3	3	55.90	112.91	ISC		12	30	52.57	107.03	ISC
	3	11	52.17	106.38	ISC	1984	1	27	53.39	109.20	ISC
	3	16	56.33	114.10	ISC		1	20	50.64	96.40	ISC
	4	12	52.97	107.52	ISC		6	19	56.61	118.02	ISC
	4	25	54.89	96.90	ISC		8	5	49.16	101.22	ISC
	4	25	49.00	121.89	ISC		11	24	52.59	98.51	ISC
	5	22	51.91	105.77	His II		11	29	48.58	119.00	ISC
	5	24	56.33	114.34	ISC		12	9	53.69	109.01	ISC
	5	27	53.94	108.86	Doser						
	5	31	56.24	111.69	ISC						
	6	25	56.81	117.64	ISC						
	8	16	50.54	96.87	Doser						
	8	25	52.01	106.43	ISC						
	11	2	55.30	110.87	ISC						
	12	1	52.41	101.12	ISC						
	12	5	57.36	122.93	ISC						
1982	1	14	54.76	110.28	Doser						
	1	24	54.92	110.29	ISC						
	1	28	53.57	108.86	ISC						
	2	19	54.04	111.75	ISC						
	2	22	56.40	114.46	ISC						
	4	16	51.47	107.10	ISC						
	6	21	52.27	106.67	ISC						
	7	27	52.42	106.91	ISC						
	7	30	53.80	104.14	ISC						

<u>Year</u>	<u>Month</u>	<u>Day</u>	<u>Latitude (°E)</u>	<u>Long.(°N)</u>	<u>Reference</u>
1985	2	23	55.68	111.01	ISC
	3	10	52.80	107.07	ISC
	4	6	51.46	100.84	ISC
	9	3	52.85	106.87	His II
	11	11	55.59	112.09	ISC
1986	1	22	55.61	109.29	ISC
	5	26	56.31	116.07	ISC
1987	2	21	55.02	111.00	CMT
	7	7	56.61	120.87	Doser
	7	7	56.68	120.98	CMT(?)
1988	12	15	46.53	95.59	CMT
1989	4	20	57.08	122.12	Doser
	4	29	57.09	122.12	Doser
	4	29	57.19	122.07	CMT(?)
1989	5	7	57.04	122.28	Doser
	5	13	50.04	105.50	Doser
	5	17	57.01	122.14	Doser
	10	25	57.52	118.81	CMT
1990	10	26	56.26	110.62	CMT

TABLE 2.I Focal mechanisms for earthquakes in Figure 2.5b

No.	Year	Month	Day	Lat.	Long.	Strike	Dip	Slip	Source*
1	1950	4	4	51.78	101.36	259	75	-163	Doser
2	1957	2	6	50.12	105.32	154	80	-10	Doser
3	1957	6	29	56.25	116.93	178	45	-22	Doser
4	1958	1	5	56.51	121.11	76	53	-123	Doser
5	1958	9	14	56.61	121.00	21	74	-120	Doser
6	1959	8	29	52.64	106.90	100	34	-35	Doser
7	1961	7	27	54.13	110.00	355	36	-127	Doser
8	1961	11	23	55.85	110.15	260	40	-90	Solonenko
9	1962	11	11	55.84	113.22	212	80	-18	Doser
10	1963	1	9	54.68	111.77	246	62	-98	Solonenko
11	1963	2	10	52.56	106.85	245	45	-68	Misharina
12	1963	2	15	55.20	111.00	242	29	-62	Misharina
13	1963	12	1	56.02	111.95	223	65	-82	Misharina
14	1965	11	21	50.52	111.92	154	80	169	Doser
15	1966	5	10	51.79	98.93	357	82	-154	Doser
16	1967	1	15	55.57	110.81	329	43	43	Doser
17	1967	1	18	56.54	120.93	59	66	-156	Das and Filson
18	1967	2	11	52.09	106.46	218	67	168	Doser
19	1970	5	15	56.79	117.90	115	71	-24	Doser
20	1970	5	18	56.82	117.85	256	80	-90	Doser
21	1971	6	14	56.10	123.60	264	73	-8	Doser
22	1971	12	18	56.85	113.73	78	84	-96	Doser
23	1972	2	26	50.45	97.15	130	75	-26	Doser
24	1972	8	9	52.81	107.74	324	71	-164	Doser
25	1972	11	25	56.19	123.56	45	74	-169	Doser
26	1973	6	16	54.80	112.69	55	54	-65	Solonenko & Solonenko
27	1974	7	1	56.09	113.81	87	10	-85	Solonenko & Solonenko
28	1975	2	6	56.29	118.08	318	65	-157	Doser
29	1976	4	1	51.06	98.03	148	80	166	Doser
30	1976	11	2	56.11	111.57	259	51	-54	Solonenko
31	1977	6	4	56.20	111.62	246	74	-74	Misharina et al.
32	1977	8	10	50.77	110.76	137	86	-11	Doser
33	1978	8	3	52.07	96.92	76	66	30	Doser
34	1979	1	10	55.27	111.48	138	38	-36	Doser
35	1979	1	10	55.41	111.28	125	85	-18	Doser
36	1979	12	5	55.55	111.36	219	51	-102	Misharina et al.
37	1981	5	22	52.05	106.32	18	18	-118	CMT
38	1981	5	27	53.94	108.86	113	52	-32	Doser
39	1981	8	16	50.54	96.87	129	86	-9	Doser
40	1982	1	14	54.76	110.28	206	80	174	Doser
41	1985	9	3	52.85	106.87	343	82	-167	Doser
42	1987	2	21	54.40	110.33	176	33	-114	CMT
43	1987	7	7	56.61	120.87	116	68	-2	Doser
44	1989	4	20	57.08	122.12	130	75	98	Doser
45	1989	4	29	57.09	122.12	196	69	167	Doser
46	1989	4	29	57.13	121.80	182	73	-177	CMT

Table 2.I continued

47	1989	5	13	50.04	105.50	171	72	-172	Doser
48	1989	5	17	57.07	122.03	18	48	-163	CMT
49	1989	5	17	57.01	122.14	124	69	156	Doser
50	1989	5	7	57.04	122.28	3	76	18	Doser
51	1989	10	25	57.81	118.65	68	40	-78	CMT
52	1990	10	26	56.26	110.62	215	56	-149	CMT

* Both CMT and Doser's source mechanisms are shown for the 29.4.1989 earthquake for the sake of comparison. Doser's first-motion solution for this event is probably more reliable based on the arrival data she presents. Sources: *Misharina* [1972]; *Das and Filson* [1975]; *Solonenko* [1977]; *Misharina et al.* [1985]; *Solonenko and Solonenko* [1987]; *Doser* [1991a,b]. All earthquake source parameters except Harvard CMT are as compiled by *Doser* [1991a, b].

TABLE 2.II Variables and constants

<i>Symbol</i>	<i>Meaning</i>
ρ_c	crustal density (2670 kg/m ³)
ρ_m	mantle density (3300 kg/m ³)
ρ_w	water density (1000 kg/m ³)
$\Delta\rho$	$\rho_m - \rho_c$
g	gravitational acceleration
G	universal gravity constant
E	Young's modulus (100 GPa)
ν	Poisson's ratio (0.25)
D	flexural rigidity
T_e	elastic plate thickness
z_m	crustal thickness
α	flexural parameter
q	heat flow
K	thermal conductivity
v_p	P-wave velocity at the Moho
M	excess mass calculated from isostatic gravity anomalies
k	wavenumber
$b(x), B(k)$	Bouguer gravity anomaly (spatial and wavenumber domains)
$h(x), H(k)$	topography (spatial and wavenumber domains)
$w(x), W(k)$	deflection (spatial and wavenumber domains)
Q	observed admittance
\hat{Q}	theoretical admittance
γ^2	observed coherence
γ_0^2	theoretical coherence
f	ratio of bottom to top loading
H_t, H_b	top and bottom "topography" (loads) in Fourier domain
W_t, W_b	top and bottom deflection due to loads in Fourier domain
Φ_0	surface porosity of sediments
k_p	e-folding depth of sediment porosity
H	depth below which sediments have density ρ_c
σ_1, σ_3	maximum compressive and extensional stress

FIGURE CAPTIONS

- Figure 2.1. Surface geology of the BRZ. General geology is from *Yanshin et al.* [1980] and *Khrenov et al.* [1983]. Note the significant distortion of this map projection.
- Figure 2.2. Generalized tectonic map of the BRZ showing the locations and names of faults and basins referred to in the text and the outlines of the four tectonic provinces. The black dot denotes Svyatnoy Nos, and fault locations are schematic. Inset: Location of the BRZ relative to other areas of deformation in Asia.
- Figure 2.3. Sediment thicknesses in Lake Baikal from multichannel seismic results of *Hutchinson et al.* [1991]. Data for the Selenga delta region (refer to Fig. 2.2) are not yet available, and the data shown here for the southern part of the North Basin and the northern part of the Central Basin represent significant extrapolation of the available MCS results.
- Figure 2.4. Topography of the BRZ from compilations of 1:500,000 topographic maps and 1:1,000,000 bathymetric maps. Bathymetry data courtesy of D. Hutchinson. (a) Shaded relief map. A=North Baikal basin; B=Central Baikal basin; C=South Baikal basin; D=Barguzin basin; E=Lower Angara Basin; F=Upper Angara Basin; G=Tunka Basin; H=Lena-Angara steppe; J=Siberian platform; K—topographic break marks position of Main Sayan fault. (b) Topographic profiles subperpendicular to the strike of the BRZ

and corresponding smoothed topography to highlight the domal nature of BRZ relief. Data used in the construction of these profiles have been supplemented by the ETOPO5 dataset where necessary.

Figure 2.5. Teleseismic data from the BRZ. (a) Location of epicenters for historical and recent earthquakes from the sources cited in the text. Uncertainty in epicentral determination may exceed 0.1° or more, particularly for the historical events. The appendix gives the date and location of earthquakes whose epicenters are displayed here. (b) Compilation of focal mechanism data from various sources (see text) to provide an overall picture of the heterogeneous nature of deformation in the BRZ. Only events for which first motion data closely constrain the position of nodal planes have been included in this map.

Figure. 2.6. Depths of earthquakes in the BRZ as determined by the ISC and *Doser* [1991a, b]. Errors are those reported by the original researchers. These data are plotted as a function of latitude for the sake of convenience, not to imply the possible existence of any correlation between source depth and latitude. The shaded region roughly corresponds to middle and upper crustal levels for the 40-45 km thick crust of the BRZ.

Figure 2.7. Seismic refraction data from *Puzirev* [1981] and *Vinnik* [pers. comm.]. (a) Contours enclose areas of constant crustal thickness, while symbols denote sites at which crustal thickness determinations were made. Note that most of Lake Baikal, except for the Selenga delta region and the area to the north, is characterized by crustal thickness in the 40-45 km range appropriate for

the entire BRZ region and the nearby platform and folded belt. (b) Compressional wave velocity at the Moho, contoured at 0.1 km/sec intervals. The region of depressed P-wave values coincides with the area of crustal thinning beneath the Selenga delta.

Figure 2.8. Distribution of data and magnitude of measured heat flow in the BRZ from the catalog of *Dushkov* [1985].

Figure 2.9. Analysis of patterns of heat flow in the BRZ. (a) Heat flow data plotted vs. topography. Heat flow for sites at which corrections have been applied to the data is shown in the top diagram (circles), whereas the bottom diagram gives observed heat flow at the rest of the BRZ sites (triangles). On the basis of sediment blanketing calculations, the heat flow in Lake Baikal should be reduced over that in surrounding areas. The fact that heat flow is actually elevated in the lake probably offers further evidence for the importance of hydrothermal processes in controlling the observed heat flow values. (b) Composite heat flow profiles across the north and south parts of the rift zone, subperpendicular to Lake Baikal. Heat flow across the terrestrial part of the southern part of the rift averages 10-20 mW/m² higher than that measured across the same zone along the northern profile. However, heat flow in the North Basin exceeds that in the South Basin by an average of 10-20 mW/m². (c) As suggested by Crane (pers. comm.) and *Crane et al.* [1991], connecting sites of constant heat flow within the lake reveals a pattern which may be consistent with elevated heat flow due to circulation of water through fault zones aligned subparallel to the basins' boundaries. The lines here connect sites at which similar heat flow values

were obtained. Note the similarities between the inferred structure along Lake Baikal and the orientation of lines of constant heat flow within the lake.

Figure 2.10. Free-air gravity anomaly map of the BRZ based on the 100 km x 100 km dataset of *Kogan and McNutt* [1987]. The Gem9 field of degree and order 10 has been removed from these data. Contour interval is 10 mgal, except over Lake Baikal.

Figure 2.11. Short Bouguer gravity anomaly profiles. (a) Location of Profiles I-IV. For position of these profiles relative to major structural and geological features, refer to Figures 2.1 and 2.3. (b) Stacked profiles of topography data and Bouguer gravity anomalies at the position of Profiles I-IV highlight their relative amplitudes. The topography shown for Profiles I and III is that which is exactly coincident with the reported position of these profiles. The poor correlation between the magnitude of the gravity low over the basin and the thickness of sediments along these profiles leads us to believe that the reported location of these profiles may be in error by up to 0.1° in latitude. Thus, the topography used in fitting Profiles I and III (see Figs. 2.14a and 2.16a) actually differs from that shown here.

Figure 2.12. Analysis of the relationship between Bouguer gravity anomalies and topography in the wavenumber domain for the region shown in Figure 2.4a. (a) Admittance (mgal/km) as a function of wavelength. The solid curves give theoretical admittance for the prescribed topographic load, the indicated values of elastic plate thickness T_e , and bottom-to-top loading

ratio of $f=0$. Dashed and dotted curves show theoretical admittance for a few values of T_e and $f=1$ and $f=5$. (b) Observed (symbols) and theoretical (curves) coherence as a function of wavelength. Theoretical coherence is calculated for several values of T_e , assuming that $f=1$. Sediment corrections have been applied to the short Bouguer profiles before the coherence calculation.

Figure 2.13. Sediment compaction curves (density vs. depth) for various values of surface porosity Φ_0 . The e-folding depth of surface porosity ($1/k_p$) is 2.5 km, and the density of rock grains which comprise the sediments is taken as 2670 kg/m³. Based on observational evidence, the preferred sediment compaction curve for Lake Baikal sediments is Curve C.

Figure 2.14. Geophysical data and theoretical and observed Bouguer gravity anomalies for Profile I. (a) From top to bottom: Heat flow anomalies, topography, observed and theoretical Bouguer gravity anomalies, and crustal thickness data and theoretical Moho deflections. Circles and triangles on the heat flow diagrams correspond to corrected and uncorrected data respectively. The theoretical Bouguer gravity curves shown here are calculated by assuming that topographic loads are regionally compensated by flexure of plates with T_e 0 (solid), 10 (dashed), and 30 km (dotted) and that $\Phi_0=0.6$ for sediments in Lake Baikal. Observed crustal thickness variations are from seismic refraction data and are plotted with theoretical deflections calculated assuming compensation of topographic loads by flexure of 0 (solid), 10 (dashed), and 30 km (dotted) thick elastic plates. (b) Comparison of observed Bouguer anomalies and theoretical gravity calculated assuming

$T_e=0, 10, \text{ and } 30 \text{ km}$ and $\Phi_0=0.2$ (dotted), 0.4 (long dash), 0.6 (short dash), and 0.8 (solid) for sediment fill in Lake Baikal. The bottom diagram shows topography along the profile (solid line) and the depth of the sediment-basement contact (dashed line) as determined from multichannel seismic data of *Hutchinson et al.* [1991].

Figure 2.15. Geophysical data and theoretical and observed Bouguer gravity anomalies for Profile II. (a) Heat flow, topography, observed and theoretical Bouguer anomalies (for $\Phi_0=0.6$ and $T_e=0, 10, \text{ and } 30 \text{ km}$), and crustal thickness and theoretical Moho deflections. (b) Observed Bouguer anomalies and theoretical gravity for all combinations of T_e (0, 10, and 30 km) and Φ_0 (0.2, 0.4, 0.6, and 0.8). Bottom diagram shows topography (solid line) and depth of sediment-basement contact (dashed line).

Figure 2.16. Geophysical data and theoretical and observed Bouguer gravity anomalies for Profile III. (a) Heat flow, topography, and observed and theoretical Bouguer anomalies (for $\Phi_0=0.6$ and $T_e=0, 10, \text{ and } 30 \text{ km}$). Few crustal thickness data are available for this profile. (b) Observed Bouguer anomalies and theoretical gravity for all combinations of T_e (0, 10, and 30 km) and Φ_0 (0.2, 0.4, 0.6, and 0.8). Bottom diagram shows topography (solid line) and depth of sediment-basement contact (dashed line).

Figure 2.17. Geophysical data and theoretical and observed Bouguer gravity anomalies for Profile IV. (a) Heat flow, topography, and observed and theoretical Bouguer anomalies (for $\Phi_0=0.6$ and $T_e=0, 10, \text{ and } 30 \text{ km}$). Few crustal thickness data are available for this profile. (b) Observed Bouguer

anomalies and theoretical gravity for all combinations of T_e (0, 10, and 30 km) and Φ_0 (0.2, 0.4, 0.6, and 0.8). Bottom diagram shows topography (solid line) and depth of sediment-basement contact (dashed line).

Figure 2.18. Crustal thickness variations from seismic refraction data (circles and triangles) plotted with theoretical Moho deflections (lines). The positions of the seismic refraction profiles are shown in Fig. 2.7. Theoretical crustal thickness calculation assumes that topographic loads are locally compensated by the density contrast across the Moho and deflection of that interface.

Figure 2.19. Correlation between surface heat flow and P-wave velocity at the Moho. The line corresponds to the predicted relationship between heat flow and seismic velocity for the simple assumptions of Equation (2.11), while heat flow and P-wave velocity pairs are indicated by the symbols. For A and C, v_p of normal crust is taken as 8.0 km/sec and T_0 is assumed to be 600°C and 1000°C respectively. For curves B and D, v_p for normal crust is 7.8 km/sec and T_0 is once again taken as 600°C and 1000°C respectively. Errors are those ascribed to the heat flow data by the original authors [Dushkov, 1985].

Figure 2.20. Yield envelopes for crustal materials and the distribution of earthquakes as a function of depth in the BRZ. (a) Yield envelopes for quartz for strain rates of 10^{-15} /sec (upper curve of each pair) and 10^{-16} /sec (lower curve) and crustal temperature gradients ranging from 15 to 25°C/km. For earthquakes to be prevalent to depths of 20 km in the BRZ, the geothermal gradient

probably cannot exceed $20^{\circ}\text{C}/\text{km}$. (b) Histogram of the depths of earthquakes shown in Fig. 2.6. The decreasing number of earthquakes with depth probably reflects the skewed nature of the ISC and Doser datasets, not the actual distribution of earthquakes.

Figure 2.21. Isostatic gravity anomaly (Observed Bouguer - calculated Bouguer for $T_e=0$ km). Integration of the isostatic gravity anomaly (Equation 2.12) yields a rough estimate of the mass deficit beneath the rift zone.

Figure 2.22. Schematic diagram of the possible driving forces for BRZ extension and the relationship of the BRZ to other tectonic elements in Asia.

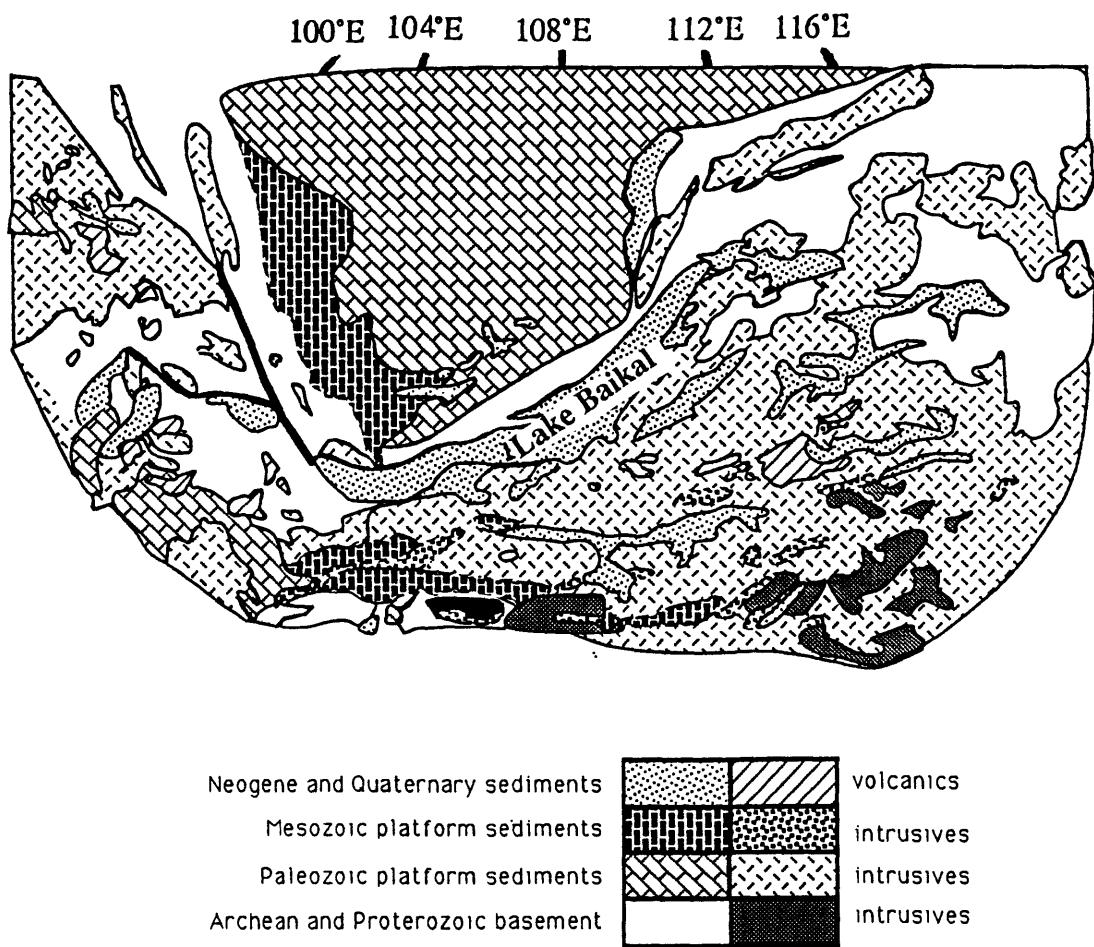


Figure 2.1

Figure 2.2

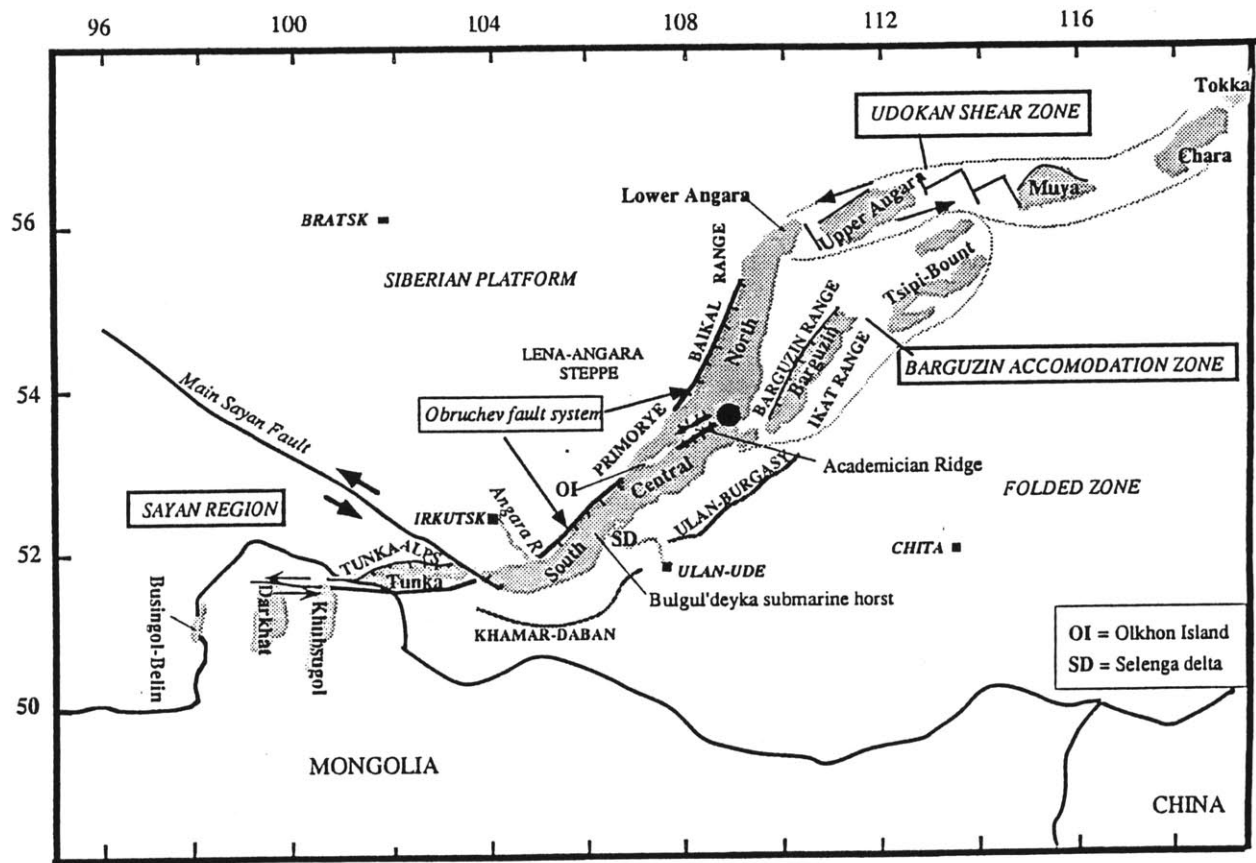
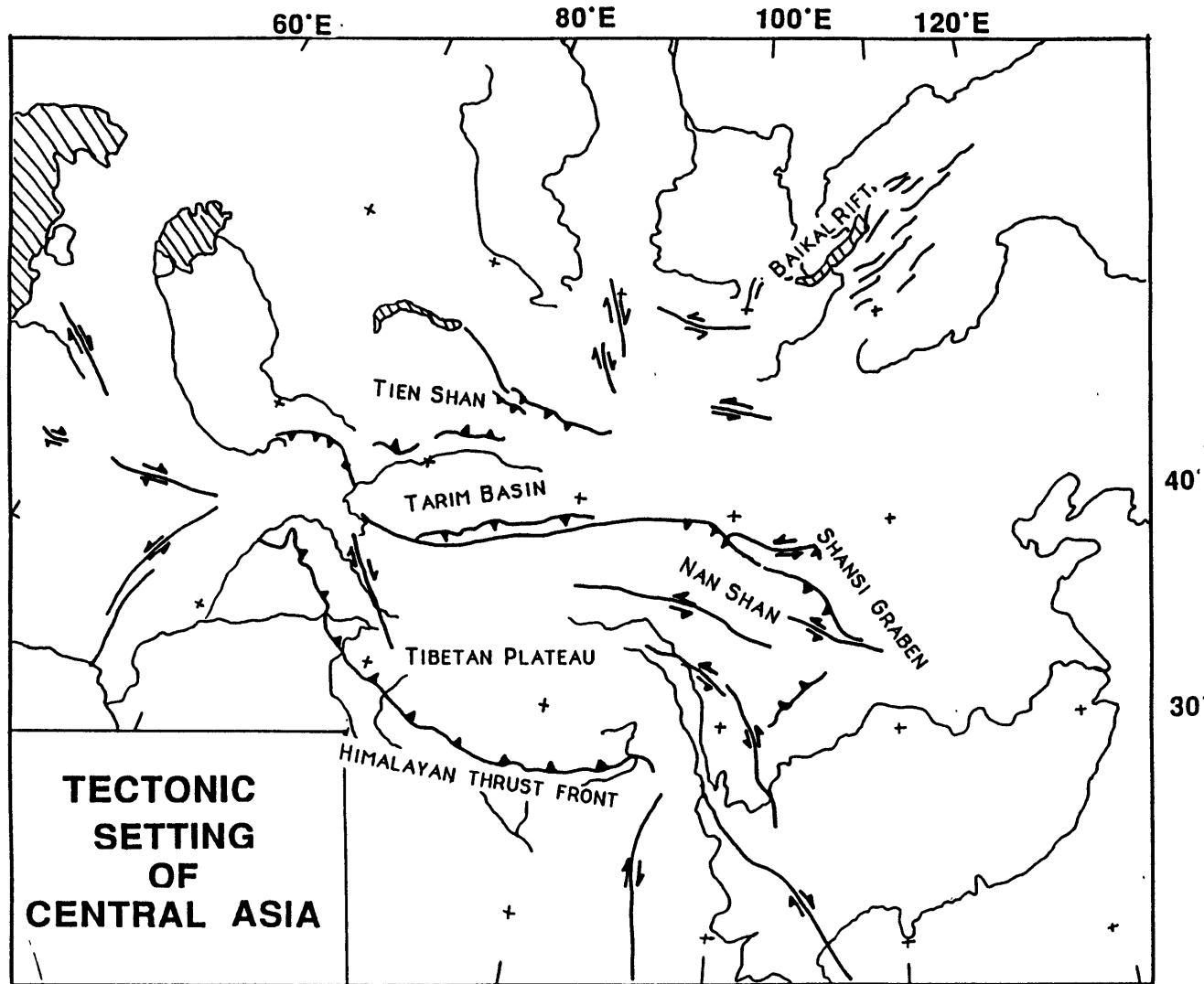
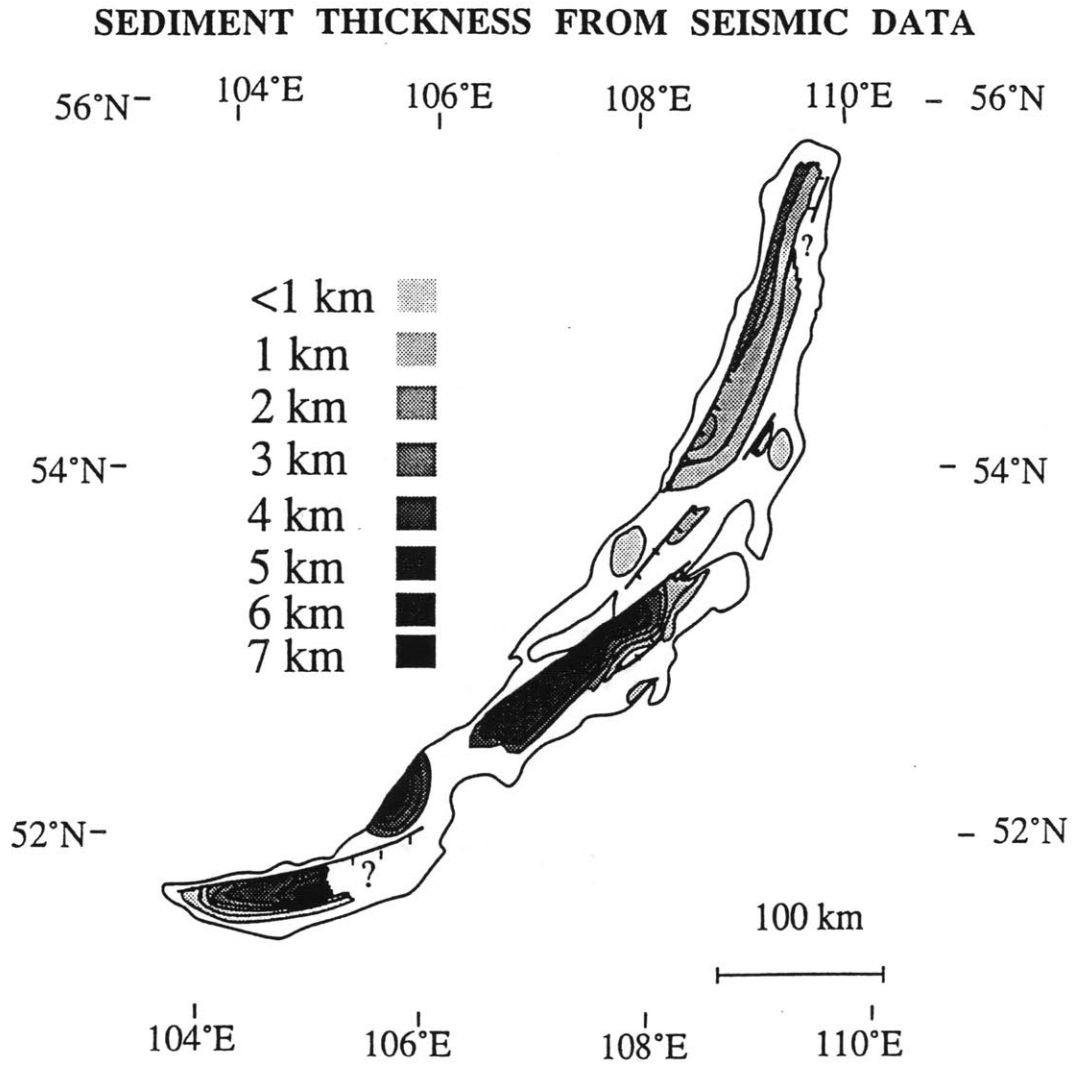


Figure 2.2 (inset)



AFTER MOLNAR & TAPPONNIER (1975)



from *Hutchinson et al.* [1991]

Figure 2.3

BAIKAL RIFT TOPOGRAPHY

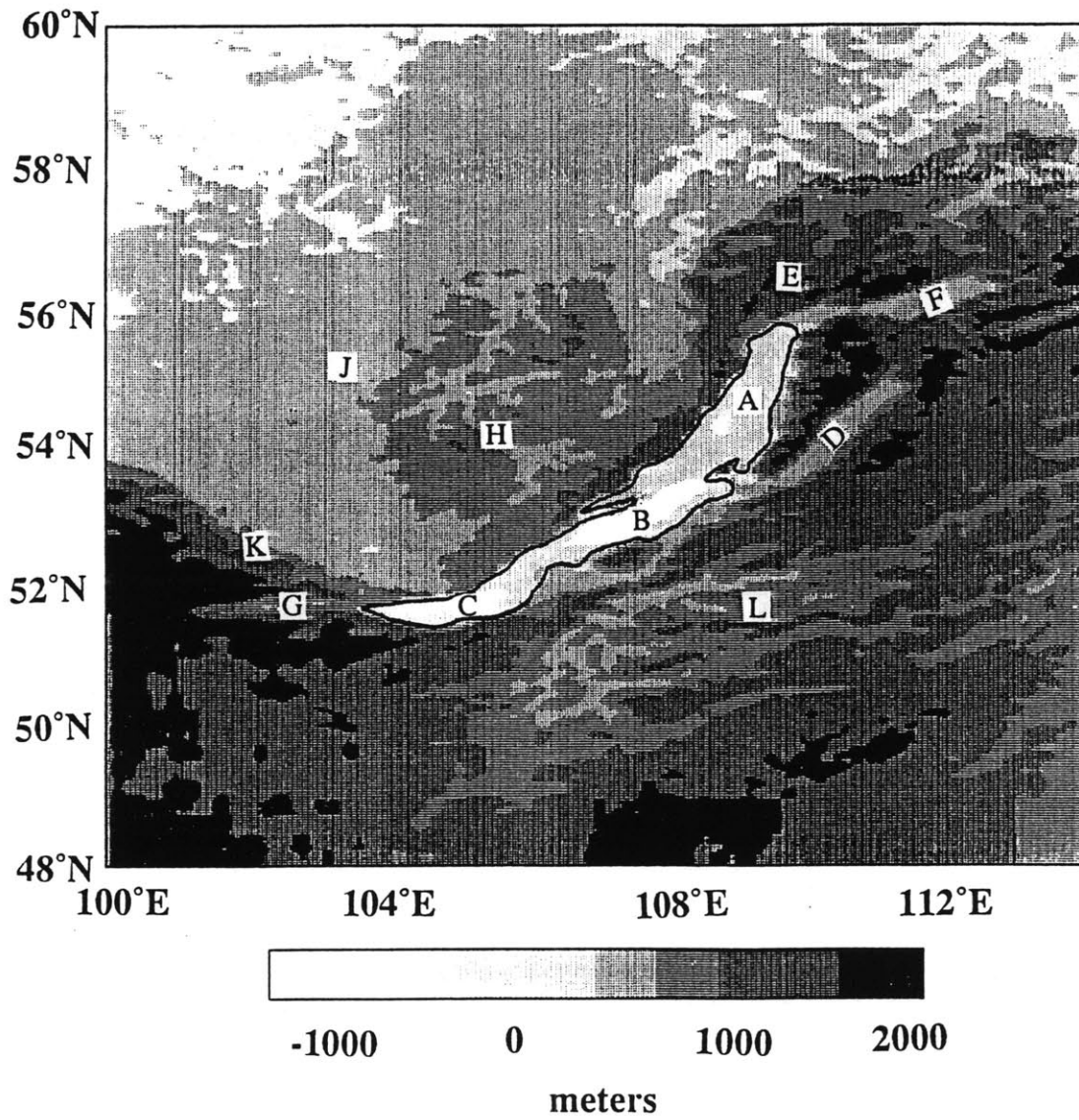


Figure 2.4a

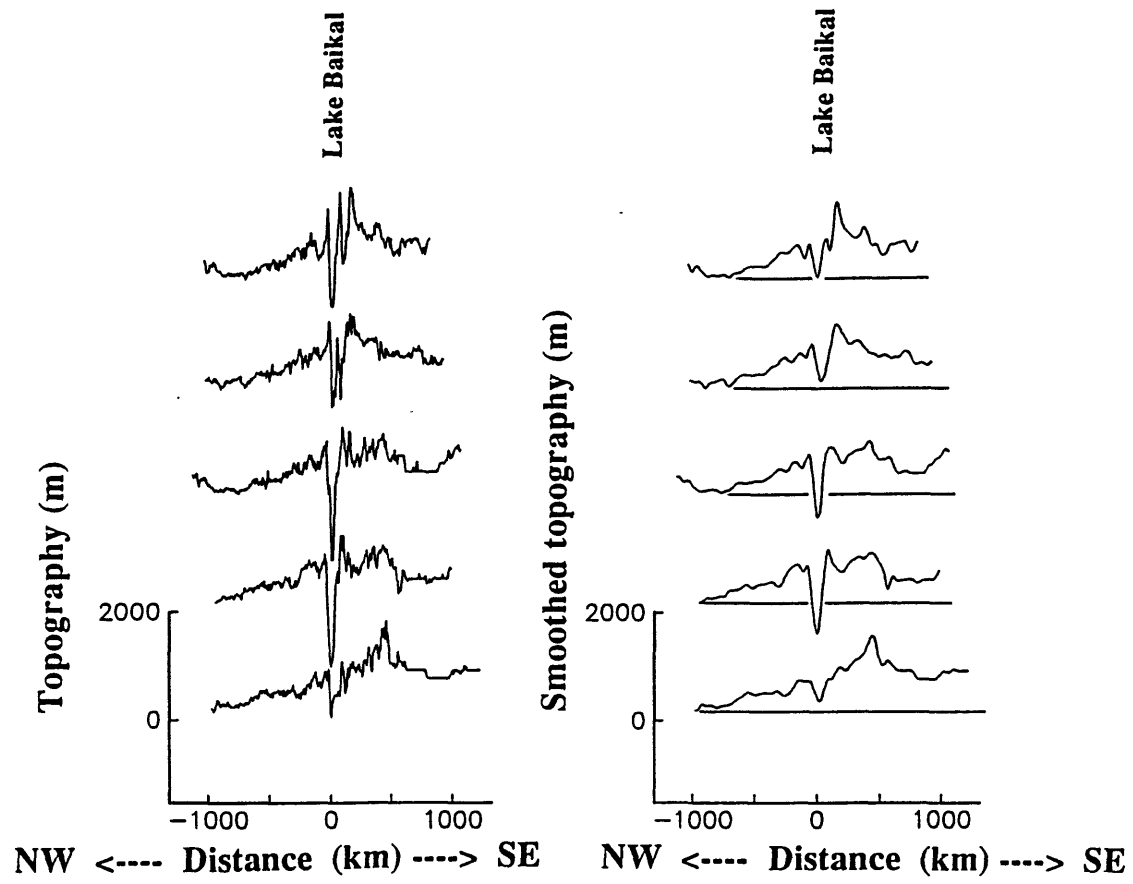


Figure 2.4b

Figure 2.5a

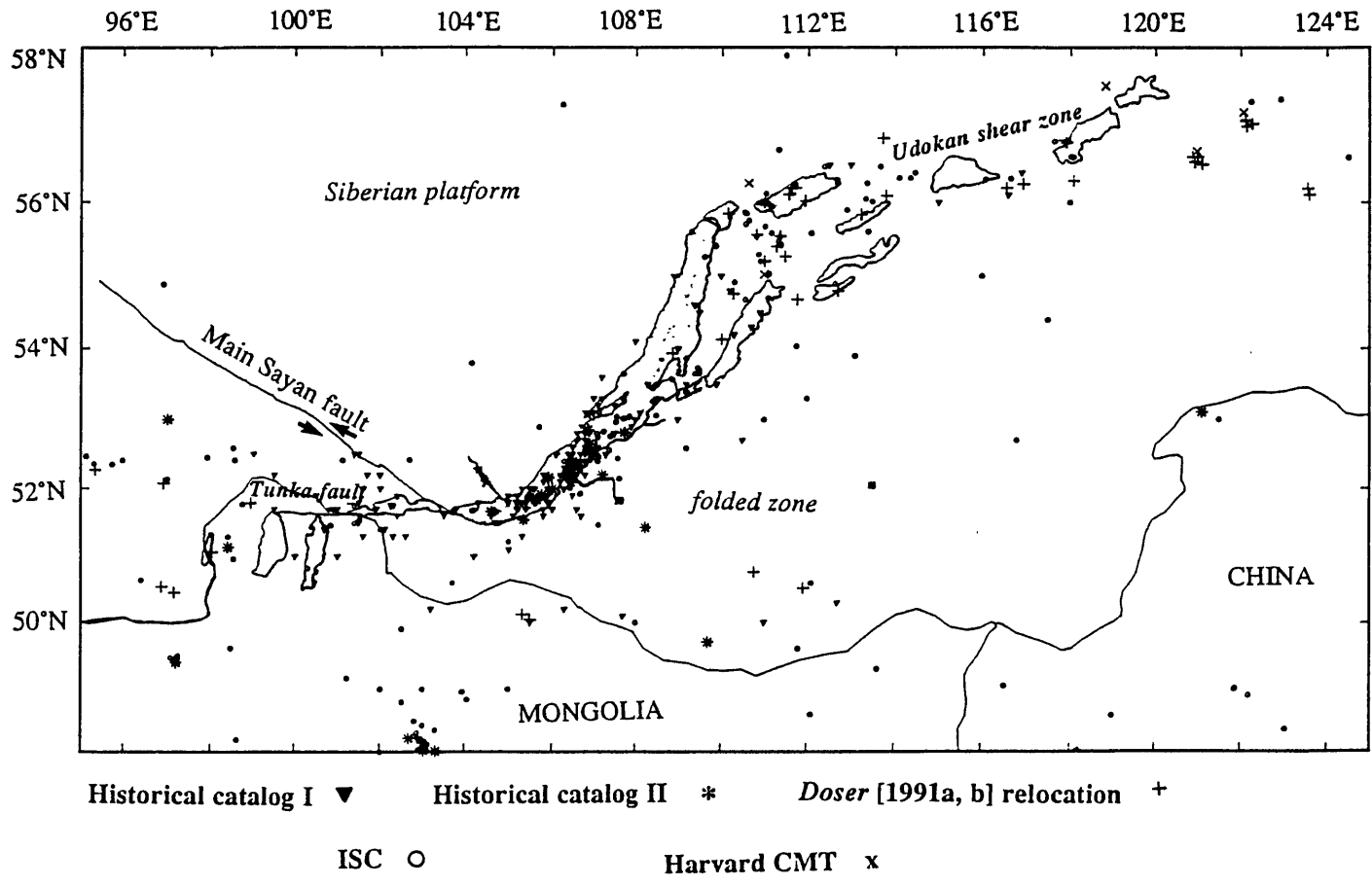
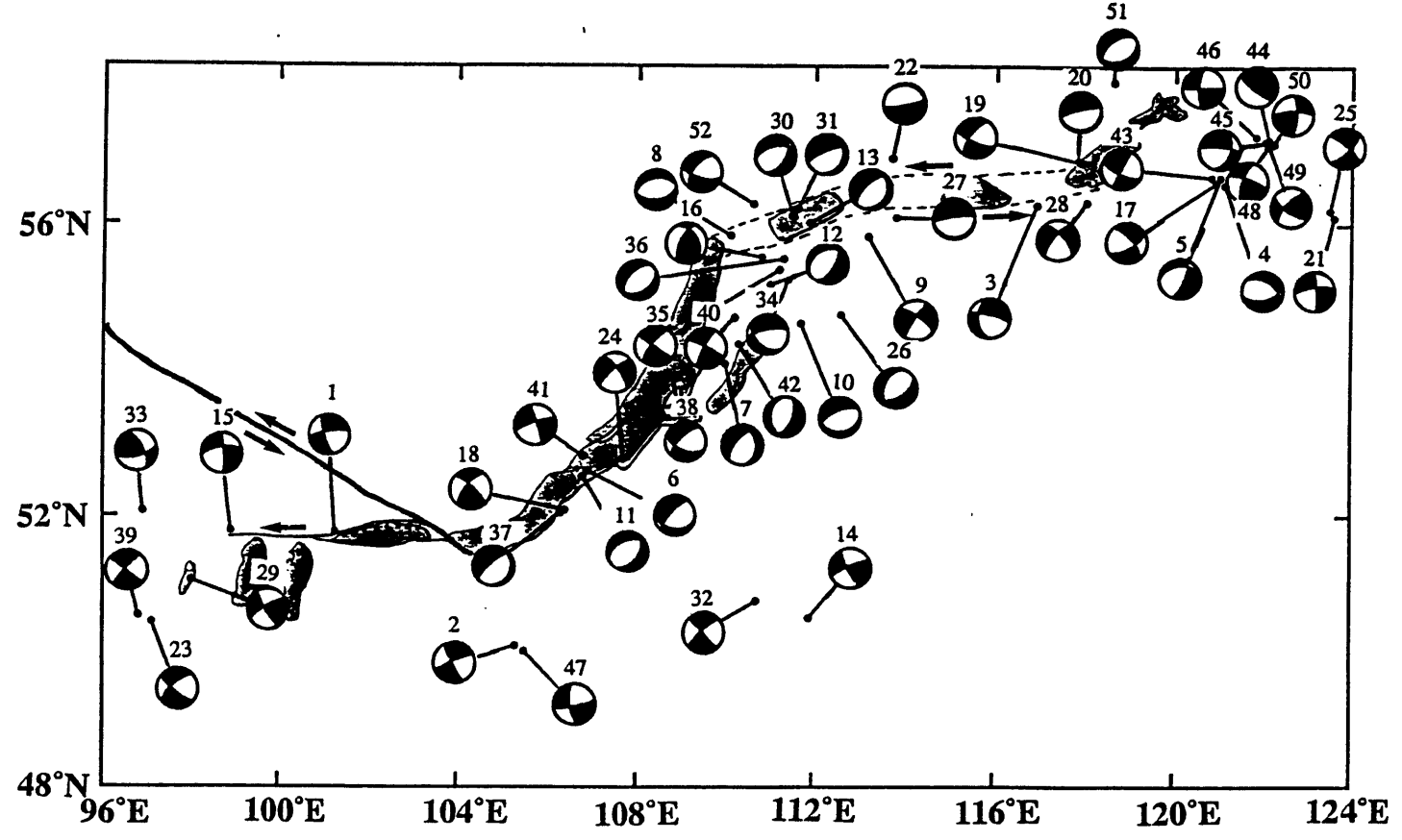


Figure 2.5b



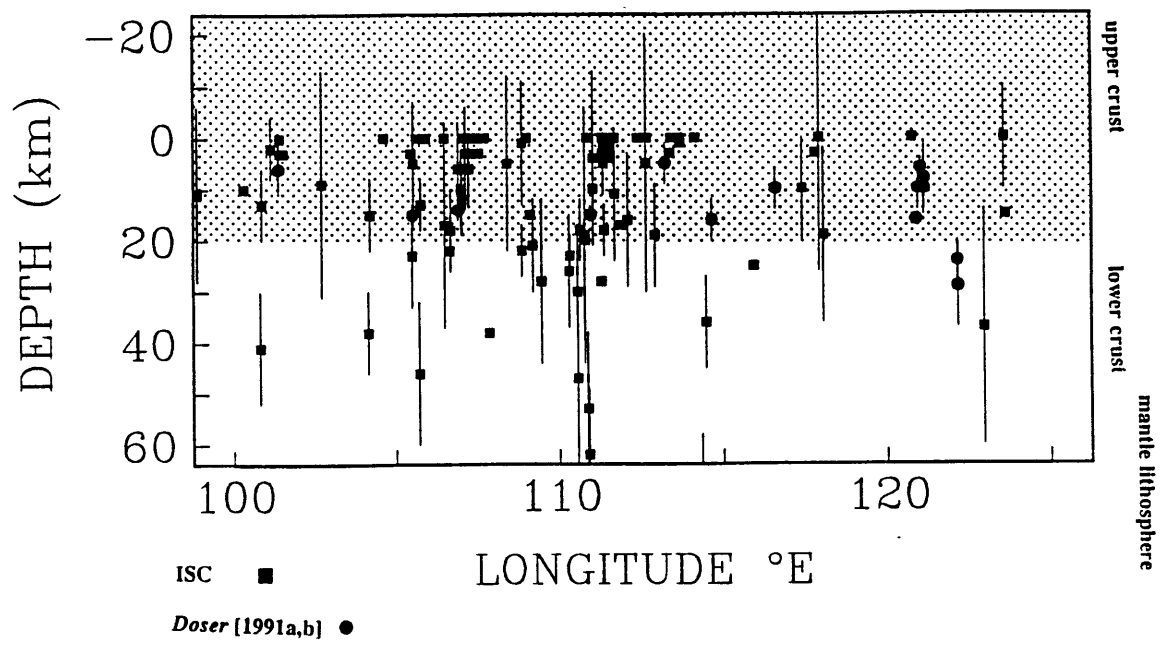


Figure 2.6

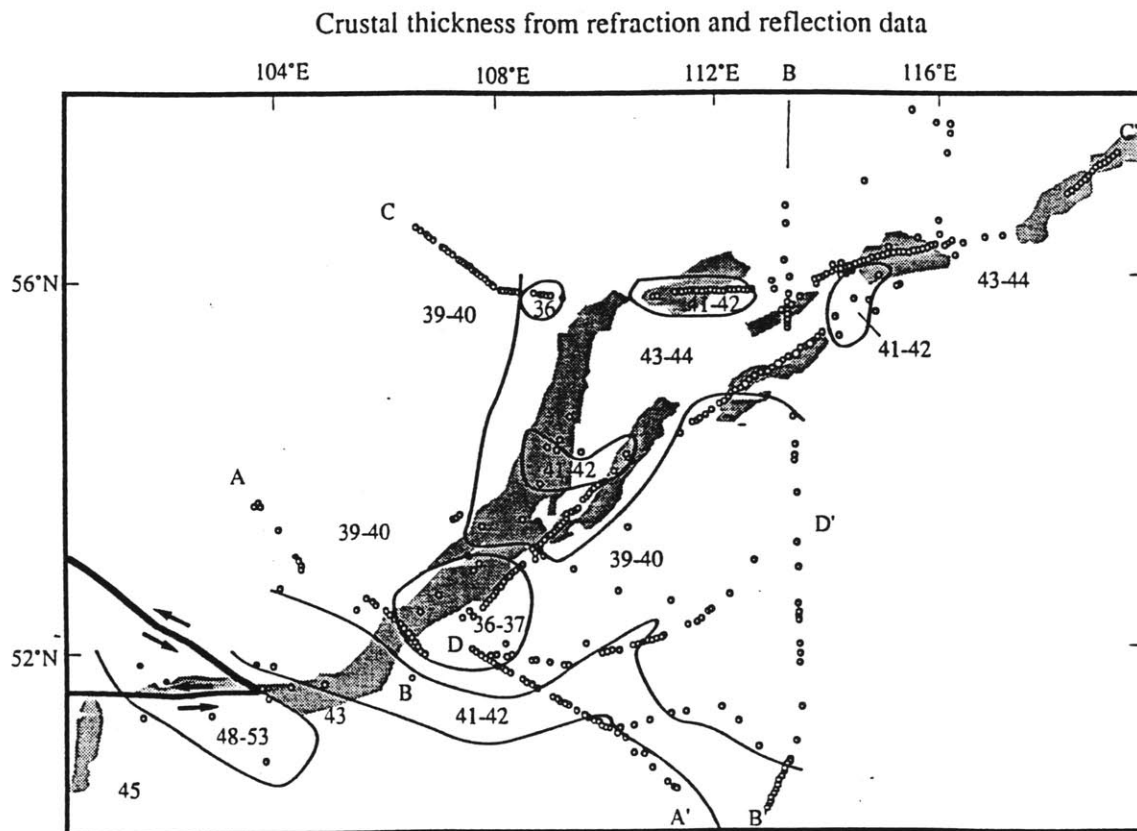
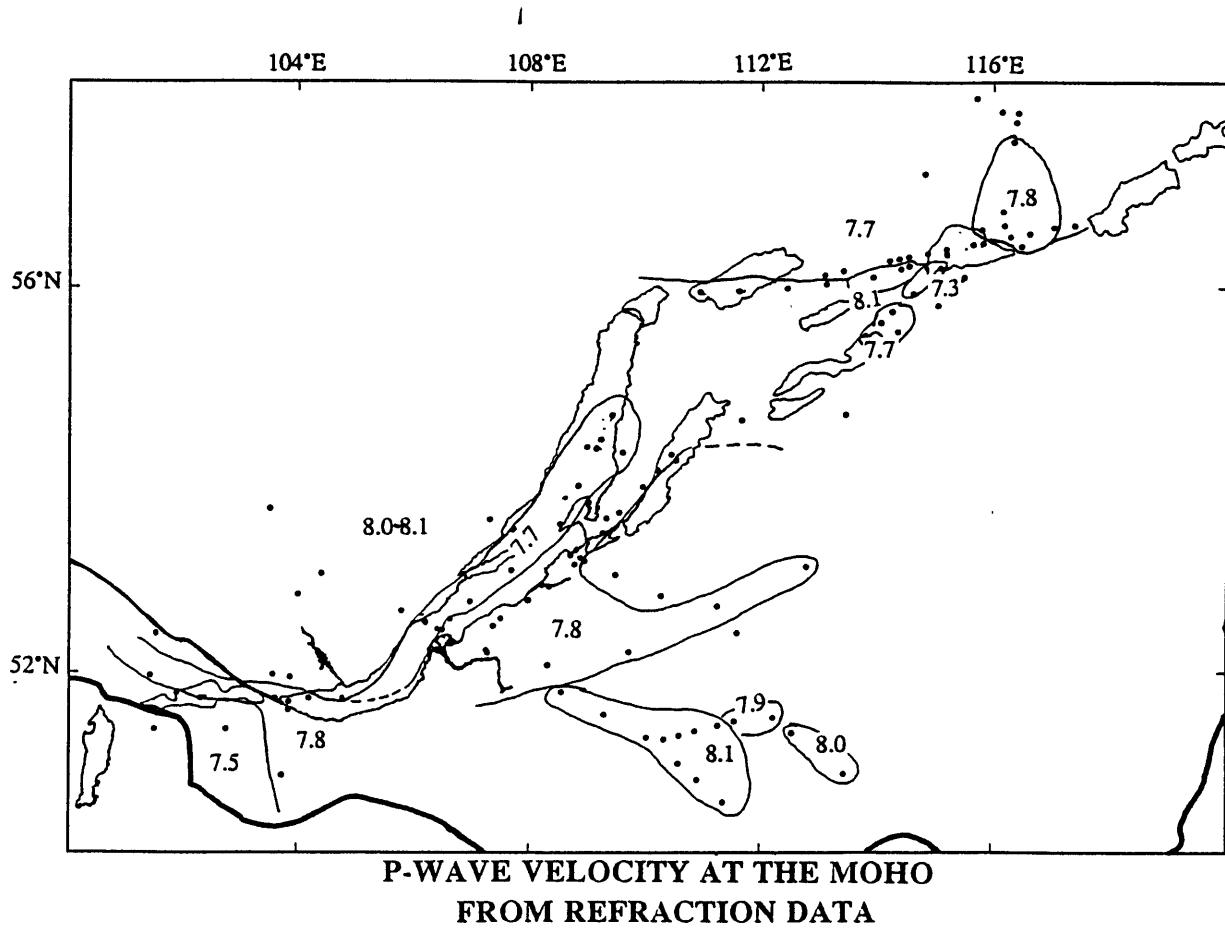


Figure 2.7a

Figure 2.7b



BAIKAL RIFT HEAT FLOW

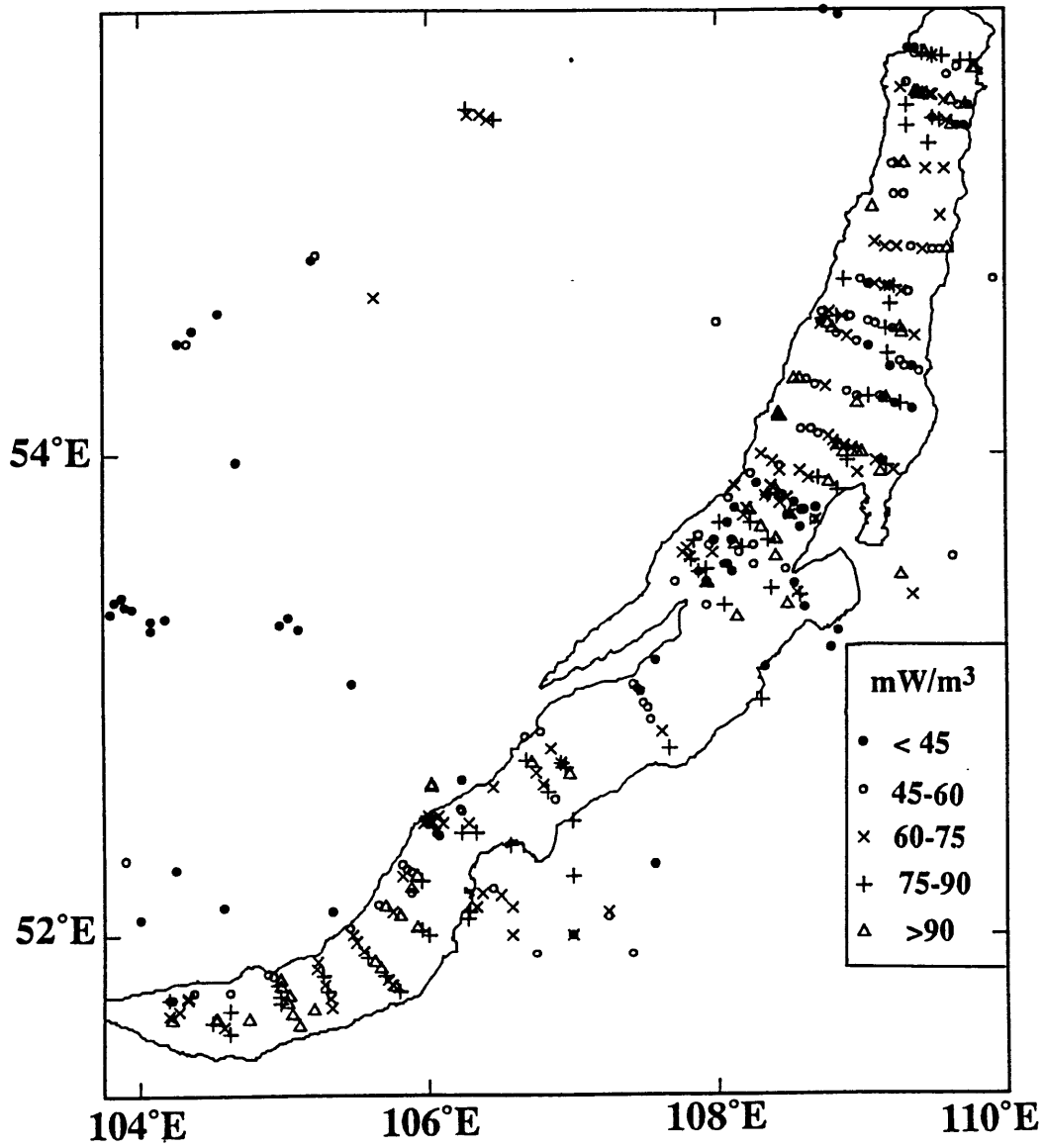


Figure 2.8

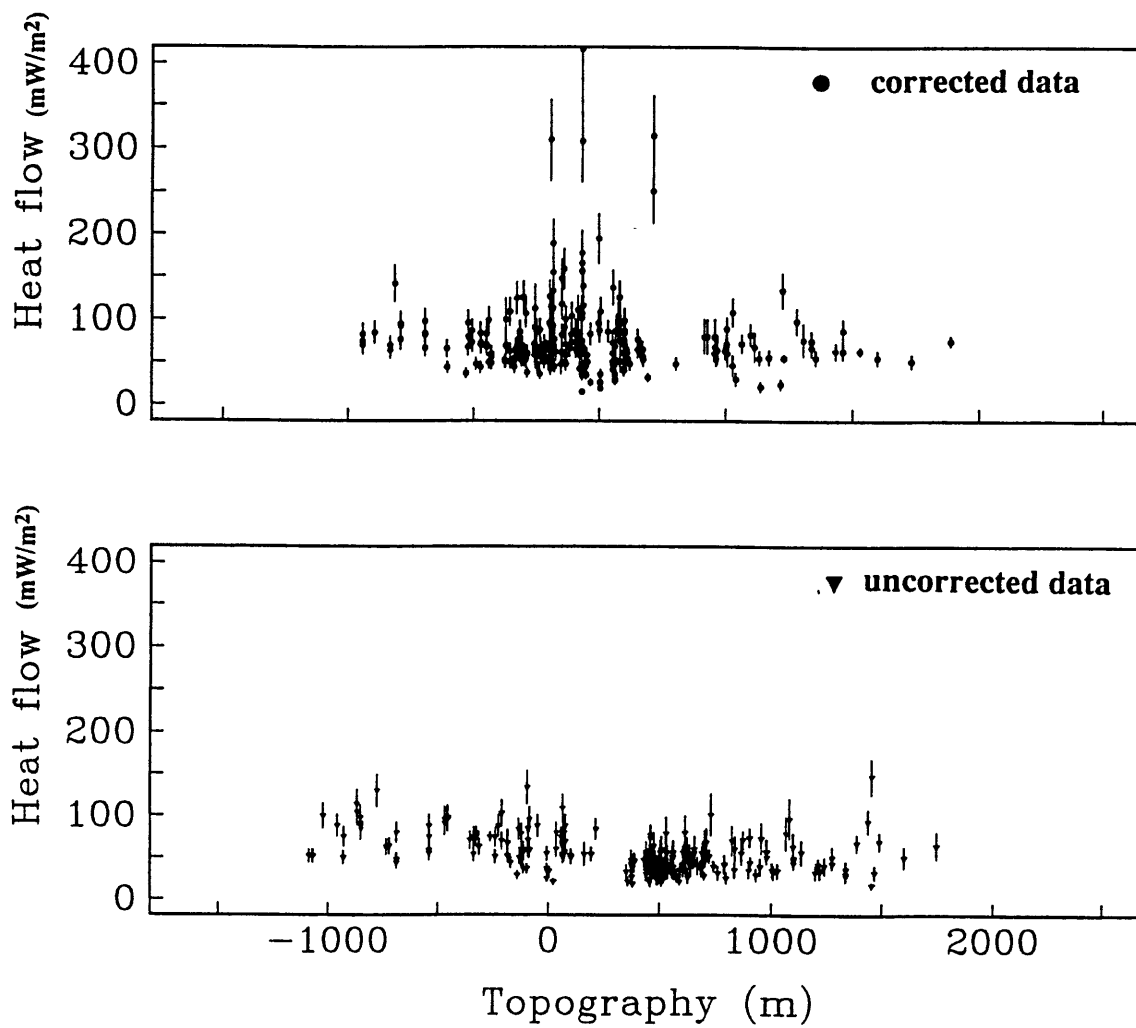
Heat flow vs. topography

Figure 2.9a

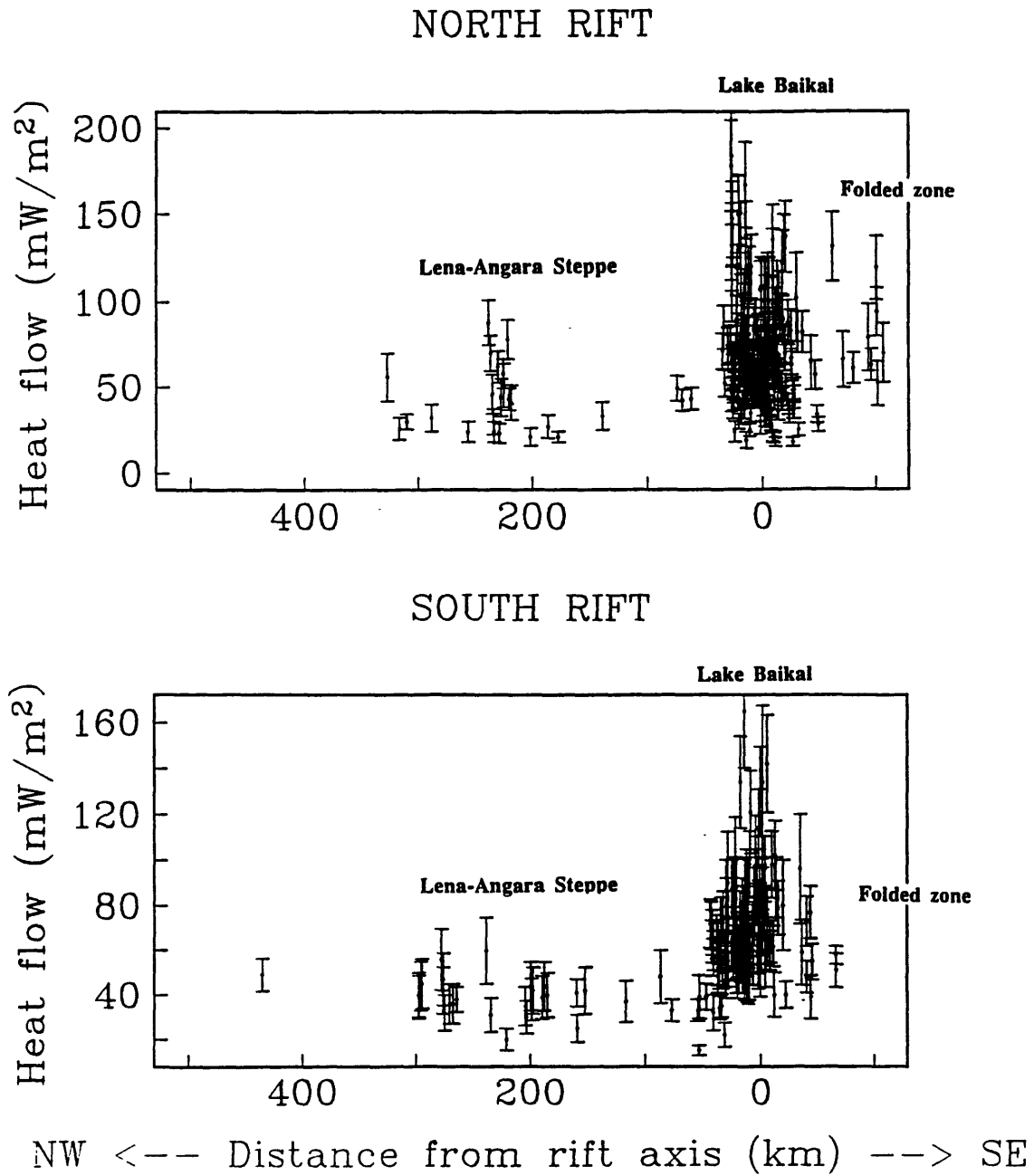


Figure 2.9b

LINES OF CONSTANT HEAT FLOW IN LAKE BAIKAL

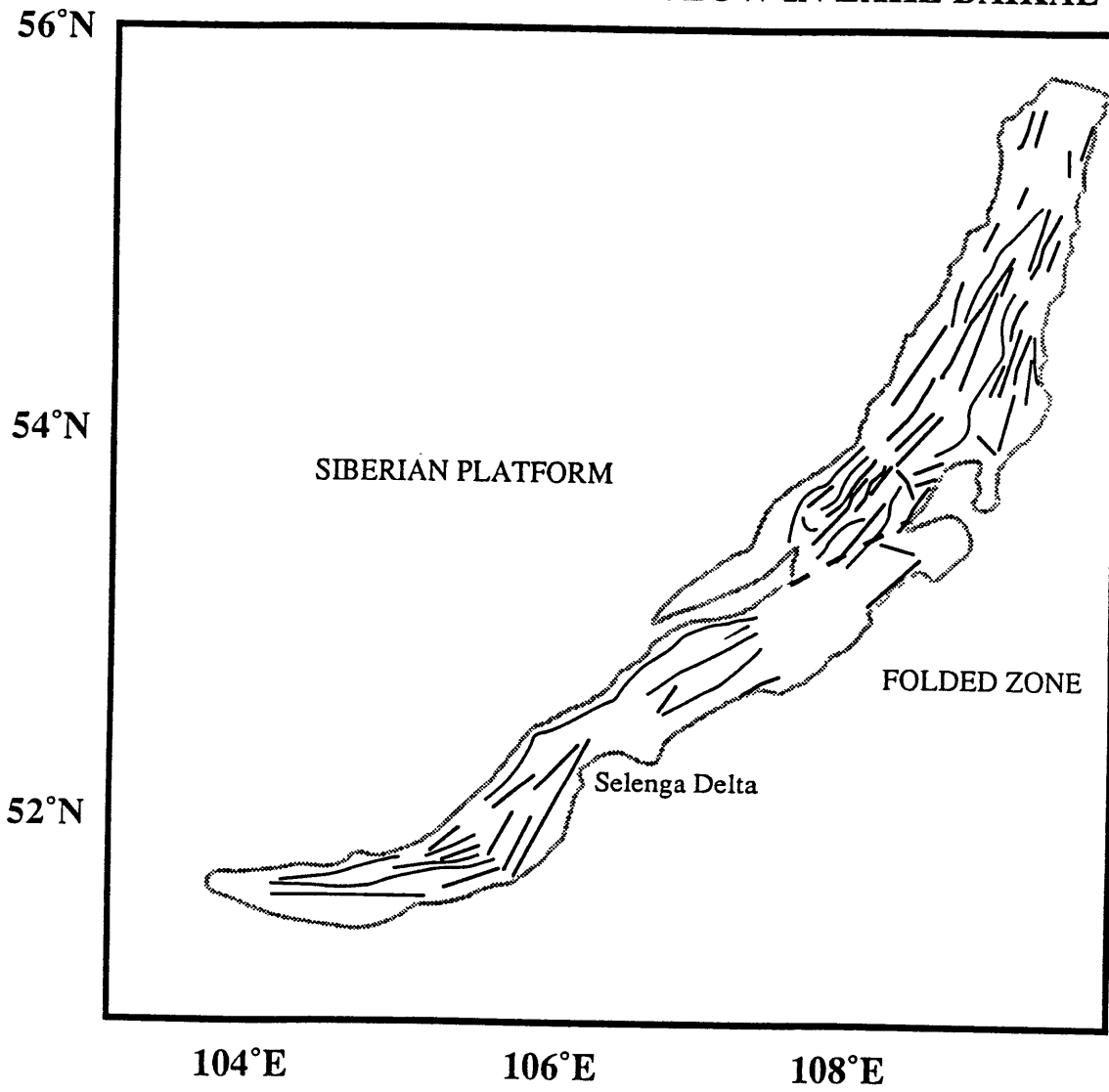


Figure 2.9c

FREE-AIR GRAVITY ANOMALIES (mgal)

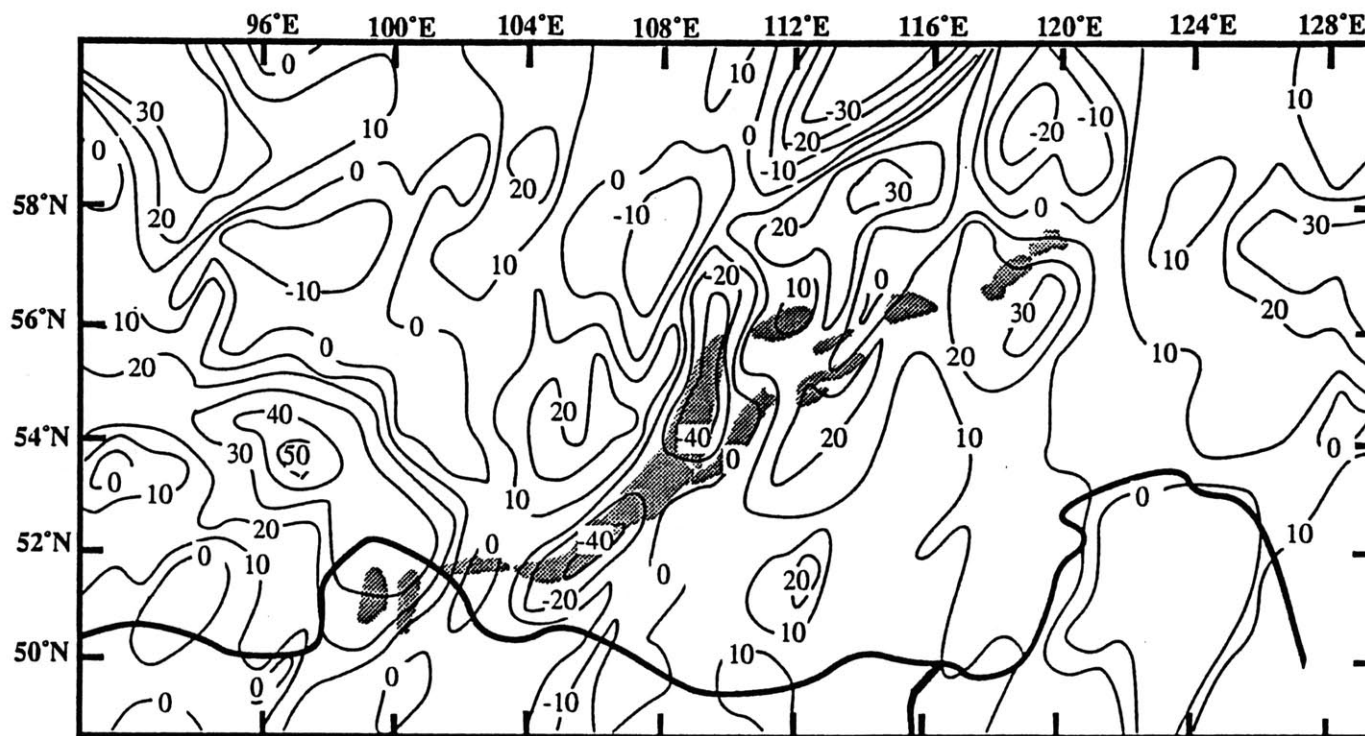


Figure 2.10

LOCATION OF BOUGUER GRAVITY ANOMALY PROFILES

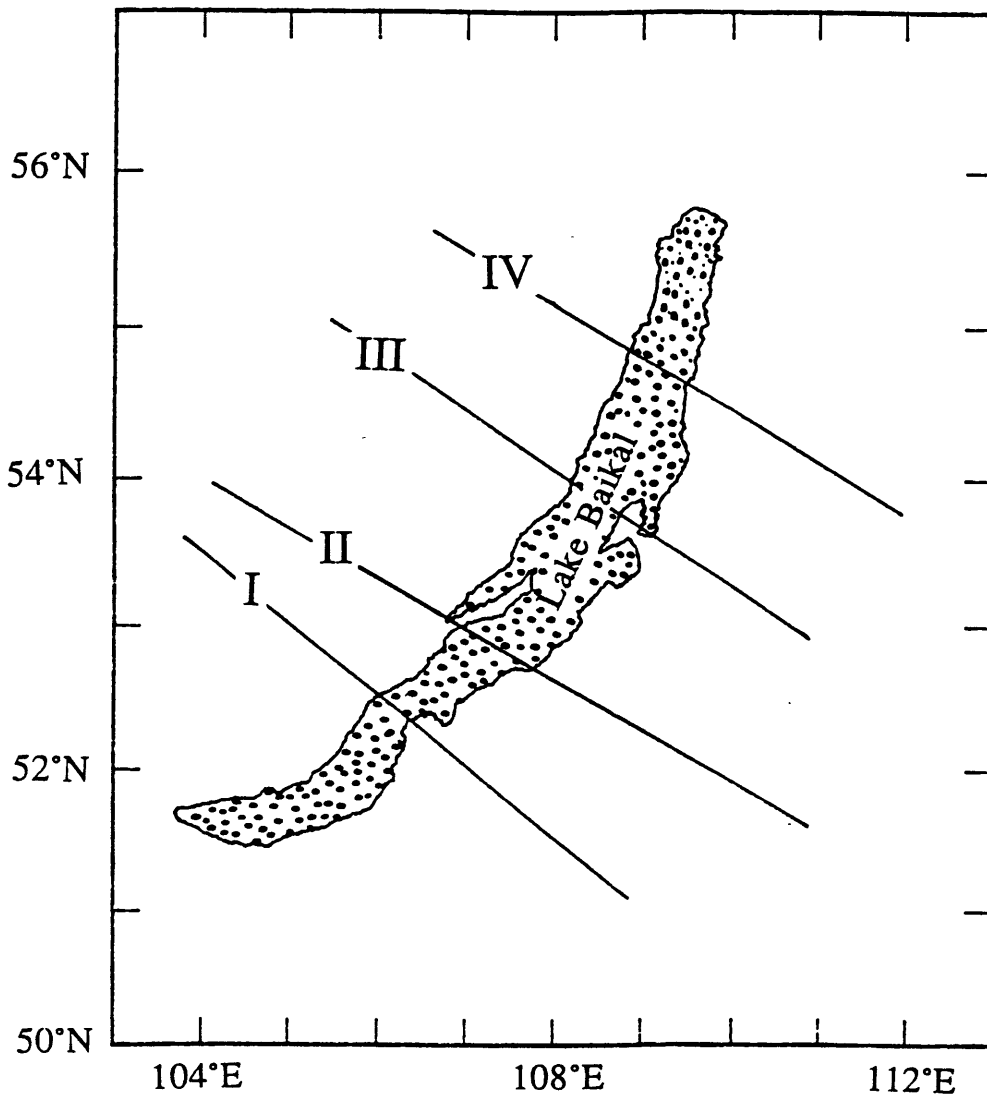


Figure 2.11a

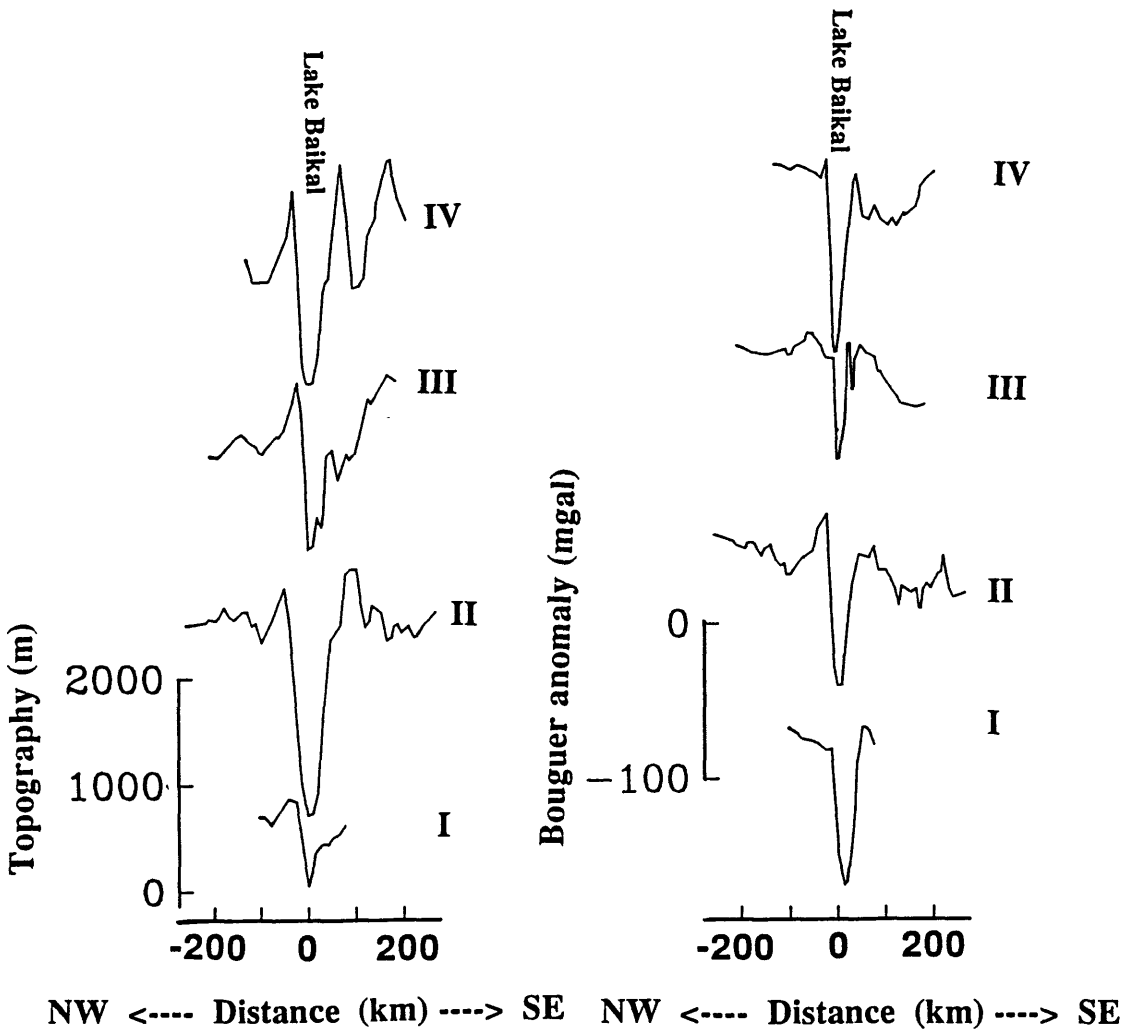


Figure 2.11b

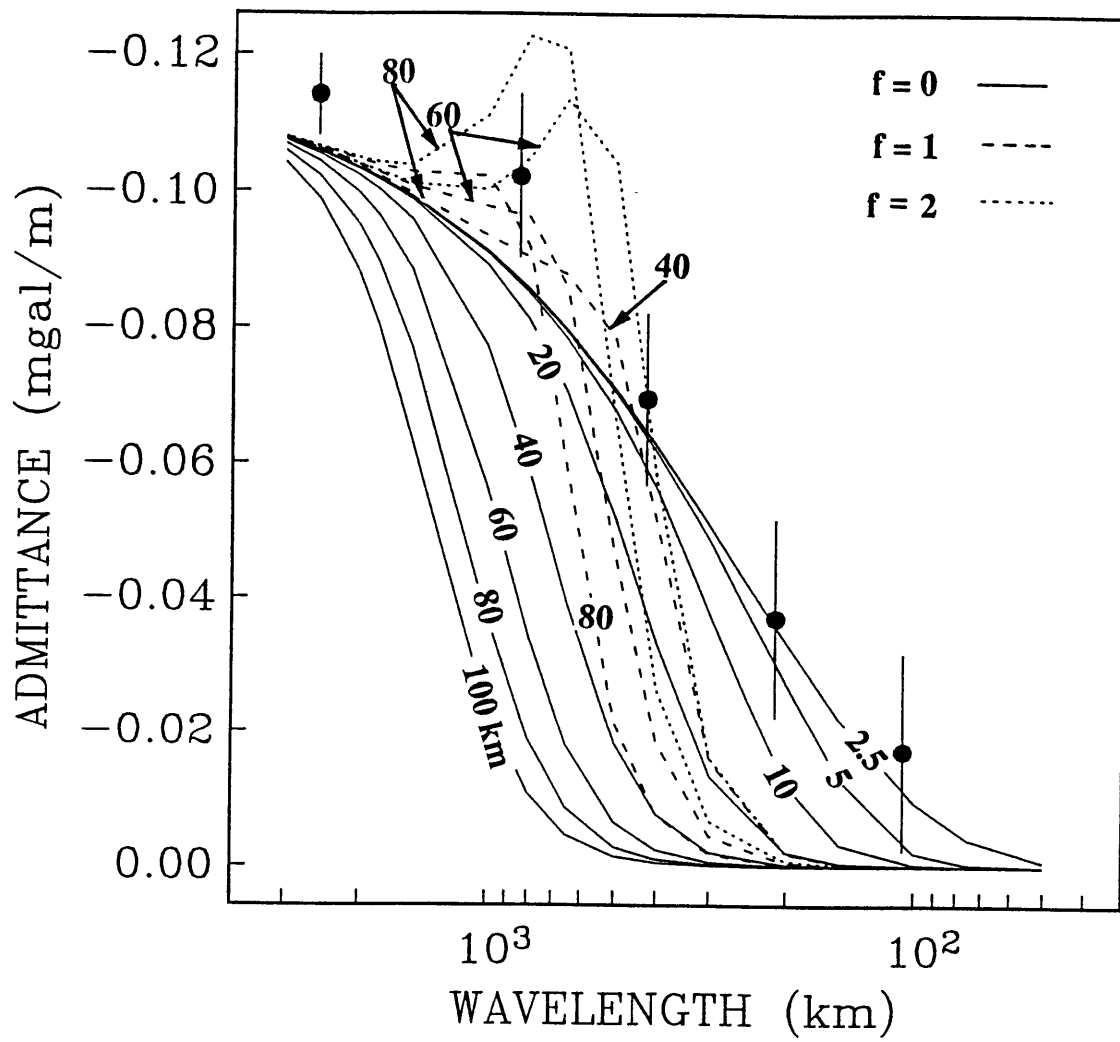


Figure 2.12a

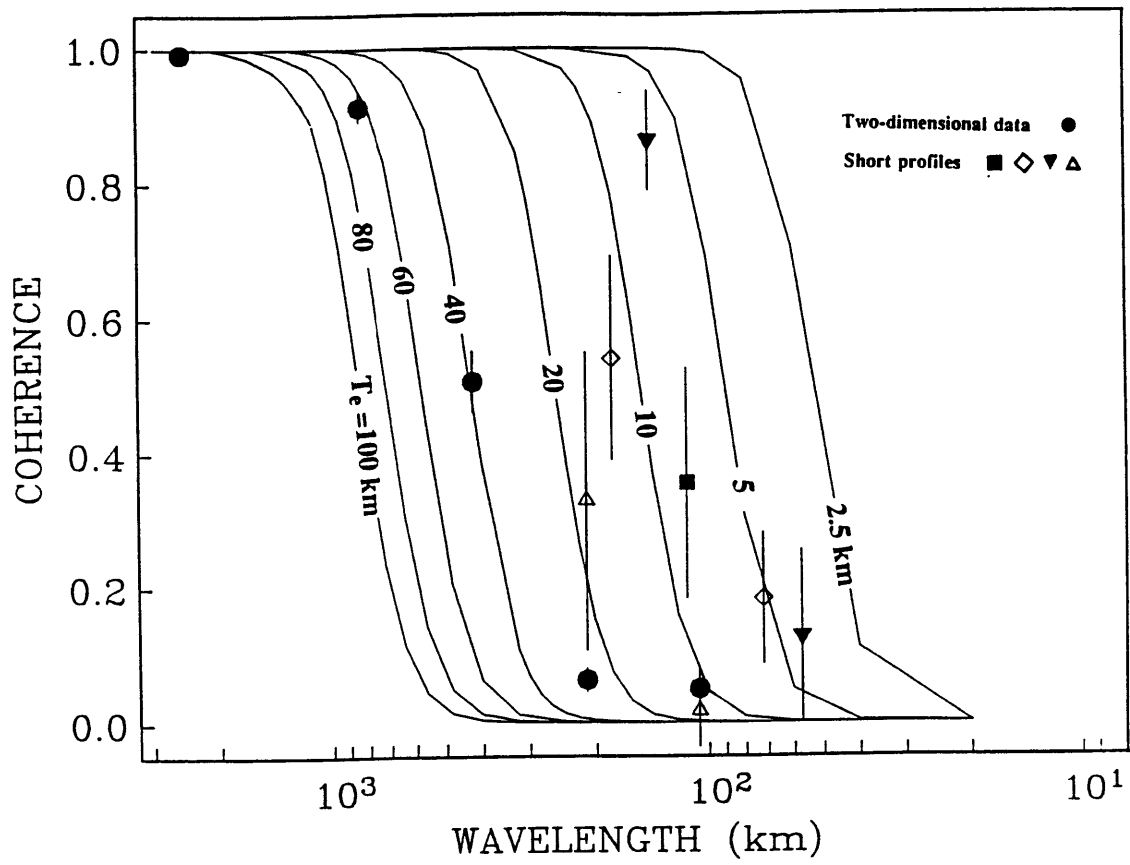
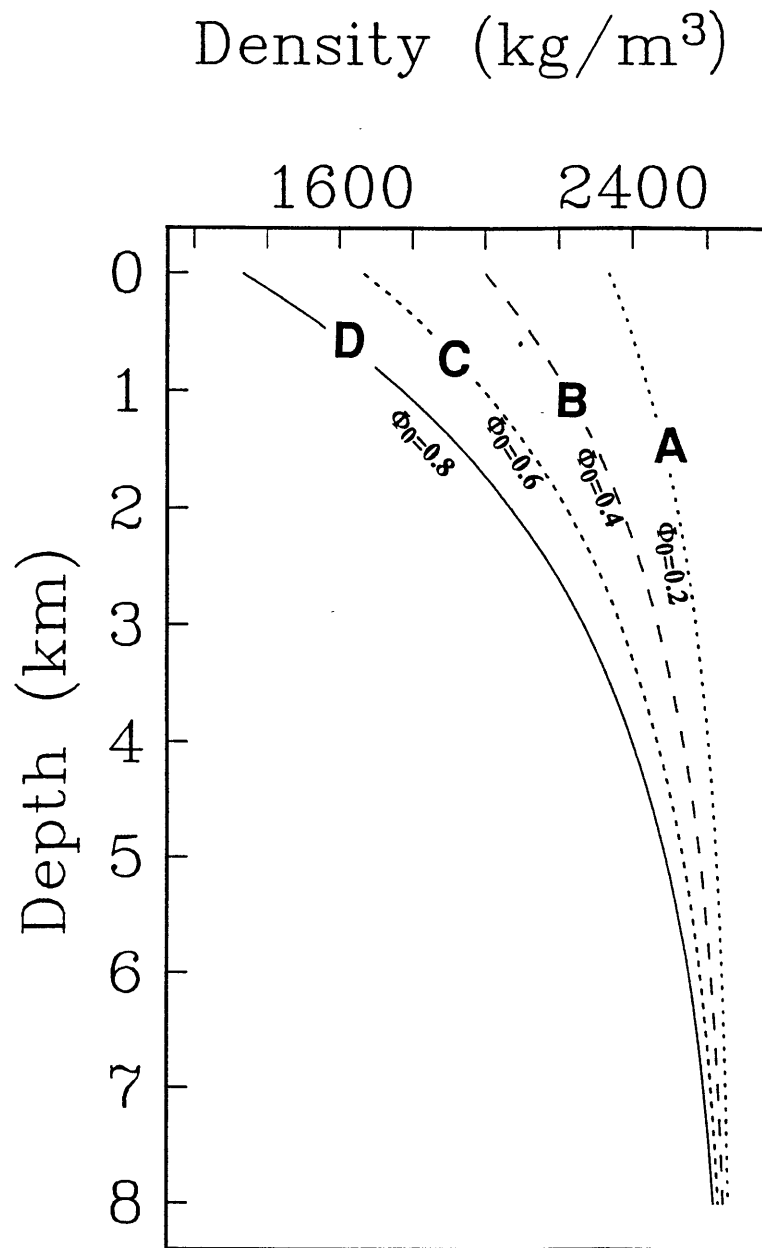


Figure 2.12b



SEDIMENT COMPACTION CURVES

Figure 2.13

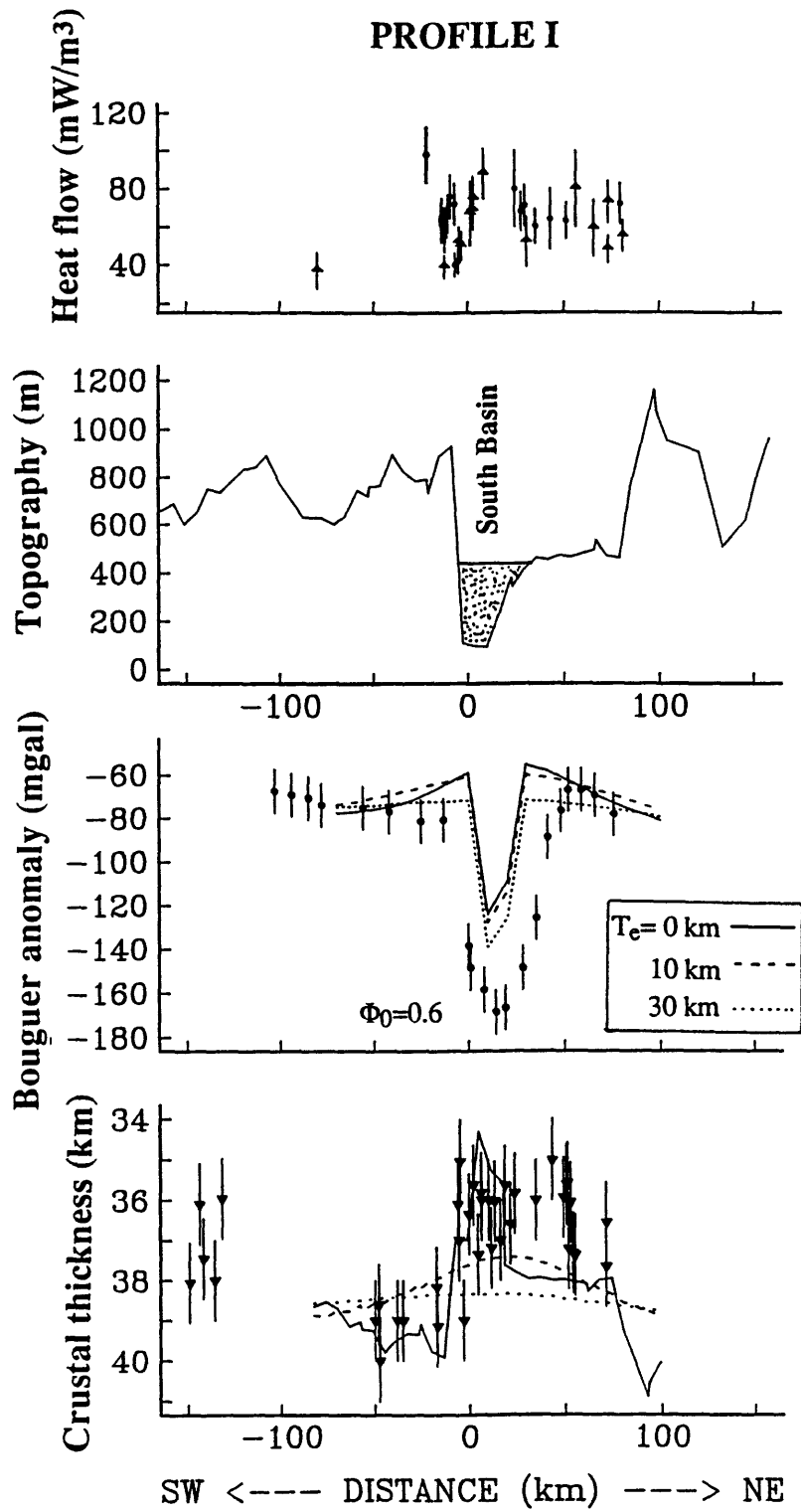


Figure 2.14a

PROFILE I

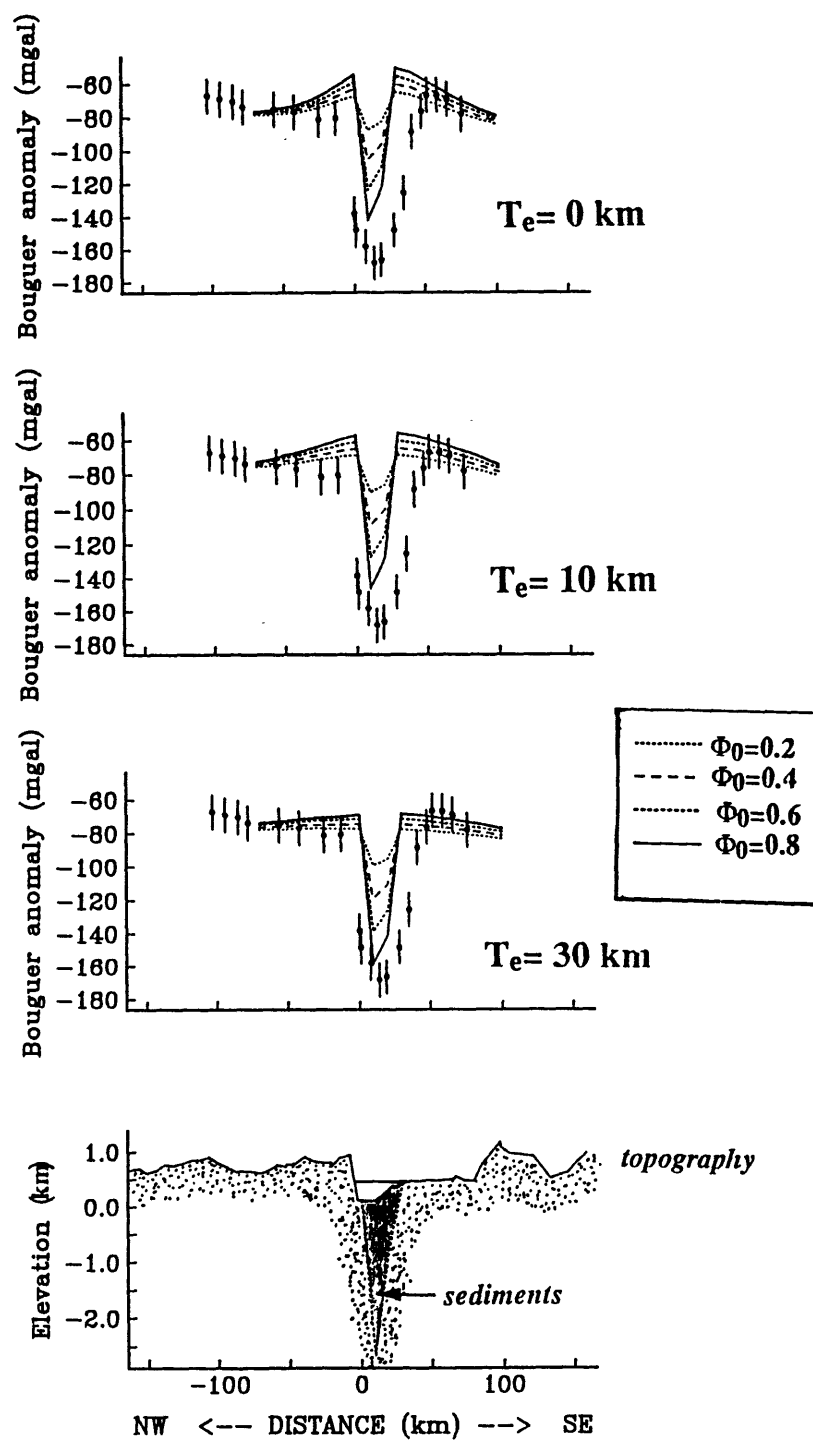


Figure 2.14b

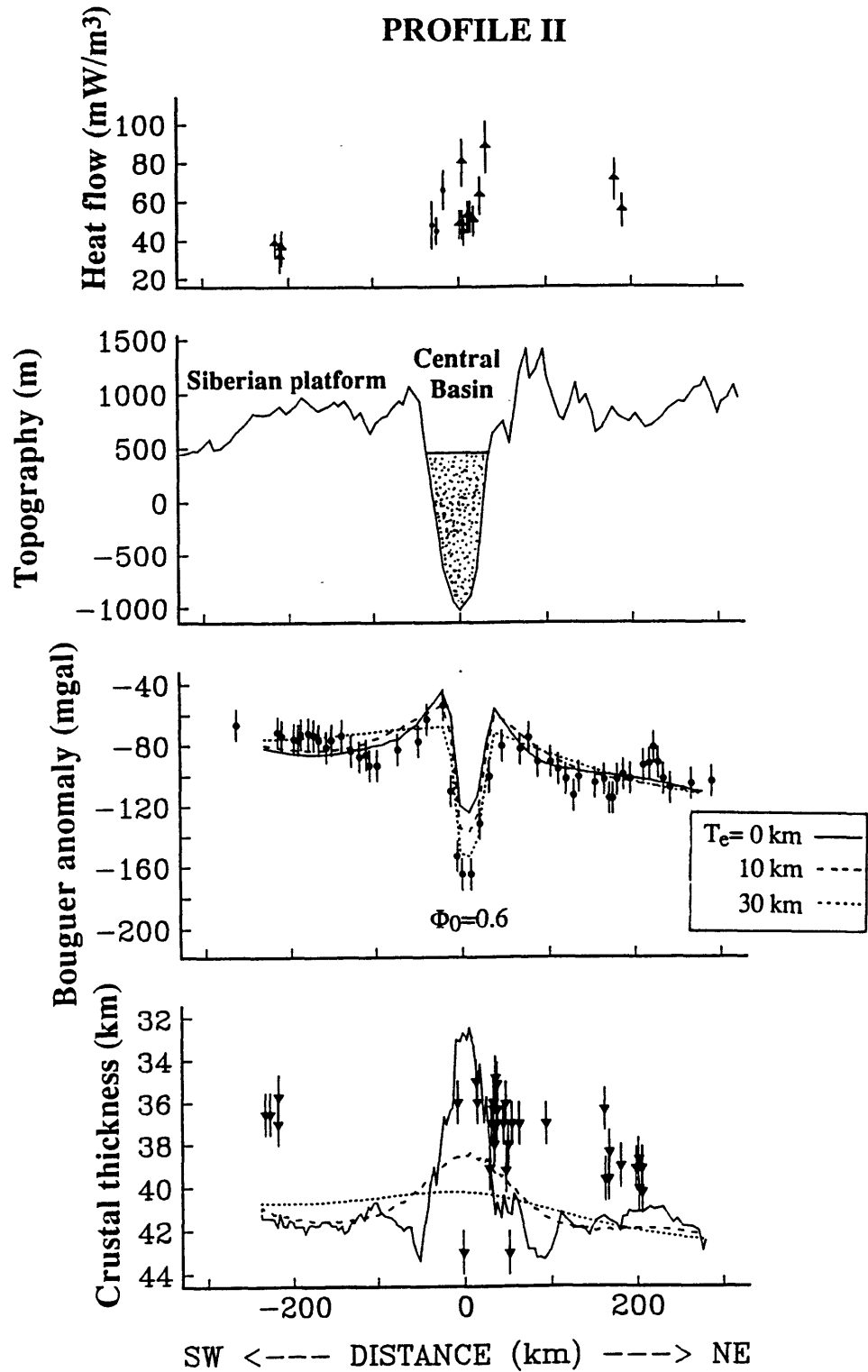


Figure 2.15a

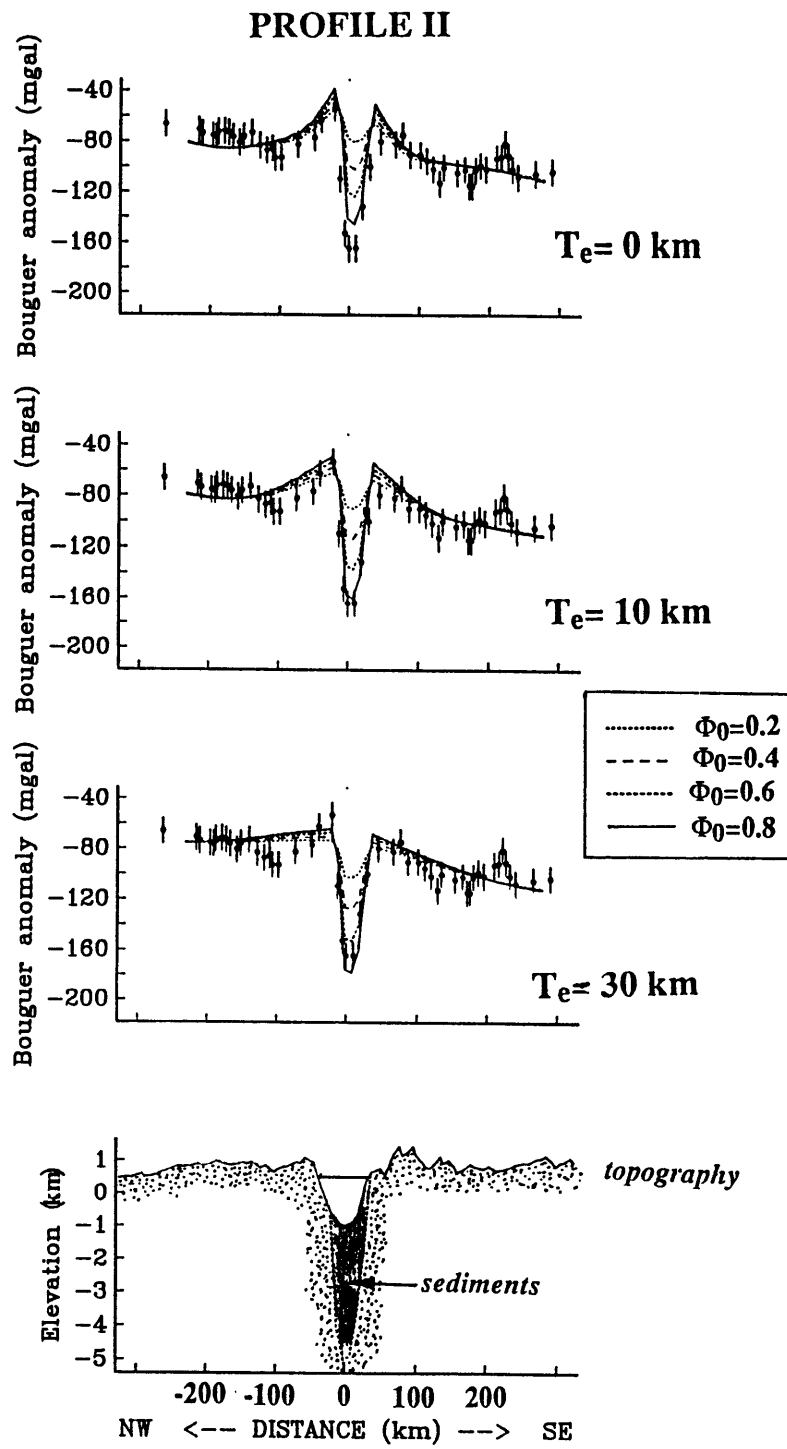


Figure 2.15b

PROFILE III

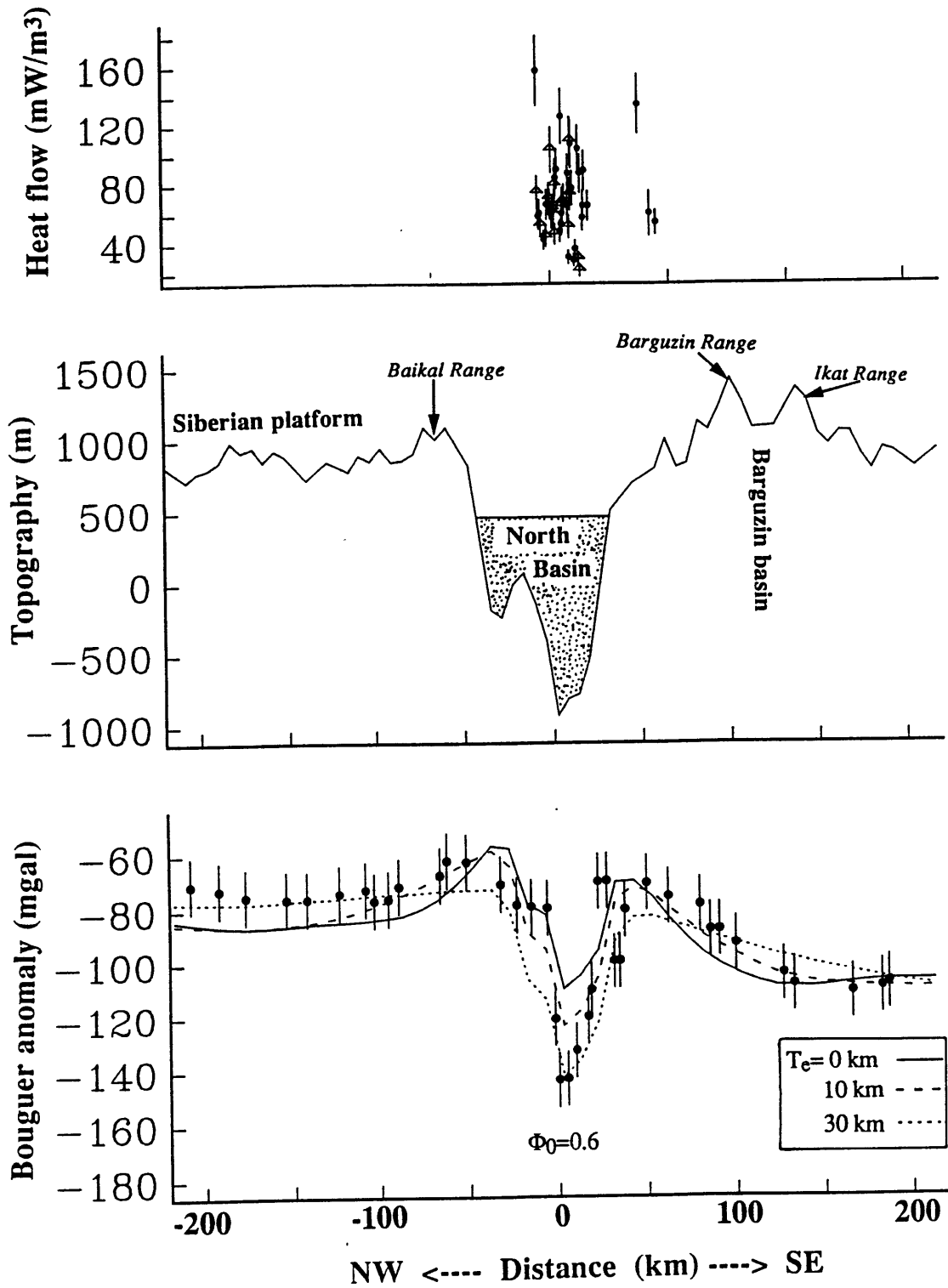


Figure 2.16a

PROFILE III

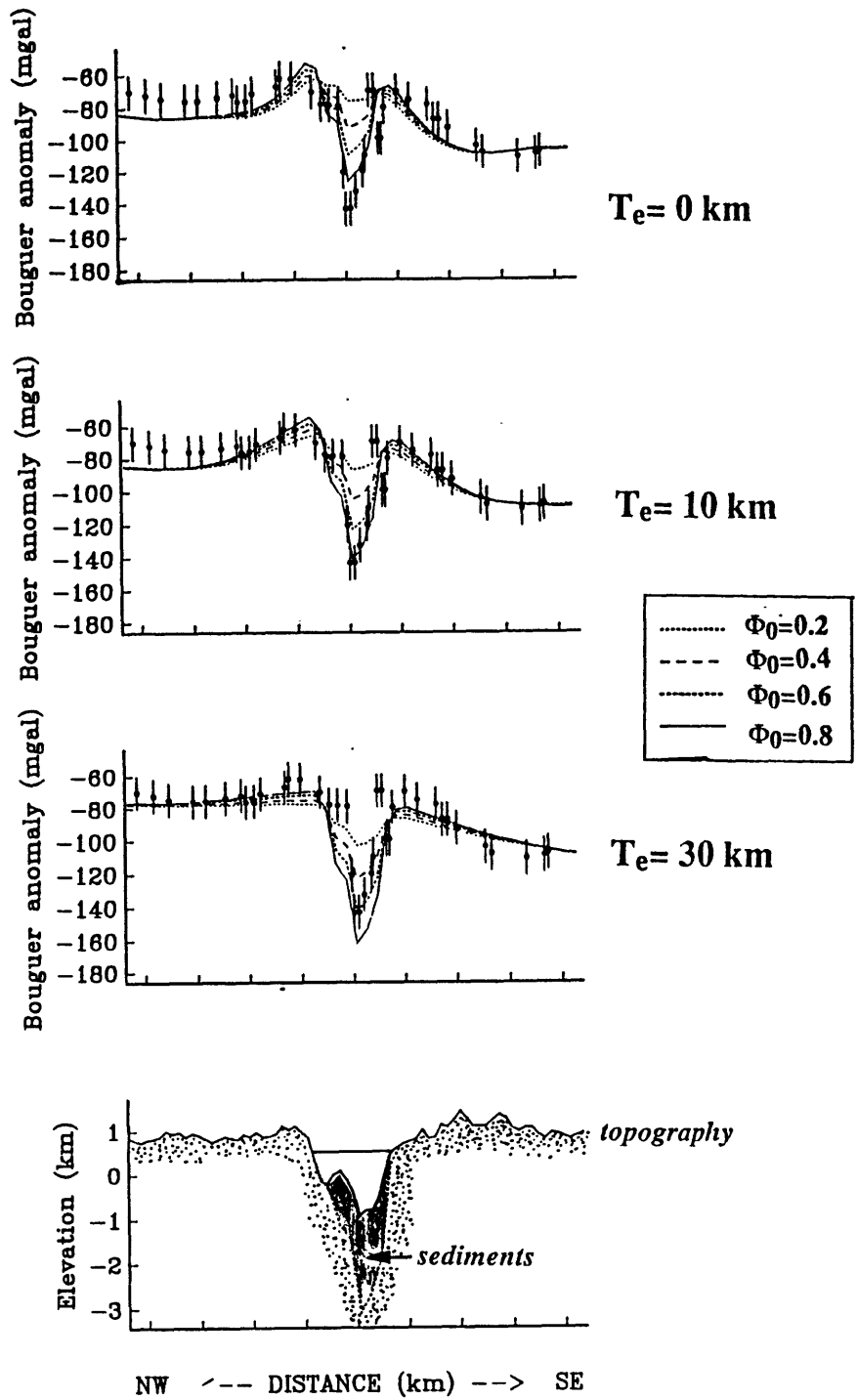


Figure 2.16b

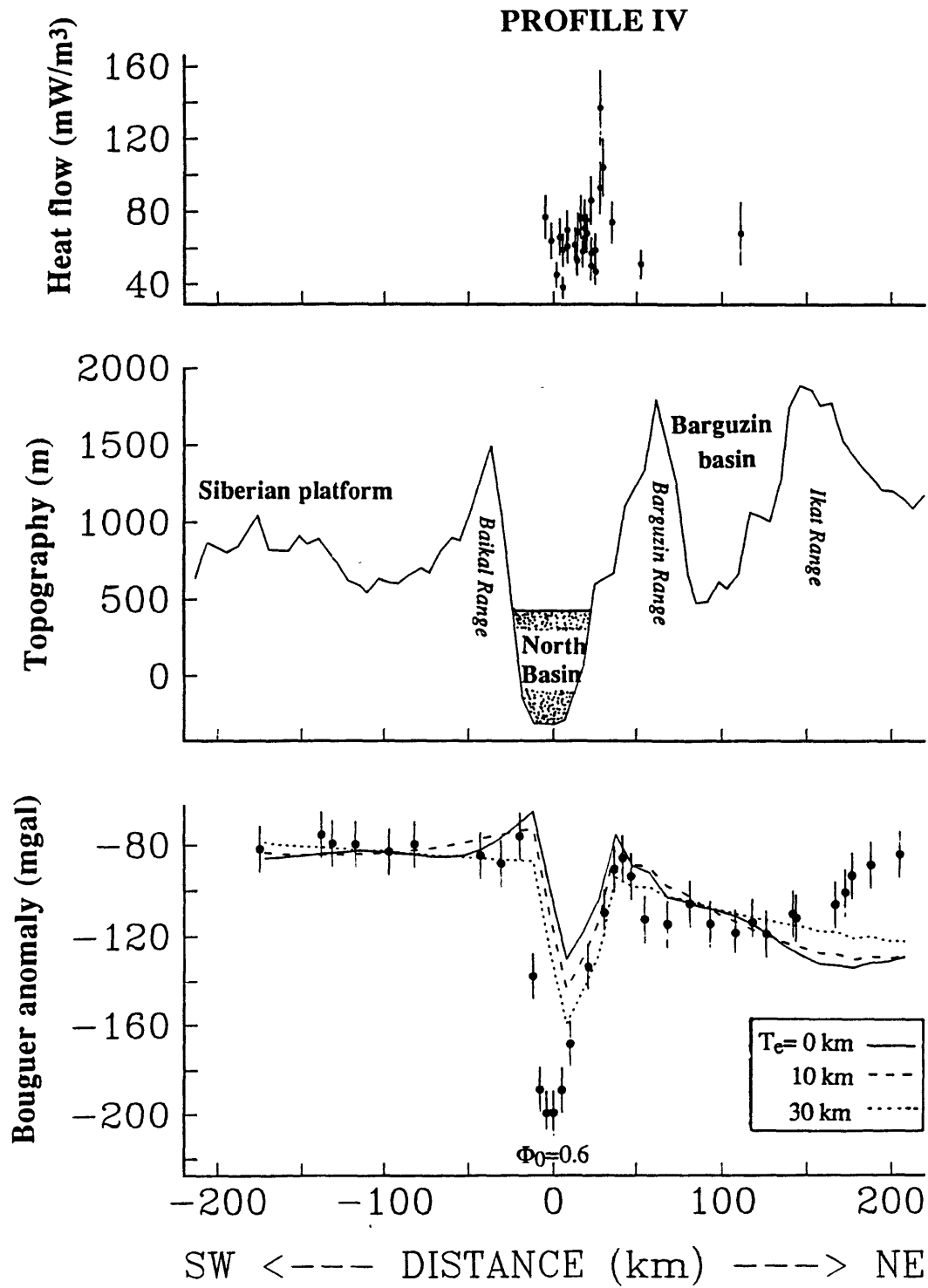


Figure 2.17a

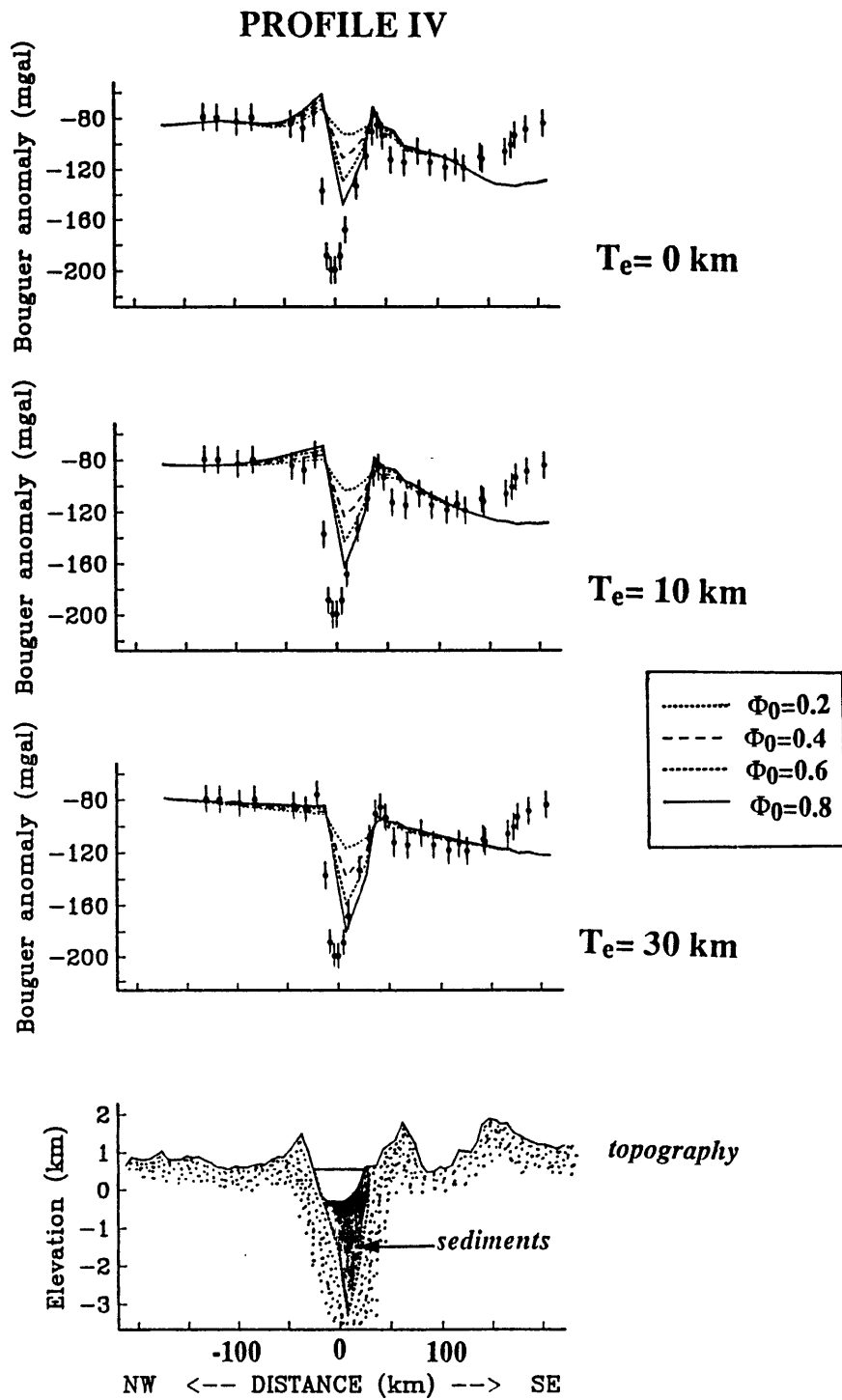


Figure 2.17b

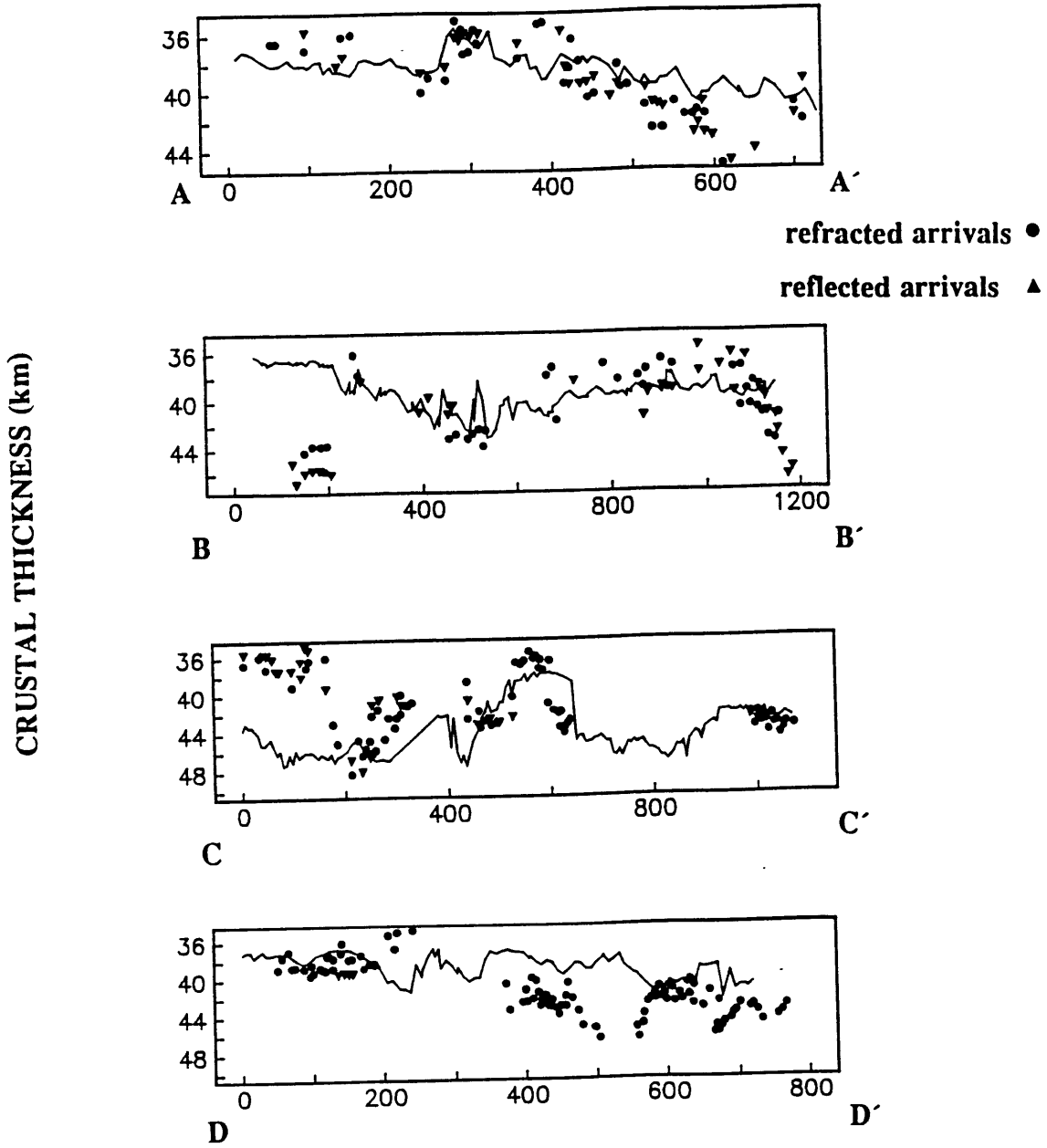


Figure 2.18

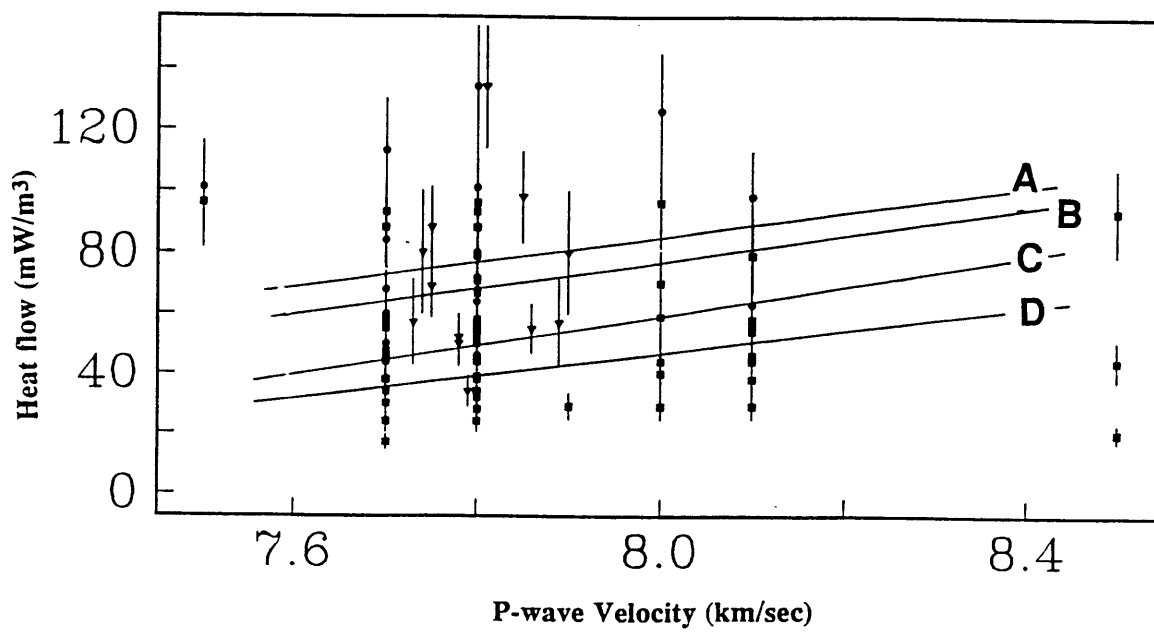


Figure 2.19

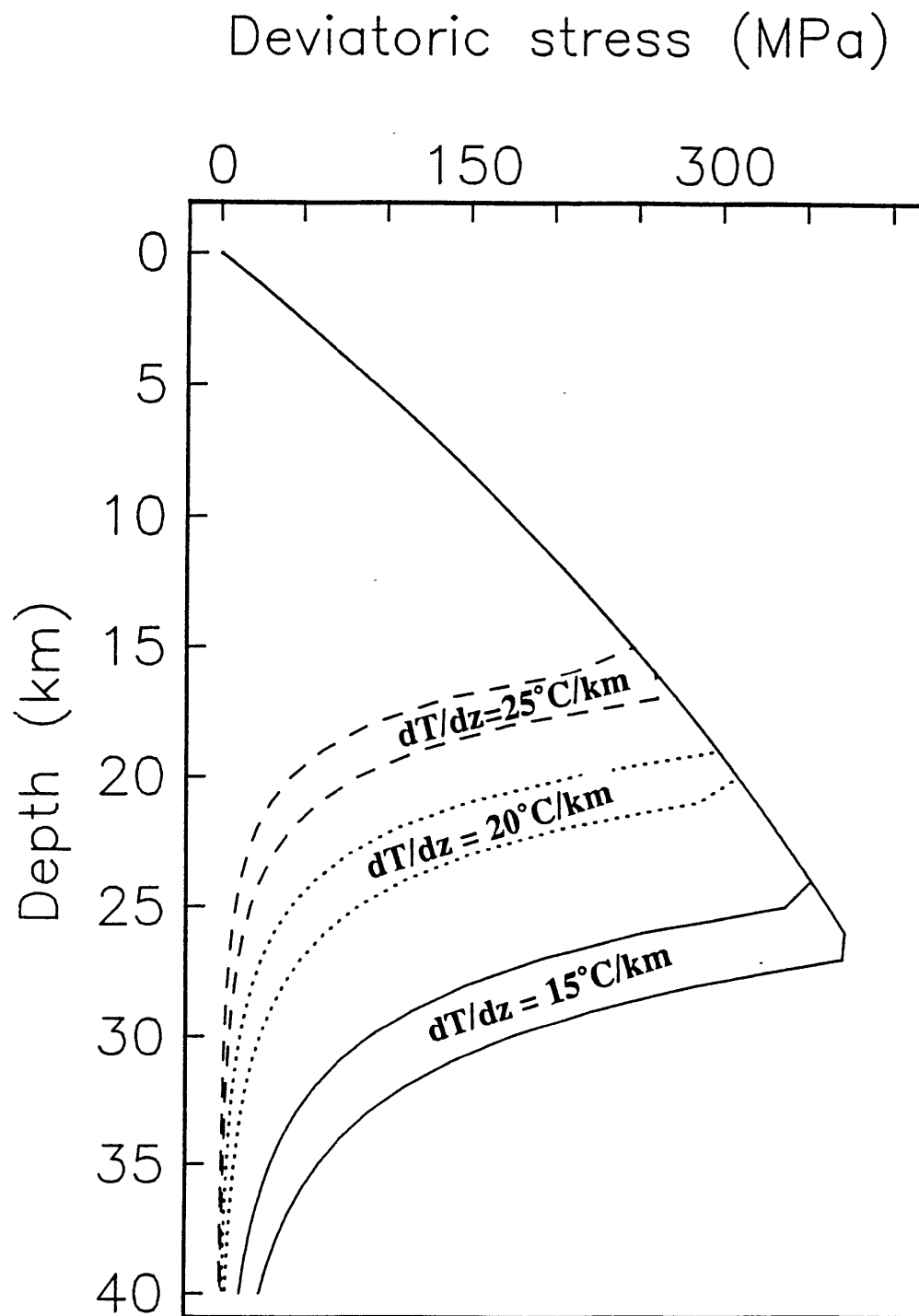


Figure 2.20a

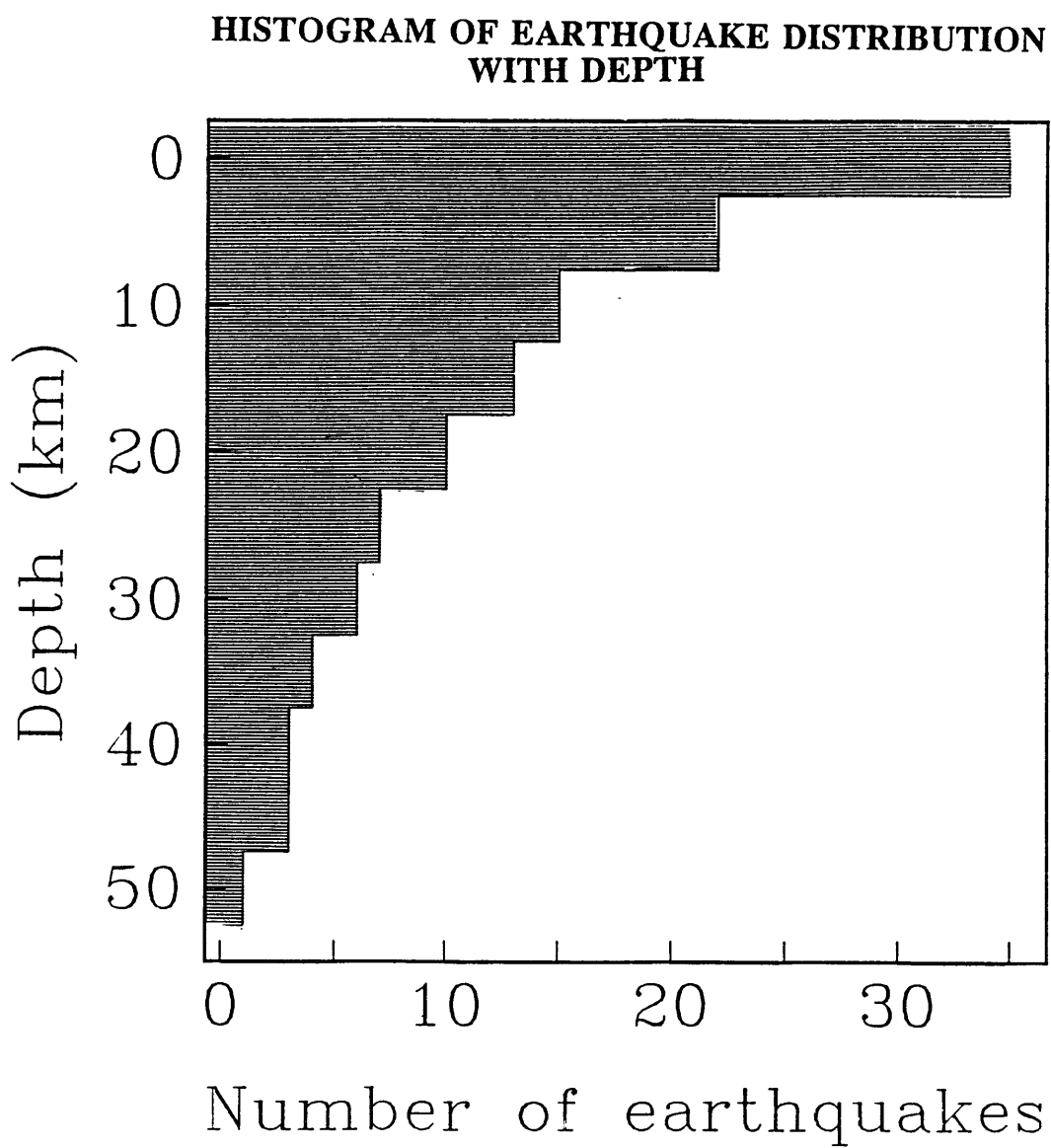


Figure 2.20b

EXCESS MASS CALCULATION

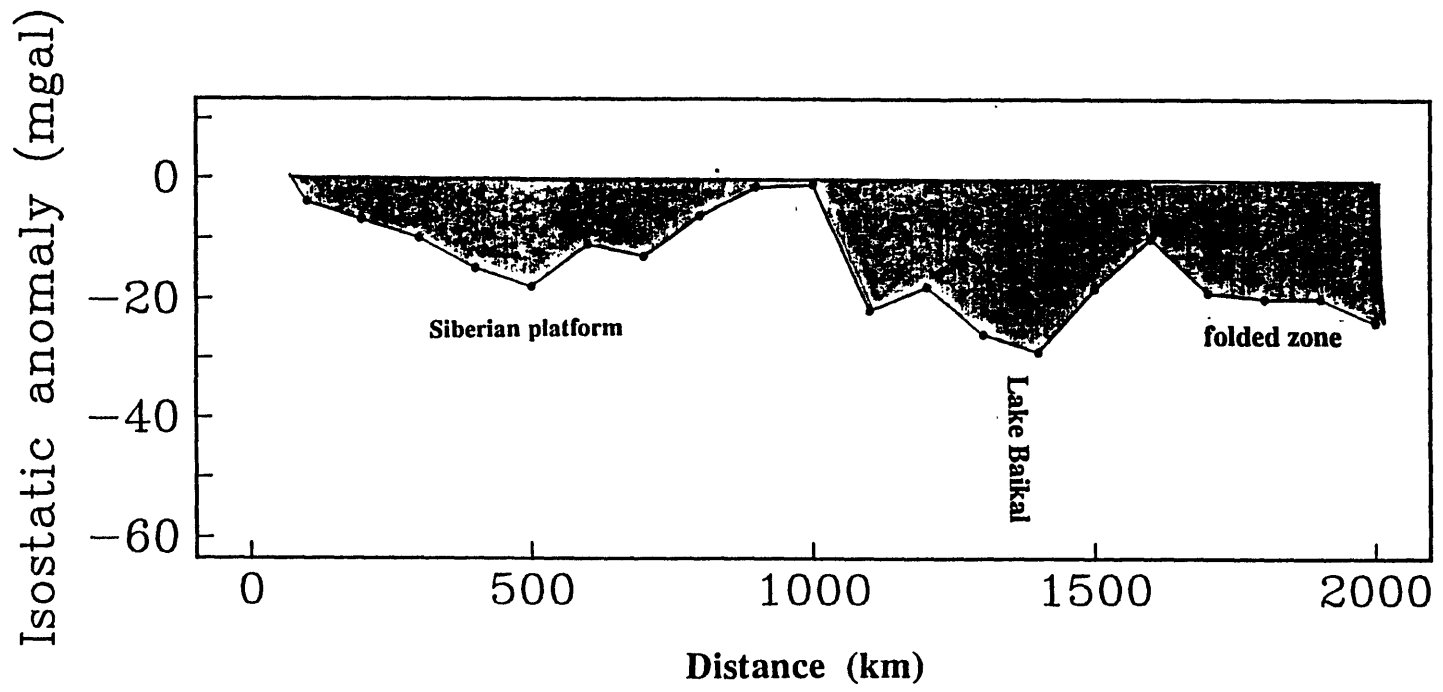


Figure 2.21

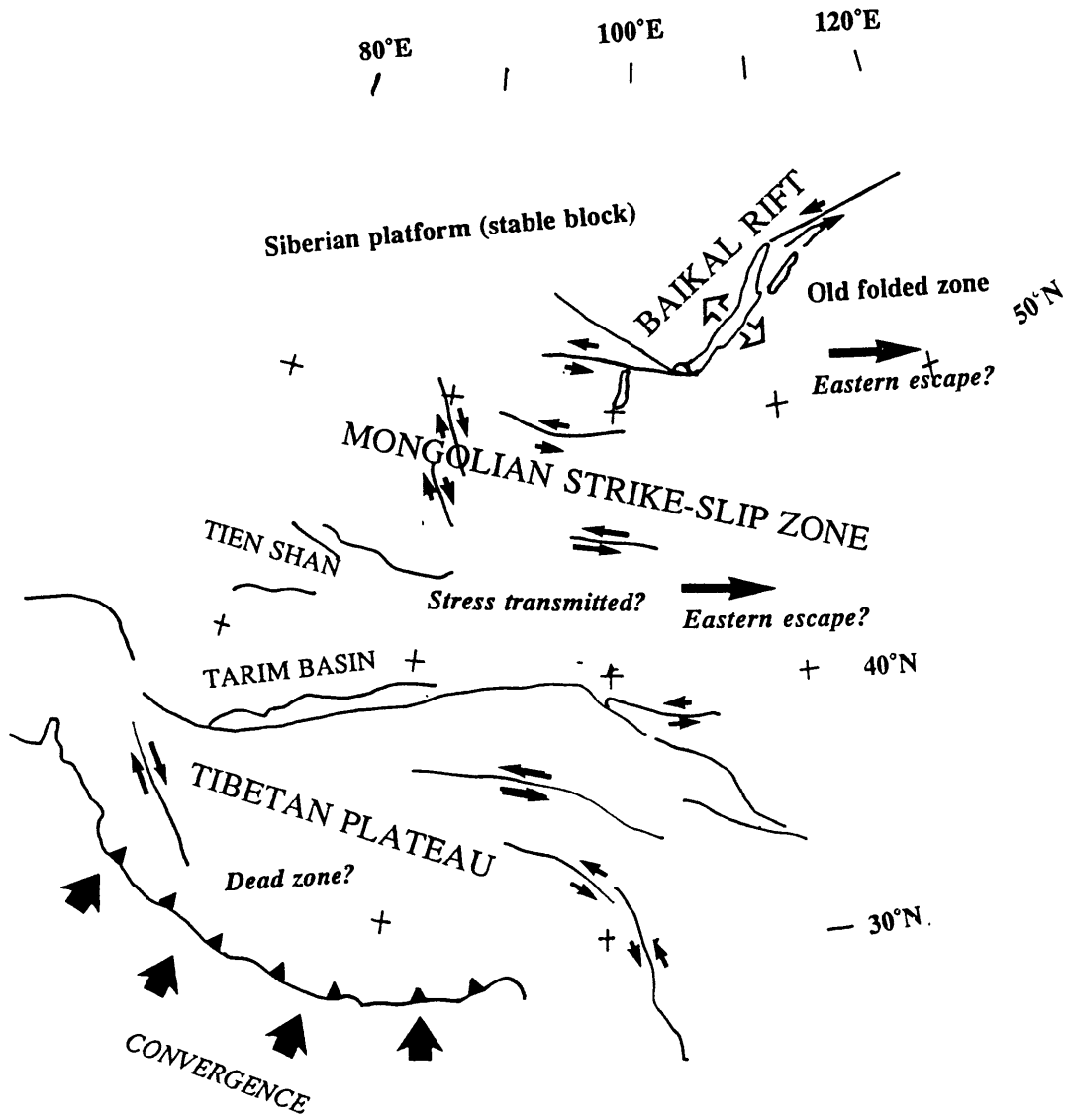


Figure 2.22

Chapter 3

Strike-slip faulting and the origin of the Baikal Rift zone

INTRODUCTION

Rifts form one class in the continuum of extensional features observed on the continents, and, within the family of continental rift systems, the Rio Grande (RGR) and East African (EAR) Rifts are considered archetypes for how localized and profound extension affects continental lithosphere. In these rift zones, master normal faults or pervasive sets of smaller normal faults control the kinematics of upper crustal deformation, and “active” processes like thermal perturbations or dynamic upwellings may drive extension from below (*e.g.*, *Wendlandt and Morgan* [1982]). Although such processes and structures are common to a broad range of rift zones, they may not adequately describe the features of all continental rift systems. In particular, the cold and discrete Baikal Rift zone (BRZ) of eastern Siberia has characteristics which clearly distinguish it from the RGR and EAR. This study focuses on the processes and structures controlling the development of the BRZ and examines the possible pull-apart origin of some parts of the rift system and the role of strike-slip motions and passive far-field plate-boundary stresses in producing some of the observed geological features and geophysical signatures.

TECTONIC FRAMEWORK

The BRZ has developed in the same tectonic settings as the more archetypal RGR: Both rifts are bounded on the west by stable tectonic elements — the irregular edge of the Siberian platform and the Colorado plateau respectively — and on the east by folded zones — a Caledonian orogenic belt in the case of the BRZ and the Sevier and Laramide Rocky Mountains for the RGR. However, whereas extensional deformation in RGR is distributed over a wide zone in a classic horst and graben pattern, rift-related faulting in the BRZ is confined to a discrete zone barely wider than Lake Baikal (40 to 100 km) along much of the rift's length. Nucleation and localization of deformation in such a discrete zone probably reflects the presence of a pre-rifting crustal weakness (Paleozoic suture) at the edge of the Siberian platform (*e.g.*, *Zamarayev and Ruzhich* [1978]) and may also imply the predominance of cold and brittle crustal rheologies and of forces between microplates in controlling the kinematics of BRZ development.

The BRZ has an S-shaped morphology, with major strike-slip zones extending westward from the southern tip of Lake Baikal and eastward from its northern tip. The outermost rift basins west of Lake Baikal's southern end trend north-south and lie within the Mongolian microplate, the most seismically active intraplate region on the continents. These north-south basins are bounded on the north by the Tunka "transform" [*Sherman and Levi*, 1977; *Sherman*, 1978; *Zonenshain and Savostin*, 1980], a left-lateral strike-slip fault readily visible on the Landsat scene and the corresponding line diagram shown in Figure 3.1. Left-lateral river offsets of greater than 10 km are observed across the Tunka fault at some locations, and *Doser* [1991a] reports three predominantly strike-slip earthquake focal mechanisms (refer to Fig. 2.5b) along the fault for large earthquakes since 1950. Thirty kilometers south of the north-south basins and approximately 130 km south of the Tunka fault lies another east-west strike-slip fault, and focal mechanisms along this

fault [Doser, 1991a] are consistent with left-lateral strike-slip displacement oriented obliquely to the fault (Fig. 2.5b). The north-south basins have a width of 35 km near the Tunka fault and narrow to 15-20 km at their southern ends, and the geometry of the basins, associated normal faults, and the two large strike-slip faults implies a partial pull-apart origin for the north-south basins. In addition, the Tunka fault and the subparallel strike-slip fault form the north and south sides of a pull-apart rhombohedral basin whose edges, clearly outlined by outcrops of Neogene volcanic rocks, act as leaky transforms (Fig. 3.1).

East of the north-south trending basins, the orientation of rift basins shifts to east-west where the east-west striking Tunka and South Baikal Basins form a conjugate pair of nearly rhombohedral basins situated between the Tunka fault and the Main Sayan fault. Landsat photos show that these two faults merge at a well-developed discrete scarp at the southwesternmost tip of Lake Baikal (Fig. 3.1) and continue eastward to form the linear southern edge of the South Baikal rhombohedral basin. The Main Sayan fault, an ancient structure reactivated as a left-lateral strike-slip fault in Cenozoic time, bounds the southwestern edge of the Siberian platform in this area and thus serves as a fundamental tectonic boundary in the region. However, the level of seismic activity on the Main Sayan fault is lower than that on the Tunka fault, and the latter structure is likely the more active one at this time. As seen in Fig. 3.1b, the discrete scarp of the Main Sayan fault and some of its splays are visible on satellite photos for at least 500 km to the northwest of Lake Baikal's southern tip [Tapponnier and Molnar, 1979], but stream offsets decrease from 15 km where the Irkut River crosses the fault 15 km northwest of the lake to only a few kilometers at a distance of 300 km from the lake along the fault. Thus, it is likely that left-lateral displacements associated with opening of the 70 km wide South Baikal Basin are distributed between the Tunka fault, reactivated portions of the Main Sayan fault, and other smaller faults. Adding even more complexity to the kinematic framework is the requirement that the Main Sayan fault, now joined with the Tunka fault, take on a dip-slip

character where it bounds the southern edge of Lake Baikal along the base of the youthful and rugged Khamar-Daban Range. From northeast to southwest across the fault, the crust thickens abruptly by 8 km [Vinnik, pers. comm.; Chapter 2] at the southwesternmost tip of the lake, but the present lack of timing constraints makes it impossible to determine whether left-lateral and dip-slip motion along the reactivated portion of the Main Sayan fault were synchronous or whether the strike-slip motion predated the onset of large-scale thick-skinned normal faulting along this margin.

Lake Baikal itself is comprised of three distinct, nearly rhombohedral rift basins arranged in an echelon pattern (Fig. 3.2). Both the bathymetric and sediment thickness profiles of the South and Central Basins display profound west-directed asymmetry. These basins are filled by up to 1416m and 1625m of water respectively and have sediment thickness of over 7 km along their steep western edges [Hutchinson *et al.*, 1991]. In contrast, the North Basin, although characterized by the same sense of west-directed asymmetry, is relatively shallow, having only 920 m of water and a maximum of 4.4 km of sediment along its western edge [Hutchinson *et al.*, 1991]. The sedimentary record in these and the off-axis BRZ basins may be consistent either with distinct stages of rifting between Eocene to Early Pliocene time and Middle Pliocene time to present [Logatchev and Florensov, 1978] or with the sudden onset of rifting at approximately 4 Ma [Artyushkov *et al.*, 1990]. During early Pliocene time, coarse sedimentation began throughout the rift zone, the North Basin began to subside rapidly, and the previously-linked South and Central Basins were separated by the uplift of a horst structure—events that imply a period of vigorous tectonism at this time. The young North Basin differs from the South and Central basins not only in its water depth, age, and sediment thickness, but also in its orientation (nearly north-south as opposed to the northeasterly trend of the South and Central basins) and seismicity levels. The large number of earthquakes (both normal and strike-slip [Chapter 2]) which occur in the South and Central basins (refer to Fig. 2.5a)

indicate that these basins continue to be active tectonic elements within the rift system. In contrast, the young North Basin is nearly aseismic and its history may be that of a passive half-graben, not active pull-apart, an interpretation corroborated by multichannel seismic results of *Hutchinson et al.* [1991].

The active Central Basin and the apparently passively opening North Basin are separated by a northeast trending line of local topographic highs extending from Olkhon Island along the lake's western shore, through the submerged Academician Ridge, and into Svyatnoy Nos, a land mass close to the lake's eastern shore. Ridge offsets on Svyatnoy Nos and the geometry of the boundary between the Central and North basins imply that normal faulting on the northeastern and southwestern sides of the Academician Ridge horst is probably accompanied by a dextral slip component of approximately 10 km. On Svyatnoy Nos, the Academician Ridge fault system is cut by a nearly perpendicular sinistral slip fault which forms the northeastern edge of the Central Basin. The magnitude of the displacement along this sinistral slip fault is also approximately 10 km, and motion on this fault and oblique (dextral) slip on the Academician Ridge fault may have occurred synchronously.

To the east of the North Basin and roughly along the strike of the Central Basin lies the large and asymmetric Barguzin Basin (Fig. 3.3), which more clearly fits the pattern of the southern part of the rift's axis. Whereas the South and Central Basins link the Tunka-Main Sayan fault system and Academician Ridge fault, the Barguzin Range and Barguzin and Tsipi-Bount Basins take up differential stress between the southern part of the rift zone and the diffuse Udokan shear zone, which extends 800km nearly due east of the northern tip of the lake. The Barguzin Basin contains the older sedimentary section missing from the young North Basin [*Nikolayev et al.*, 1985], and, in contrast to the nearly aseismic North Basin, is the site of many earthquakes [Chapter 2]. Thus, passive (aseismic) widening of the North Basin is probably accommodated by coseismic movement of faults

bounding the Barguzin Basin, which apparently served as the site of extensional deformation in the northern part of the rift zone's axis prior to opening of the North Basin and probably continues to be the locus of active deformation in the northern part of the BRZ.

The Udokan left-lateral shear zone extends nearly due east of the northern tip of Lake Baikal and trends subparallel to the Tunka fault located 450 km to its south. The five rift basins of the Udokan shear zone are arranged in an en echelon pattern and, close to Lake Baikal, have the form of perfectly rhombohedral pull-aparts. Near the intersection of the Barguzin accommodation zone and the Udokan shear zone lies the slightly crescent-shaped Muya Basin, a non-rhombohedral basin that marks the position of the northeastward shift in strike of the shear zone where it turns to follow the edge of the Aldan Shield. Within the shear zone, a key difficulty is distinguishing the faults which are actively moving from those which move only sympathetically in response to jostling of other blocks. The only obvious indicator of the amount of displacement in a direction parallel to the overall sense of shear is left-stepping stream offsets in the rhomboid Upper Angara basin. This loose constraint yields estimates of ~10 km of displacement, but the total amount of displacement across the shear zone is probably several times greater over a period of millions of years. The Udokan shear zone has the highest level of seismicity of any subregion of the BRZ, and focal mechanisms presented by *Doser* [1991b] show that both normal and strike-slip motions occur within the shear zone.

STRIKE-SLIP DISPLACEMENTS AND RIFT DEVELOPMENT

Although some workers (*e.g.*, *Balla et al.* [1991]) have recognized the existence of large-scale strike slip faults in the BRZ, most studies focus more sharply on the role of normal faulting in the rift's evolution. Normal faults occur throughout the BRZ in basin-

bounding or range-front positions, and vertical displacements occasionally exceed 10 km [Sherman *et al.*, 1973]. Such large displacements are observed on the Obruchev normal fault system, which forms the western edge of the South and Central Lake Baikal Basins and links the Academician Ridge fault and Main Sayan and Tunka faults. An analogous normal fault in the northern part of the BRZ might be the Barguzin basin-bounding fault, whose southern end abuts the Academician Ridge fault. These large-scale normal faults form at high-angles to the associated strike-slip structures and appear to be dragged into the fault zones by shearing to both the north and south. Such normal faults may develop in response to differential strain between shear zones, implying a pull-apart origin for most of the axial BRZ basins. Within a given shear-normal fault-shear system, differences in the rates of displacement along the bounding northern and southern strike-slip structures may also explain the asymmetry of the associated pull-apart basins. For example, if the amount of strike-slip displacement along the Main Sayan-Tunka fault system is significantly larger than the strike-slip component of displacement along the Academician Ridge fault system, then the Obruchev fault system, and not a fault bounding the eastern edge of the lake, could be the preferred site of normal-sense crustal displacements and could produce the profound westward thickening of sediments and deepening of the bathymetry in this part of the rift. The S-shaped form of the entire BRZ and of the rift axis itself also supports its interpretation as a primarily strike-slip feature. Microstructural studies of deformed rocks show that differential strain between subparallel shear planes can produce extensional cracks with sinistral forms. Extrapolating these results to a megascopic scale, the axial part of the BRZ may serve the same purpose as an extensional crack, acting as a weak link that relieves differential strain between the left-lateral shear couple formed by the Tunka and Udokan shear zones.

The extreme thickness of sediments in the South and Central Basins of Lake Baikal may also be a consequence of the pull-apart origin of these basins. Lack of age constraints renders the precise reconstruction of basin subsidence histories impossible, but, by any estimation, the BRZ is a young rift system which has formed within the past 40 Ma. If the part of the South and Central Basin sedimentary piles deposited since the early Pliocene (4 Ma) tectonic event has a thickness of only 4 km compacted (roughly equivalent to maximum sediment thickness in the young North Basin), producing this amount of subsidence on such geologically short time scales requires sedimentation to occur in conjunction with active faulting which deepens the basin. Classic models for basin development (*e.g.*, Royden and Keen [1980]) require crustal stretching of 300% and 225% for 4 km of water-loaded initial subsidence if the crust represents 30% and 20% of the total lithospheric thickness respectively. Sediment-loaded initial subsidence of 4 km can be achieved with approximately 35% crustal stretching for $\rho_{\text{sed}}=2400 \text{ kg/m}^3$ and crustal thickness representing 20 to 30% of the total lithospheric thickness. More careful application of basin analysis methods to the axial basins of the BRZ may confirm the result implied by these rough calculations—namely that the amount of crustal stretching required to produce the observed “initial” subsidence significantly exceeds the observed amount of crustal stretching (estimated at 0 to 15% based on crustal thickness variations [Chapter 2] and 5 to 15% based on analysis of a variety of geological and geophysical data [Zorin, 1971; Logatchev and Florensov, 1978]). Furthermore, the observed subsidence cannot include an appreciable component due to thermal relaxation of the lithosphere since the time scale over which thermal effects become significant is longer than 4 my.

Theoretical and field-based studies of the evolution of small pull-apart basins show that they typically develop within a few million years and undergo subsidence of several kilometers during active displacement on associated strike-slip faults [Steckler and Watts, 1982; Pitman and Andrews, 1985]. Application of these results to large pull-aparts (*e.g.*,

at the scale of the Pannonian or Vienna Basin systems [*Royden et al.*, 1982; *Royden*, 1985]) is complicated by the importance of thin-skinned deformation in some settings. The scale of the axial BRZ basins lies between that of the small and large pull-aparts, and conclusions about the degree of decoupling between the uppermost crust and underlying material must await better geological and geophysical data. Abundant evidence for fault-controlled sedimentation in the South and Central Basins includes not only the marked westward thickening of sediments but also truncation of sedimentary layers along basin-bounding faults [*Nikolayev et al.*, 1985]. Although the North Basin shares some of these features, the nearly complete lack of seismicity compared to the more southerly basins imply not an active pull-apart origin, but rather a passive half-graben origin, for this part of the BRZ, an interpretation corroborated by multichannel seismic results of *Hutchinson et al.* [1991].

DISCUSSION

The BRZ has long been interpreted as a passive rift system, one which developed in response to plate-boundary stresses transmitted across the 2700 km expanse of deformed Asian lithosphere between the Himalayan collisional front and the edge of the Siberian platform. Although the stress field produced as a result of ongoing convergence at the India-Asia boundary cannot be easily predicted, simple calculations show that stresses can probably be transmitted laterally across tectonic features [*Molnar and Lyon-Caen*, 1988] and may change in direction over distances as short as several hundred kilometers [*Royden and Burchfiel*, 1987]. Thus, passive rifting may be a viable mechanism for the initiation of the BRZ and the development of other tectonic provinces within Asia (*e.g.*, the Tibetan plateau and the Mongolian strike-slip belt). On the other hand, studies of internal deformation in Asia using plane strain viscous sheet numerical models [*England and*

McKenzie, 1982, 1983] and plane stress laboratory experiments with plasticine [Tapponnier *et al.*, 1982] do not yield extension at the site of the BRZ, but predict only large-scale strike-slip motions in this part of Asia. If these models are correct, then we must consider two hypotheses: either a mechanism other than passive rifting is responsible for the development of the BRZ or our preconceived notions of how extension occurs in continental rift zones do not apply to the BRZ.

This study cannot fully resolve the role of active versus passive processes in driving BRZ initiation and development, but comparisons of geological and geophysical observations in the BRZ to those from the thermally-driven RGR and the dynamically-driven East African Rift offer a first-order assessment of the relative importance of active mechanisms in the BRZ and thus of our first hypothesis. Low terrestrial heat flow of 45 to 60 mW/m² (vs. greater than 100 mW/m² for the RGR [Reiter *et al.*, 1975] and 70-100 mW/m² for the EAR [Jessop *et al.*, 1975] respectively), high seismicity to depths of 20 km (vs. seismicity to only 12-15 km in the RGR), estimated elastic plate thickness of 30 km (vs. 21 km, 27 km, and 31 km for Ethiopian, Western Branch, and Kenyan rifts respectively [Ebinger *et al.*, 1989] and 16 km for the RGR [Bechtel *et al.*, 1990; Ruppel, unpublished manuscript]), and only small amounts of volcanism, representing a continuous spectrum of alkali to tholeiitic magmas [Kiselev *et al.*, 1978], (vs. effusive and distinctly bimodal volcanism in both the RGR and EAR systems) clearly distinguish the BRZ from the “active” rift systems. The BRZ is probably the youngest of the three rifts, however, and effects of deep-seated thermal perturbations take approximately 5 my to propagate through 40 km thick continental crust and 50 my to reach equilibrium. Thus, the 900 km wide Bouguer gravity residual low of 15-20 mgal [Diament and Kogan, 1990], the 1700 km wide and 400m high topographic dome, and seismic [Puzirev, 1981] evidence for an intracrustal low-velocity zone may indicate that thermal and/or dynamic processes contribute to the evolution of the BRZ. The relationships between so-called “passive” and

“active” mechanisms are, however, difficult to resolve. Plate-boundary stresses can cause thermal perturbations or changes in convective flow patterns, and thermal or dynamic processes may in turn lead to reshuffling of continental microplates in the BRZ area and buildup of intraplate stresses. Furthermore, the two stages of rifting recognized in the BRZ by early workers may be a consequence of mixed driving forces: initiation at 40 Ma as a result of passive plate-boundary stresses followed by reactivation and sudden extension in middle Pliocene time due to the effects of an active process. Recent studies show that passive rifting of continental lithosphere with a layered rheology can create basins as deep as those in the BRZ within several million years [Bassi, in press], and, if these results can be successfully applied to a real rift basin like that of the BRZ, invocation of an active rifting process may prove unnecessary.

The second hypothesis proposes that the criterion used for evaluating the applicability of the extant models of Asian deformation to the problem of the evolution of the BRZ is not correct. As a continental rift, the BRZ is certainly the site of extensional deformation, but the observed small amount of net extension, estimated at 10-30 km [Zorin, 1971; Logatchev and Florensov, 1978] and 3-7% [Artyushkov *et al.*, 1990] from basin subsidence analyses, implies that the BRZ probably should not take on the classic form of a highly extended terrain (*e.g.*, markedly thinned crust, normal faults, vertically-oriented compressive stresses) in the numerical or laboratory models. Coupled with the fact that the models for Asian deformation make no attempt to include the effects of juxtaposing the rigid and irregular boundary of the Siberian platform against the more plastic lithosphere of southern Asia, the inability to produce an extensional deformation at the site of the BRZ is not surprising. On the other hand, formulating new models does not increase our understanding of the kinematics of intraplate deformation in response to plate-boundary stresses. In fact, even the present simplistic models, which predict large-scale strike-slip faulting as the primary mode of internal deformation in Asia, are consistent with

the thesis of this study: that most of the initial opening of the BRZ, in particular its southern part, is the direct or indirect result of displacements along strike-slip faults and the development of associated pull-apart features. Thus, the loose agreement between the strike-slip interpretation of BRZ evolution and the results of the numerical and laboratory models indicates that passive plate-boundary forces could at least contribute to the development of strike-slip structures. This result in no way precludes the involvement of mantle processes beneath the BRZ in driving strike-slip or normal fault displacements or further rifting.

CONCLUSIONS

The morphology of the BRZ, the thickness of Pliocene and younger sediments in Lake Baikal, and observed offsets on strike-slip faults support the interpretation that the axial part of the BRZ has opened due to left-lateral strike-slip displacements. Far-field boundary stresses associated with ongoing convergence of India and Asia may cause the accumulation of stresses between microplates in the BRZ region and thus drive strike-slip movements and net eastward “escape” of the microplates which comprise the rift zone. This interpretation is grossly consistent with the results of numerical and laboratory experiments, and, in geophysical data which may eventually image thermal perturbations or dynamic upwellings at depth beneath the rift, such “passive” plate-boundary processes remain the preferred driving force for rifting in the BRZ. The BRZ may be the only existing example of an evolved intracontinental rift in which large-scale strike-slip displacements can account for most of the observed opening of the axial zone although recent studies suggest that parts of the East African Rift zone may also develop as a result of oblique extension along “transform” faults [*Chorowicz and Sorlien, in review*]. In the BRZ, the predominance of a strike-slip mode of basin formation over more typical

graben-type faulting may explain why this rift is the coldest, most discrete, and least volcanic of all intracontinental rift systems. Comparisons of the BRZ with an analogous rift system—the strike-slip Dead Sea Rift [*Garfunkel et al.*, 1981]—may provide additional clues about the future of the BRZ.

ACKNOWLEDGEMENTS

Discussions with L. Royden, K. Hodges, D. Hutchinson, B.C. Burchfiel, P. Burkholder, and P. Kaufmann led to substantial clarification of the ideas presented here and improvement of the text. This study was supported by NASA grant NAG5-1084 to M. K. McNutt. I thank C. Thurber for first suggesting the purchase of Landsat images and D. Hutchinson, G. Bassi, and C. Sorlien for providing preprints of the work.

FIGURE CAPTIONS

Figure 3.1. Landsat photo of the southern end of the BRZ and line drawing showing major structural features. North-south oriented basins associated with movement along the Tunka fault: (A) Busingol-Belin basin (B) Darkhat depression (C) Lake Khubsugol (Khubsugol basin). Conjugate east-west basins: (D) Tunka basin and southern rhombohedral part of the South Basin of Lake Baikal. (E) 15 km left-lateral offset in the Irkut River where it crosses the reactivated portion of the Main Sayan fault. Black dots denote location of cinder cones, and gray areas mark location of Neogene volcanics. Note the rhombohedral form outlined by these volcanic rocks, which mark the edges of a “leaky” pull-apart between the Tunka fault and the parallel strike-slip fault to the south.

Figure 3.2. Landsat photo and line drawing of the entire BRZ, with special emphasis on basins of Lake Baikal and their relationship to other rift basins. Lines with circles denote pre-rifting lineaments in the Siberian platform. Tunka-Main Sayan shear zone: (A) Busingol-Belin basin, (B) Darkhat depression, (C) Lake Khubsugol, and (D) Tunka basin. Features of the axial part of the rift zone: (E) Selenga Delta, (F) overlapping fault segments forming topographic highs and lows stepping along the eastern lake shore, (G) Olkhon Island, (H) Academician ridge, (J) Svyatnoy Nos (note offset ridge), (K) Barguzin basin, (L) Tsipi-Bount basin. Udokan shear zone: (M) Lower Angara basin, (N) Upper Angara basin, (P) Muya basin. The Tokka and Chara basins, the outermost basins of the Udokan shear zone,

are not shown here. These basins lie east and north of the Muya basin along the edge of the Aldan shield.

Figure 3.3. Close-up Landsat photo and line diagram of the structures of the Barguzin region and the Udokan shear zone. Note the relationship between the shear zone and the Barguzin basin, which serves as the locus of extensional deformation in the northern part of the rift's axis. (A) Academician Ridge, (B) Svyatnoy Nos, (C) Lower Angara basin, (D) Upper Angara basin, (E) Muya basin, and (F) Tsipi-Bount basin. Gray area marks the Vitim plateau, the major region of Neogene volcanism in the BRZ outside the Tunka area.

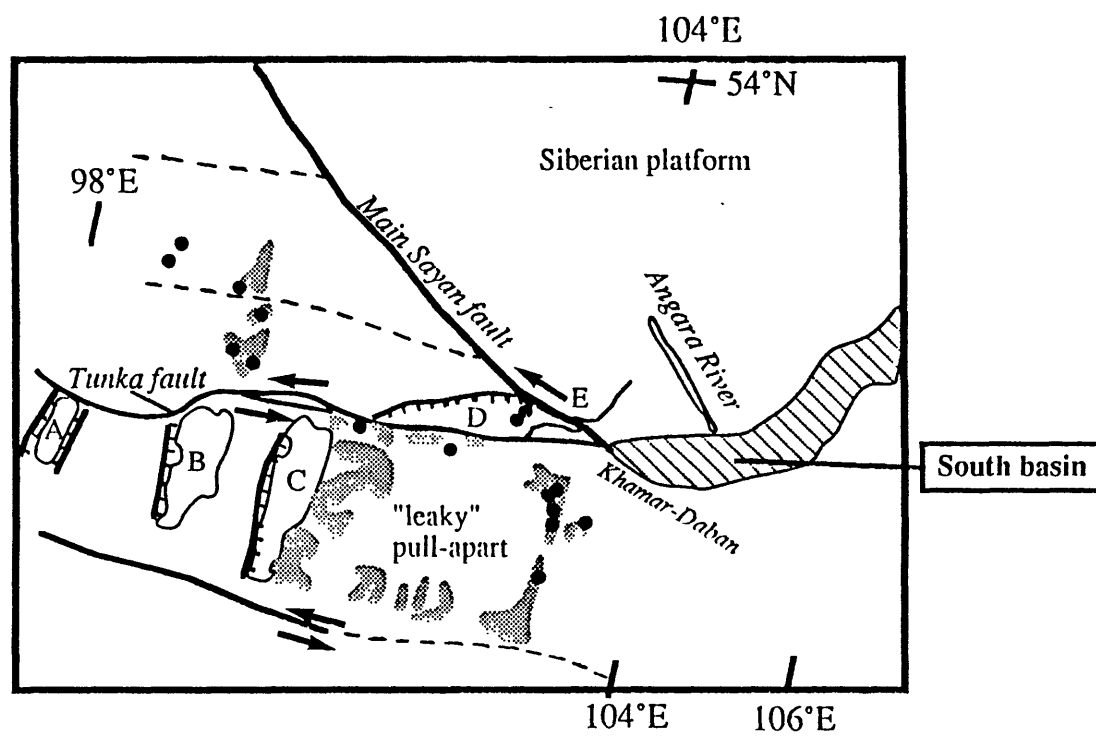


Figure 3.1

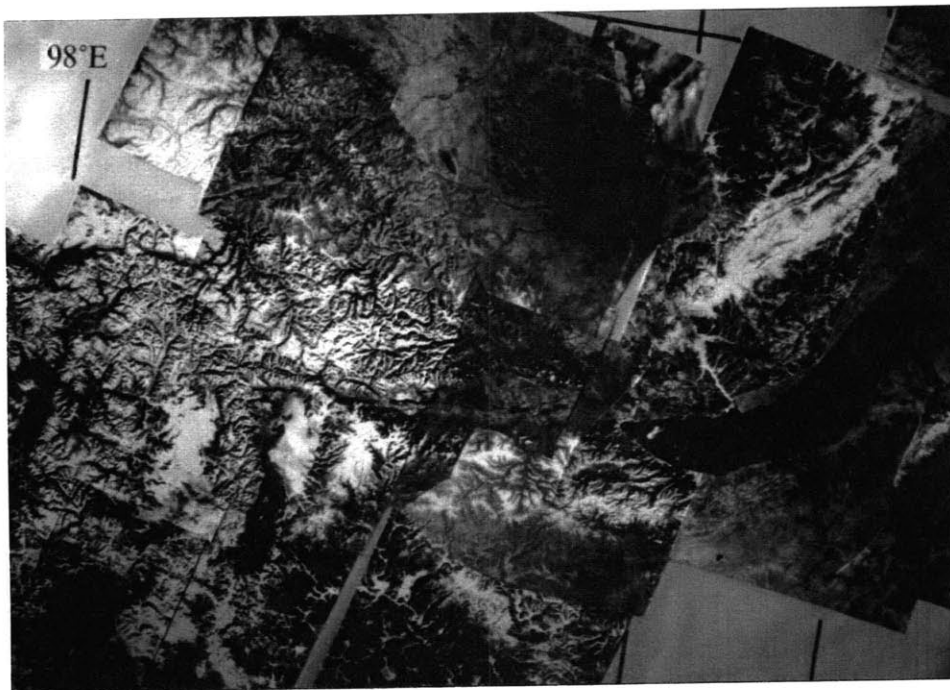


Figure 3.1
(continued)

blank page
(back of photograph)

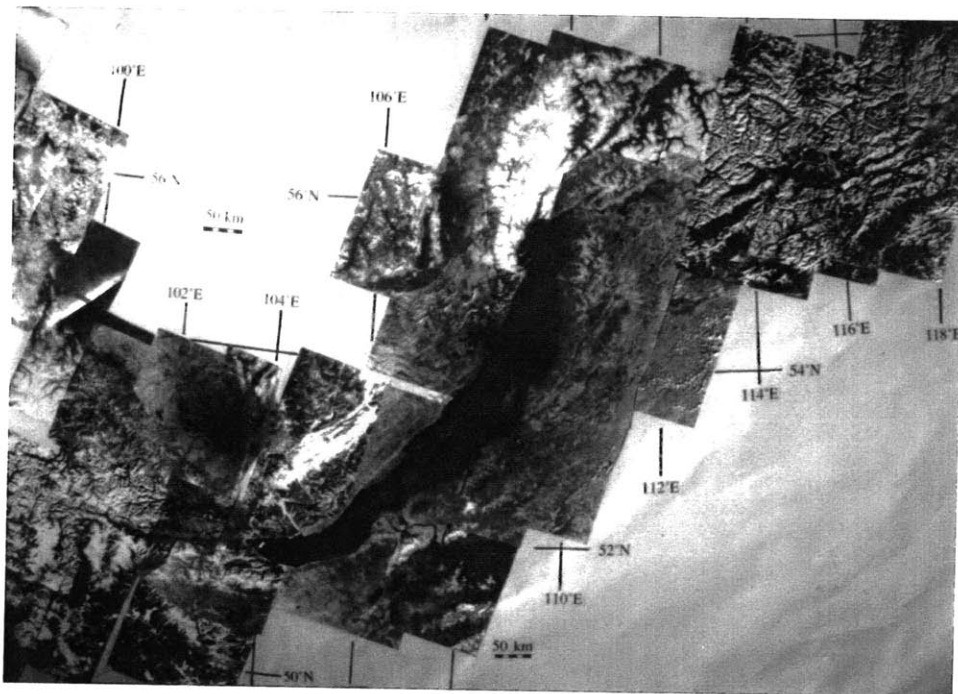
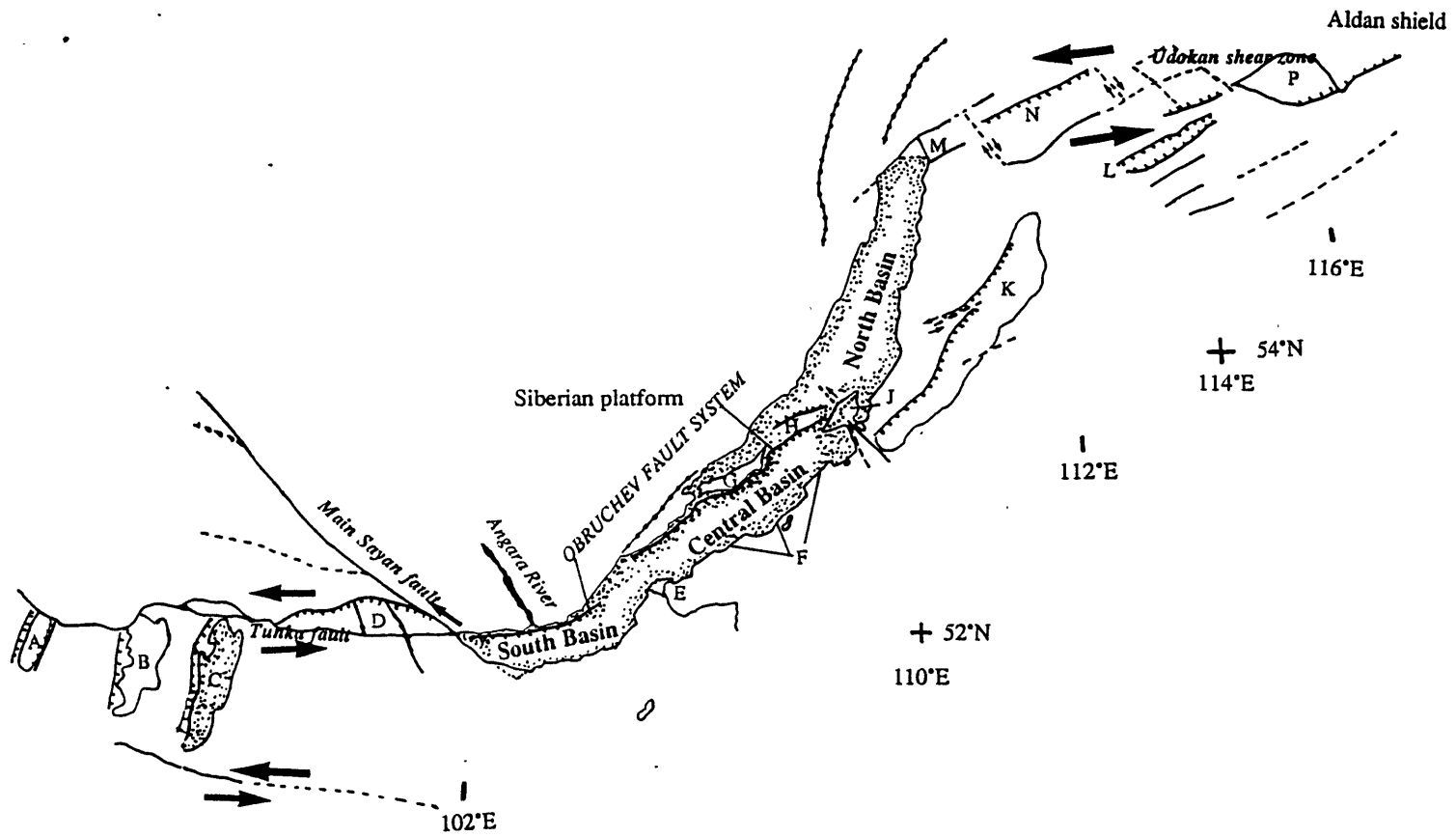


Figure 3.2

blank page
(back of photograph)

Figure 3.2
(continued)



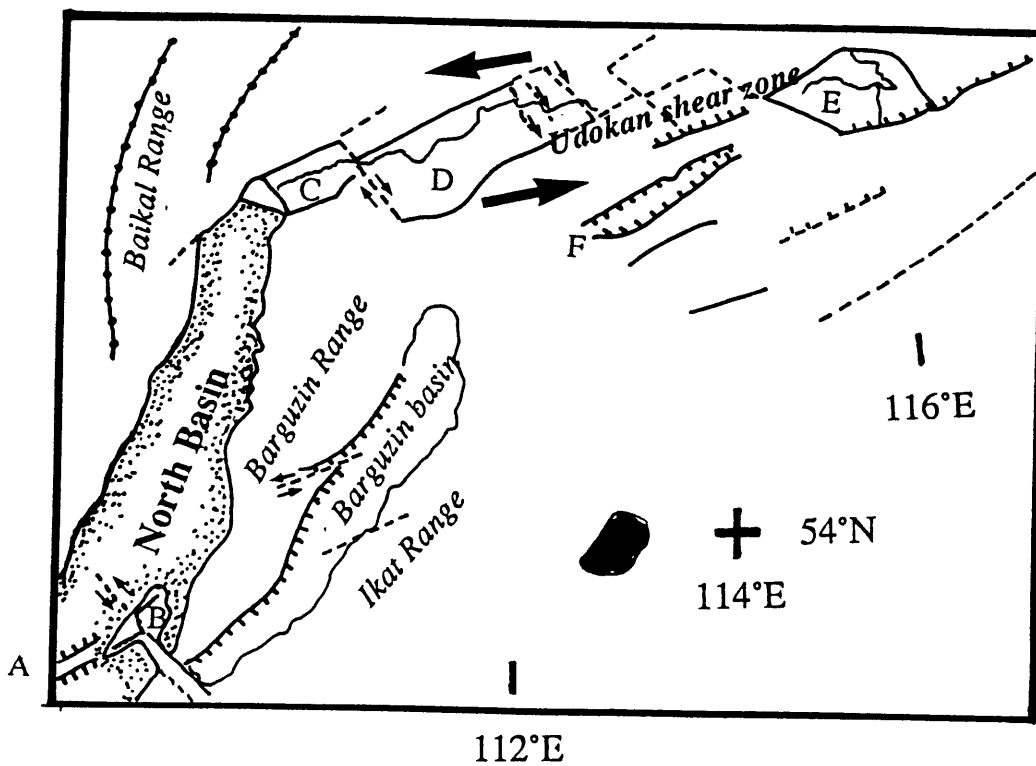


Figure 3.3

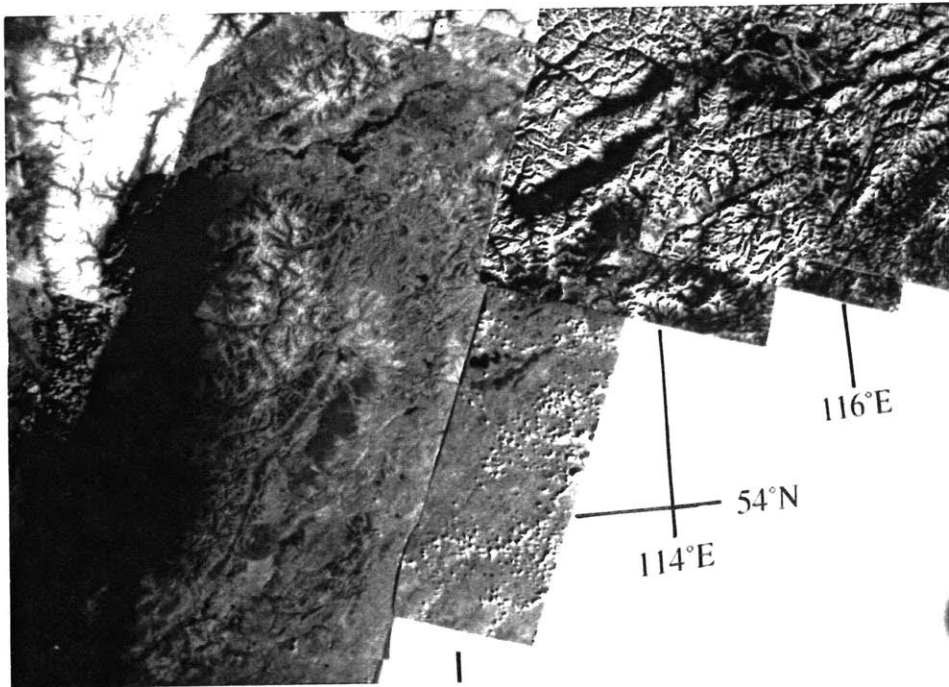


Figure 3.3
(continued)

blank page
(back of photograph)

Chapter 4

Pressure-Temperature-Time Paths from 2D Thermal Models: Prograde, Retrograde, and Inverted Metamorphism

INTRODUCTION

Metamorphic and geochronologic data from ancient mountain belts provide the principal constraints on the thermal evolution of the lower crust during orogenesis. Techniques have been developed for the inversion of such data in order to establish thermal parameters [Royden and Hodges, 1984; McNutt and Royden, 1987]. Generally, however, significant uncertainties in geothermometric, geobarometric, and geochronologic data hamper the application of simple inversion techniques in most compressional settings. In the absence of better metamorphic data, developing a more generalized picture of the thermal evolution of compressional terrains requires the use of theoretical forward-modeling techniques.

This goal was first recognized by *Oxburgh and Turcotte* [1974] who developed one-dimensional models for the thermal effects of thrust emplacement to explain deformation in the Alps. Later work by *England and Thompson* [1984] greatly increased the sophistication of the one-dimensional models to include the effects of variations in many parameters, including radioactive heating rate, heat flow, and thermal conductivity. Both of these studies relied on assumptions of instantaneous thrust emplacement and one-dimensional (vertical) heat conduction, and the instantaneous juxtaposition of a “hot” thrust

nappe on a “cold” footwall produced the now-familiar, post-thrusting sawtooth geotherm, which is characterized by a large temperature inversion along the thrust fault. In recent years, thermobarometric data from large-scale overthrust terrains like the Himalaya [*LeFort et al., 1987; Hubbard et al., 1991*] have lent support to models predicting thermal inversions in the vicinity of major thrust zones. At the same time, two-dimensional analyses of the thermal effects of time-transgressive thrust emplacement [*Shi and Wang, 1987; Ruppel et al., 1988*] have failed to reproduce the post-thrusting thermal inversion of earlier one-dimensional models.

The study described in this paper was motivated by the apparent contradiction between metamorphic data consistent with long-lived thermal inversions and two-dimensional models which yield such inversions only for thrust emplacement at unrealistically high rates [*Shi and Wang, 1987*]. In order to re-examine the problem of the thermal evolution of the continental lithosphere during and after compressional tectonism, we first compare the results of older, instantaneous one-dimensional models with a new, time-transgressive, two-dimensional model. We then evaluate the effects of fault geometry, thrusting and erosion rates, burial and unroofing mechanism, and variations in heat flow, radioactive heating, and frictional stress on the morphologies of pressure-temperature (PT) and, in some cases, temperature-time (Tt) paths of metamorphic rocks. Finally, the model results are considered in terms of uncertainties in geothermometric and geobarometric data, and we explore the implications of our results for the derivation of new inversion techniques.

THE TWO-DIMENSIONAL MODEL

The thermal evolution of the continental lithosphere during and after compressional deformation can be described by the two-dimensional heat flow equation. Before and after tectonism, only conduction and internal heating (radioactivity) affect the lithosphere's

temperature structure. During the compressional event, however, the movement of the hanging wall relative to the footwall results in the advection of heat through the lithosphere. The model formulation employed here separates the conductive and advective components of the thermal problem. Instead of solving the full heat flow equation including nonlinear advective terms at each time step, we first physically displace a Lagrangian temperature grid superimposed on the hanging wall block relative to the fixed Eulerian grid of the entire problem, thereby accomplishing advection. This advective step is followed by a conductive step in which temperatures are recalculated on the Eulerian grid at mesh points spaced 0.5 km in the vertical direction and 0.25 to 1.0 km in the horizontal direction. The close vertical (z -direction) spacing of mesh points prevents inaccuracies from developing due to large changes in thermal gradients (d^2T/dz^2) close to the fault surface. In the horizontal (x) direction, thermal gradients (dT/dx) and changes in thermal gradients (d^2T/dx^2) are typically smaller, and discontinuities across the fault surface are therefore not an important consideration. Horizontal spacing is instead chosen so that the ratio of horizontal to vertical grid spacing equals the cotangent of the fault's dip.

The two-dimensional heat flow equation is solved on a finite-difference grid using an unconditionally stable alternate direction implicit (ADI) technique [*Spanier, 1967; Press et al., 1986*]. Boundary conditions, illustrated in Figure 4.1a, are constant temperatures of 273K (0°C) at the surface and 1573 K (1300°C) at the base of the lithosphere, whose depth remains fixed at all times. At the sides of the grid, we impose a boundary condition of no net horizontal heat flow and pad the grid to a distance greater than the horizontal diffusive length scale of the problem. Diffusivity is held constant at 10^{-6} m²/sec throughout the lithosphere, and thermal conductivity in all the cases presented here is 3 W/m-K, corresponding to specific heat capacity of 1200 kJ/kg-K and density of 2670 kg/m³.

The model's simple fault geometry, shown in Fig. 4.1, approximates the zone of thrusting as a single, discrete structure. The fault dips constantly at an angle of ϕ

(measured from the horizontal) between the surface and distance 0, where it bends to follow the base of the crust at 30 km. During thrusting, rocks in the footwall block move to progressively deeper levels only in the z -direction while rocks at all positions in the hanging wall are translated only in the x -direction and maintain the same depth throughout the thrusting interval. This formulation, illustrated in Fig. 4.1b, allows the Earth's surface to remain flat during thrusting and greatly simplifies thermal calculations. Thrust emplacement thickens only the crust in these models, and the base of the lithosphere therefore remains at a constant depth throughout compression and subsequent unroofing. The mechanical effects of compression are also ignored by the model, and we therefore do not consider any uplift or subsidence that may accompany thrust emplacement.

Initial geotherms are generated assuming constant heat flow q_m into the base of 30-km-thick crust and a corresponding constant thermal gradient between this depth and the 1573K (1300°C) isotherm. For q_m of 31.2 mW/m², this calculation yields a background geothermal gradient of 10.4 K/km and lithospheric thickness of 125 km. Overprinted on this background geotherm is the temperature contribution due to radioactive heating at a constant rate r distributed homogeneously in the upper l_r km of the pre-thrusting crust. By combining the mantle flow and radioactive heating components, we generate a steady-state initial geotherm that can be applied at all positions to create a laterally-homogeneous initial thermal structure for the lithosphere. Figure 4.2 shows two initial geotherms used in this study. No radioactive heat is required to produce Initial Geotherm A, a linear steady-state gradient of 10.4 K/km. Initial Geotherm B is generated with radioactive heat production held constant at 3 μ W/m³ in the upper 20 km of crust and with background geothermal gradient of 10.4 K/km.

Lateral variations in the syn- and post-compressional configurations of the radioactive layer play an important role in the two-dimensional thermal evolution of the thickening lithosphere. Figure 4.1b illustrates how the disruption of a radioactive layer of original

thickness l_r by displacement of the hanging wall results in a laterally heterogeneous pattern of heat production. In Zone I, which lies outside the area affected by thrusting, the radioactive layer is undisturbed. Zone II, between the surface break of the thrust fault and distance 0 km (where the fault bends to follow the base of the crust), has the most complicated distribution of heat producing layers. At the surface break, the radioactive zone remains intact, but the thickness of the radioactive layer then increases linearly, reaching twice its prethrusting thickness at a distance of $l_r \cdot \tan \phi$. Finally, in Zone III, the footwall radioactive layer has been thrust completely under the hanging wall crust, resulting in complicated thermal effects in the hanging wall lower crust sandwiched between the two heat-producing layers. As thrusting continues, Zone I material will move into the Zone II regime, and Zone II rocks will develop the sandwich structure of Zone III.

GEOLOGICAL RELEVANCE

The degree to which theoretical models for PTt paths of metamorphic rocks are applicable to the real world depends on formulating a model based on geologically reasonable assumptions. The thrusting model described above assumes constant thickness for the crust, lithosphere, and radioactive layer; a single, discrete, and constantly dipping fault; volume-conserving deformation associated with thrust fault emplacement; constant burial and unroofing rates; no fluid circulation in the crust or lithosphere; constant temperature boundary conditions; and constant rates of radioactive heat production. In most cases, relaxing these assumptions has little or no effect on the morphologies of PTt paths and the general characteristics of the thermal regime during and after tectonism. On the other hand, many of these assumptions are inconsistent with geologic observations, and the implications of these inconsistencies deserve further scrutiny.

As shown by previous workers, one of the most important factors controlling the peak temperatures reached by metamorphic rocks during tectonic events is the initial thermal state of the lithosphere. The steady-state initial geotherms used here imply that a period of relative quiescence precedes the onset of tectonism and that thermal regimes are laterally homogeneous on a province-wide scale prior to thrusting. In real settings, a tectonic province is not a closed system, and many processes, including intrusion of magmas, fluid circulation, erosion, and metamorphic reactions, may result in a net addition or subtraction of heat. The link between compression or extension and the onset of magmatism has proved difficult to resolve; in some examples, such as the Wopmay orogen [Lalonde, 1989], magmatic activity even spans the entire pre-tectonic and post-tectonic interval. Wide variation in radioactive element concentrations also contribute to lateral differences in thermal regimes before, during, and after tectonism. However, our inability to predict the patterns of major thermal disturbances like magmatic intrusions or more minor differences like variations in radioactive content makes their inclusion impossible in the general models presented here.

In real settings, thrust faults do not have constant dip and often propagate stepwise, following less competent rock layers. Fault surfaces are commonly curved, not planar, and faulting may be accompanied by the formation of breccias, gouges, and brittle (cataclastic) and ductile (mylonitic) shear fabrics. Deformation in fault zones rarely conserves volume, and major faults that penetrate deeply enough to cross the mid-crustal brittle-ductile transition probably degenerate from fairly discrete features to more diffuse zones of deformation. Even within the brittle regime, however, wide zones of deformation surround thrust faults. A further complication is introduced by field observations of small thrust faults that reshuffle slices within more diffuse zones of deformation, and poor timing relationships between these smaller thrusts and major faults make it difficult to analyze the thermal effects of the larger features.

The development of many scales of geologic structures are directly affected by extensively studied ductile and brittle processes, but the thermal consequences of nonplanar fault surfaces and distributed fault displacement in shear zones are more poorly understood. Results presented below for faults with dips ranging from shallow (26°) to steep (63°) imply that fault dip is not an important factor in controlling lithospheric thermal regimes during thrust emplacement. Near major zones of deformation, small scale faults, even those that develop synthetically during the principal thrusting event, probably cause only small, short-lived temperature perturbations on local scales. In fact, a far more serious concern is the post-metamorphic juxtaposition of fault slices with slightly different metamorphic histories; misinterpretation of field relationships may lead to improper conclusions about PT paths and metamorphic thermal regimes. Distributed fault displacement in shear zones is an even more difficult problem to address without a better understanding of the factors contributing to the development of diffuse zones of deformation near major faults. The simplified model used here admittedly makes no attempt at reproducing these mechanical effects of fault displacement, but, except in the case of heating by internal friction, the total thermal effect of displacement across a wide zone of deformation should never be larger than that associated with movement along a single discrete zone.

Many simple models for the mechanical and thermal effects of faulting allow major fault zones to penetrate to the base of the lithosphere. The occurrence of large earthquakes below the base of the crust [*Chen and Molnar*, 1983] does provide some evidence for the continuation of discontinuities into the upper mantle, but most of these anomalous earthquakes are confined to subduction zones, where the forcible injection of cold slabs into hotter underlying mantle causes cold temperatures to prevail to greater depths. In general, rheological considerations render penetration of the faults to the base of the lithosphere unlikely. As noted above, thrust faults probably do not continue as fairly discrete zones of deformation even to the base of the crust in most cases. In the model

used here, allowing the fault to penetrate to the base of the lithosphere would have the greatest effect on footwall temperatures beyond position 0 in Fig. 4.1b for slow rates of thrusting. Flattening of the fault at mid-crustal levels instead of at the base of the crust would have a much more dramatic effect on temperatures and result in significantly less heating of footwall rocks during and after thrusting.

The overall thermal budget of tectonically-active areas may be dramatically affected by fluid circulation in the lithosphere, a factor completely ignored by these models. In addition to meteoric water, lithospheric fluids may include the products of metamorphic reactions, melt formation processes, dewatering of hydrous phases in highly-stressed gouges, and liberation of pore fluids during compaction. Despite relatively low thermal conductivities, fluids move heat through the lithosphere on time scales much shorter than those associated with tectonic movements (advection of rock particles) or thermal relaxation (heat conduction). To date, geophysical modeling of the role of fluids in heat flow has focused on subduction complexes [Peacock, 1990] and accretionary prisms [Barr and Dahlen, 1989], while simple overthrust terrains have received little attention. The presence of hydrothermal springs near many major fault zones offers clear evidence that fluid circulation may occur along crustal discontinuities in some areas, and the importance of channeled fluid flow on the local thermal structure in collisional settings can be inferred from the thermochronologic data of Copeland *et al.* [1991] for the central Nepalese Himalaya.

Fluid circulation has also been invoked to explain disparities between the high frictional coefficients predicted by both rock mechanics experiments and some in-situ stress measurements and the low frictional coefficients consistent with coseismic deviatoric stress drops and the small heat flow anomalies near major fault zones. Although rock mechanics experiments by Morrow *et al.* [1982] and Logan and Rauenzahn [1987] on pure montmorillonite and on hydrated clay gouges yield frictional coefficients as low as 0.15

and 0.2–0.5, respectively, in-situ stress measurements near some fault zones [Zoback and Healy, 1984] indicate that shear stresses are considerably greater (60-100% of lithostatic stress), in agreement with results from laboratory experiments on dry quartz [Byerlee, 1978]. Such large frictional coefficients should produce large heat flow anomalies and coseismic deviatoric stress drops in major fault zones, but observations near transform [Lachenbruch and Sass, 1973] and subduction plate boundaries are consistent only with small coefficients of friction. Molnar and England [1990] concluded that none of the existing constraints on shear stresses, including the maximum depths of Himalayan earthquakes and possibly inaccurate heat flow data from subduction zones, precludes shear stresses as high as 100 MPa along major thrust faults, particularly in the presence of fluid circulation that may act to lower the apparent heat flow anomaly. For most of the results presented here, frictional heating due to displacement on the fault is neglected; this formulation implies that shear heating is negligible, or, alternately, that fluid circulation acts to remove heat as quickly as it is generated. We also examine the effects of shear heating proportional to lithostatic pressure with "effective" frictional coefficients ranging from 0.15 to 0.6. These "effective" frictional coefficients may be interpreted as representing the combined effects of shear heating and some component of fluid circulation that quickly carries heat outside the closed system from within the fault zone.

The models developed here ignore the episodic nature of many tectonic events and assume constant rates of burial and unroofing in most cases. These rates are typically calculated by combining real geobarometric and geochronologic data and computing the slope of the PTt path. Retrograde metamorphism often obscures or completely overprints prograde PTt paths and the associated textural information, and currently active thrust terrains therefore offer the best hope for constraining possible rates of burial in compressional settings. In subduction zones, underthrusting occurs at plate velocities, sometimes as fast as tens of kilometers per million years. The thermal models presented

here more closely approximate simple continental overthrust terrains, where time-averaged thrusting rates might range from 0.5 to 5 mm/yr (0.5 to 5 km/my). Burial rate corresponds to the vertical component of the thrusting rate vector, and, for shallowly dipping faults, may be significantly smaller than the thrusting rate. Far easier to constrain than burial rate is unroofing rate which can be inferred from PTt paths or occasionally directly measured. Tectonic unroofing by movement along normal faults occurs at rates of at least 1 mm/yr [Anderson *et al.*, 1988] and potentially an order of magnitude faster [Hodges *et al.*, 1989]. Erosion rates vary widely depending on climate, elevation, and other factors, but are likely to be significantly slower than rates of tectonic denudation. For most of the results presented here, time-averaged unroofing rates have been taken as 1 to 5 mm/yr, but the qualitative thermal effects of faster denudation can be predicted easily from these models.

The two-dimensional nature of the model used here requires that not only the vertical extent, but also the horizontal extent, of thrust faulting lie within physically realistic limits. For most of the test cases, the lateral extent of thrusting is taken as 30 km although this value is occasionally as large as 120 km. Displacements on the order of tens of kilometers are plausible for major thrust zones; in very large scale overthrust terrains like the Himalaya, workers estimate fault displacements as large as 100 km or more [Gansser, 1964; Molnar, 1984]. Fault displacements smaller than those used here would result in small perturbations to the initial thermal structure distributed over narrow regions (greater dT/dx values), whereas larger fault displacements encourage the development of thermal regimes of wide regions of lateral heterogeneity but smaller dT/dx values.

COMPARISON WITH ONE-DIMENSIONAL MODELS

Thickening of the lithosphere by movement along thrust faults is clearly neither an instantaneous nor a one-dimensional process. Early instantaneous models for temperature perturbations were important in describing the basic morphology of PTt paths, but ignored the important time-transitive and two-dimensional thermal effects accompanying thrust emplacement. Although lateral advection of heat must be included in any description of time-transitive thrusting, lateral conduction of heat is often ignored based on the assumption that lateral thermal gradients (dT/dx) are small relative to vertical thermal gradients (dT/dz). Figures 4.3a and 4.3b show contour plots of the ratio R of dT/dx to dT/dz in the thickened crust immediately following the emplacement of a 30-km thick thrust sheet at 5 mm/yr along a 45° fault. Lateral advection of heat during thrusting is included in the models corresponding to Figs. 4.3a and 4.3b, but lateral conduction of heat is ignored for the top diagram. In the absence of lateral heat conduction, the problem reduces to the solution of the one-dimensional heat flow equation; R changes rapidly near the fault, reaching values greater than 5 in the hanging wall lower crust, proximal to the dipping fault surface. This high ratio of dT/dx to dT/dz does not alone violate the assumption that lateral heat conduction can be ignored, particularly if thermal gradients in both directions are small (less than a few degrees per kilometer). However, where R exceeds 5 in Fig. 4.3a, dT/dx is greater than 10 K/km while dT/dz is less than 2 K/km. Since large lateral thermal gradients are probably not realistic for homogeneous crust containing no anomalously radioactive rock units and no magmatic intrusions, Fig. 4.3a implies that lateral heat conduction should be included when calculating the thermal evolution of the thickening lithosphere. As shown in Fig. 4.3b, solving the heat flow equation in two dimensions significantly reduces R , yielding a maximum value of 0.5 to 1. For $R=0.5$, dT/dx and dT/dz are approximately 4 and 8 K/km respectively.

The effects of combined advection and conduction in both the horizontal and vertical directions can be examined by comparing the non-dimensionalized PT paths of footwall rocks at different horizontal positions and the same structural levels. Figure 4.3c compares the PT paths of rocks less than 1 km beneath the fault and rocks greater than 15 km beneath the fault at horizontal positions of -15 km and 0 km. Because these rocks have different pre-thrusting depths and temperatures, these parameters are plotted proportional to their initial values. Rocks close to the fault and buried to 32 times their original depths by thrust emplacement undergo greater heating at position 0 than at position -15 km. Maximum thrusting buries footwall rocks at position -15 km beneath only 15 km of hanging wall material and therefore causes less heating due to the conduction from the hot hanging wall block. At greater depths beneath the thrust fault (near the bottom of Fig. 4.3c), the different amounts of burial at positions 0 and -15 km have almost no effect on PT path morphology because conductive effects have not yet fully propagated to these depths. The only major difference between PT paths of footwall rocks at different horizontal positions and depths greater than 15 km below the fault is the slope of the prograde path. Where advection (passive burial to greater depths by thrust emplacement) is the only heating mechanism, as for the rock at -15 km distance, the synthrusting path takes on a linear form. At distance 0 km, heating occurs primarily by advection, but the addition of small amounts of conducted heat produces a curved synthrusting PT path.

These results indicate that some subtle variations in footwall PT paths are linked to the horizontal positions of rock packages relative to the fault surface. The relatively rapid 5 mm/yr thrusting rate of this example serves as a good comparison to one-dimensional models; slower and more realistic thrusting rates allow more time for the relaxation of thermal gradients, but also contribute to the development of a more laterally heterogeneous thermal structure.

Figure 4.4 offers a direct comparison between the PTt paths and post-thrusting geotherms produced by one-dimensional instantaneous and two-dimensional non-instantaneous thermal models. In Fig. 4.4a, the sawtooth geotherm results from instantaneous emplacement of the upper 30 km of Geotherm B on footwall rocks with the same radioactive heat distribution ($3 \mu\text{W}/\text{m}^3$ in the upper 20 km) and a background gradient that yields 273K at 30.5 km depth and 1573K at 125 km depth. This one-dimensional model contrasts with the dashed and dotted post-thrusting geotherms produced by emplacement of a 30 km thick hanging wall along a 45° thrust fault at 1 mm/yr and 5 mm/yr respectively. Using an initial thermal structure described by Geotherm B, the post-thrusting distribution of radioactive elements is the same as for the one-dimensional case with a 20 km thick layer in the upper parts of both the hanging wall and footwall. For fast thrusting, Fig. 4.4a shows that hanging wall and footwall temperatures are, respectively, colder and hotter than those produced by instantaneous one-dimensional thrust emplacement and everywhere colder than initial Geotherm B. Slow thrusting yields a post-thrusting geotherm that is hotter than both the sawtooth geotherm and the fast thrusting geotherm. Compared to the initial geotherm, slow thrusting results in nearly the same temperatures in the hanging wall, colder footwall temperatures, and hotter temperatures at the base of the hanging wall where conductive effects associated with the footwall radioactive layer play an important role.

The differences between post-thrusting geotherms for one-dimensional instantaneous and two-dimensional time-transitive thrust emplacement appear to be most significant in the upper kilometers of the footwall. Fig. 4.4b illustrates how these small differences in post-thrusting thermal structure translate to large differences in the PT paths of hanging wall and footwall rocks carried closer to the surface by erosion at 1 mm/yr during the post-thrusting interval. For the one-dimensional instantaneous case, initial relaxation of the sawtooth geotherm accompanied by the first erosional increment produces immediate

cooling and heating along nearly isobaric paths for hanging wall and footwall rocks respectively. At 10 km above the fault surface, cooling continues throughout the uplift history of the rock for the instantaneous case, but a rock at the same position on the geotherm produced by two-dimensional thrust emplacement at 5 mm/yr heats 25K in the first 3 km of uplift and then cools as it nears the surface. Maximum temperatures are attained at the initial depth of 20 km immediately following thrusting for the instantaneous case, but several million years after thrusting at a depth of approximately 17 km for the two-dimensional model. Immediately below the thrust fault, isobaric heating during the initial time interval is followed by heating to a maximum temperature of 640K after approximately 5 km of unroofing in the one-dimensional case. In contrast, the same rock reaches a maximum temperature of 740K after 8 km of unroofing in the two-dimensional case. Ten kilometers below the thrust, the isobaric cooling associated with initial relaxation of the sawtooth geotherm raises the temperature of the rock only 50K, and the maximum temperatures for the one and two-dimensional models are reached at approximately the same depth (after 10 km of unroofing) and differ by only 50K. The most important differences between the one and two-dimensional models occur in the hanging wall and proximal to the thrust fault in the footwall. Two-dimensional models yield consistently higher post-thrusting temperatures and, in the case of hanging wall rocks several kilometers from the thrust fault, PT path morphologies different from those produced by one-dimensional instantaneous models. The example presented here is meant to be representative of the general differences between one and two-dimensional models. Various factors, most notably the distribution of radioactive heat, the magnitude of thermal constants, and thrusting and denudation rates will produce one and two-dimensional thermal histories both more different and more similar than those shown here.

TWO-DIMENSIONAL PATHS: EFFECT OF POSITION IN THE THICKENING LITHOSPHERE

As evident from the two-dimensional PT paths shown in Fig. 4.5, the positions of rocks within the hanging wall or footwall and relative to the thrust fault have important effects on the thermal histories of rocks in the two-dimensional model. These plots illustrate the footwall (solid lines) and hanging wall (dashed lines) PT and Tt paths for rocks 0.5 and 10 km below and above a fault dipping at 45°. Within the footwall, rocks initially at 0.5 and 10 km depth relative to both the surface and the thrust fault undergo heating during burial as the result of juxtaposition of hot hanging wall rocks against cooler footwall rocks, the complicated effects associated with disruption of the radioactive layer, and re-equilibration of lithospheric thermal structure during the erosional period. Footwall rocks proximal to the fault surface undergo slightly more rapid heating (larger dT/dt) and greater amounts of heating for each kilometer of burial (larger dT/dP) than those several kilometers from the fault surface. In contrast, hanging wall rocks undergo rapid cooling as they are juxtaposed against cool footwall rocks during thrusting, with rocks immediately above the thrust fault experiencing more rapid cooling (larger absolute dT/dt) than those 10 km above the fault.

Differences between the thermal histories of rocks at various levels within the hanging wall or footwall are accompanied by differences in Tt paths (Fig. 4.5b). Most importantly, the models show that rocks 0.5 km above (hanging wall) and 0.5 km below (footwall) the fault surface do not undergo the same absolute temperature change during thrust emplacement. The “kinks” in the Tt paths mark the end of the thrusting interval and separate the period of syntectonic temperature changes from the phase of initial heating then cooling during unroofing. In the case presented here, the initial temperature difference between hanging wall and footwall rocks eventually juxtaposed by the thrusting event is

approximately 300K. One-sixth of the initial temperature difference is taken up by syntectonic cooling of hanging wall rocks while syntectonic heating of footwall rocks accounts for the remainder. Relative differences in the absolute temperature changes experienced by the hanging wall and footwall rocks can be attributed to the relative importance of the combined effects of advection and conduction in each case. Footwall rocks undergo heating due to advection to deeper crustal levels and conduction from overthrust hot hanging wall rocks. In contrast, the position of hanging wall rocks relative to the surface remains constant during crustal thickening and the only important temperature effect is the juxtaposition of hot hanging wall rocks against cool footwall rocks along the fault surface. These hanging wall rocks therefore undergo cooling during at least the initial phases of thrusting. The amount of heating that follows the initially rapid cooling event is principally a function of the rate of radioactive decay in the juxtaposed footwall rocks and the duration of the thrusting event. In this example, the hanging wall rock proximal to the thrust fault attains a maximum temperature less than 25K hotter than its initial temperature after 7 km of unroofing, but the rock 10 km above the fault surface never reaches a temperature higher than its initial temperature during the entire thrusting and unroofing event. In contrast, footwall rocks continue heating well beyond the end of the thrusting interval and reach maximum temperatures 75-100 K hotter than post-thrusting temperature after 7 km of unroofing (7 my) close to the thrust surface and after 10 km of unroofing (10 my) at a depth of 10 km below the thrust.

SIMPLE SHEAR (THRUST FAULTING) VS. PURE SHEAR THICKENING

The morphologies of extensional PTt paths produced during thinning of the lithosphere due to homogeneous stretching (pure shear) or movement along discrete fault zones (simple shear) are discussed in Chapter 5. The analogous deformation mechanisms for

compressional settings are thrust faulting (simple shear) and homogeneous thickening (pure shear). As described above, thrust faulting disrupts the laterally homogeneous initial thermal structure of the crust to create a post-compressional temperature regime characterized by significant lateral variations and complicated radioactive layer geometries. On the other hand, crust thickened by pure shear maintains lateral thermal homogeneity during and after compression, and the radioactive layer is not disrupted but only thickened. Boundary conditions, thermal constants, and initial thermal structure are the same for both the pure shear and simple shear models, but, due to the homogeneous nature of pure shear deformation, the problem can be simplified to solve the heat conduction equation in the vertical direction only.

The contrasting thermal structures produced by pure shear and simple shear thickening result from differences in patterns of heat advection and deformation distribution. In the thrust model, displacement of the hanging wall relative to the footwall results in no internal deformation in either block, and distances between particles on the same side of the fault remain constant at all times. The pure shear model is more complicated: Pure shear thickening of a crustal block of length l and thickness t_c by an amount β (<1 for compression) results in post-tectonic dimensions of βl and t_c / β respectively. During compression, distances between particles decrease in the horizontal direction and increase in the vertical direction. This difference in the distribution pattern of internal deformation combined with the different thermal effects of pure shear and simple shear thickening may result in distinct PT and Tt morphologies for each mode of compression.

Fig. 4.6 shows the PT and Tt paths followed by a rock originally at 9 km depth buried to 30 km depth by 21 km of lateral overthrusting on a 45° fault and by pure shear compression with $\beta=0.3$. In order to separate thermal effects associated with differences in how the radioactive layer is thickened from those resulting merely from the thrusting mechanism, the thermal histories in Fig. 4.6 were generated using both Initial Geotherms A

(no radioactive heating) and B. For Initial Geotherm A, the increase in temperature with depth (dT/dP) is positive and nearly linear at about 6K/km for the thrusting (simple shear) mechanism, but pure shear thickening produces isothermal compression during the syncompressional period. The isothermal portion of the PT path is also observed when pure shear thickening occurs instantaneously instead of over a 21 my period. The non-instantaneous nature of the pure shear thickening in this case has two competing effects, one that tends to heat the lower part of the mantle lithosphere conductively and one that tends to cool the thickening lithosphere more with each time step. At the base of the lithosphere (125 km depth and 1573K), thermal gradients become increasingly large as thickening progresses and colder material is carried to deeper depths. In the course of a million years, conductive relaxation of the perturbed geotherm causes temperatures to be affected only within 5.5 km of the base of the lithosphere. However, the time-averaged rate of thickening is approximately 3 km/my, and the net consequences of the competing heating and cooling effects are small temperature increases in the lowermost 1.5 km of the lithosphere, or lowermost 31.5 km in 21 my.

During unroofing, the rock buried by movement on a thrust fault follows the pattern previously observed, with maximum temperature reached after several million years and several kilometers of erosional denudation. For the rock buried by pure shear, the maximum temperature occurs during the thrusting interval and the unroofing event is accompanied only by cooling. It should be noted that the overall sense of the PT path for the rock buried by pure shear is opposite to those generated by any of the other theoretical models used in this study.

The addition of radioactive heating to the initial thermal structure (Geotherm B) produces a different pattern of PT and Tt paths than those discussed above. In Fig. 4.6a, the PT paths for the pure shear and simple shear thickening mechanisms are now similar, with fairly linear synthrusting portions followed by the attainment of maximum temperature

at nearly the same depth following a few million years of erosional unroofing. During pure shear thickening, the radioactive layer is thickened, and conservation of the total amount of radioactive heat contained in a cross-section of the thickening lithosphere requires that material “move” into a given vertical column from the sides but that the spacing between individual points in the radioactive layer move further apart. This results in thickening of the radioactive layer and increase in radioactive heat production by a factor of $1/\beta$. During both thrusting and the subsequent period of erosional denudation, a greater amount of heating is therefore expected in the pure shear thickening model. The morphology of the Tt path for this model also differs from the concave Tt curve for the simple shear case. Constant burial rate produces a fairly linear Tt path for the rock buried by movement on a thrust fault, but pure shear thickening occurs at different rates, with most rapid burial near the end of the compressional period. Thus, dT/dt increases sharply near the end of the thickening event.

THE BURIAL PATH

The burial paths of rocks in the shortening crust are also affected by fault geometry and the rate of footwall burial and thrust emplacement. The results below show burial PT and Tt paths that reflect the thermal effects of thrusting at different rates and along faults with different dips. Unless stated otherwise, each plot shows the burial paths for four rocks, two each in the hanging wall and footwall of the thrust fault. The two footwall rocks do not undergo lateral translation during faulting but are simply buried beneath increasing amounts of hanging wall rock at each compressional time step. Thus, the depth of the rock below the surface increases during thrusting, but the depth of the rock relative to the thrust fault remains constant at all times. The two hanging wall rocks whose thermal

evolution is represented in each plot have been translated laterally by thrust emplacement, but their depths relative to both the surface and the thrust fault remain constant at all times.

Fault dip

Figure 4.7a shows the PT paths of a rock 0.5 km below thrust faults dipping at approximately 26° and 63° (cotangents of 2 and 0.5 respectively) for two initial thermal structures. The rate of updip movement along the thrust fault has been held constant at $2\sqrt{5}$ mm/yr, corresponding to burial rates of 2 mm/yr and 4 mm/yr for the 26° and 63° faults respectively. In order to distinguish the effects of displacing the radioactive layer from those associated solely with different fault dips, we show burial PT paths generated with both Geotherm A (steady-state and no radioactive heating) and B (steady-state for radioactive heating at $3 \mu\text{W}/\text{m}^3$ in the upper 20 km). For the PT paths generated using Geotherm A, wide variation in the fault dip produces only a 40 K difference in temperature immediately following thrusting, with rocks near the more shallowly dipping fault undergoing the most syntectonic heating. The heating path for the rock in the footwall of the 26° fault has smaller dT/dP and larger dT/dt (not shown) than those for rocks near the more steeply dipping fault. During the syntectonic phase, slopes of the PT and Tt paths obey the chain-rule relation: $dT/dP \cdot dP/dt = dT/dt$, where dT/dP refers to the slope of the PT path, dP/dt is the burial rate, and dT/dt is the slope of the Tt path. Holding the resolved velocity along the fault surface constant leads to different burial rates (dP/dt), and the relative differences between dT/dP and dT/dt for the 26° and 63° faults are therefore exactly as would be predicted.

When radioactive heating is added to the initial geotherm (Geotherm B), the relative patterns of the PT paths for the 26° and 63° fault change slightly. During the first half of burial, approximately to the depth of 15 km, the PT curves are nearly indistinguishable. To this depth, however, the 26° and 63° curves maintain the same relative positions as the

example using initial Geotherm A, and dT/dP remains fractionally smaller for the shallower fault. The 63° path crosses the 26° PT path below 15 km depth, and the final temperature just below the thrust fault is 40K lower for the 63° fault than for the 26° fault. The addition of radioactive heating alters the morphology of the PT paths from linear to curved. Greater heating associated with the 26° fault is probably related to the much greater horizontal extent of Zone II (see Fig. 4.1) for shallow faults and the greater effects of lateral thermal gradients.

Some of the slight differences between the PT paths for the 26° and 63° faults in Fig. 4.7a result from the choice to equate resolved updip velocity instead of burial rate (dP/dt). Two-dimensional modeling of extensional PTt paths [Chapter 5] indicates that, for the same rate of uplift relative to the surface (dP/dt), PT and Tt paths for footwall rocks beneath normal faults dipping at a variety of angles are nearly the same. The comparable case for compressional settings is shown in Fig. 4.7b, where the burial rate has been held constant at 2 mm/yr for faults dipping at 26° , 45° , and 63° . As in the case of constant updip velocity, the PT paths for burial at a constant rate using Geotherm A show that rocks in the footwall of shallowly dipping faults have smaller dT/dP than footwall rocks of steeply dipping faults. Rocks in the footwall of the shallowly dipping fault undergo less net heating at a lower rate than rocks beneath steeply dipping fault surfaces, consistent with the chain-rule relationship discussed above. At the end of the thrusting interval, the temperature difference between the 26° and 63° paths using constant burial rates is 50K, only slightly greater the post-thrusting temperature difference produced by holding the updip resolved velocity constant.

The addition of radioactive heating to the initial thermal structure produces PT paths with morphologies similar to those observed in the presence of radioactive heating for constant updip resolved velocity. The curvature of the PT path is greatest for the steeply dipping fault and crosses the 26° and 45° paths at a depth of approximately 20 km. With

constant burial rate, the PT paths for the 26°, 45°, and 63° faults are nearly indistinguishable and are separated by a maximum of only 10K at any time during the burial history.

Burial rate

Fig. 4.8 shows the PT and Tt paths for a 45° fault and three different burial rates. Clearly, burial rate has a significant effect on the amount of footwall heating and hanging wall cooling. Fast burial results in steeper PT paths, and, as shown later, burial at rates even higher than those tested here would produce nearly isothermal compression. Slow rates of burial cause larger and less rapid temperature changes than faster burial rates. For burial at 1 mm/yr, heating of footwall rocks 0.5 km below the fault surface results in a syntectonic temperature change of about 400K whereas 5 mm/yr of burial causes only a 300K rise in temperature. Rocks 10 km below the fault experience smaller relative temperature changes of 350K and 250K for burial rates of 1 mm/yr and 5 mm/yr, respectively. In contrast to the footwall rocks, material in the hanging wall undergoes initial cooling that lasts from 6 my for a 5 mm/yr burial rate to 12 my for burial at 1 mm/yr. For a linear steady-state initial geotherm with no radioactive heat production, cooling of hanging wall rocks would continue until the end of the syntectonic interval in all cases. In the presence of radioactive heating, however, thickening of an upper crustal radioactive layer produces complicated heterogeneities in the lateral thermal structure of the lithosphere, and hanging wall rocks cool a small amount over several million years before being reheated due to radioactive effects. The cooling and reheating of hanging wall rocks are most pronounced close to the thrust fault, and, as expected, the cooling interval lasts longer with increasing distance from the thrust surface.

One of the most important results of one-dimensional modeling of PT paths was the prediction that peak temperatures in regional metamorphic terrains are attained several

million years following the end of the compressional interval, during the period of unroofing to shallower crustal levels [England and Richardson, 1977]. Figure 4.8a demonstrates that the time elapsed between the end of compressional interval and the attainment of maximum temperature is approximately the same for the three rates of burial presented here. The depth at which maximum temperature is attained also appears to be linked only weakly to the rate of burial or the amount of syntectonic heating. Peak temperatures occur within a 3 km range for rocks nearer the surface and a 5 km range for the rock at a post-thrusting depth of 40 km. The post-thrusting temperature differences produced by varying the burial rate are reduced by about half at the depths of peak temperature conditions and completely disappear once half the total amount of unroofing has occurred. These observations imply that unroofing rate, not different burial rate, is the more important factor controlling the morphology of a PT path, an inference that will be examined at greater length below.

THE UNROOFING PATH

Typically, petrologic and geochronologic data provide better quantitative constraints on the retrograde, rather than prograde, paths of metamorphic rocks. Thus, understanding the morphology of retrograde PTt paths, typically followed during unroofing of a metamorphic terrain, is particularly important for the interpretation of metamorphic rocks. We consider here the thermal effects of different unroofing mechanisms (pure shear and simple shear extension and erosional denudation) and different rates of erosional unroofing.

Unroofing mechanism: pure shear, simple shear, and erosion

Tectonic denudation and erosion are the mechanisms by which metamorphic rocks are brought to the surface. Work by England and Jackson [1987] and that in Chapter 5 focus

on the thermal effects of tectonic unroofing via pure shear and simple shear extension of the crust. Pure shear thinning results in movement of rocks from deeper to shallower levels by homogeneous thinning of the lithosphere. The radioactive layer retains its form but is thinned and stretched by the pure shear event, reducing the amount of radioactive material at any vertical position. Simple shear describes unroofing as a consequence of movement on structurally higher normal faults. Complicated horizontal geometries, analogous to those associated with thrust displacement, develop as the result of denudation via a simple shear mechanism, and the amount of unroofing therefore varies with horizontal position. Disruption of the radioactive layer during normal faulting contributes significantly to the development of lateral thermal gradients, but the radioactive layer is not uniformly thinned as in the pure shear case. Erosion, the final denudation mechanism considered here, is assumed to affect an area uniformly, removing the same amount of material at each horizontal position. Unlike pure shear and simple shear, erosion does not conserve radioactive heat production, and the radioactive layer is simply passively removed along with other crustal material. This difference is the distinguishing factor between tectonic processes like pure and simple shear and passive processes like erosion. On the other hand, both pure shear thinning and erosional unroofing are one-dimensional processes that do not contribute to the development of lateral thermal gradients, and the dimensional similarity between the mechanisms proves more important in controlling the morphologies of PTt paths than the differences in how the radioactive layer is affected.

In order to understand the relative effects of unroofing deep crustal rocks via pure shear, simple shear, and erosion, we compared the retrograde PT and Tt paths for a rock originally at 30 km depth that loses 27 km of overburden in 27 my (Fig. 4.9). Two pure-shear mechanisms are presented: "Uniform" pure shear thins the entire lithosphere using $\beta=10$, and "modified" pure shear thins the upper 30 km (the crust) by a factor of 10 and

leaves the mantle lithosphere undeformed. Both types of pure shear produce the required 27 km of thinning in the upper 30 km of the lithosphere.

Fig. 4.9 shows the PT paths for each of these mechanisms and for two initial thermal structures. In Fig. 4.9a, the direct comparison of the effects of different unroofing mechanisms has been facilitated by the use of a linear initial geotherm with no radioactive heating (Geotherm A of Fig. 4.2), eliminating the need to consider complicating effects associated with disruption of the radioactive layer. The thermal histories shown in Fig. 4.9b correspond to Initial Geotherm B, which includes a layer of radioactive heat in the upper crust. For both initial geotherms, simple-shear thinning by movement along a normal fault dipping at 45° produces a slightly concave PT path with nearly constant dT/dP . Pure shear of the entire lithosphere yields isothermal decompression during most of the unroofing history for Geotherm A and during the first 10 km of unroofing with Geotherm B. Modified pure shear, in which only the crustal lithosphere is thinned, is characterized by initially isothermal uplift relative to the surface and dT/dP values that become more negative steadily throughout the rocks' unroofing history. Finally, erosional unroofing produces a PT path that lies between paths for uniform pure shear and simple shear.

The similarity between the nearly isothermal PT path observed in the early stages of erosional unroofing and pure shear thinning underscores the one-dimensional nature of these processes. Although the simple shear and erosional PT paths display some important theoretical differences, these curves are separated by a maximum of 75K and 150MPa during the unroofing history depicted in Fig. 4.9b. Given the fact that the best thermobarometric data have nominal precision limits of several tens of kelvins and roughly 100MPa at the 95% confidence level (*e.g.*, Hodges and McKenna [1987]), Fig. 4.9 implies that the PT paths produced by various unroofing mechanisms cannot be distinguished easily. However, all of the paths in Fig. 4.9 correspond to a fixed rate of

denudation. In real settings, tectonic unroofing likely occurs much more quickly than erosion, and it is therefore important to consider the effect of denudation rate on PTt paths if we intend to explore the possibility that certain paths might be diagnostic of tectonic unroofing.

Denudation Rate

The retrograde path depends most critically on the rate at which a given rock horizon is carried closer to the surface through tectonic or erosional unroofing. This is illustrated in Figure 4.10, which shows PT and Tt paths for rocks 0.5 below and 10 km above and below a 45° thrust fault that moved at a rate of 2 mm/yr for 15 my. The thrusting event was followed immediately by erosional unroofing of the upper 30 km of thickened crust at rates 1, 2, or 5 mm/yr over 30, 15, and 6 my respectively. Important differences distinguish the PT paths produced by erosional unroofing at different rates: Fast unroofing causes the initial decompression phase to be accompanied by very little net heating, producing a nearly isothermal unroofing curve. Because some heating occurs during the unroofing stage for all of the examples presented here, there is a change in the concavity of PT curve about an inflection point at the depth of maximum temperature. At depths greater than that at which peak temperature conditions prevail, the path has small and fairly constant dT/dP . After passing through peak temperature, the absolute temperature change per kilometer of uplift (dT/dP) and the rate of cooling (dT/dt) increase.

In the section above, we noted that, when different burial rates are coupled with the same unroofing rates, temperature differences existing immediately following the end of thrusting are largely eliminated after half of the net unroofing has occurred. As a result, peak temperatures are attained at nearly the same depths during the unroofing phase. Fig. 4.10a clearly underscores the dependence of the morphology of retrograde PT paths on the unroofing rate, not the burial rate. For faster unroofing, peak temperatures occur at

significantly shallower depths and slightly lower temperatures than for slow unroofing. Similar sets of curves may be drawn for different unroofing mechanisms, and the salient characteristics are much the same: rapid unroofing (by whatever mechanism) produces a pronounced “nearly isothermal” decompression signature in PT paths during the early stages of unroofing and rapid cooling in the later stages of unroofing. If rapid unroofing is characteristic of tectonic denudation, then large dP/dT and dT/dt slopes for retrograde portions of PT and Tt paths are highly suggestive of tectonic denudation.

IMPORTANCE OF INITIAL THERMAL STRUCTURE

Many previous theoretical models for the thermal histories of metamorphic rocks from compressional terrains have failed to produce peak temperatures as high as those commonly indicated by geothermobarometric analyses. One possible explanation for the disparity between observational and theoretical results is that the pre-thickening lithosphere is actually much hotter than commonly assumed. Models for continental lithosphere typically employ an initial thermal structure derived by adding radioactive heating to geotherms for old oceanic lithosphere of about 125 km thickness [*Parsons and Sclater, 1977*]. In recent years, studies of flexural rigidity [*McNutt et al., 1988*], Curie isotherms, and earthquake depths [*Chen and Molnar, 1983*] have implied that geothermal gradients in orogenically-active areas may be much higher than those in the usual oceanic analog. The widespread association of magmatism and orogenesis, as well as studies linking thermal weakening of the lithosphere to the onset of tectonic activity indicate that geothermal gradients can be as high as 25 or 30K/km prior to large-scale lithospheric thickening. Here we examine how relatively hot initial lithospheric thermal structure affects the PTt histories of metamorphic rocks from compressional terrains, focusing primarily on the

effects of increasing basal heat flow, changing the rate and distribution of heat production from radioactive decay, and introducing shear heating along the fault zone.

In this section, we introduce two new kinds of diagrams in an effort to facilitate comparison of two-dimensional modeling results with expected thermobarometric and thermochronologic data. The first, referred to as a TMAX plot, illustrates the maximum temperature attained by rocks as a function of their initial structural distance from the thrust fault. The second, a P_{TMAX} diagram, shows the pressure conditions at the time of maximum temperature. Such diagrams are important because “peak metamorphic conditions” derived through petrologic study of prograde mineral assemblages in metamorphic rocks with simple thermal histories are thought to represent maximum temperature conditions [England and Richardson, 1977; Spear and Peacock, 1989]. Unroofing rate and the position of a rock horizon relative to the fault govern the amount of time that elapses between the end of thrusting and the attainment of peak temperature, and peak metamorphic conditions are therefore reached at different times at various levels in the crust. Hanging wall rocks often experience maximum temperature conditions before the onset of thrusting or at the very end of the thrusting interval, whereas the temperature of footwall rocks invariably continues to rise during the initial stages of the unroofing period. The depths at which footwall rocks proximal to the fault surface reach maximum temperature may therefore be shallower than those at which nearby hanging wall rocks attain their maximum temperatures, producing P_{TMAX} curves characterized by a jog at the position of the fault.

Increased mantle heat flow

One regional source of heating that could be responsible for the relatively high temperatures experienced by metamorphic rocks from some compressional terrains is increased heat flow into the base of the crust. Although evidence increasingly suggests that

the continental and oceanic mantle lithosphere differ in thickness [Jordan, 1978], radioactivity, and rheology [McNutt *et al.*, 1988], the mantle heat flow figure of 30 mW/m^2 derived by Sclater *et al.* [1980] for the oceans is still routinely applied to continental settings, even in orogenically active regions. Here we test the effects of three different values of increased mantle heat flow on the peak metamorphic conditions and PT paths. The chosen mantle heat flow values of 31.2, 45 and 60 mW/m^2 correspond to background geothermal gradients of 10.4, 15, and 20 K/km respectively. Coupled with the 1573K temperature boundary condition at the base of the lithosphere, these background thermal gradients (Fig. 4.11a) require lithospheric thicknesses of 125 km for the lowest heat flow value (Initial Geotherm B), 95 km for the 45 mW/m^2 value (Initial Geotherm C), and 86.5 km for a flow of 60 mW/m^2 (Initial Geotherm D). Thrust emplacement at 2 mm/yr for 15 my and subsequent erosional unroofing at 1 mm/yr for 30 my produces the PT path morphologies shown in Fig. 4.11b for footwall rocks 0.5 km and 10 km below the thrust fault. Compared to PT paths generated using Initial Geotherm B and varying burial rate (Fig. 4.8b), crustal thickening mechanism (Fig. 4.9), and erosional unroofing rate (Fig. 4.10a), the PT paths of Fig. 4.11b show maximum temperatures up to 250K hotter at a depth of 10 km below the thrust fault. Clearly, increased heat flow into the base of the mantle can produce the high temperatures experienced by some metamorphic rocks from compressional terrains.

The TMAX curves shown in Fig. 4.11c are nearly the same as the initial geotherms of Fig. 4.11a in the hanging wall and the top of the footwall. In the absence of local thermal heterogeneities associated with lithology, intrusive activity, radioactivity, fluid circulation, and frictional heating, this result implies that peak metamorphic conditions for these rocks should closely approximate the geothermal gradient that preceded the onset of deformation. In footwall rocks, TMAX curves are strictly representative of the pre-thrusting geothermal gradient only for mantle heat flow values close to the 30 mW/m^2 , but are still within

nominal temperature uncertainties of $\pm 50\text{K}$ of the pre-thrusting gradient for higher heat flow values.

While these results predict no step or inversion in temperatures across the fault zone, Fig. 4.11c implies a pressure inversion of up to 150-175MPa at the position of the fault and significant differences in the times at which certain minerals cooled through their closure temperatures on either side of the fault. During the thrusting interval, the base of the hanging wall block cools more for a hot initial geotherm than for a cold one. Although the net amount of postthrusting conductive heating of the base of the hanging wall block due to radioactivity at the top of the underlying footwall block is the same in all three cases, only for the cool initial geotherm can this heating overcome the synthrusting cooling effect to reset temperatures near the fault zone in the bottom few kilometers of the footwall block.

Radioactive heat production

High rates of radioactive heat production is another mechanism capable of producing high metamorphic temperatures on a regional scale. Fig. 4.12a shows initial geotherms (E, F, B, and G), corresponding to radioactive heat production at rates of $3 \mu\text{W}/\text{m}^3$ in the upper 10 km (Geotherm E), and 1.5, 3, and $6 \mu\text{W}/\text{m}^3$ in the upper 20 km of the pre-deformational crust (Geotherms F, B, and G respectively). In each case, the initial thermal structure is the steady-state geotherm calculated from superposition of the radioactive layer on a background gradient of $10.4\text{K}/\text{km}$, produced by a mantle heat flow of $31.2 \text{mW}/\text{m}^2$. Fig. 4.12b illustrates the dramatic effects of variations in the rate of radioactive heat production on the PT paths of footwall rocks 0.5 and 10 km below the thrust fault. The initial geotherms in Fig. 4.12a vary by a maximum of 300K at a depth of 30 km or 40 km, but, at these same depths along the synthrusting portion of the PT paths, temperatures vary by over 400K . As a consequence, TMAX for rocks at different structural levels differs about 425K between the coolest (Initial Geotherm E) and hottest (Initial Geotherm G)

thermal structures (Fig. 4.12c). High rates of radioactive heat production can clearly produce temperatures of 1000K or higher in some parts of the footwall.

An interesting characteristic of the TMAX curves for various rates and distributions of radioactive heat production is a small thermal inversion of up to 25K at the position of the thrust fault when the total amount of integrated heat produced by radioactive heating is relatively small, either due to concentration of radioactive elements in only the uppermost few kilometers of crust (Initial Geotherm E) or radioactive element abundances that are relatively low (Initial Geotherm F). In these cases, the inversion, shown in Fig. 4.12c, arises because rocks in the hanging wall experience maximum temperature at the onset of thrusting and undergo cooling throughout thrusting and erosion, whereas footwall rocks reach their maximum temperature during unroofing. The thermal effects of thrust disruption of the radioactive layer are greatly reduced when heat production rates are low or the layer lies in only the upper few kilometers of the crust. Juxtaposition of the base of the hot hanging wall against the top of the cool footwall results in little conductive heating of the hanging wall rocks due to footwall radioactivity and little conductive heating of footwall rocks as a result of thick radioactive layers in the hanging wall. While Initial Geotherms B and G produce no inversion in the peak conditions, high rates of radioactive heating cause significant differences between the initial and peak conditions. At a depth of 40 km (structural distance of +10 km), the peak temperature and initial geotherm curves vary by about 150K for Initial Geotherm G, indicating that, in regions of high radioactive heat production distributed over much of the upper and middle crust, TMAX curves provide poor constraints on the initial prethrusting geothermal regime.

Across the fault zone, the P_{TMAX} plots for Initial Geotherms E and F show the same 150MPa pressure inversion as seen above for the case of high mantle heat flow. The attainment of peak metamorphic conditions occurs diachronously, implying that thermochronologic data will indicate a wide range in cooling ages both within the fault

blocks and across the fault zone. The P_{TMAX} curve for Initial Geotherm G has no inversion but departs from the lithostatic gradient at about -20 km structural distance (at 10 km depth) and has a significantly shallower slope. A comparison of the P_{TMAX} curves for the hot mantle flow geotherms (D of Fig. 4.11c) and for the hot radioactive heating geotherm (G of Fig. 4.12c) underscores the close connection between the “source” of excess heat in the crust and the resulting P_{TMAX} conditions. Whereas high mantle heat flow, a lithospheric heat source, produces an inversion in the P_{TMAX} curve at the position of the fault, excess crustal heat in the form of higher radioactivity leads to no such pressure inversion. With the hot initial geotherm (G), the base of the hanging wall undergoes appreciable conductive heating due to the proximity of a thick layer of radioactivity at the top of the footwall, and temperatures are reset from their initial values up to 20 km from the fault zone. Low amounts of radioactivity or thinner radioactive layers do not cause the hanging wall to undergo significant post-thrusting heating and therefore lead to the development of the P_{TMAX} inversion.

Shear heating

Shear heating along thrust faults has been examined as a cause of high metamorphic temperatures [Scholz, 1980], anatexis [England and Molnar, 1990; England et al., 1991], and increased heat flow near fault zones, but theoretical consideration of the effects of shear heating is complicated by disagreement over appropriate frictional coefficients, the role of fluids in transporting heat along crustal discontinuities, and the width of zones over which shearing occurs. In the examples presented here, we adopt a simple model in which the coefficient of friction μ is constant along the entire fault surface, and the temperature change ΔT due to shear heating during each time interval τ is given by the expression for frictional heating of a half-space:

$$\Delta T = \frac{2\mu pu}{K} \sqrt{\frac{\kappa t}{\pi}} \quad (4.1),$$

where p denotes lithostatic pressure at the fault zone calculated with density 2670 kg/m^3 , u is horizontal velocity of the hanging wall relative to the footwall, and κ and K are diffusivity and conductivity respectively [Turcotte and Schubert, 1973]. At each time interval, ΔT is added at the footwall node directly adjacent to the fault, implying the concentration of shear heating at a single discrete zone instead of throughout a wider zone of fault deformation.

The range of frictional coefficients used here is 0 to 0.6. Low frictional stresses are consistent with the low heat flow values near large transform faults like the San Andreas [Lachenbruch and Sass, 1973] and with rock mechanics experiments on clay gouges [Morrow et al., 1982]. On the other hand, rock mechanics experiments on dry quartz [Byerlee, 1978] support the use of frictional coefficients greater than 0.5. Models generated using small frictional coefficients assume either that shear heating is not an important factor or that much of the heat associated with movement in fault zones is dissipated by highly conductive fluids that move on time scales much smaller than those associated with heating of crustal rocks.

Fig. 4.13a shows the PT paths of a horizon 0.5 km below the thrust fault (well within the zone of maximum potential shear heating) for a variety of frictional coefficients between 0 and 0.6. Without shear heating, dP/dt decreases as the maximum depth is neared, giving the PT paths their characteristic curvature. Increased amounts of shear heating impart greater linearity to the synthrusting PT curves, and the temperature at maximum depth is 250K hotter for the highest frictional coefficient than for the case of no shear heating. Because shear heating and thrusting end simultaneously, however, the onset of erosion at the end of the thrusting interval is accompanied by immediate cooling near the thrust fault. This effect is most dramatically seen for the $\mu=0.6$ path, where a small loop

with sense opposite that of the larger PT loop has developed. In this extreme case, the rock near the fault has its maximum temperature at the end of the thrusting interval. The fact that the erosional PT path subsequently crosses itself indicates that the initial effect of discontinuation of shear heating is short-lived and that the normal conductive re-equilibration of geotherms during the period of erosional unroofing soon takes over.

TMAX and P_{TMAX} curves for the range of frictional coefficients are shown in Fig. 4.13b. Maximum temperatures of hanging wall rocks for $\mu=0$ and $\mu=0.3$ vary by up to 75K in the hanging wall. In contrast, the same range of frictional coefficients produces peak conditions that are nearly indistinguishable in the footwall. For $\mu=0.15$, a 150MPa pressure inversion, caused by rocks at shallower crustal levels attaining maximum temperatures at greater depths during unroofing than adjacent rocks at deeper crustal levels, occurs at the top of the footwall. When shear heating is greatest near the fault zone (*i.e.*, when frictional coefficients are high), the pressure inversion is displaced to greater depths and reduced in amplitude. This effect is a result of the nature of frictional heating, which is only added to the crust during the thrusting interval. Rocks in the hanging wall and proximal to the fault in the footwall attain peak temperatures nearly simultaneously close to the end of tectonism, but rocks at deep levels in the footwall continue heating conductively during unroofing. It should be noted that the TMAX curves for hanging wall and near-fault footwall horizons approximate the geotherm at the end of thrusting.

The addition of shear heat only at the top of the footwall causes a small-wavelength temperature inversion of up to 100K amplitude in the TMAX curve for the highest coefficient of friction. In more realistic models, shear heat might be added over a wider zone of deformation near the fault, but the effective coefficient of friction would likely be lower than the extreme value of 0.6 used here. Such wide zones of shear heating would, however, serve both to heat the entire thickened crust by conduction and possibly to produce a long-wavelength temperature inversion of greater amplitude. This is an

important finding considering the controversies that have arisen regarding the likelihood of preserving inverted metamorphic gradients in the geologic record. Early one-dimensional models based on instantaneous emplacement of hot rocks on cold rocks (*e.g.*, *Oxburgh and Turcotte* [1974]) produced inverted geothermal gradients. When thrust emplacement at realistic rates was introduced into these models (*e.g.*, *Shi and Wang* [1987]), such inversions disappeared. The fact remains that inverted metamorphic gradients are not terribly uncommon in the geologic record, and have been found in tectonic settings ranging from subduction complexes (*e.g.*, *Peacock* [1987]) to continent-continent collision zones (*e.g.*, *Andreasson and Lagerblad* [1980]). We agree with *England et al.* [in review] that shear heating may play an important role in the creation of inverted metamorphic gradients, but we hasten to add that there are many examples of inverted gradients that have developed far from major fault zones and the effects of any associated shear heating.

Simultaneous thrusting and erosion

Most of the models discussed here have focused on a two-step process of thrust sheet emplacement followed by erosional unroofing. In real settings, compression and erosion probably occur simultaneously, and the combination of primarily lateral (thrusting) and primarily vertical (erosion) advective processes may contribute to the development of inverted temperature gradients and their preservation by metamorphic rocks.

Figure 4.14 shows PT paths, post-thrusting geotherms, and T_{MAX} and P_{TMAX} for cases in which thrusting and erosion occur sequentially (curve B) and simultaneously. (curves H, J, and K). In all cases, overthrusting thickens the crust by a maximum of 30 km, and erosional unroofing continues until a total of 30 km of material has been removed. However, when erosion and thrusting occur simultaneously to any degree, the net amount of burial never reaches 30 km. The sequential case (curve B) corresponds to thrusting at 2 mm/yr from 0 to 15my followed by erosional unroofing at 1 mm/yr from 15my to 45my.

In case H, erosional unroofing begins halfway through the compressional interval (at 7.5my), and continues for 22.5 my after the end of thrusting. Cases J and K correspond to the simultaneous onset of thrusting and erosion at 0 my, but the ratio of burial to unroofing rates is 2:1 for case J and 5:1 for case K. The thrusting intervals endure 15my and 6my respectively, and erosional unroofing continues for 15my and 24my after the end of compression.

The PT paths shown in Fig. 4.14a demonstrate that a greater degree of simultaneity between thrusting and erosion produces less net burial and heating and therefore smaller differences between the synthrusting and postthrusting thermal evolution of footwall rocks immediately below the fault. Sequential thrusting and erosion (case B) yield fairly constant synthrusting dT/dP values and the characteristic pattern of synerosional heating and cooling discussed at length above. The onset of erosion during the thrusting interval (case H) results in higher dT/dP , but the temperature and depth immediately following thrusting are 50K and 7.5 km smaller than for the sequential case. Using the same ratio of burial to unroofing rates (2:1) as for cases B and H, case J illustrates that synchronous thrusting and erosion over the first 15 my greatly modify the morphology of the PT path. The synthrusting and postthrusting PT paths are separated by only 50K and 75MPa, and synthrusting dT/dP is greater and synerosional dT/dP smaller than for sequential case B.

When thrusting and erosion occur simultaneously, the postthrusting depth of the fault surface is shallower than in the sequential case, and the presence of hot footwall rocks closer to the Earth's surface should produce a higher geotherm. Figure 4.14b shows the geotherms immediately following thrusting for the endmember sequential (B) and simultaneous (J) cases. The form of the geotherm for case B represents the effects of advection only in the lateral direction as a result of thrust emplacement, while the geotherm for case J has been affected by an additional vertical advective and conductive component associated with erosional unroofing. The postthrusting geotherms in Fig. 4.14b differ by a

maximum of only 50K within the footwall, indicating that lateral advection of heat during thrusting exceeds cooling associated with erosional unroofing by only a small amount. Note that this pattern of net heating in the footwall does not produce an inversion in the postthrusting geotherms.

Figure 4.14c shows that an increasing degree of simultaneity of thrusting and erosion leads to larger inversions of TMAX and P_{TMAX} across the fault. As expected, when the ratio of burial to unroofing is large as in case K, thrusting predominates, and the TMAX and P_{TMAX} curves are similar to the sequential case. A 2:1 ratio of burial and unroofing rates and simultaneous onset of thrusting and erosion (case J) produce an inversion of over 100K and nearly 400MPa at the fault zone. Such a large contrast in recorded temperatures and pressures across the fault lies outside the range of nominal uncertainties in geothermobarometric data. However, a burial to unroofing rate ratio of 5:1 is probably more realistic in most geologic settings, and such high ratios produce TMAX and P_{TMAX} inversions too small to detect using current analytic techniques.

INVERTED POST-THRUSTING GEOTHERMS vs. TMAX

In the shear heating case, TMAX conditions are attained synchronously on both sides of the fault at the end of the thrusting interval, and the TMAX curve therefore roughly corresponds to a post-thrusting geotherm in the vicinity of the fault. This result contrasts with those obtained assuming other sources of excess heat. For excess radioactive heating or higher mantle heat flow, TMAX is recorded diachronously across the fault zone, and TMAX curves coincide more closely with the initial geotherm (particularly in the hanging wall) than with the post-thrusting geotherm. These observations are important in light of the widespread acceptance of the “sawtooth” (inverted) geotherm as representative of the post-thrusting thermal regime in large-scale compressional terrains and the implication that

this geotherm should be recorded by rocks in the vicinity of the fault zone. Previous workers (*e.g.*, Shi and Wang [1987]) have shown that two-dimensional non-instantaneous thrusting models produce a post-thrusting temperature inversion only when thrusting rates are greater than a few centimeters per year. Figure 4.15 shows the PT paths, post-thrusting geotherms, and TMAX conditions for fast burial rates (5–40 mm/yr). As predicted, the synthrusting PT paths become increasingly isothermal with higher thrusting rates, but significant temperature inversions in the post-thrusting geotherm only develop when burial rate reaches 40 mm/yr. In settings such as subduction zones, where underthrusting may occur at near plate velocities, such a post-thrusting geotherm could be maintained over several million years, but the duration of thrusting is typically shorter and thrusting rates much lower in generalized compressional settings. More importantly, the TMAX curve of Fig. 4.15c shows only a small thermal inversion (~25K) for the fastest thrusting rate tested here. Postthrusting geothermal inversions should theoretically never be recorded by metamorphic rocks in the vicinity of the fault zone since hanging wall rocks directly adjacent to the fault undergo significant heating and metamorphic overprinting during rapid conductive relaxation of the inverted geotherm following thrusting.

DISCUSSION

Our purpose in the preceding paragraphs was to explore the influence of various boundary conditions and mechanisms of burial and unroofing on the morphology of PTt paths using two-dimensional thermal models. We now examine the extent to which petrologic and thermochronologic data may be useful in reconstructing the thermal structure of ancient orogenic belts.

Pressure-Temperature Paths from Natural Samples

Conventional thermobarometry using mineral rim compositions aims to establish the PT conditions at the time of final equilibration between various minerals in the matrix of a sample. For samples with a simple prograde history, a common assumption is that rim thermobarometry may be used to establish peak metamorphic conditions [Spear and Peacock, 1989]. Theoretically, it should be possible to generate profiles of T_{MAX} and P_{TMAX} as a function of structural level in a metamorphic terrain using rim thermobarometry and to compare these data to the theoretical curves in this paper in order to constrain the ancient thermal structure of the terrain. Two factors conspire to limit the effectiveness of this approach: uncertainties in rim thermobarometry and the propensity of many thermobarometers to re-equilibrate during cooling.

Sources of uncertainty in thermobarometric data include non-systematic errors (related to analytical uncertainties and solution behavior that changes as a function of P, T, and composition) and systematic errors associated with the techniques used to calibrate thermobarometers. The non-systematic component results in PT imprecisions that are commonly on the order of 20-50K and 100-150MPa at the 95% confidence level, whereas the systematic component leads to 2 σ accuracy limits of greater than 100K and 200MPa for the best-calibrated thermobarometers [Hodges and McKenna, 1987; McKenna and Hodges, 1988]. Data with such uncertainties may permit us to establish whether or not some anomalous heat (*e.g.*, high rates of radioactive heat production, high mantle heat flow, or significant shear heating) are necessary to achieve the observed PT conditions, but cannot provide a basis for distinguishing among these potential heat sources. In addition, rim thermobarometric data alone are too imprecise to constrain the mechanism or rates of burial and unroofing.

An additional complexity arises because many samples continue to re-equilibrate after peak metamorphic conditions are achieved and as the sample is transported to the surface

[*Thompson and England, 1984; Spear and Florence, 1990*]. In some cases, thermobarometric data from such samples may record portions of retrograde PT trajectories [*Hodges and Royden, 1984*], while in others these data may be completely erroneous due to dissimilarities in the reaction kinetics of different thermobarometers [*Frost and Chacko, 1989*]. In either case, comparison of TMAX and P_{TMAX} profiles from natural samples that have experienced retrogression with theoretical curves is clearly a pointless exercise.

Kinetic factors dictate that we should have greater success in reconstructing the retrograde (post-TMAX) PT paths of natural assemblages than we have in recovering the prograde path. Rim thermobarometry on variably retrograded samples [*Hodges and Royden, 1984*], thermobarometry using inclusion suites in zoned porphyroblasts [*St-Onge, 1987*], thermodynamic modeling of zoned porphyroblasts [*Spear and Selverstone, 1983; Spear, 1989*], and fluid inclusion thermobarometry [*Hollister et al., 1979*] constitute an impressive arsenal of techniques that can be used to constrain retrograde PT paths. All of these techniques are subject to analytical imprecision and variably justified implicit assumptions (see *Hodges [1991]* for a discussion). Reconstruction of the PT path for a particular structural horizon often involves the integration of data from a number of samples that record equilibrium conditions at different times during unroofing [*e.g., Hodges and Walker, 1990*]. In these cases, application of the same methodology to different samples serves to reduce the effects of systematic errors on PT path reconstructions. Generally speaking, we can recover the *topology* of portions of a PT path with much higher precision than we can recover the *absolute coordinates* of any part of the path. This implies that petrologic data can place important constraints on tectonic and thermal processes that strongly influence the shape of the retrograde path. Our modeling results show that this part of the PT path is largely controlled by the unroofing rate.

Time-temperature paths from natural samples

Using a variety of mineral-isotopic systems, it is possible to reconstruct significant portions of the retrograde Tt paths of metamorphic rocks [e.g., *Wagner et al.*, 1977]. The most commonly used systems ($^{40}\text{Ar}/^{39}\text{Ar}$ in hornblende, muscovite, biotite, and potassium feldspar; fission tracks in sphene, zircon, and apatite) record the times at which samples pass through nominal closure temperatures ranging from 780 to 380 K with precisions of roughly 50 to 75K [*Hodges*, in press]. All of the Tt information obtained using these systems thus reflects the late stages of unroofing of a metamorphic horizon. Once again, field data are more likely to place effective constraints on unroofing rates than on initial thermal conditions.

The importance of integrative PTt studies and inverse modeling

With the wide availability of one-dimensional thermal modeling algorithms [*Haugerud*, 1986; *Spear and Peacock*, 1989], there is a great temptation to compare PTt paths for natural samples with simplistic modeling results and make broad inferences about the thermal histories of metamorphic terrains. Forward modeling of metamorphism is extremely useful for identifying those boundary conditions and tectonic processes that can strongly influence PTt paths in natural samples, but it is an ineffective tool for quantifying these parameters. Our forward modeling results indicate that either PT data or Tt data, independent of one another, may be able to distinguish in a general way between very rapid and very slow unroofing. However, a more direct way to address the problem of unroofing rate without reliance on thermal modeling of any kind is: 1) establish dP/dT during unroofing using petrologic data; 2) establish dT/dt using thermochronologic data; 3) use the chain rule to obtain dP/dt ; and 4) convert dP/dt to dz/dt (time-averaged unroofing rate) using an appropriate lithostatic pressure gradient. The geologic literature is largely devoid of examples of this procedure because relatively little integrative petrologic and

geochronologic research has been done, and because the relative kinetics of metamorphic reactions and diffusive loss of radiogenic isotopes are such that most recorded PT paths are for temperatures above 750K and most Tt paths are for temperatures below 750K [*Hodges, 1991*]. In the future, this situation will probably change as a consequence of more effective collaboration between metamorphic petrologists and geochronologists and more aggressive use of mineral-isotopic systems with high closure temperatures (*e.g.*, U-Pb monazite, with a closure temperature of roughly 980K [*Parrish, 1988*]).

If unroofing rates of metamorphic terrains can be constrained independently using petrologic and geochronologic data, then inverse modeling techniques may prove useful in learning more about the thermal structure of ancient orogenic belts. Early attempts at such inverse modeling [*Royden and Hodges, 1984; McNutt and Royden, 1987*] were limited to one dimension and reflected a very simplistic view of unroofing processes, but they serve as guides for establishing the kinds of information that will be required for the next, more sophisticated generation of inverse techniques to produce useful information. In particular, *McNutt and Royden [1987]* showed that uncertainties in the magnitude and distribution of radioactive heat production have a profound effect on how well geotherms can be reconstructed from PTt data. There have been very few attempts to measure actual regional variations in heat production in metamorphic terrains, leaving many questions about the relative importance of radioactivity and mantle heat flow in driving metamorphism. There is every reason to believe that integrative geochemical, petrologic, geochronologic, and structural studies in the coming years will provide the necessary boundary conditions to permit detailed inverse modeling of thermal processes.

CONCLUSIONS

This study challenges the assumptions and results of previous one-dimensional models [England and Thompson, 1984] for the thermal evolution of the lithosphere in compressional settings and seeks to establish general classes of prograde and retrograde paths for footwall and hanging wall rocks buried by thrust emplacement and unroofed by various mechanisms. Although the calculations presented here do not show evidence for large qualitative differences in the PT and Tt paths of footwall rocks at different horizontal positions in a two-dimensional model, we demonstrate that lateral thermal gradients occasionally are one-half as large as vertical thermal gradients, rendering the one-dimensional approximation poor in many instances. Direct comparisons between the PT paths produced by unroofing footwall rocks buried by one-dimensional instantaneous thrusting and two-dimensional non-instantaneous thrusting indicate that the simpler models underestimate the peak temperatures reached during retrograde metamorphism by up to 100K. Furthermore, the disruption of the layer of crustal material that produces heat production during thrust emplacement is shown to have an appreciable effect on the thermal evolution of the lithosphere, an effect completely ignored by one-dimensional models. The disruption of the radioactive heating layer plays an important role in heating hanging wall rocks following an initial period of cooling associated with their juxtaposition against cool footwall rocks during thrust emplacement. In general, the PT path morphology of these hanging wall contrasts with that for footwall rocks, which undergo heating during the entire thrusting period.

Burial paths produced by simple pure shear thickening of the lithosphere and thickening due to the emplacement of a thrust sheet differ most notably when no radioactive heating occurs. In this case, the pure shear PT curve follows an isothermal decompression trajectory while the PT path of a footwall rock buried by simple shear undergoes significant

heating during compression. The geometry of thrust faults appears to play no significant role in controlling the morphology of PT paths, and thrust faults dipping 26°, 45°, and 63° produce almost exactly the same PT paths for the same burial rates. When thrust dip is held constant at 45° and burial occurs at 1, 2, and 5 mm/yr followed by erosional unroofing at 1 mm/yr, the synthrusting PT paths have predictably smaller dT/dP for higher rates, but temperatures at the end of the thrusting interval differ by less than 100K between the endmember cases.

Overall, the mechanism and rate of unroofing exercise greater control over the morphology of complete PT paths than prograde conditions. Pure shear thinning of the lithosphere, erosional unroofing, and tectonic denudation associated with movement along normal faults produce temperatures that vary by up to 200K at some depths. Pure shear thinning and erosional unroofing yield short isothermal decompression paths during the initial stages of uplift relative to the surface, but cooling is nearly constant at about 12K/km in the example used here. The temperatures immediately following the end of unroofing vary by only 80K for the three unroofing mechanisms however. Tests of post-thrusting erosional unroofing at rates of 1, 2, and 5 mm/yr prove that the depth at which peak temperature (P_{TMAX}) is attained and the magnitude of the peak temperature (T_{MAX}) are most sensitive to unroofing rate. Faster unroofing causes peak temperatures to be reached earlier in the unroofing history, at shallower depths, and at lower temperatures. Footwall rocks buried tens of kilometers below the surface experience these effects most dramatically.

The observations of high temperatures (in excess of 900K) and so-called "inverted geotherms" in metamorphic suites from many compressional settings leads to a consideration of the effects of increased mantle heat flow, different radioactive heating rates, and shear heating associated with thrust emplacement. Processes that affect the entire crust, like increased heat flow into its base, are most efficient in producing high

footwall temperatures. Freezing "inverted geotherms" into rocks presents greater difficulties due to the demonstrated difficulty of first generating large inversions (requiring burial rates greater than 40 mm/yr) and second maintaining these inversions that tend to relax quickly during postthrusting conductive re-equilibration. It seems more likely that commonly observed inverted "geotherms" may be related rather to inversions in peak conditions. Such inversions in the TMAX conditions develop at moderate thrusting rates and coefficients of friction greater than about 0.5.

A major obstacle to complete understanding of the relationship between PTt paths and changes in the various parameters that describe thrusting is the poor preservation of the prograde (syncompressional) part of the PTt path in most settings. Overprinting of the prograde path during retrograde metamorphism often leaves only textural clues to the thermal regime that preceded peak temperature and pressure conditions and makes comparison of real data with theoretical models for prograde metamorphism impossible in many instances. Petrologic and geochronologic data provide the greatest constraints on the retrograde history of metamorphic rocks. Inasmuch as the retrograde path is principally controlled by unroofing rate, this parameter is the easiest to recover through inverse modeling of PTt data. By establishing unroofing rates in this manner and constraining radioactive heat production through geochemical studies, it should be possible to examine the relative importance of other factors (mantle heat flow, shear heating, and convective heat transport) in driving the thermal evolution of orogenic belts.

ACKNOWLEDGEMENTS

This study was completed independent of and, for the most part, simultaneous with the work of P. Molnar and P. England. P. Molnar engaged in open discussions and

correspondence about his collaborative efforts and candidly commented on the manuscript. Comments by L. Royden led to many improvements and to the incorporation of the simultaneous thrusting and erosion results. A. Macfarlane discussed this work with C.R. at many stages, and, along with M. Hubbard, incited interest in the inverted Himalayan metamorphic data. Discussions with J. Knapp, J. Fredrich, D. Silverberg, L. McKenna, and E. Buchovecky resolved many aspects of data and models. A. Gunstensen and M. Bergman offered advice on numerical methods and implementation, and T.H. Jordan made possible free computer time on the Alliant FX/40 during the development phase of this project. Computer costs were supported by a Presidential Young Investigator award to L. Royden. Salary for C.R. was paid by M.K. McNutt, who graciously permitted the pursuit of this project in conjunction with unrelated research.

FIGURE CAPTIONS

Figure 4.1. Schematic diagram of the geometry of the thermal model used in this study. (a) Boundary conditions are constant temperatures of 273K at the surface and 1573K at the base of the lithosphere (125 km depth) and no horizontal heat flux at the sides of the box. Radioactive material lies in a laterally homogeneous upper crustal layer (stippled pattern) prior to the onset of faulting. The thrust fault dips at an angle ϕ (measured from the horizontal) between the surface and the base of the crust (30 km depth), where it flattens to follow the Moho. (b) During thrust emplacement, rocks in the hanging wall block are translated only in the x -direction (to the left in this diagram), while rocks in the footwall move only in the z -direction as they are buried beneath the hanging wall. The surface remains flat at all times, and the base of the lithosphere is held constant at a depth of 125 km. The 0 km distance mark along the bottom of the box moves to the left during thrusting and denotes the position of the bend in the thrust fault. Zones I, II, and III refer to the configuration of the fault-disrupted radioactive layer and are described in the text. The pairs of circles, triangles, and squares demonstrate how the relative positions of points on opposite sides of the fault change as thrusting progresses.

Figure 4.2. The initial geotherms used for most of the models presented here. Initial Geotherm A has constant thermal gradient of 10.4 K/km between the surface and the base of the lithosphere (125 km) and no crustal radioactive heat. Initial Geotherm B is a steady-state geotherm calculated by superimposing radioactive heating at a rate of $3 \mu\text{W}/\text{m}^3$ in the upper 20 km

of the crust on the background gradient of 10.4 K/km used for Geotherm A. The background mantle flow is 31.2 mW/m² in both cases, but surface heat flow for Geotherm B is about 60 mW/m² compared to 31.2 mW/m² for Geotherm A.

Figure 4.3. Lateral and vertical thermal gradients, post-thrusting isotherms, and non-dimensional PT paths for 30 km of movement at 5 mm/yr along a thrust fault dipping at 45°. The duration of thrusting is 6 my, and the initial thermal structure is given by Geotherm B in Fig. 2. (a) Lateral (dT/dx) and vertical (dT/dz) thermal gradients immediately following the end of thrusting for cases of with and without lateral heat conduction, corresponding to two-dimensional and one-dimensional thermal models respectively. One-dimensional thermal models assume that dT/dx is much smaller than dT/dz and that lateral conduction can therefore be ignored. However, the ratio of dT/dx to dT/dz in the absence of lateral heat conduction exceeds 5 near the fault in this example. Including the effects of lateral heat conduction causes the ratio of dT/dx to dT/dz to drop to 0.5 near the fault. (b) Isotherms in the thrust zone immediately following the cessation of thrusting. (c) The non-dimensional depth-temperature paths of footwall rocks proximal to the fault (top) and far from the fault (bottom) during thrust emplacement and the subsequent period of erosional unroofing at 1 mm/yr. Non-dimensional depth-temperature plots allow the direct comparison of the thermal evolution of rocks at the same depth relative to the fault but which have undergone different amounts of burial due to their different horizontal positions. Footwall rocks proximal to the fault (top diagram) at horizontal distances of 0 (30 km of burial) and -15 km (15 km

of burial) are greatly affected by conduction from the warm base of the hanging wall block, and the rock at distance 0 heats much more than the rock at -15 km distance. Rocks far beneath the fault surface (bottom diagram) at the same horizontal positions heat almost exclusively by advection (passive burial to greater depths) during the thrusting interval and therefore have similar depth-temperature paths.

Figure 4.4. A comparison of results obtained with a one-dimensional instantaneous thrust model and a two-dimensional model with thrusting along a 45° fault at 1 mm/yr (dashed line) for 30 my and 5 mm/yr (dotted lines) for 6 my. (a) Geotherms for the one- and two-dimensional models following emplacement of 30 km of hanging wall material. Instantaneous emplacement in the one-dimensional case produces the sawtooth geotherm first discussed by *Oxburgh and Turcotte* [1974], while thrusting at 5 mm/yr (dotted line) for the two-dimensional case yields colder hanging wall temperatures and warmer footwall temperatures than the one-dimensional case. The slow thrusting case (1 mm/yr—dashed line) results in temperatures hotter than the instantaneous case throughout the lithosphere and particularly in the footwall. (b) The post-thrusting PT paths for rocks in the hanging wall and footwall blocks of the one- (solid lines) and two-dimensional (dotted lines) models for unroofing at 1 mm/yr. From the bottom of the plot to the top, the solid curves denote rocks 10 km below the fault (+10), 0.5 km below the fault (+0.5), 0.5 km above the fault (-0.5), and 10 km (-10) above the fault. The dotted curves correspond to rocks 10 and 0.5 km below the fault (+10 and +0.5) and 10 km above the fault (-10) and formerly buried by thrusting at 5 mm/yr.

Figure 4.5. PT and Tt paths for rocks at different structural levels in the thickening lithosphere demonstrate how thermal histories are affected by position of rocks relative to the fault surface.. These thermal histories result from 30 km of emplacement on a 45° fault at a rate of 2 mm/yr for 15 my followed by erosional unroofing at 1 mm/yr for 30 my. Initial thermal structure is given by Geotherm B of Fig. 2. (a) The solid lines denote the PT paths of footwall rocks 10 km (+10) and 0.5 km (+0.5) below the fault surface, and dashed lines mark the PT paths of hanging wall rocks 0.5 km (-0.5) and 10 km (-10) above the fault surface. Net heating at 10 km below the fault is significantly greater than heating just below the fault surface where conductive effects associated with the juxtaposition of the warm base of the hanging wall are most pronounced. Thus, the advective effects associated with burial beneath the hanging wall (primarily seen 10 km below the fault) heat these deep footwall rocks more efficiently than conduction heats the footwall rocks proximal to the fault surface. (b) The Tt paths for rocks 10 km and 0.5 km below (solid lines) and above (dashed lines) the fault surface. The dot marks the end of the thrusting interval and the onset of erosional unroofing. Note that most of the initial temperature difference between rocks just above and below the fault is taken up by heating of the footwall rock instead of cooling of the hanging wall rock.

Figure 4.6. PT and Tt paths for rocks carried from 9 to 30 km depth by pure shear thickening with $\beta=0.3$ (solid lines) and overthrusting (simple shear) of 21 km on a 45° fault at 1 mm/yr (dashed lines). Thickening lasts for 21 my in each case and is followed by erosional unroofing at 1 mm/yr for 30 my.

These results were generated using both Initial Geotherm A and B of Fig. 2 in order to separate the effects of tectonic mechanism from those associated with the evolution of complicated radioactive layer geometries during thickening. (a) For Initial Geotherm A, PT paths show isothermal compression for the pure shear case and the usual pattern of syntectonic heating for the simple shear case. Note that the morphology of the syntectonic and synerosional PT path for pure shear thickening with initial geotherm A has a sense opposite to all others presented here. With Initial Geotherm B, the pure shear and simple shear mechanisms produce similar PT paths, but thickening of the radioactive layer in the pure shear case causes greater net heating during both thrusting and unroofing. (b) Tt paths for the pure shear and simple shear cases. The dot marks the end of the compressional interval and the onset of erosional unroofing. With Initial Geotherm A, the pure shear path shows the effects of the isothermal compression phase evident in the PT path. When radioactive heating is added (Initial Geotherm B), the rock carried to greater depths by pure shear initially heats more slowly than the rock buried by simple overthrusting but the slope of the Tt curve increases rapidly after 5 my. Maximum temperatures are obtained simultaneously in the pure shear and simple shear cases generated with Initial Geotherm B since erosional unroofing, not mode of tectonism, exercises the dominant control over heating after the end of thrusting.

Figure 4.7. Synthrusting PT paths for a rock 0.5 km below thrust faults dipping at various angles and buried to a depth of 30 km by movement along the fault. To distinguish between the effects of fault geometry (fault dip) and those

associated with lateral disruption of the radioactive layer, both Initial Geotherms A and B were used to generate these plots. (a) PT paths for thrusting at a constant updip velocity of $2\sqrt{5}$ mm/yr along faults dipping at approximately 26° and 63° , corresponding to burial rates of 2 mm/yr and 4 mm/yr. For both Initial Geotherms A and B, a wide variation in fault angles produces little difference in the synthrusting PT paths. (b) PT paths with burial rate held constant at 2 mm/yr for faults dipping at 26° , 45° , and 63° . Previous workers have shown that burial rate, not fault dip, controls the morphology of PT paths in extensional terrains, and this plot indicates that geometry also has little effect on PT paths in compressional settings, both in the presence of radioactive heating (Initial Geotherm B) and in its absence (Initial Geotherm A).

Figure 4.8. PT and Tt paths for rocks 0.5 km below the fault and buried to a depth of 30 km by different rates of movement along a 45° thrust. These curves correspond to emplacement of a 30 km thrust sheet at burial rates of 1, 2, and 5 mm/yr (thrusting for 30, 15, and 7.5 my respectively) followed by unroofing at 1 mm/yr for 30 my. Initial thermal structure is given by Initial Geotherm B of Fig. 2. (a) PT paths for a footwall rock proximal to the fault zone show dependence on burial rate, but the net temperature difference is less than 100K at maximum depth. (b) Tt paths for the thrusting at different burial rates and subsequent erosion unroofing at 1 mm/yr. The form of the PT and Tt paths is exactly as would be predicted from the chain rule relation $dT/dP \cdot dP/dt = dT/dt$. The same amount of time elapses between the end of thrusting and the attainment of maximum temperature for each of the three cases.

Figure 4.9. Theoretical post-thrusting PT paths for a rock carried from 30 km to 3 km by uniform pure shear ($\beta=10$ throughout the lithosphere), modified pure shear ($\beta=10$ only in the 30-km-thick crust), erosional unroofing at 1 mm/yr, and normal faulting that yields a tectonic denudation rate of 1 mm/yr. The scale of both figures is the same to facilitate comparison. (a) With Initial Geotherm A, pure shear thinning produces nearly isothermal decompression, while simple shear (normal faulting) unroofing results in a nearly linear PT path. Erosion and modified pure shear, both one-dimensional mechanisms which primarily affect the crust on the time-scale of this test (27 my), yield nearly indistinguishable PT paths. (b) When radioactive heat is added (Initial Geotherm B), the pure shear path is isothermal only for the first few kilometers of thinning, although the overall morphology of the PT path resulting from unroofing by normal fault displacement remains unchanged. In addition, modified pure shear produces a path more clearly distinct from the erosional unroofing path than before due to the different effects of each mechanism on the configuration of the radioactive layer.

Figure 4.10. PT and Tt paths for thrusting at 2 mm/yr along a 45° fault followed by erosional unroofing at 1, 2, and 5 mm/yr, corresponding to erosional intervals spanning 30, 15, and 6 my. The synthrusting part of the PT path is not shown. (a) PT paths for rocks 10 km above the fault (-10) and 0.5 and 10 km (+0.5 and +10) below the fault for the three unroofing rates. Note that both the value of the maximum temperature attained during the rock's thermal history and the depth (time) at which that temperature is

reached depend completely on the rate of erosional unroofing. (b) Tt paths corresponding to the PT paths of part (a). Maximum temperatures are attained shortly after the end of thrusting for the shallowest rocks but not until significantly later for the deeper rocks.

Figure 4.11. Initial geotherms, footwall PT paths, and peak conditions for different initial thermal states related to variations in mantle heat flow. Thrusting lasts 15 my at a rate of 2 mm/yr along a 45° fault followed by unroofing at 1 mm/yr for 30 my. (a) The initial geotherms corresponding to different values of mantle heat flow. Initial Geotherm B (solid line) is the same as in Fig. 2 and corresponds to mantle flow of 31.2 mW/m². Initial Geotherms C (dotted line) and D (dashed line) are produced by the same radioactive heat structure used for Initial Geotherm B but now superimposed on background mantle flow of 45 and 60 mW/m² respectively. (b) PT paths for footwall rocks 0.5 km (solid lines) and 10 km (dashed lines) below the fault for the three initial thermal structures. At ten kilometers below the fault, higher mantle heat flow has a dramatic effect on the maximum temperatures attained during thrusting and unroofing. (c) Peak conditions (T_{MAX} and P_{TMAX}) as a function of post-thrusting structural distance from the fault. Negative structural distance denotes the hanging wall block, and positive structural distance the footwall block. Higher mantle heat flow produces no apparent temperature inversion (bottom plot), but does result in a pressure inversion (top plot) of up to 150 MPa at the position of the fault. T_{MAX} conditions differ only slightly from the initial geotherm, implying that, in this case, T_{MAX} may provide information about the lithosphere's prethrusting thermal state. The similarity of the curves for initial

geotherms C and D is partially a numerical effect associated with the coarse sampling interval used to extract P_{Tt} datapoints from the fine mesh of the thermal model. Boxed numbers on the P_{TMAX} curves give the times at which maximum metamorphic conditions are recorded. P_{TMAX} coincident with the lithostatic gradient implies attainment of T_{MAX} at the beginning of the thrusting interval at 0 my. Square symbols mark times for the P_{TMAX} curve corresponding to geotherm B and triangles denote times associated with geotherms C and D. At the bottom of the hanging wall, P_{TMAX} is frozen in at about 21 my after the onset of thrusting (6 my after the beginning of erosion) for Geotherm B but at 0 my for Geotherms C and D. Immediately below the fault at the top of the footwall, P_{TMAX} is recorded at 22 my for the hot initial geotherms but slightly earlier (~21.5 my) for Geotherm B.

Figure 4.12. Initial geotherms, PT paths, and peak conditions for different rates and distributions of radioactive heating. Thrusting occurs over the first 15 my at a rate of 2 mm/yr along a 45° fault and is followed by erosional unroofing at 1 mm/yr for 30 my. (a) Initial Geotherm B (solid line) is the same as in Fig. 2 and corresponds to radioactive heating at 3 $\mu\text{W}/\text{m}^3$ in the upper 20 km of the precompressional crust. Initial Geotherm E (short dashed line) has the same rate of radioactive heating but confined to the upper 10 km of the crust. Radioactive heating is 1.5 and 6 $\mu\text{W}/\text{m}^3$ in the upper 20 km of crust for Initial Geotherms F (dotted line) and G (long dashed line) respectively. (b) PT paths for footwall rocks 0.5 (solid lines) and 10 km (dotted lines) below the fault for different radioactive heat distributions. (c) Peak metamorphic conditions (T_{MAX} and P_{TMAX}) plotted as a function of

postthrusting structural distance from the fault. Negative distance denotes hanging wall block. Cool initial geotherms (E and F) produce TMAX and P_{TMAX} curves marked by a inversions of up to 50K and 150 MPa at the position of the fault. For these geotherms, TMAX differs little from the original geothermal gradient (40 km depth corresponds to structural distance of +10 km). With a hot initial geotherm (G), TMAX is between 50 and 100K greater than the initial geotherm in much of the crust, particularly in the footwall, and P_{TMAX} departs from the lithostatic gradient high in the hanging wall at a structural distance of -20 km from the fault. Times at which TMAX is attained are shown in the boxes on the P_{TMAX} curve, with diamond symbols marking times for Initial Geotherm G and circles denoting times for Initial Geotherms E and F. Times for Geotherm B are given in Fig. 11c. The lithostatic gradient corresponds to TMAX recorded at the onset of thrusting (0 my). Note that TMAX is attained between about 17 my (2 my after the cessation of thrusting and the onset of erosion) and 21.5 my at structural distances of -20 to 0 km when Initial Geotherm G is used, implying significant conductive heating of the hanging wall block due to high radioactivity at the top of the underthrust footwall block.

Figure 4.13. PT paths and peak conditions for shear heating proportional to lithostatic pressure and various frictional coefficients. Thrusting occurs over the first 15 my at a burial rate of 2 mm/yr along a 45° fault followed by unroofing at 1 mm/yr for 30 my. Shear heating occurs only during the phase of thrust emplacement, and the lithosphere's initial thermal state corresponds to Geotherm B. (a) The PT paths of rocks 0.5 km below the thrust fault for frictional coefficients μ of 0 (long dashed), 0.15 (dotted), 0.3 (solid), and

0.6 (short dashed). The addition of heat directly at the thrust fault causes rapid heating during the synthrust period. When shear heating stops, the rock immediately cools, producing a loop at the onset of erosion. (b) T_{MAX} and P_{TMAX} as a function of postthrusting structural distance from the fault. Negative distance denotes the hanging wall block, and numbers on the curves correspond to frictional coefficient. At the fault surface, a small inversion occurs in the T_{MAX} curve for the case of high frictional coefficient, but more significant inversions would develop if shear heating were distributed through a wider fault zone. The lithostatic gradient on the P_{TMAX} curve is denoted by the long dashed line, which corresponds to 0 frictional coefficient and curve B of Figs. 11c and 12c. For nonzero frictional coefficients, the P_{TMAX} curves are slightly sublithostatic in the hanging wall, and T_{MAX} is attained not at the onset of thrusting (0 my) but at the end of thrusting and associated shear heating (15 my). At structural distance of +10 (10 km below the fault), T_{MAX} conditions are reached at 24 my for $\mu=0$, 23.5 my for $\mu=0.15$, 22 my for $\mu=0.3$, and 16 my for $\mu=0.6$. High frictional coefficients lead to the synchronous attainment of T_{MAX} and the freezing in of the postthrusting geotherm. Just as in the tests of mantle heat flow and different amounts of radioactive heating, T_{MAX} is reached diachronously when heating occurs as a result of shear along a fault whose frictional coefficient is low. However, high mantle heat flow or low amounts of radioactive heating can produce a time step of over 20 my across the fault in our examples, whereas the maximum time step associated with low frictional coefficients in this plot is less than 8 my.

Figure 4.14. PT paths, post-thrusting geotherms, and TMAX and P_{TMAX} for the case of thrusting and erosion occurring with various degrees of simultaneity. Curves B, H, and J correspond to burial to unroofing rate ratios of 2:1. Case B is the same as above, with thrusting during the first 15 my followed by erosional unroofing during the next 30 my. For case H, thrusting occurs over the first 15 my, but erosional unroofing begins halfway through the thrusting interval. Case J corresponds to the simultaneous onset of thrusting and erosion at 0 my, with erosion continuing for 15 my after the end of the compressional event. Case K shows another example of simultaneous onset of thrusting (0-6my) and erosion (0 - 30my), this time with a ratio of burial to denudation rate of 5:1. (a) Simultaneous erosion and thrusting produce narrower PT loops and syn- and post-thrusting paths which are similar. These results imply that the sequential thrusting and erosion pattern used in most of the models presented here yields a PT path which bounds the range of all the PT paths produced by cases in which thrusting and erosion are simultaneous for even a few million years. (b) Post-thrusting geotherms for cases B (sequential thrusting and erosion) and J (simultaneous onset of thrusting and erosion). Simultaneous erosion and thrusting for case J causes the fault to be at a shallower depth following the end of compression. Note that, for these ratios of burial rate to unroofing rate, no inversion is present in the post-thrusting geotherm even when thrusting and erosion occur simultaneously. (c) TMAX and P_{TMAX} show that temperature inversion of up to 100K and a pressure inversion of nearly 300MPa should be preserved across the fault zone for small ratios of burial rate to unroofing rate and for the case of simultaneous onset of thrusting and erosion. Higher ratios (e.g., 5:1 for case K) of burial to unroofing rate

produces a temperature inversion of only 50K and a pressure inversion of 200MPa.

Figure 4.15. PT paths, post-thrusting geotherms, and TMAX for fast burial rates. Thrusting occurs along a 45° fault at burial rates of 5 (short dashed), 10 (dotted), 20 (long dashed), and 40 (solid) mm/yr, corresponding to compressional intervals of 6, 3, 1.5, and 0.75 my respectively. Erosional unroofing at 1 mm/yr begins immediately following thrusting and lasts for 30 my. (a) PT paths for footwall rocks 0.5 and 10 km below the thrust fault and buried an additional 30 km by emplacement of the hanging wall. Very rapid thrusting produces increasingly isothermal synthrusting PT paths. (b) Postthrusting geotherms for the rapid thrusting cases show a temperature inversion at the position of the fault. (c) TMAX as a function of structural distance (negative distance denotes hanging wall) for burial rates of 5 (dashed) and 40 (solid). Note that the TMAX curves do not resemble the postthrusting geotherms, and a maximum inversion of only 25K occurs for the fast thrusting case. An inversion of this magnitude is not significant given nominal uncertainties of $\pm 50\text{K}$ on thermometric data. Rapid conductive relaxation of the postthrusting thermal inversion leads to heating and metamorphic overprinting at the base of the footwall block, and the low temperatures are therefore not recorded by the rocks.

BOUNDARY CONDITIONS

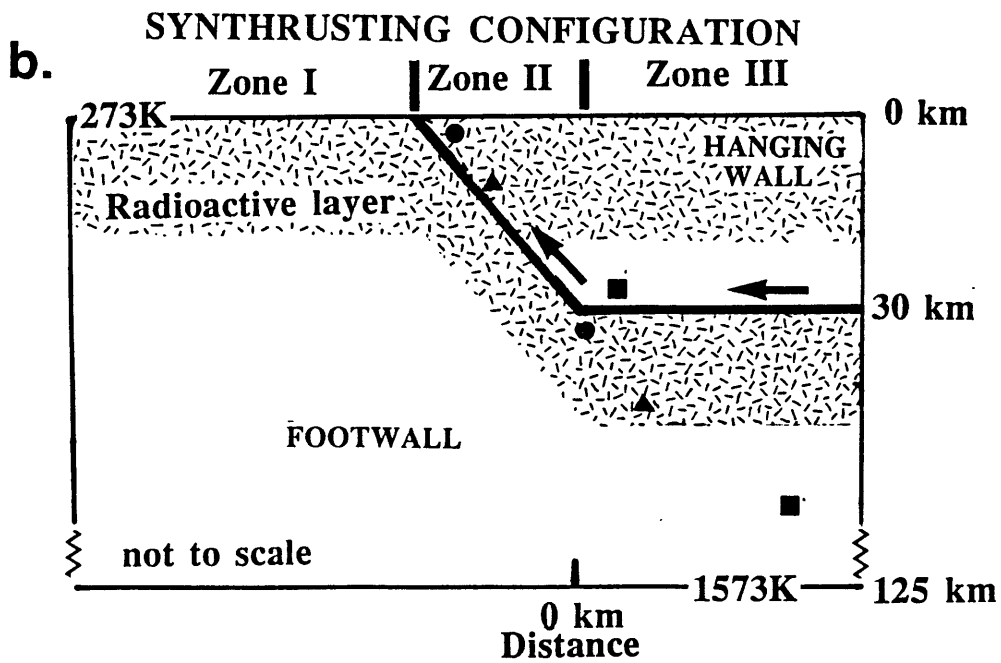
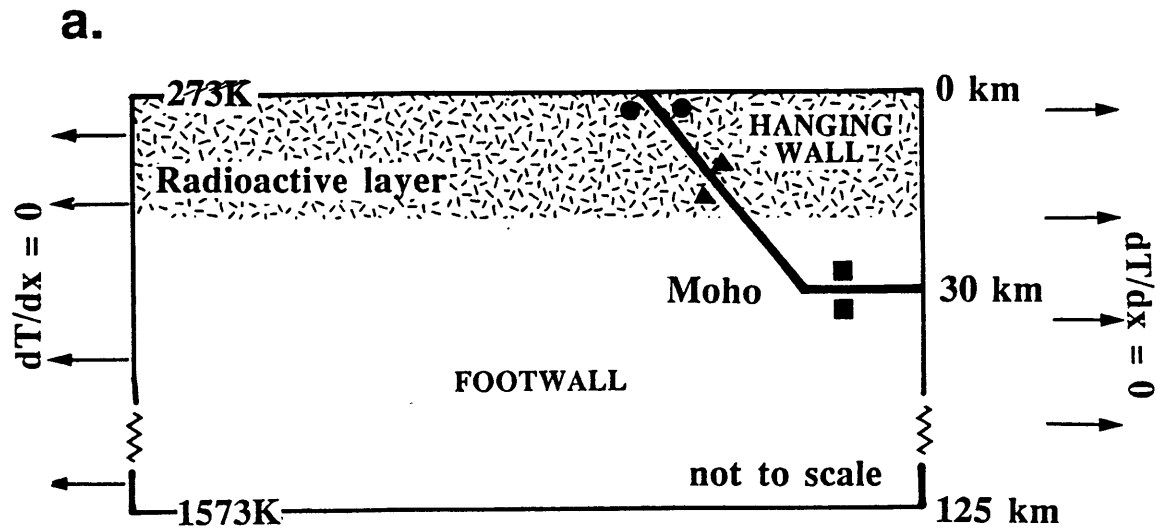


Figure 4.1

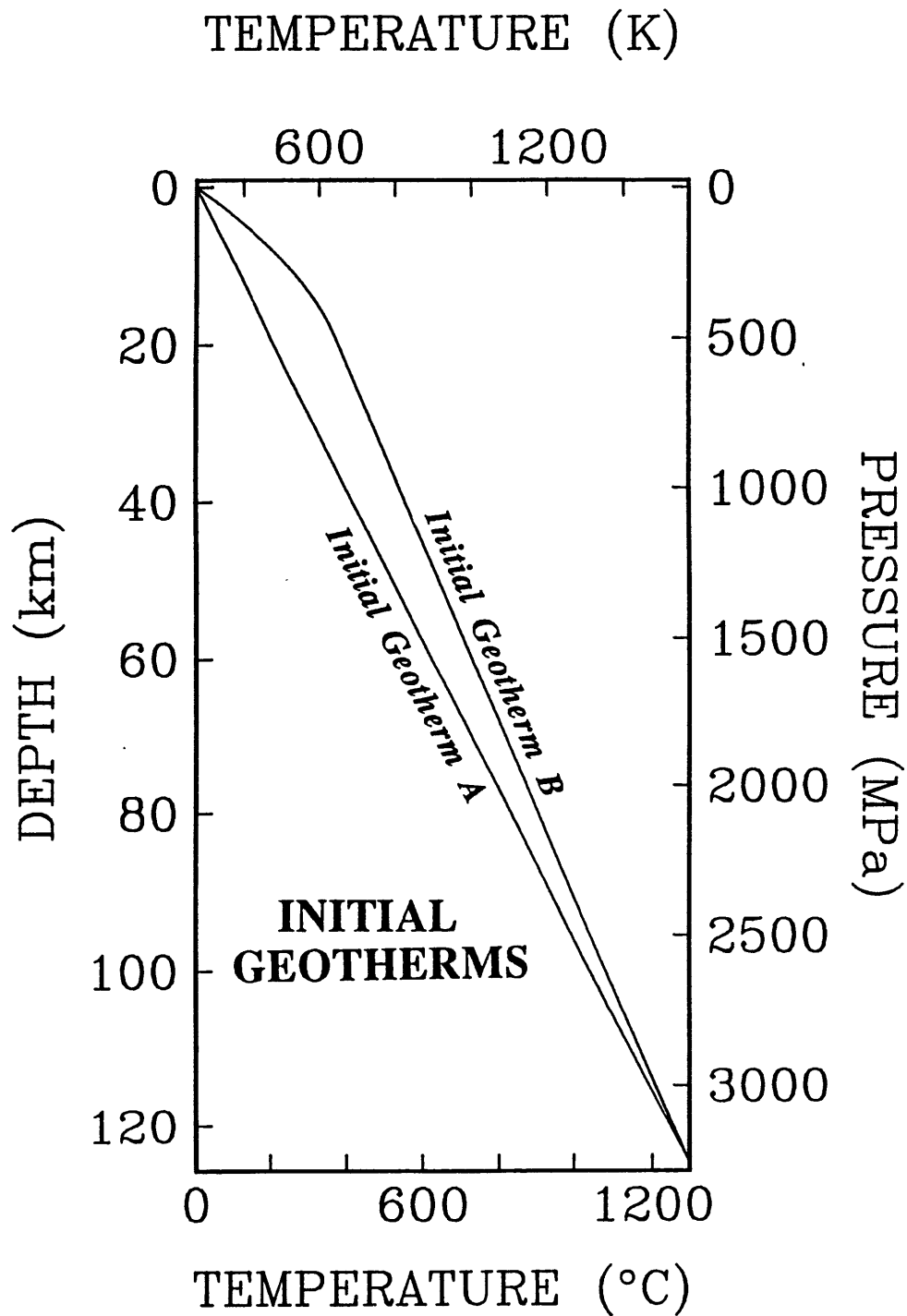


Figure 4.2

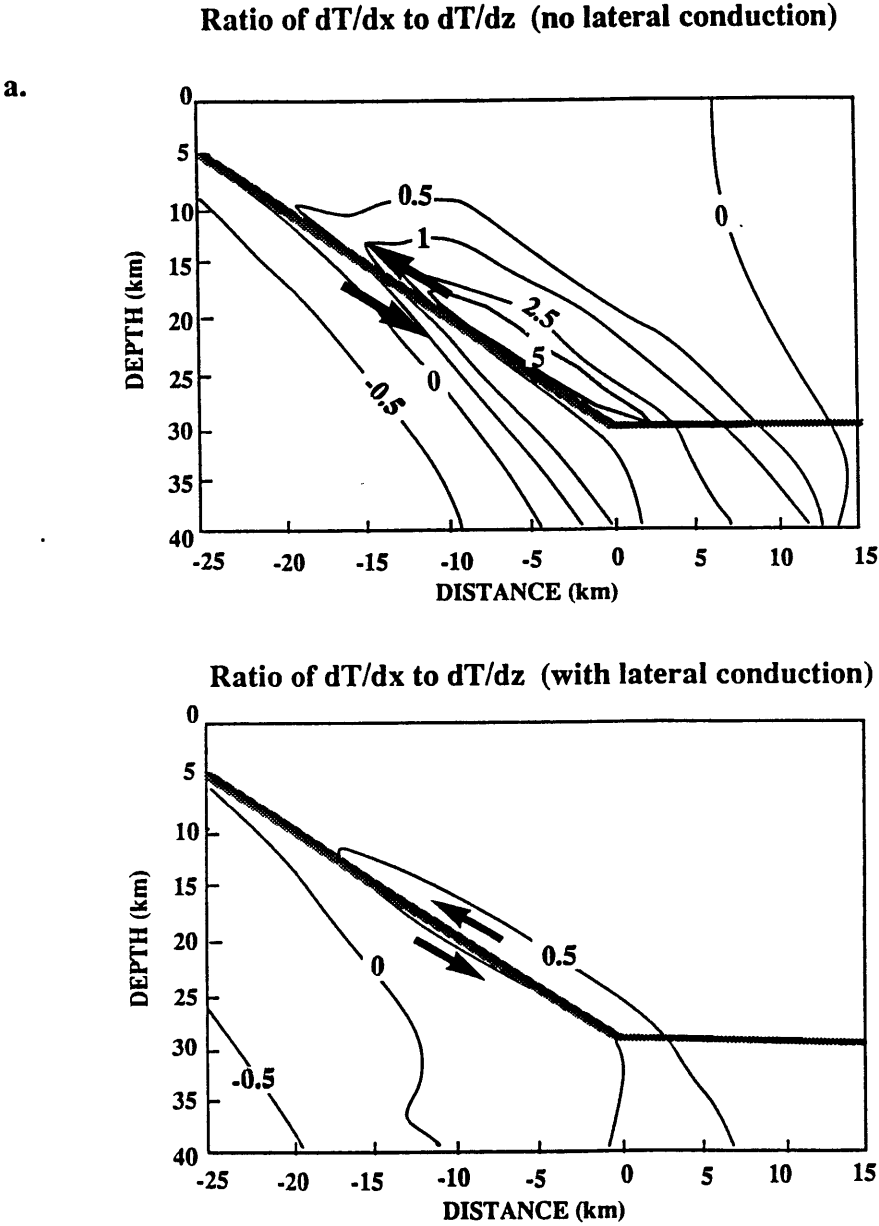


Figure 4.3a

B

POST-THRUSTING ISOTHERMS

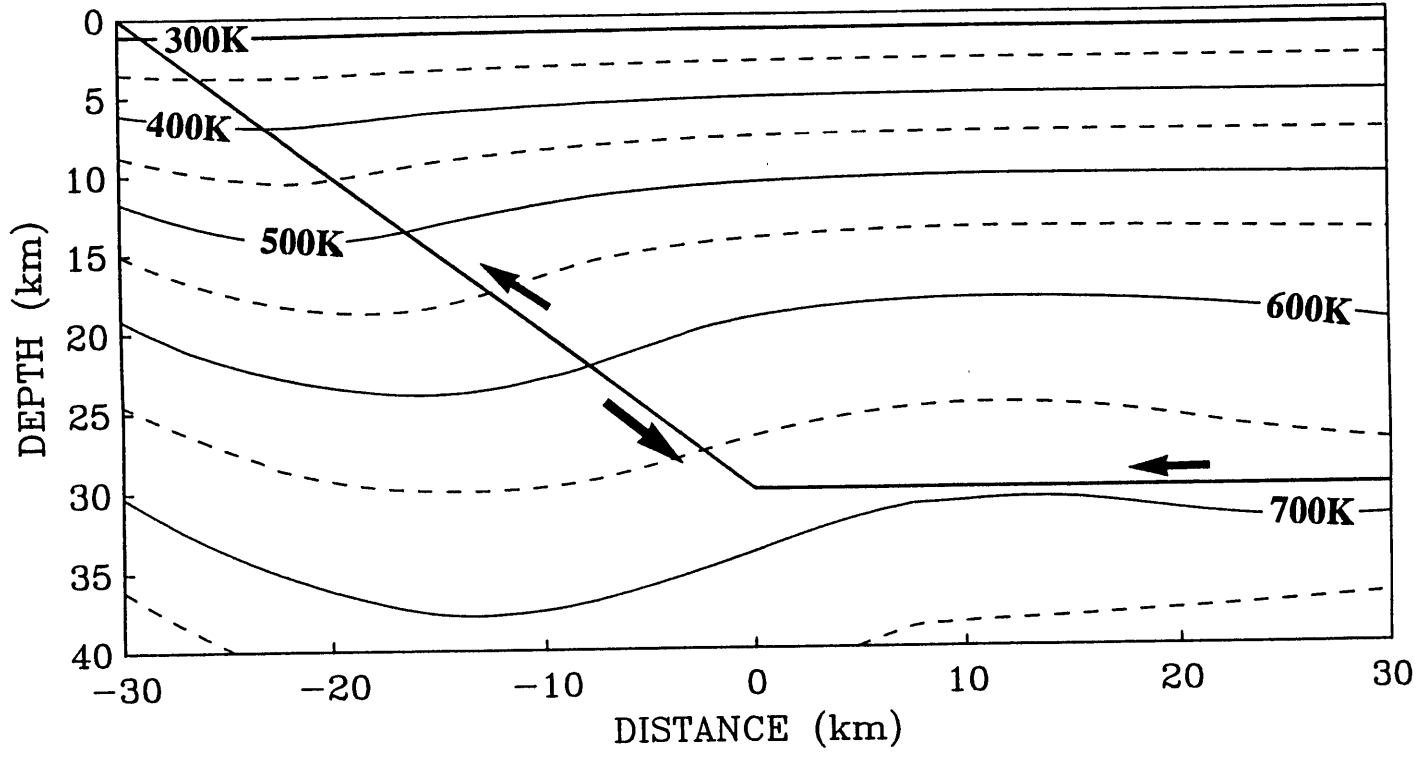


Figure 4.3b

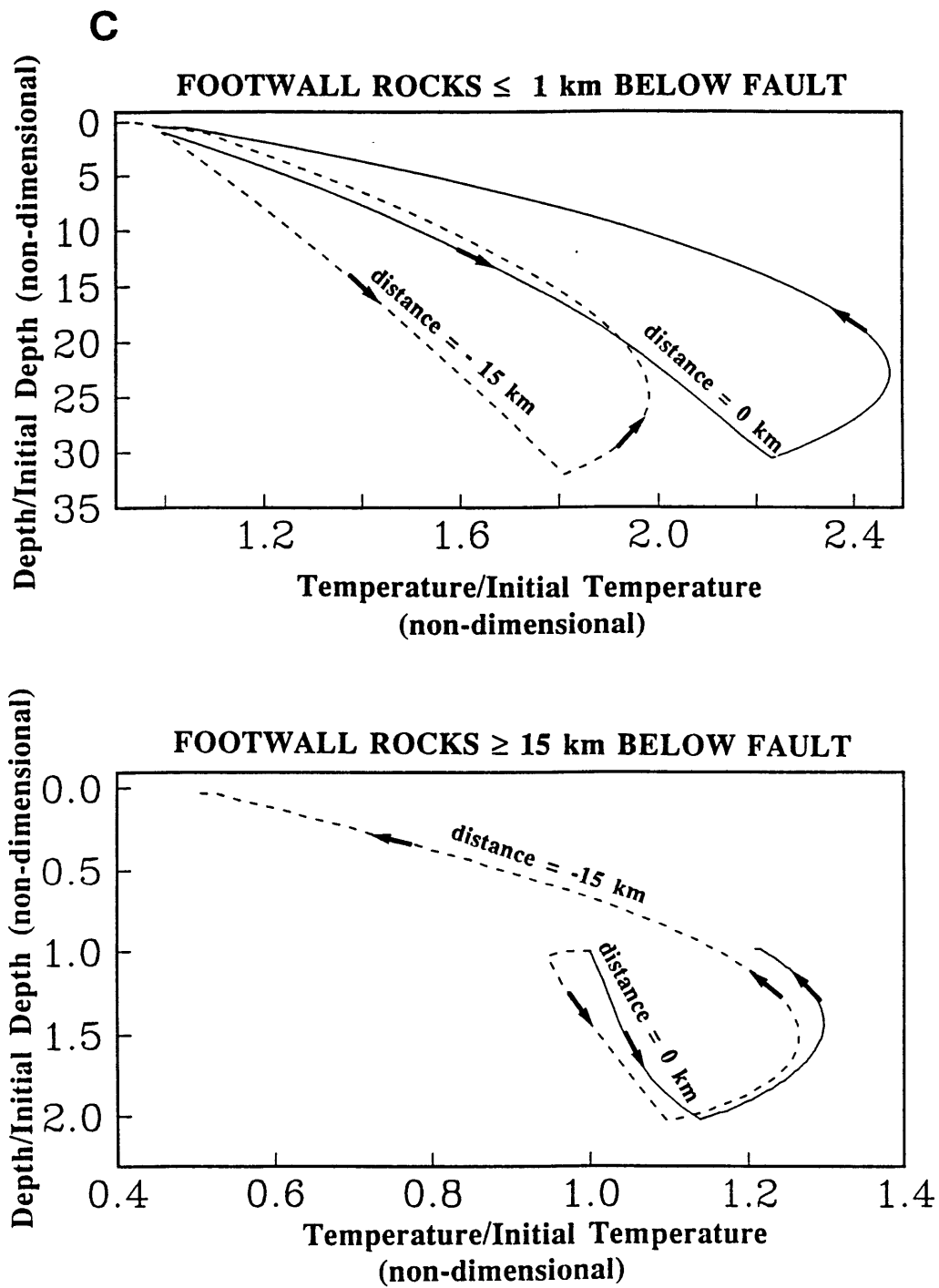
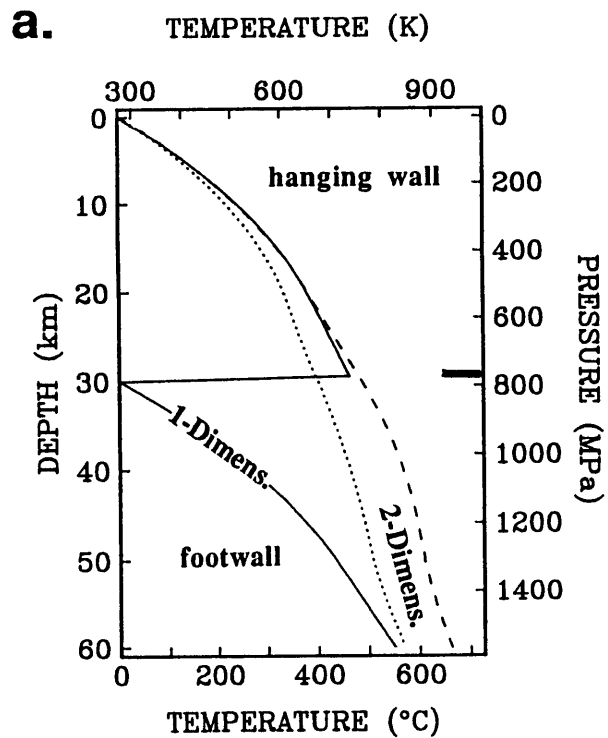


Figure 4.3c

POST-THRUSTING GEOTHERMS



P-T PATHS

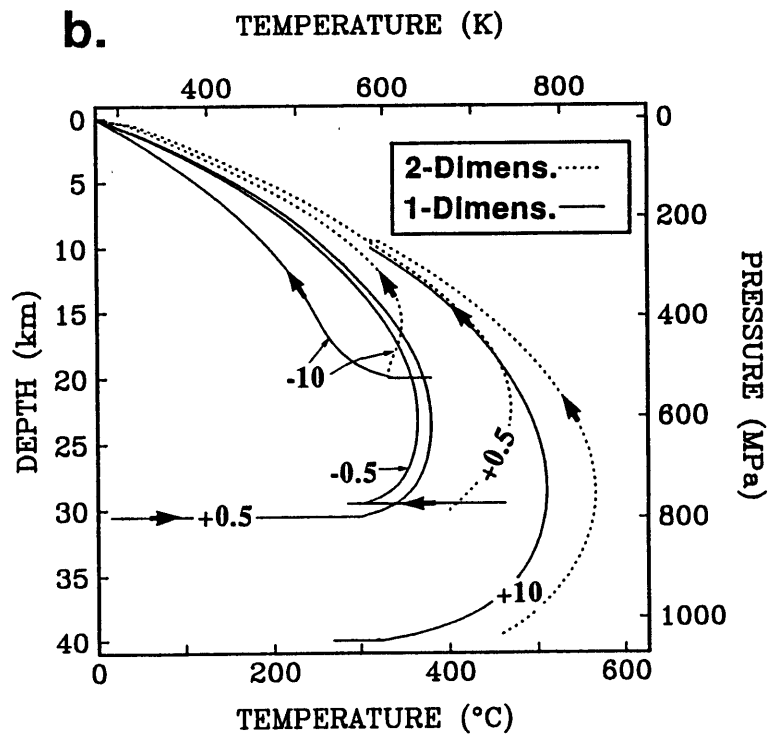


Figure 4.4

Figure 4.5

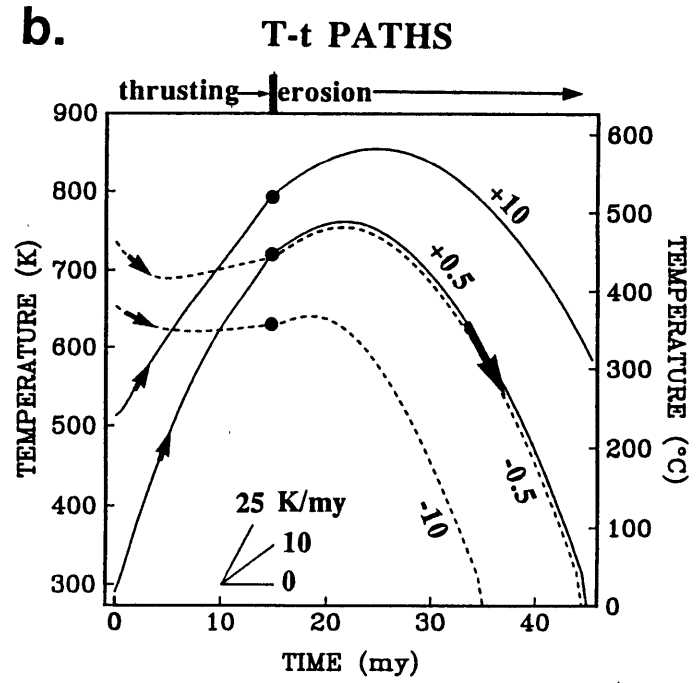
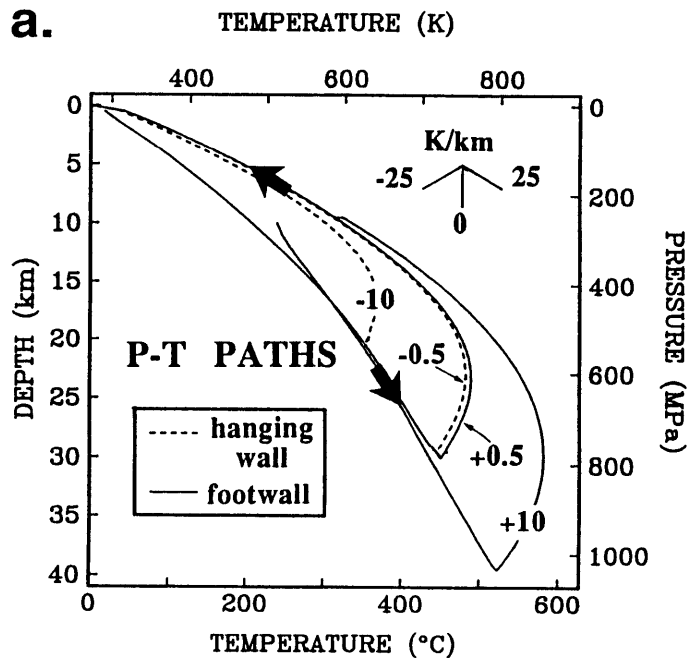


Figure 4.6

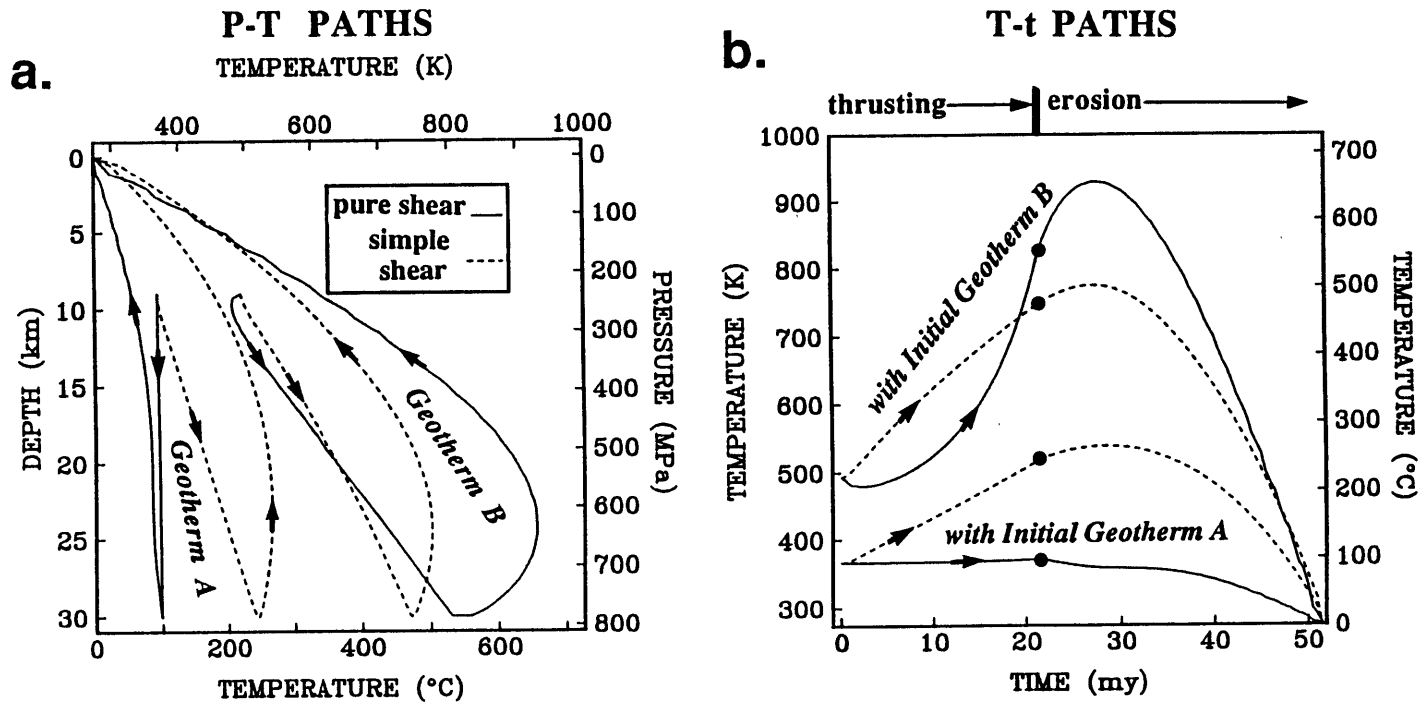


Figure 4.7

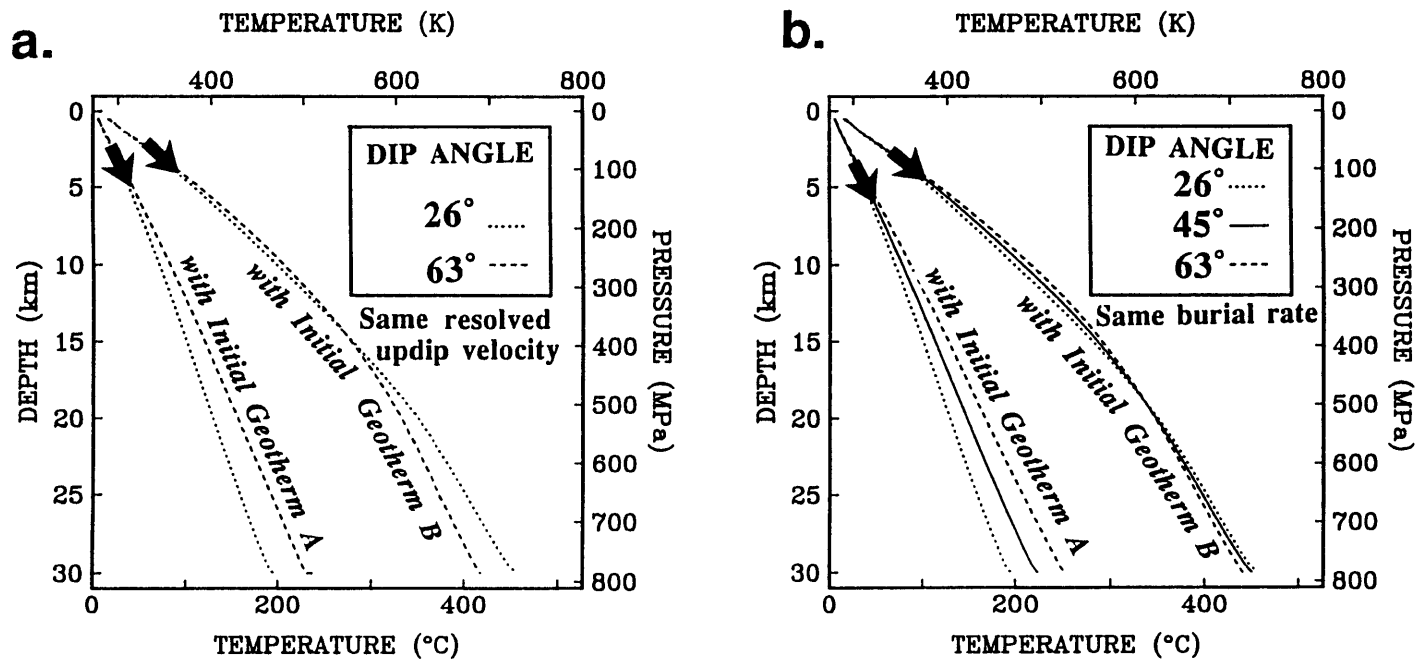


Figure 4.8

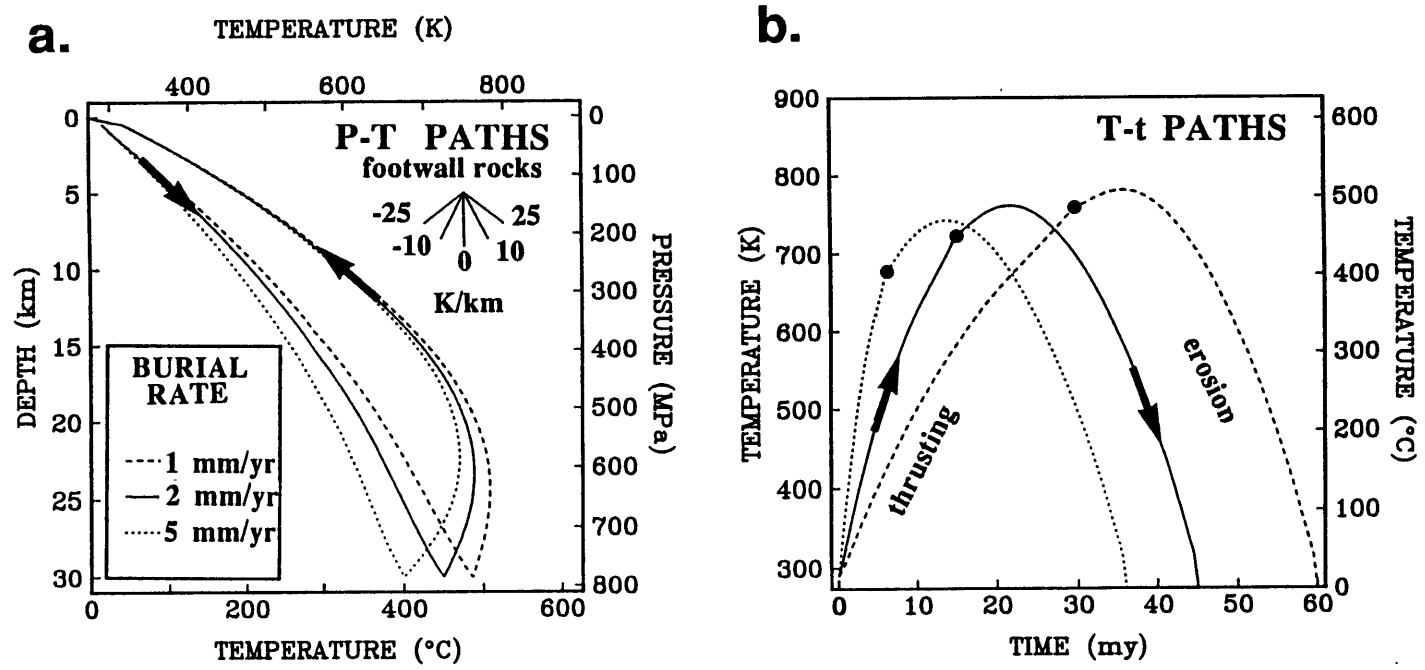


Figure 4.9

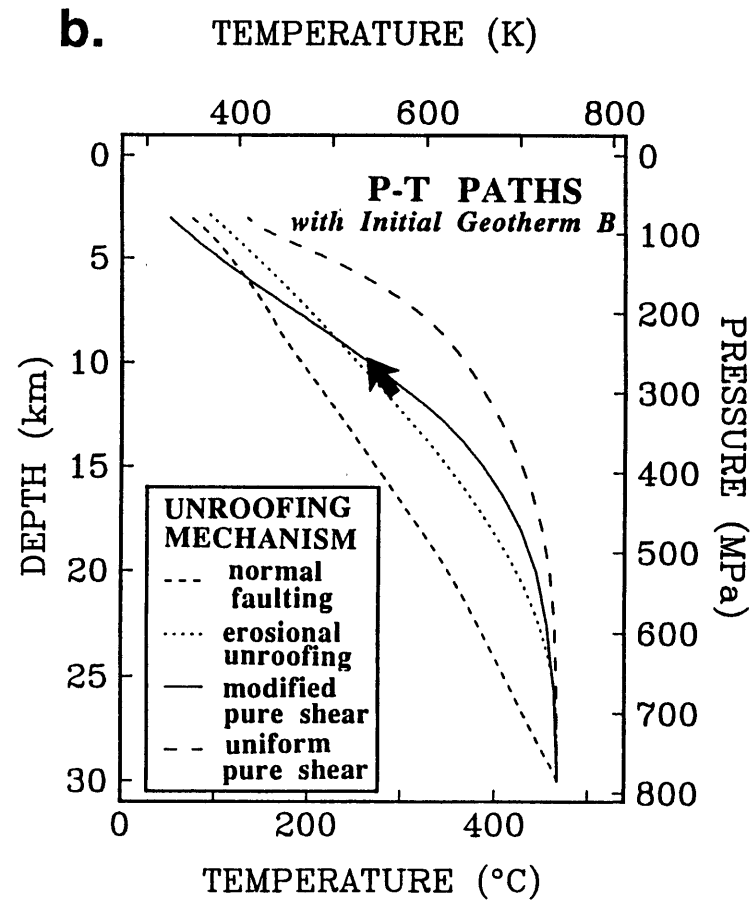
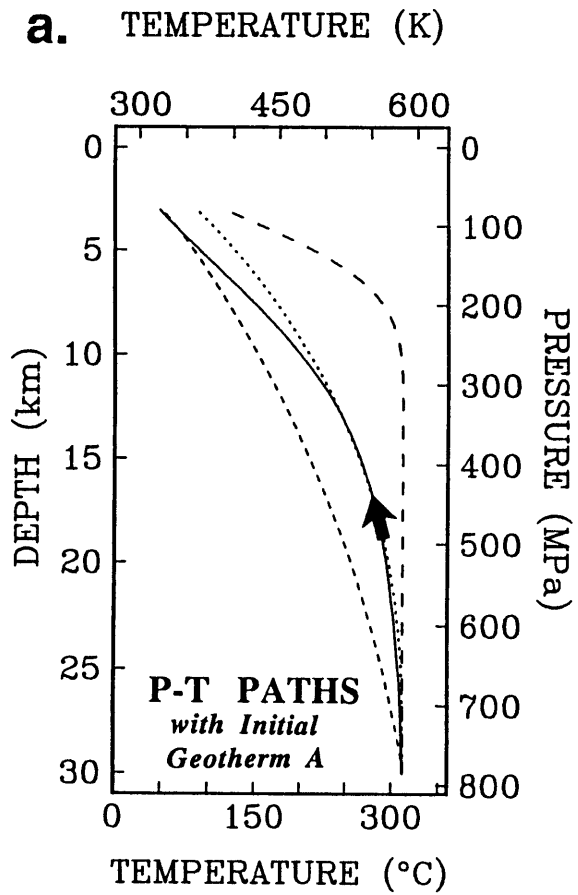
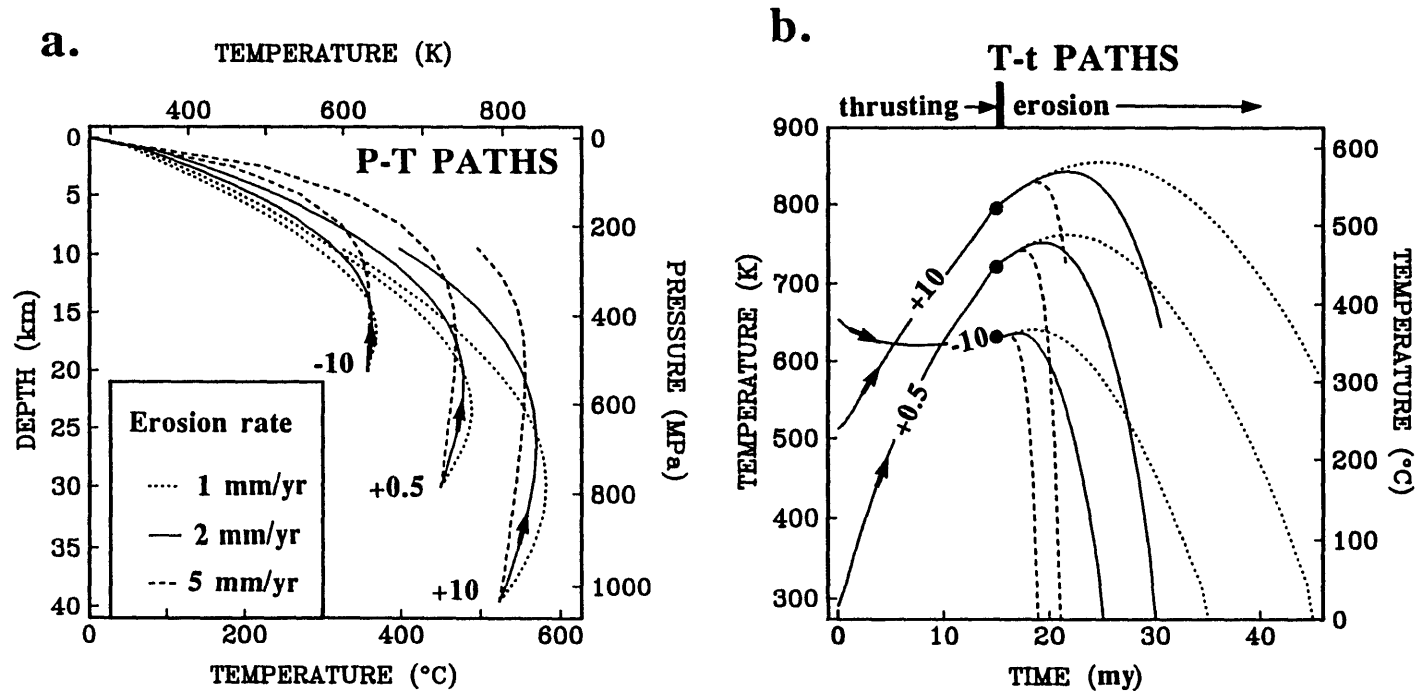
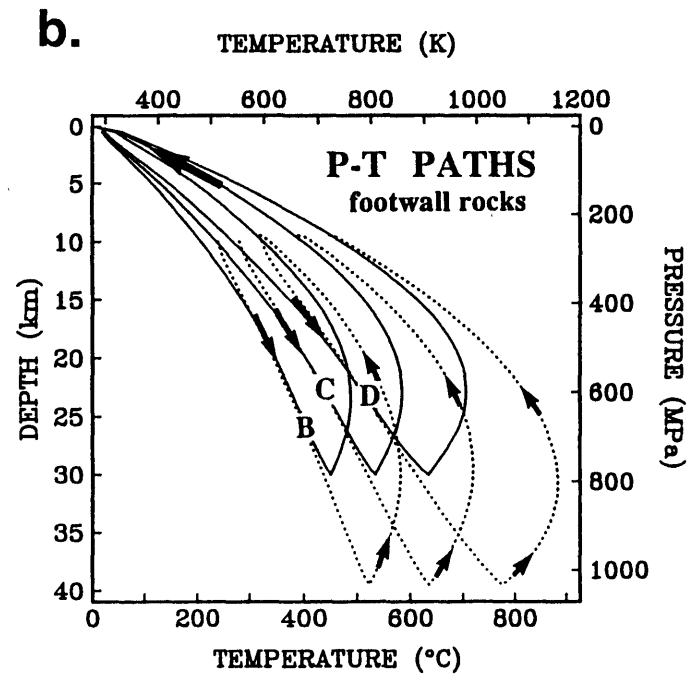
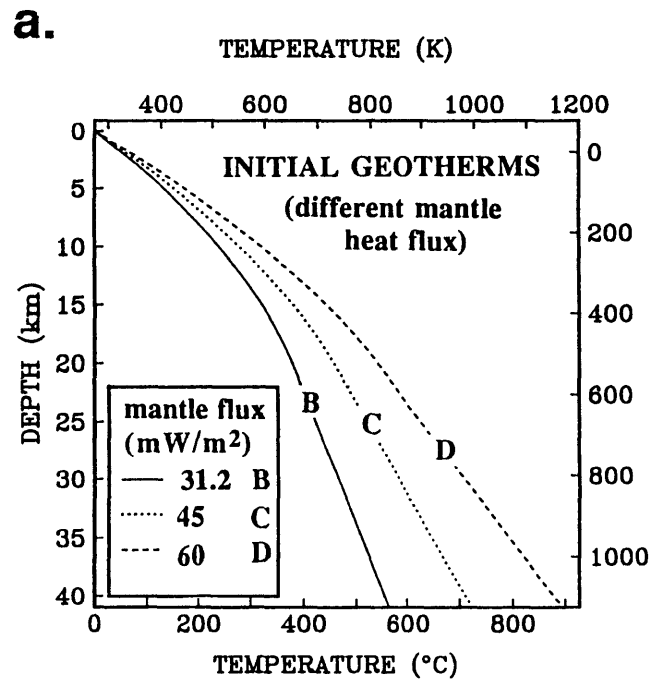


Figure 4.10



Figures 4.11a and 4.11b



c.

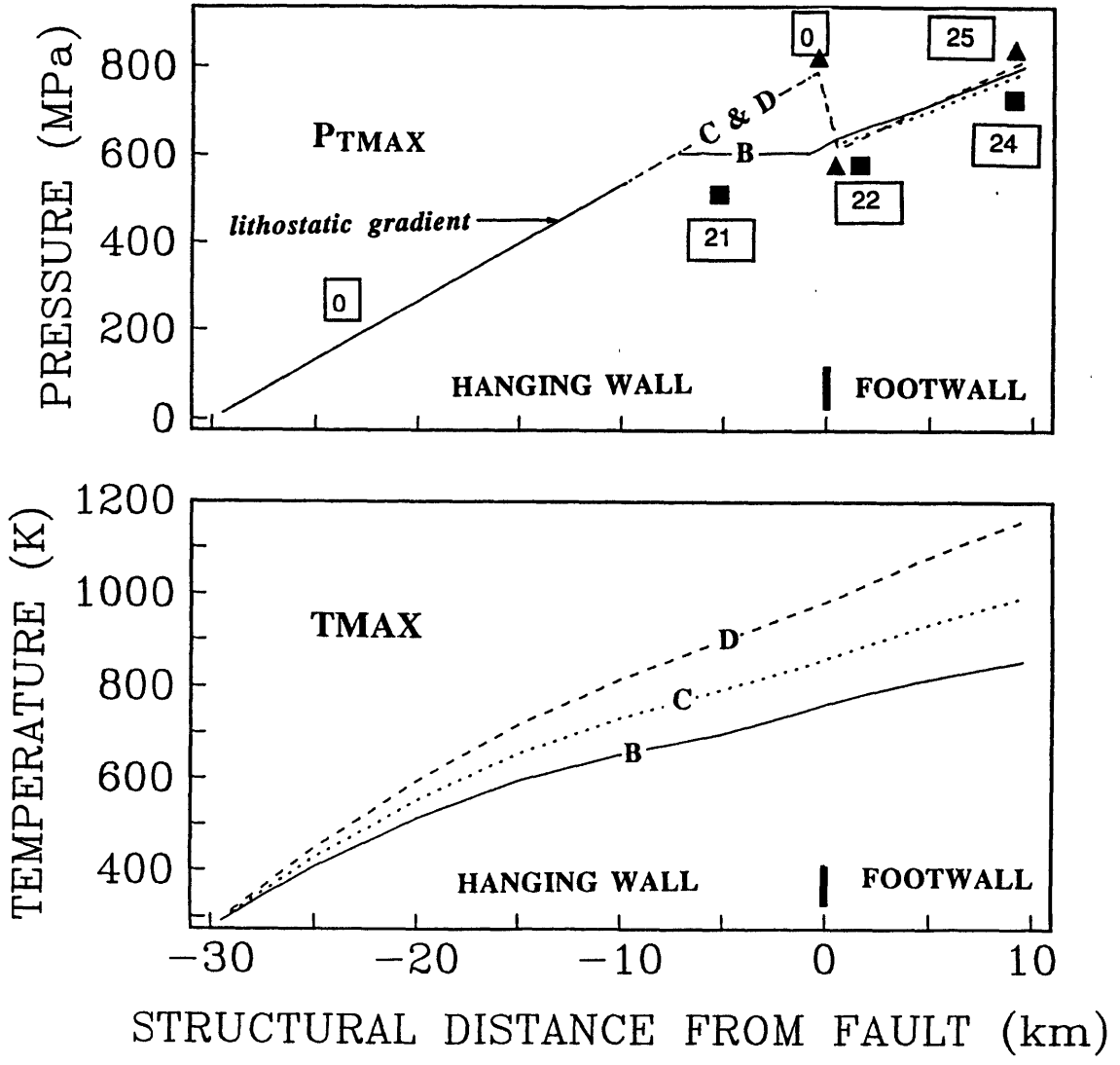
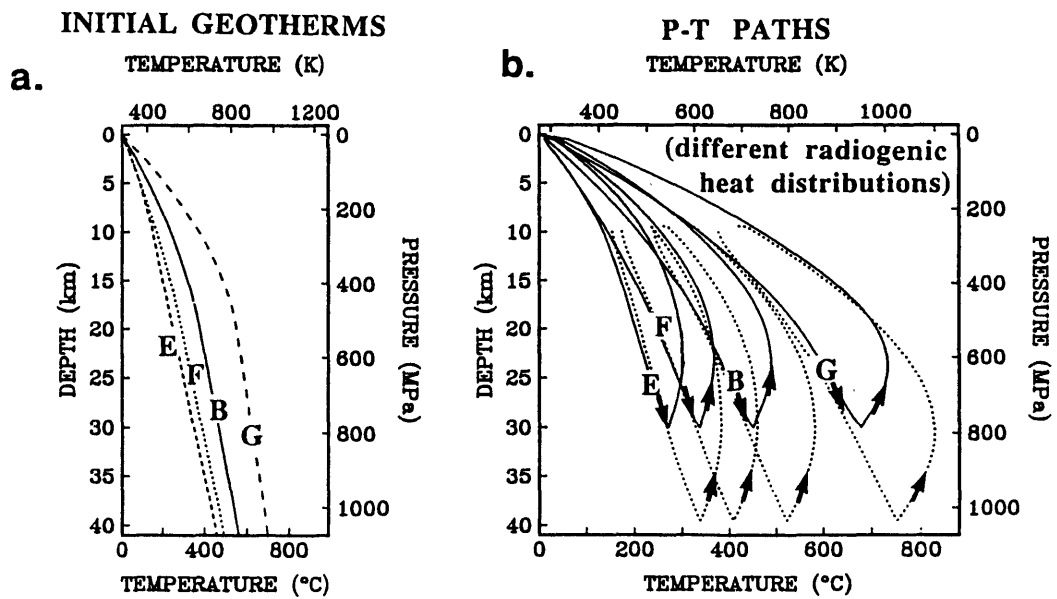


Figure 4.11c

Figures 4.12a and 4.12b



c.

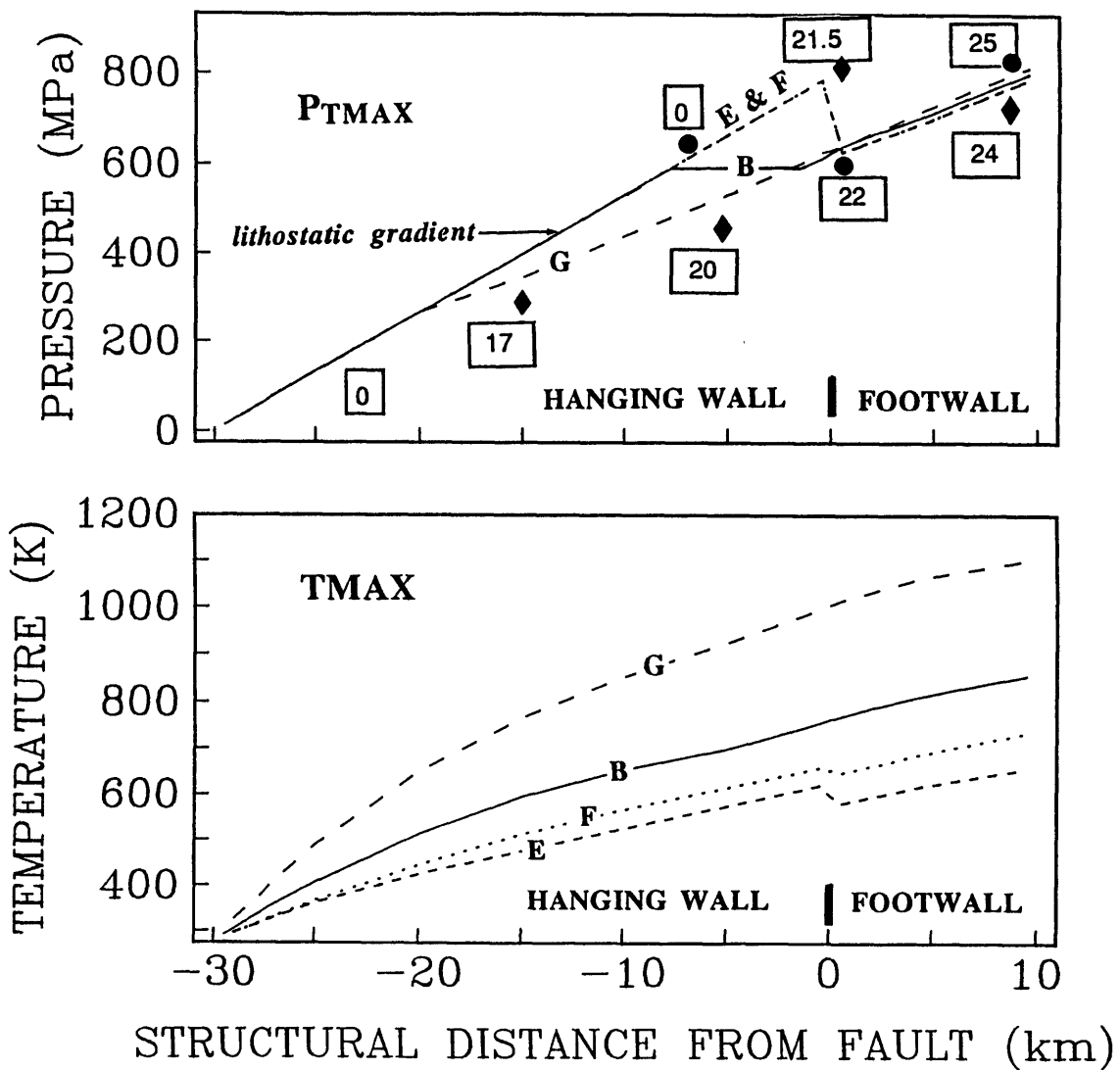


Figure 4.12c

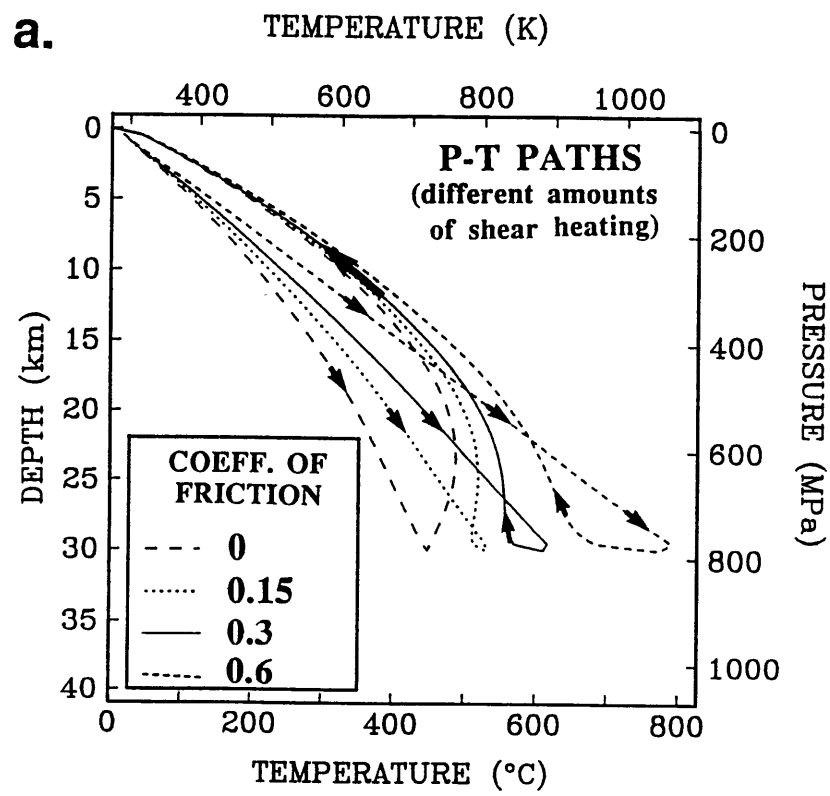
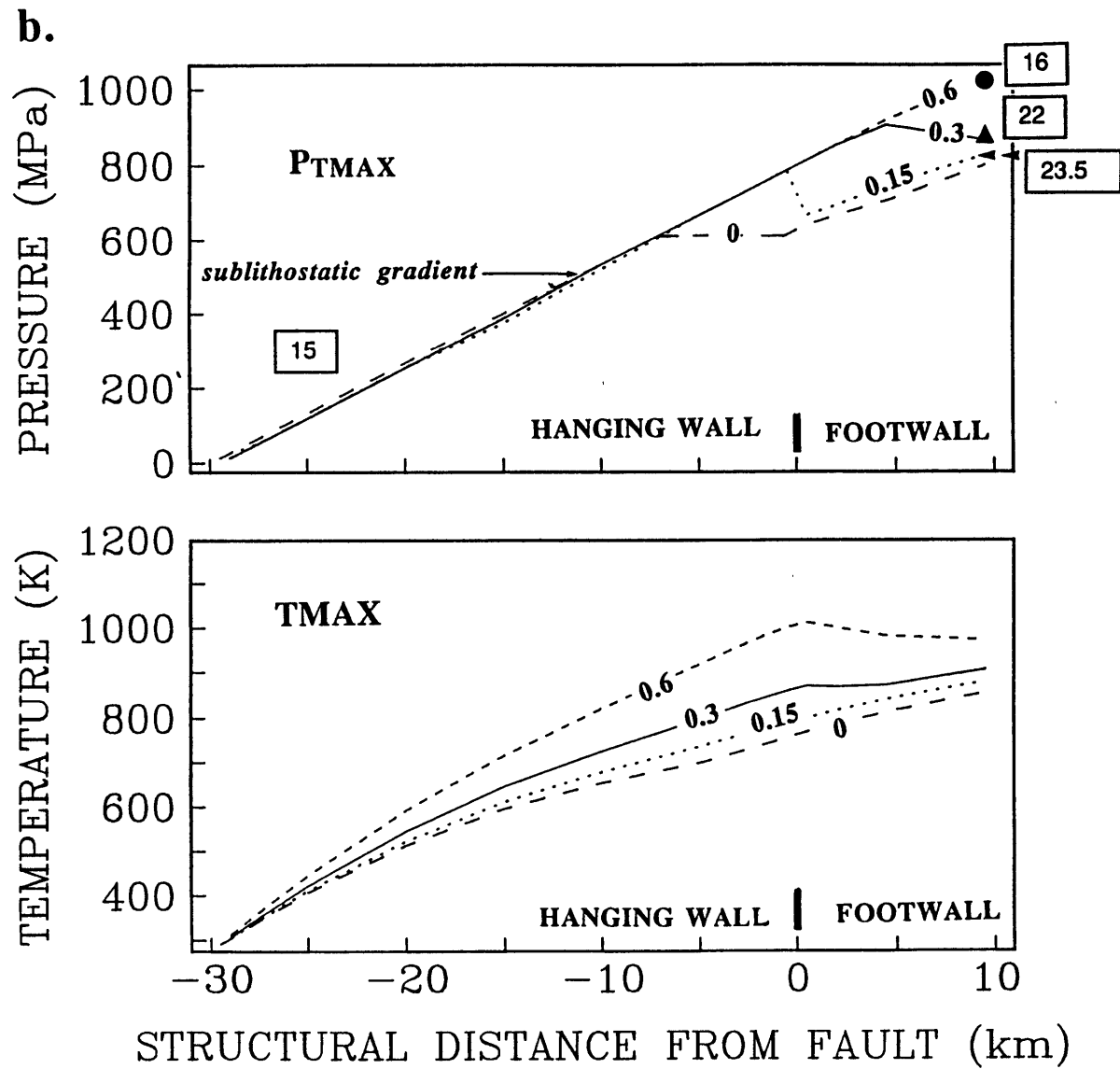
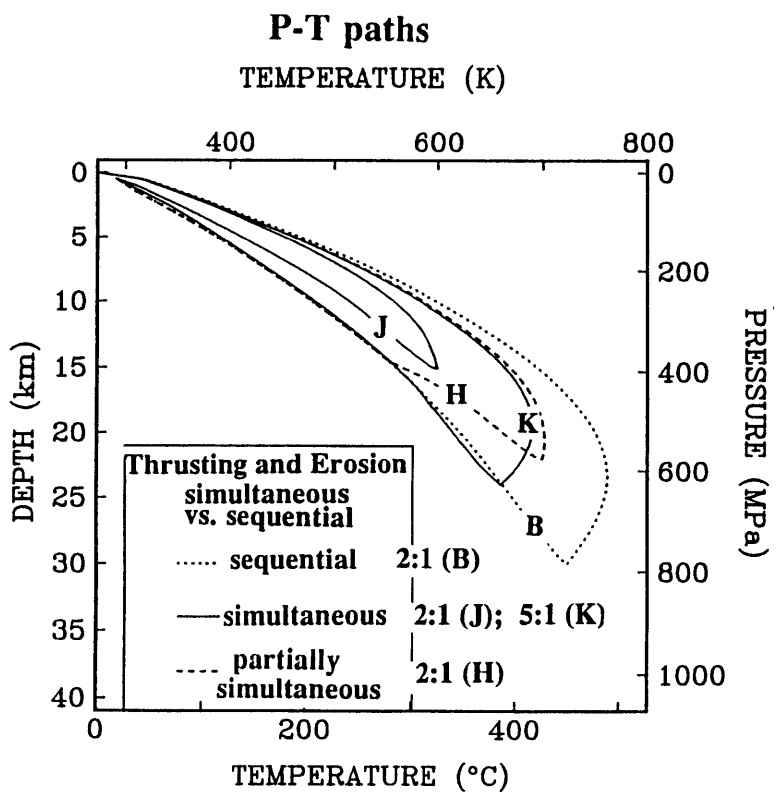


Figure 4.13a

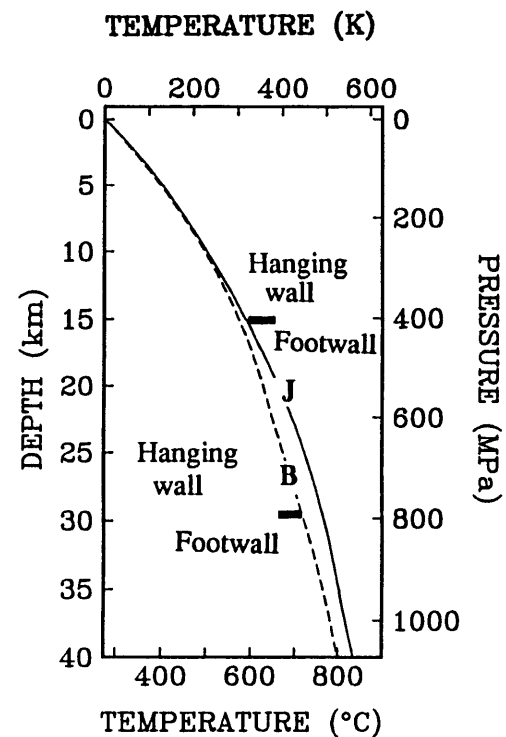
Figure 4.13b



Figures 4.14a and 4.14b



Geotherms immediately post-thrusting



C

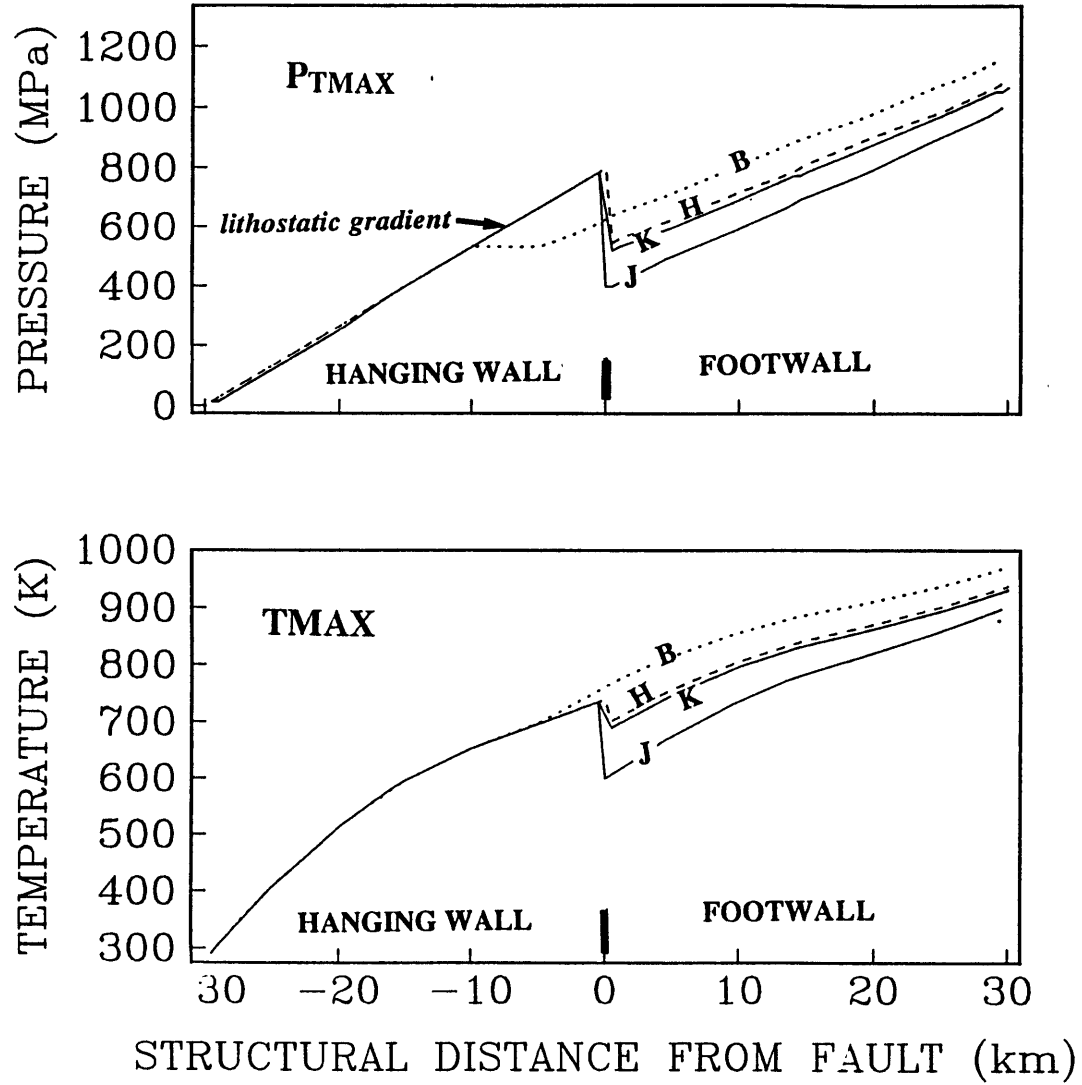
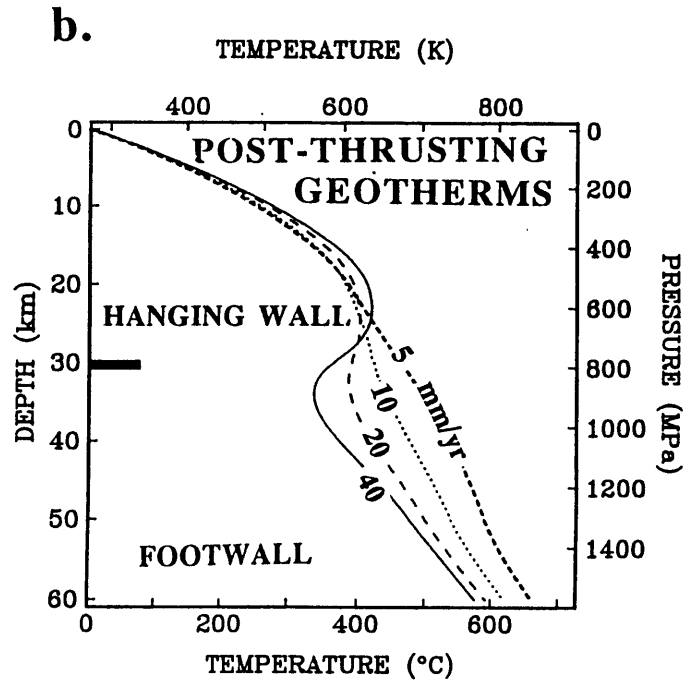
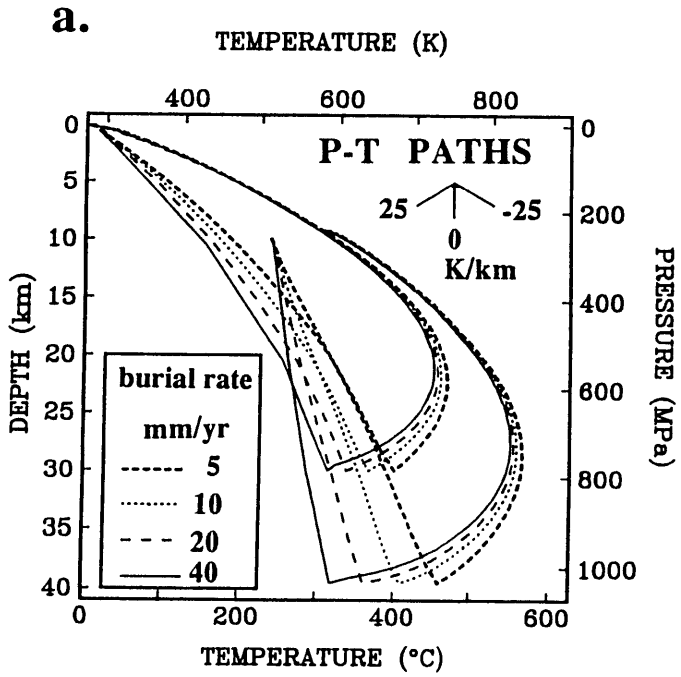


Figure 4.14c

Figures 4.15a and 4.15b



c

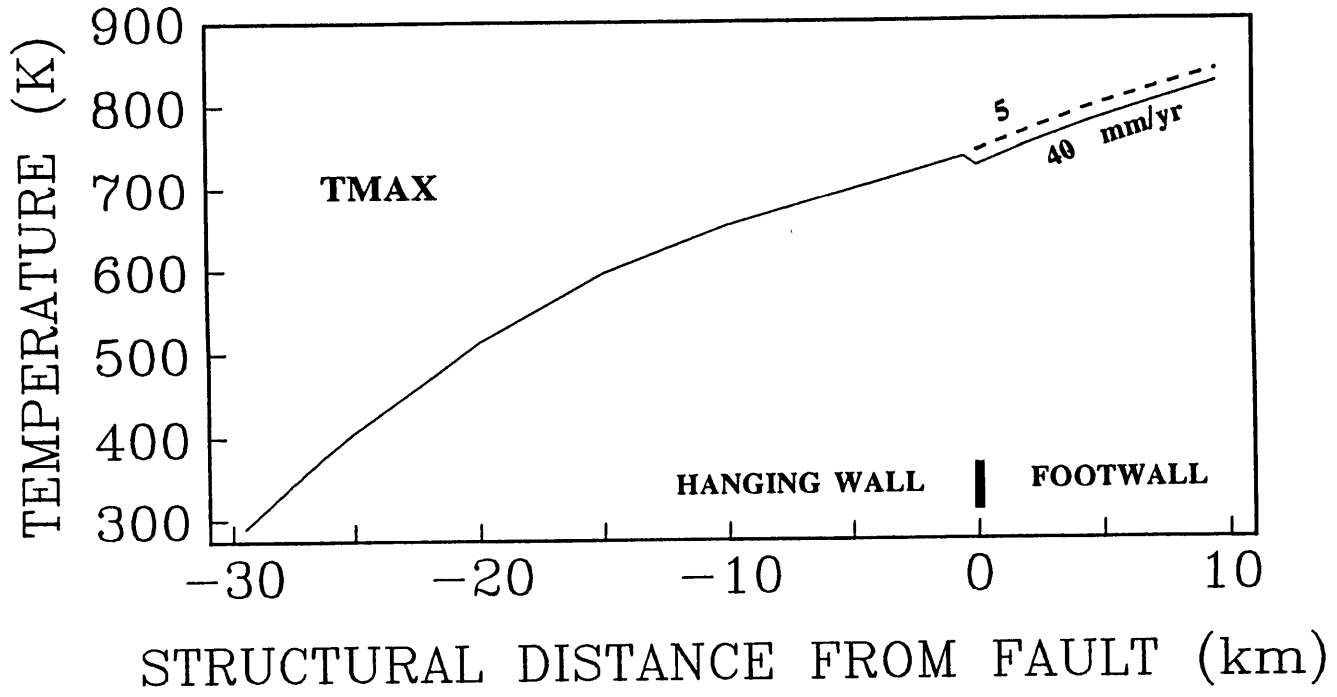


Figure 4.15c

Chapter 5

Thermal modeling of extensional tectonics: Application to pressure-temperature-time histories of metamorphic rocks

INTRODUCTION

In recent years, much attention has been focused on the processes and structures associated with extension of the continental lithosphere. Controversy over the nature of crustal thinning in highly extended terranes has led to the emergence of two major theories. The first theory, referred to as the simple shear model, proposes that extreme thinning of the crust occurs by normal displacement along master detachment surfaces or a series of imbricate surfaces [Wernicke, 1981, 1985]. During displacement of the hanging wall, footwall rocks from progressively deeper crustal levels are exposed. An alternate theory, the pure shear model, explains extreme continental extension as the result of penetrative ductile stretching of the lithosphere [Hamilton and Myers, 1966; Stewart, 1971]. Pure shear of the lithosphere does not result directly in the unroofing of deeply buried rocks but instead causes rocks at intermediate and deep crustal levels to be brought nearer the surface by stretching of the entire lithospheric column. (The terms pure shear and simple shear are used in this paper in the sense of Wernicke [1985] and do not have any rock mechanical connotations.) These two extensional models, illustrated in Figure 5.1, represent end-members of the full range of mechanisms proposed to explain large-scale extension; several workers (*e.g.*, Miller *et al.* [1983]; Gans [1987]) have proposed intermediate extensional mechanisms that combine brittle deformation or large-scale faulting in the upper crust with ductile deformation in the lower crust and lithosphere.

Distinguishing between the proposed extensional mechanisms requires not only the analysis of available structural and geophysical data but also an understanding of the theoretical thermal and mechanical effects of thinning the lithosphere. *Zuber et al.* [1986] used a strength-stratified lithospheric model in attempting to establish theoretical constraints for the type of extensional deformation observed in the Basin and Range. *Furlong and Londe* [1986] use theoretical one-dimensional models for the thermal and mechanical effects of pure shear and simple shear extension in the Basin and Range to argue that both extensional mechanisms predict the general features of the observed gravity, heat flow, and topography data. Recent work by *Buck et al.* [1988] has shown, however, that simple shear and pure shear extension produce distinct heat flow and topography signatures and that observations in the Red Sea area are most consistent with thinning of the lithosphere by pure shear over a zone that has narrowed since the initial rifting event.

Although geophysical observations have not proved particularly diagnostic of the regional extensional mechanism, the study of the local thermal evolution of individual rocks during extension may be important in understanding the effects of pure shear and simple shear. Recent advances in metamorphic petrology and thermochronology have provided a new means of reconstructing the pressure-temperature-time (PTt) evolution of rocks from metamorphic terranes (*e.g.*, *Spear et al.* [1984]; *Thompson and England* [1984]). If simple shear and pure shear of the lithosphere produce distinctive thermal and uplift histories, it may be possible to use PTt data generated for metamorphic rocks that occur in such extensional settings as the metamorphic core complexes of the North American Cordillera [*Coney*, 1979; *Armstrong*, 1982] to constrain the relative importance of the two extensional mechanisms. One of the primary goals of this study is to understand how variations in extensional parameters and styles affect the PTt paths of metamorphic rocks unroofed or uplifted from intermediate and deep crustal levels.

METHODS AND MODELS

Modeling the thermal evolution of the extending lithosphere requires solving the heat flow equation for temperature structure as a function of position and time. Lithospheric extension via simple shear is most properly modeled as a two-dimensional problem with mass movement and heat flow in both the horizontal and vertical directions. Figure 5.2 illustrates the model geometry of lithosphere extending via the simple shear mechanism. The physical system involved in simple shear of the lithosphere is modeled here by extracting the footwall block from beneath the hanging wall block at a constant rate throughout the extensional period and requiring the unroofed detachment to remain at $z=0$. Although material is transported both vertically and horizontally along the fault surface, the horizontal thermal gradients are generally much smaller than the vertical thermal gradients, and we found that, in most cases, temperatures in the models that ignore horizontal conduction of heat are within a few percent of those generated by the full two-dimensional models following several million years of relaxation. Nevertheless, the simple shear models presented below are full two-dimensional solutions to the heat flow equation. For the case of laterally homogeneous stretching of the lithosphere described by the pure shear mechanism, one- and two-dimensional solutions produce the same results because no lateral thermal gradients are created by the extensional process.

We use standard one- and two-dimensional explicit discretization of the conductive heat flow equation [Carslaw and Jaeger, 1959] with added heat production terms. The magnitudes of time and distance steps in the finite difference grid were chosen as 1250 years and 500 m for most simple shear cases and 10^4 years and 1000 m for the pure shear models in accordance with mathematical constraints on the stability of the system. This fine spacing of grid points eliminates the possibility that significant inaccuracies can develop where $\partial^2 T / \partial z^2$ is large due to temperature discontinuities at the detachment surface.

The angles of dip of the faults used in the simple shear cases were chosen such that the fault passed exactly through a grid point at every 500-m depth increment. Most of the runs were done using a fault whose dip angle has an integral cotangent of 6, corresponding to a dip of 9.5°.

We model the lithosphere as a homogeneous slab with uniform initial thickness (125 km), uniform diffusivity ($10^{-6} \text{ m}^2/\text{sec}$) and conductivity ($3.12 \text{ W/m}^\circ\text{C}$), and a laterally invariant initial geotherm. Radiogenic heat production was assumed to be $1.5 \mu\text{W/m}^3$ in the upper 10 km of the crust and zero elsewhere. Boundary conditions are constant temperatures of 0°C at the surface and 1300°C at the base of the lithosphere (125 km). For the two-dimensional models we impose additional constraints of zero horizontal heat flux at the sides of the grid. The position of the sides of the grid were chosen to be sufficiently far from the breakaway zone that the temperature structure in the extending region was not affected by the zero heat flux boundary conditions at the sides.

Two initial temperature structures were used. The first is given by:

$$T=T_m \left[\frac{1-e^{-Cz/L}}{1-e^{-C}} \right] \quad (5.1),$$

which satisfies the boundary conditions of $T=T_m$ at $z=L$ (base of lithosphere) and $T=0$ at $z=0$ (surface). Temperatures of approximately 500°C and pressures equivalent to 30 km depth are often observed together in metamorphic terranes, and we solved for $C \approx 1.5$ to fit this constraint. This geotherm is termed the perturbed initial geotherm and is shown in Figure 5.3. In order to determine the dependence of PTt paths on the choice of an initial geotherm we also present one model in which the initial geotherm is equal to the background equilibrium geotherm or steady state geotherm defined by maintaining a constant temperature of 0°C and 1300°C at the top and bottom of the lithosphere and a radiogenic heat production rate of $1.5 \mu\text{W/m}^3$ in the upper 10 km of the lithosphere. We

ignore frictional heating along the fault as a possible source of thermal perturbations in the extending lithosphere.

Extension via pure shear and simple shear affect the distribution and magnitude of heat sources in different ways. Simple shear of the lithosphere does not change the magnitude of the heat sources but causes the distribution to be disturbed by the downdip movement of the hanging wall (or updip movement of the footwall). On the other hand, pure shear extension by a factor β thins a lithospheric slab of thickness z with heat production A to thickness z/β and reduces heat production to A/β in a vertical column. Because the time scale of extension and subsequent thermal relaxation is much shorter than the half-lives of important radiogenic isotopes, we ignore the decrease in heat production through time.

Our models assume that unroofing results exclusively from extension of the lithosphere and not from any associated erosion. Incorporating erosion into the extensional models renders them less applicable to the generalized problem of lithospheric thinning but also more realistic. Since conduction of heat takes place primarily in the vertical direction even in the two-dimensional models, the qualitative effects of erosion are essentially the same as a faster rate of uplift. Moreover, in most geologic settings, observations indicate that the rate of erosion is probably small compared with the rate of unroofing by faulting.

The rate of movement along faults is generally measured either along the fault surface or along the horizontal, but comparison between simple shear and pure shear models is easiest if displacement along the detachment surface is measured in terms of the vertical distance between the surface and a rock particle in the footwall of the detachment fault. The rate at which the footwall rocks move upwards relative to the surface will be referred to as the unroofing rate (or uplift rate) and is equal to the product of the horizontal displacement rate and the tangent of the angle of dip of the fault surface. In simple shear models, both the extension rate and the unroofing rate are held constant. For pure shear

models, except where specified otherwise, the extension rate is held constant, meaning that the uplift rate decreases with time.

GEOLOGIC RELEVANCE

In the models presented below we examine the uplift and thermal paths of intermediate and deep rocks brought nearer to the surface via pure shear of the lithosphere by amounts ranging from 200 to 900%. Most of the geologic data from highly extended terranes fall in the lower and middle parts of this range of values. In the Snake Range of east central Nevada, *Miller et al.* [1983] estimate that progressive ductile to brittle deformation beneath a large-scale detachment accounts for 300-550% extension. In other extensional settings, such as the rifted margin of the Nova Scotia and Labrador shelves, a modified pure shear model with 30-300% lithospheric extension accompanied by the introduction of additional heat into the subcrustal lithosphere has successfully been applied in the analysis of thermal and subsidence data [*Royden and Keen*, 1980]. Generally, pure shear thinning up to 400% seems to be consistent with structural and geophysical data in several types of extensional settings. Larger estimates of lithospheric pure shear can be obtained if part of the thinning is incorrectly attributed to extension as opposed to erosion.

Comparison of our simple shear models to observations in extensional terranes can be made on the basis of total displacement along the low-angle normal fault and on the rate of slip along the fault. For all but one of the simple shear models, the total amount of displacement lies in the 80- to 120-km range. Displacements on this order are observed in many extensional settings (e.g., 60 km throw on the Snake Range décollement reported by *Bartley and Wernicke* [1984]). The chosen range of displacements therefore seems reasonable in light of the geologic data. Slip rates along normal faults are estimated at up to or more than about 10 mm/yr [*Davis and Lister*, 1988]. Generally, we confine the

displacement rates in our models to the range of 6-12 mm/yr, although we also present PTt paths generated by slip at an upper limit of 25 mm/yr to show the effects of very fast uplift rates.

The simple shear models presented here require simplification of the geometry of the large-scale normal faults. Although single large-scale low-angle normal faults are thought to play an important role in many extensional terranes (e.g., the Snake Range décollement as described by *Bartley and Wernicke* [1984]), much of the movement associated with simple shear extension is accommodated along sympathetic normal faults in the hanging wall of the larger normal faults. Because of the thermal and geometric complications introduced by the presence of multiple sets of faults, we have chosen to present here only the results of simple shear extension via displacement along a single low-angle detachment surface. Although we recognize that displacement along smaller faults is an important mechanism in some extensional settings, a study of these geometries is beyond the scope of this paper.

In all of the simple shear models we track only the PTt paths of rocks that are within 10 km of the detachment surface because these rocks experience the largest thermal effects related to unroofing and movement of cool hanging wall material over the detachment surface. Rocks located deeper than about 10 km below a detachment fault are also less commonly exposed at the surface by movement on the detachment, even when extension is coupled with erosion.

PURE SHEAR VERSUS SIMPLE SHEAR

In order to compare the effects of uplifting a rock particle via the pure shear and simple shear mechanisms we charted the PTt paths of rock particles whose initial depths, final depths, and duration of uplift are the same in both modes of extension. The first

group of models compares the PTt paths of rocks uplifted from intermediate and deep crustal levels. We charted the PTt paths of a rock particle initially at 30 km depth and uplifted to a depth of 3 km at an uplift rate of 1 mm/yr (Figure 5.4). Uplift via simple shear was accomplished by assuming that the rock particle was initially located 3 km below a detachment fault dipping 9.5°. The total extension period thus lasted 27 m.y., and the horizontal displacement rate was about 6 mm/yr. Uplift via pure shear was assumed to occur over the same time interval at a constant rate of extension with a total extension of $\beta=10=900\%$. Although this β value is very large and would result in the thinning of a 125-km-thick lithosphere to less than 15 km, it is useful for our theoretical approach because it permits direct comparison of the thermal effects of rocks that begin and end at the same depth, although uplifted by different extensional mechanisms.

The temperature-time curves for the simple shear and pure shear models are similar, although the syntectonic cooling rate decreases with time in the pure shear model and increases for the case of lithospheric thinning via the simple shear mechanism. In the pure shear case, rocks remain hotter for a longer period of time after they have reached their final depths. For the simple shear model, the rate of cooling per kilometer of uplift is about 10°C/km between 500° and 300°C but greater than 18°C/km between 300° and 100°C. The form of the depth-temperature path for the pure shear case contrasts with that of the simple shear model and is characterized by a period of isothermal uplift in the first 10 km or more of uplift, followed by simultaneous cooling and uplift at a rate of 40°C/km between 300° and 100°C.

Note that by holding the extension rate constant in the pure shear case the uplift rate for any particle was constrained to decrease through time. It is therefore not clear from Figure 5.4 whether the differences between the pure shear and the simple shear PTt paths are entirely a reflection of the extensional mechanisms, or whether they partly result from time-dependent variations in uplift rate. While it is difficult to think of a physical

mechanism that would result in a constant uplift rate via pure shear, it is informative to compute the PTt paths that result from a constant uplift rate via pure shear and compare them with the paths generated by the simple shear mechanism.

Figure 5.5 shows the PTt paths generated by simple shear and pure shear of the lithosphere with a constant uplift rate of 1 mm/yr in both cases. Comparison of Figures 5.4 and 5 shows that for the pure shear model the constraint of constant uplift rate slows the cooling of the uplifted particle with time and also eliminates the period of isothermal uplift that immediately follows the onset of extension. Figures 5.4 and 5.5 together indicate that purely vertical conduction of heat in the pure shear model is not as efficient in cooling the extending lithosphere as the combined effects of conduction and the movement of cool hanging wall rocks over deeper and hotter rocks in the simple shear case.

In order to compare the thermal and uplift paths of rocks at deep crustal levels to those of rocks at intermediate crustal depths we charted the PTt paths of rocks initially at 15 km depth uplifted to 3 km depth again at an uplift rate of 1mm/yr (Figure 5.6). For the simple shear case the fault dip was again taken to be 9.5°, the horizontal displacement rate was 6 mm/yr, and the particle lies 3 km below the detachment surface. For the pure shear case, extension was assumed to occur at a constant rate, with a total extension given by $\beta=5.0$ or 400% extension.

The time-temperature paths for this midcrustal rock display the same qualitative relationships as those shown in Figure 5.4a for a deep crustal rock. For the simple shear case, the depth-temperature curve of the rock from mid-crustal depths has the same overall shape as that of the rock from deep crustal levels. In the pure shear models, however, the depth-temperature curves show significant qualitative differences in the uplift and thermal histories of intermediate and deep crustal rocks. The rock from deep crustal levels undergoes initial isothermal uplift, but a rock from intermediate crustal levels experiences little, if any, isothermal uplift. The cooling of rocks is caused by a complex interaction of

uplift rate, depth relative to the surface, geothermal relaxation, and distribution and magnitude of heat sources. The simultaneous onset of cooling and uplift for a midcrustal rock in the pure shear model is related to all of these factors.

The features of the PTt paths presented here also depend on the choice of initial thermal structure for the lithosphere. For example, if the steady state geotherm is used instead of the perturbed geotherm (Figure 5.3), rocks at any initial depth have lower initial temperatures and therefore undergo less net cooling during the unroofing episode. Figure 5.7 shows the temperature-time and depth-temperature paths for a deep crustal rock (30 km) uplifted to shallow crustal levels (3 km) via the simple shear and pure shear mechanisms using the initial conditions used for Figure 5.4 but with the steady-state initial geotherm in the place of the perturbed geotherm. Note that the form of the paths is qualitatively similar to those shown for the perturbed initial geotherm (Figure 5.4), but the increase in cooling rate with time (and therefore curvature of the paths) for the simple shear case is more pronounced when the steady state geotherm is used. For the pure shear mechanism, the PTt path is nearly isothermal during the first 8 m.y. (or 23 km) of extension.

As discussed above, a reasonable upper bound on the rate of displacement along these faults is probably several centimeters per year. In order to examine the effects of very fast uplift rates on the PTt paths generated by the two different extension mechanisms we charted the PTt path of a rock particle uplifted at a rate of 4 mm/yr (Figure 5.8), corresponding to a horizontal displacement rate of 24 mm/yr. The initial conditions are the same as those used to generate Figure 5.4 except for the higher rate of unroofing and horizontal displacement and the correspondingly shorter duration of extension (6.75 m.y. as opposed to 27 m.y.). The rate of extension in the pure shear case was held constant.

The nearly vertical slope of the syntectonic portion of the temperature-time path in Figure 5.8a indicates that even when the uplift rate is very rapid, most of the cooling still

takes place during the extensional period. From Figure 5.8b, however, it is clear that for the pure shear case, almost all of this cooling occurs in the final 7 km of uplift, resulting in an isothermal depth-temperature curve between 30 and 10 km depth. In the simple shear case, cooling and uplift occur simultaneously from the onset of extension, and the increase in cooling rate per kilometer of uplift is reflected in the concavity of the depth-temperature curve.

MODIFIED PURE SHEAR

One weakness of the pure shear model as it is described above is that it assumes that the lithosphere is subject to the same amount of extensional deformation at every point. This uniform pure shear model ignores thermal, mechanical, and compositional heterogeneities in the lithosphere, particularly a postulated brittle to ductile transition between the upper and lower lithosphere. Additionally, extra heating in the lower lithosphere may result from thermal perturbations caused by magmatic underplating, small-scale mantle convection, intrusion of magmatic material, or other processes associated with rapid upwelling of the asthenosphere. Because these heating processes greatly complicate thermal models, we choose to mimic them by using a large β value for the lower lithosphere and a smaller stretching parameter for the uppermost lithosphere.

In order to compare the thermal and uplift paths produced by simple shear and uniform and modified pure shear of the lithosphere we chose to monitor the PTt conditions of a rock uplifted from deep (30 km) to intermediate (10 km) crustal levels at an uplift rate of 1 mm/yr. The extensional episode spanned 20 m.y. in each model. For uniform pure shear of the lithosphere, β , determined by the ratio of the initial to final depths of the uplifted rock, was chosen as 3.0 (or 200% extension of the lithosphere). In the modified pure shear model we chose 10 km as the depth to the zone of decoupling and tested two

models, one with upper lithosphere parameter $\delta=1.66$ and lower lithosphere parameter $\beta=5.0$ and another with $\delta=2.0$ and $\beta=4.0$. In the simple shear case we monitor a rock particle initially at a depth of 30 km as it is uplifted to 10 km by movement along a detachment dipping at 9.5° . The rock particle is located 10 km below the detachment fault and unroofed at 1 mm/yr, corresponding to horizontal displacement of the hanging wall at 6 mm/yr.

Figure 5.9 shows the depth-temperature and time-temperature paths of the rock carried from 30 to 10 km depth via the simple shear and uniform and modified pure shear mechanisms, using the perturbed initial geotherm. As expected, the time-temperature paths for the simple shear and uniform pure shear cases have the same qualitative relationship observed in Figures 5.4a and 5.6a, although the extensional period is shorter. A minor difference between uplift from deep to intermediate crustal levels (Figure 5.9) and uplift from deep to shallow crustal levels (Figures 5.4a and 5.6a) by the uniform pure shear and simple shear mechanisms shows up in the amount of posttectonic cooling necessary to reach the equilibrium temperature. Rocks uplifted from deep to intermediate crustal levels experience greater cooling during the posttectonic period primarily because, at their final depths, they are still far below the surface, and the cooling effects associated with uplift or unroofing have not fully propagated downward to intermediate crustal levels.

For the case of uplift via modified pure shear Figure 5.9 shows that the PTt paths of lower lithosphere rocks depend on the amount of heating in the lower lithosphere, represented by β in our models. For the model with the smaller β value of 4 the temperature-time and depth-temperature curves are similar to those generated by uniform pure shear extension of the entire lithosphere, but cooling occurs more slowly and uplift is nearly isothermal over a longer portion of the temperature-depth path. Raising the β value still higher to 5 decreases the cooling rate to the point that the rock arrives at its final depth 40°C hotter than for the uniform pure shear model and 70°C hotter than for the simple shear

model. Cooling for the modified pure shear model with $\beta=5$ occurs at a rate of $3^\circ\text{C}/\text{km}$ between 30 and 15 km depth compared with $5^\circ\text{C}/\text{km}$ for the case of $\beta=4$, nearly $7^\circ\text{C}/\text{km}$ for uniform pure shear, and $10^\circ\text{C}/\text{km}$ for the simple shear model.

SIMPLE SHEAR MODELS

In the discussion above we have focused primarily on explaining how different extensional mechanisms affect the PTt paths of rocks unroofed or uplifted from intermediate and deep crustal levels. Another goal of this study is to understand how variations in the extensional parameters that describe normal faulting affect the PTt paths of footwall rocks. Toward this end, we first designed simple shear models to study how the PTt paths of footwall rocks are affected by the dip angle of the detachment surface when the unroofing rate (or uplift rate) is held constant. We chose dip angles that have integral cotangents of 12, 6, 4, and 2, corresponding to dips of 4.7° , 9.5° , 14° , and 26.6° . In each model the footwall was unroofed at a rate of 1 mm/yr until 20 km of tectonic denudation had occurred. The total duration of extension was 20 m.y., and the rates of horizontal displacement were 12, 6, 4, and 2 mm/yr, respectively.

Furlong and Londe [1986] have previously noted that if horizontal heat conduction is ignored, the depth-temperature and temperature-time paths are dependent only on the unroofing rate and are independent of fault dip because changes in fault dip have no meaning in the absence of lateral conduction of heat. Therefore comparison of temperature-time and depth-temperature paths for rocks unroofed at the same rate below detachments dipping at different angles is an implicit test of the importance of lateral heat conduction in determining the morphology of PTt paths.

Figure 5.10 illustrates the temperature-time and depth-temperature paths of a rock uplifted from 25 to 5 km depth by displacement along a simplified low-angle normal fault.

In each case the rock experiences nearly 300°C of syntectonic cooling followed by less than 50°C of posttectonic isobaric cooling. During the syntectonic period, different fault dips produce the same temperature-time and depth-temperature paths because displacement of the hanging wall relative to the footwall and vertical conduction of heat predominate as the principal modes of heat transport. Divergence of these paths in the first 40 m.y. of posttectonic cooling is caused by conductive cooling across exposed detachment surfaces dipping at different angles. The qualitative relationships reported here for rocks from this depth range are also observed for rocks uplifted from shallower crustal levels. The lower initial temperature of shallower rocks simply reduces the amount of overall cooling these rocks experience during uplift and thermal reequilibration.

Figure 5.10 indicates that for faults that dip less than about 30° horizontal conduction of heat has no effect on the depth-temperature path and no effect on the temperature-time path during active unroofing. Posttectonic cooling is only marginally affected by fault dip. Given the errors inherent in measuring metamorphic temperatures and pressures (see below), the horizontal conduction of heat can be safely neglected for faults that dip 30° or less. Figure 5.10 also shows that the horizontal displacement rate during extension does not significantly affect the temperature-time and depth-temperature paths, provided that the unroofing rate is fixed. For gently dipping faults the only parameter that affects the paths of foot wall rocks is the unroofing rate.

In order to test the effects of varying the unroofing rate we compared the depth-temperature and temperature-time paths for rocks that begin at 25 km depth and are uplifted to 5 km depth by displacement along a fault dipping 9.5°. The rocks are initially located 5 km below the fault and are unroofed at 0.5, 1.0, and 2.0 mm/yr, corresponding to horizontal displacement rates of 3, 6, and 12 mm/yr and extensional episodes lasting 40, 20, and 10 m.y., respectively. These variations in the rate of unroofing produce marked changes in the slopes of the temperature-time and depth-temperature paths (Figure 5.11).

This occurs because most of the cooling of rocks located 5 km below the detachment occurs during movement on the fault. For the faster unroofing rates, more posttectonic cooling is necessary to reach equilibrium because the downward propagation of cooling associated with the movement of cooler hanging wall rocks over deeper and hotter footwall rocks cannot keep pace with rapid unroofing. Cooling therefore continues after the unroofing of the footwall has stopped, and the rock unroofed at 0.5 mm/yr reaches its final depth approximately 70°C cooler than does the rock unroofed at 2.0 mm/yr.

The slope of the depth-temperature curves is approximately the same for the different rates of unroofing, particularly during the last half of the extensional period. Between temperatures of 300° and 200°C the slope of the temperature-depth path is 16°C/km for each case. During the first part of the syntectonic period, however, the rock unroofed at a rate of 0.5 mm/yr undergoes 15°C/km of cooling between 400° and 300°C, while unroofing at 2.0 mm/yr causes only 11°C/km of cooling. Clearly, the temperature-depth paths are not very sensitive to a variation by a factor of 4 in the unroofing rate, particularly during the last part of the extensional period.

DISCUSSION

In detail, pure shear and simple shear extensional mechanisms produce similar temperature-time paths but different pressure-temperature (PT) paths. PT paths for rocks uplifted by pure shear are nearly isothermal (high dP/dT) during the initial stages of uplift, whereas PT paths for rocks uplifted by simple shear are characterized by moderate dP/dT and fairly constant slopes. Isothermal uplift would be observed in simple shear settings only if the initial geotherm were roughly isothermal with depth. Temperature-time paths for pure shear and simple shear have similar morphologies, although cooling rate (dT/dt) decreases with time for the pure shear models and increases with time for the simple shear

case. The primary difference between temperature-time paths produced by pure shear and simple shear is the amount of posttectonic cooling necessary for rocks to reach equilibrium temperature: rocks from simple shear settings are generally cooler by the end of the extensional episode than rocks uplifted by pure shear and must therefore undergo less posttectonic cooling.

It is appropriate to ask whether PTt data for extensional terranes can constrain the mechanism of extension. The answer depends on the magnitude of uncertainties involved in PTt path calculations. Pressure-temperature paths are determined through a combination of standard thermobarometric techniques [Essene, 1982], mineral inclusion thermobarometry [St-Onge, 1987], and thermodynamic modeling of mineral zoning [Spear and Selverstone, 1983]. Although the propagation of analytical uncertainties through thermobarometric calculations is straightforward [Hodges and Crowley, 1985; Hodges and McKenna, 1987], the uncertainties in thermodynamic modeling are less well constrained. The nominal uncertainties in the position of pressure-temperature points on a path are 50°C and 1 kbar. If we note that the range of pressures over which PT measurements may typically be made is only about 7 kbar (between 30 and 10 km depth) and the range of temperatures is only about 400°C (250°-650°C), then we cannot expect to reconstruct the slope of a pressure-temperature path with even moderate precision. This precision is insufficient to distinguish between pure shear and simple shear uplift except in instances of uplift rates corresponding to very rapid displacement along the fault zone or significant heating (corresponding to large β values) in the lower lithosphere during pure shear extension.

Uncertainties in temperature-time paths include errors in calculated ages for various mineral-isotope systems, as well as uncertainties in the closure temperatures of these systems. On the basis of the propagation of nominal uncertainties in diffusion data for radiogenic species through closure temperature equations (*e.g.*, Dodson [1973]), we

calculate closure temperature uncertainties of roughly 25°-75°C for many commonly used mineral-isotope systems (*e.g.*, hornblende K-Ar, biotite K-Ar, and microcline K-Ar). Absolute age uncertainties of the order of a few million years are realistic for Tertiary cooling events like those that occurred in the North American metamorphic core complexes and even greater for older events. Given these uncertainties, it is difficult or impossible to differentiate between various extensional mechanisms using current petrologic techniques and temperature-time data from a single rock particle or from rock particles that have been uplifted from the same structural (crustal) level.

With the limitations imposed by current petrologic techniques the best method for distinguishing between pure shear and simple shear mechanisms may lie in analysis of samples collected from the broadest possible range of structural levels. Clearly, examination of PTt paths for rocks in both the hanging wall and the footwall of a detachment fault should reveal if uplift were accomplished primarily through movement along that particular fault or primarily by pure shear extension and thinning of the crust. Comparison of footwall samples from different structural levels may also enable one to determine if the vertical separation between those samples was greater in the past than at present. Ultimately, however, the best prospect for distinguishing between simple shear and pure shear mechanisms through petrologic work lies in improving the precision of metamorphic temperature and pressure measurements. Even an improvement in precision to $\pm 25^{\circ}\text{C}$ and ± 0.5 kbar could enhance our capability to constrain types of extensional deformation-based petrologic data.

CONCLUSIONS

1. Temperature-time paths for rocks uplifted via pure shear thinning and extension of the lithosphere are, in some instances, different from those produced by rocks uplifted at

the same rate by simple shear unroofing along large, gently dipping normal faults. In particular, rocks from pure shear settings reach their final depth at higher temperatures than do rocks uplifted by simple shear, and experience a greater amount of posttectonic cooling. However, it would be difficult or impossible to distinguish the temperature-time paths of rocks uplifted by pure shear from those of rocks uplifted by simple shear but at a more rapid rate.

2. The depth-temperature paths of rocks uplifted from deep crustal levels (30 km depth) via pure shear extension are often characterized by a period of nearly isothermal (high dP/dT) uplift during the early stages of extension, but rocks from intermediate crustal levels (15 km depth) experience a markedly shorter period of isothermal uplift. In contrast, simple shear uplift along low-angle normal faults produces almost linear depth-temperature paths with moderate dP/dT . Isothermal depth-temperature curves would be expected for the simple shear case only if the initial geotherm were isothermal with depth.

3. An important factor in determining the characteristics of the thermal and uplift histories of deep crustal rocks in a pure shear model modified to include additional heating in the lower lithosphere is the amount of heating, described by stretching parameter β , in the lower lithosphere. These modified pure shear models, with large amounts of lower lithospheric heating, generally produce PTt paths characterized by lower syntectonic cooling rates and a more protracted period of nearly isothermal uplift.

4. For a given initial geotherm the single factor controlling the PTt paths of rocks unroofed below gently dipping normal faults is the rate at which unroofing takes place (unroofing rate is defined as the rate of uplift relative to the surface). For faults that dip less than about 30° , changing the fault dip and the rate of horizontal displacement has no appreciable effect on either the PT path or on the syntectonic part of the time-temperature path and only a marginal effect on the post-tectonic part of the temperature-time path. These results indicate that for faults that dip about 30° or less, horizontal conduction of heat

is not very important and for most purposes can be ignored. These results further indicate that a consideration of more detailed geometric models (e.g., listric fault geometries) is not warranted because the fault geometry is only important insofar as it affects the unroofing rate of footwall rocks.

5. Propagation of typical uncertainties in real pressure-temperature and temperature-time data shows that it is difficult or impossible to distinguish between various extensional mechanisms solely on the basis of PTt data derived from a single sample or from a single structural level through the use of current geothermometric and geobarometric techniques. With the limitations imposed by current petrologic techniques the best method for distinguishing between pure shear and simple shear mechanisms may be the analysis of samples collected from the broadest possible range of structural levels. Ultimately, however, the best prospect for distinguishing between simple shear and pure shear mechanisms through petrologic work lies in improving the precision of metamorphic temperature and pressure measurements to $\pm 25^{\circ}\text{C}$ and ± 0.5 kbar.

ACKNOWLEDGEMENTS

C. Keen, an anonymous reviewer, and particularly K. Furlong provided helpful and thoughtful reviews. This work was supported by National Science Foundation grant EAR-8407730 to K.H. and L.R.

FIGURE CAPTIONS

- Figure 5.1. Schematic diagrams of (a) pure shear and (b) simple shear extensional models after *Wernicke* [1985].
- Figure 5.2. Simple shear thermal model. In our models the footwall is pulled out from beneath the hanging wall, unroofing a portion of the detachment surface. The breakaway is defined as the point at which the fault intersects the surface. Boundary conditions are zero horizontal heat flux along the sides of the two-dimensional grid and 0° and 1300°C at the surface and 125 km depth, respectively.
- Figure 5.3. The initial geotherms used in this study. The perturbed geotherm is described by the function given in the text and is chosen to fit an initial condition of 500°C at 30 km. The perturbed geotherm will decay to the steady state resulting from the superposition of the background thermal gradient of 10.4°C/km and the effects of constant heat production at $1.5 \mu\text{W}/\text{m}^3$ due to radiogenic sources in the upper 10 km.
- Figure 5.4. (a) Temperature-time and (b) depth-temperature paths for rocks uplifted from 30 to 3 km by simple shear (solid lines) and pure shear (dashed lines) of the lithosphere using the perturbed initial geotherm. For the simple shear case the detachment surface dips at 9.5°, lies 3 km above the rock particle, and is unroofed at 1 mm/yr by horizontal displacement of the hanging wall at 6 mm/yr. Extension rate is held constant for the pure shear model, and

the duration of extension is 27 m.y. for both cases. Dots mark the end of the extensional period.

Figure 5.5. (a) Temperature-time and depth-temperature paths for rocks uplifted from 30 to 3 km by simple shear (solid lines) and pure shear (dashed lines) of the lithosphere using the perturbed initial geotherm. For the simple shear case, the detachment surface dips at 9.5° , lies 3 km above the rock particle, and is unroofed at 1 mm/yr by horizontal displacement of the hanging wall at 6 mm/yr. Uplift rate is constant for the pure shear case at 1 mm/yr, and the duration of extension is 27 m.y. in each model. Dots mark the end of the extensional period.

Figure 5.6. (a) Temperature-time and (b) depth-temperature paths for rocks uplifted from 15 to 3 km by simple shear (solid curves) and pure shear (dashed curves) of the lithosphere, using the perturbed initial geotherm. For the simple shear case, the detachment surface dips at 9.5° , lies 3 km above the rock particle, and is unroofed at 1 mm/yr by horizontal displacement of the hanging wall at 6 mm/yr. Extension rate is constant for the pure shear case, and extension lasts 12 m.y. for both models. Dots mark the end of the extensional period.

Figure 5.7. (a) Temperature-time and (b) depth-temperature paths for rocks uplifted from 30 to 3 km by simple shear (solid curves) and pure shear (dashed curves) of the lithosphere using the steady state initial geotherm. For the simple shear case, the detachment surface dips at 9.5° , lies 3 km above the rock particle, and is unroofed at 1 mm/yr by horizontal displacement of the

hanging wall at 6 mm/yr. Extension rate is constant for the pure shear case, and extension endures for 27 m.y. for both models. Dots mark the end of the extensional period.

Figure 5.8. (a) Temperature-time and (b) depth-temperature paths for rocks uplifted from 30 to 3 km by simple shear (solid curves) and pure shear (dashed curves) of the lithosphere, using the perturbed initial geotherm. For the simple shear case, the detachment surface dips at 9.5° , lies 3 km above the rock particle, and is unroofed at 4 mm/yr by horizontal displacement of the hanging wall at 24 mm/yr. Extension rate is constant for the pure shear case, and extension lasts 6.75 m.y. Dots mark the end of the extensional period.

Figure 5.9. (a) Temperature-time and (b) depth-temperature paths for rocks uplifted from 30 to 10 km by simple shear (solid curves) and uniform and modified pure shear (dashed curves) of the lithosphere, using the perturbed initial geotherm. The modified pure shear cases correspond to an extension factor δ above 10 km depth and an extension factor β below 10 km depth. For the simple shear case the detachment surface dips at 9.5° , lies 10 km above the rock particle, and is unroofed at 1 mm/yr by horizontal displacement of the hanging wall at 6 mm/yr. Extension rate is constant for the pure shear cases as described in the text, and the duration of extension is 20 my. Dots mark the end of the extensional period.

Figure 5.10. (a) Temperature-time and (b) depth-temperature paths of rocks uplifted from 25 to 5 km depth via simple shear. The detachment faults dip 4.8° , 9.5° ,

14.0°, and 26.6°. The unroofing rate is 1 mm/yr, and the rock is 5 km below the detachment surface in each case.

Figure 5.11. (a) Temperature-time and (b) depth-temperature paths of rocks uplifted from 25 to 5 km depth via simple shear at unroofing rates of 0.5, 1.0, and 2.0 mm/yr. The dip of the fault is 9.5°, and the rock is 5 km below the detachment surface in each case.

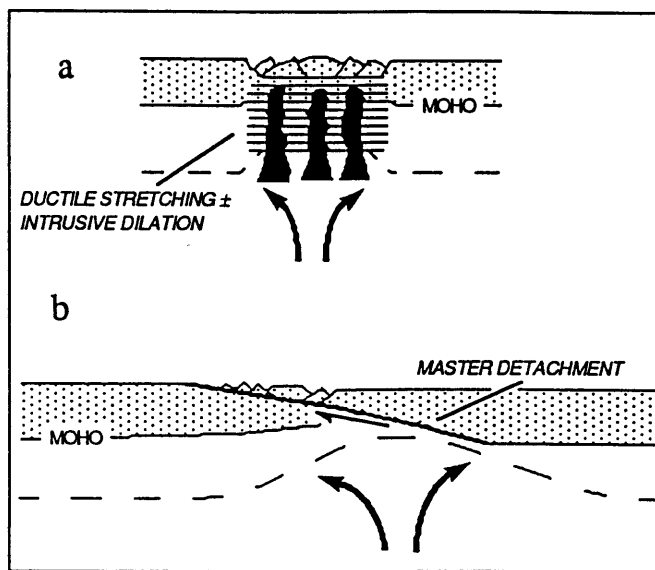
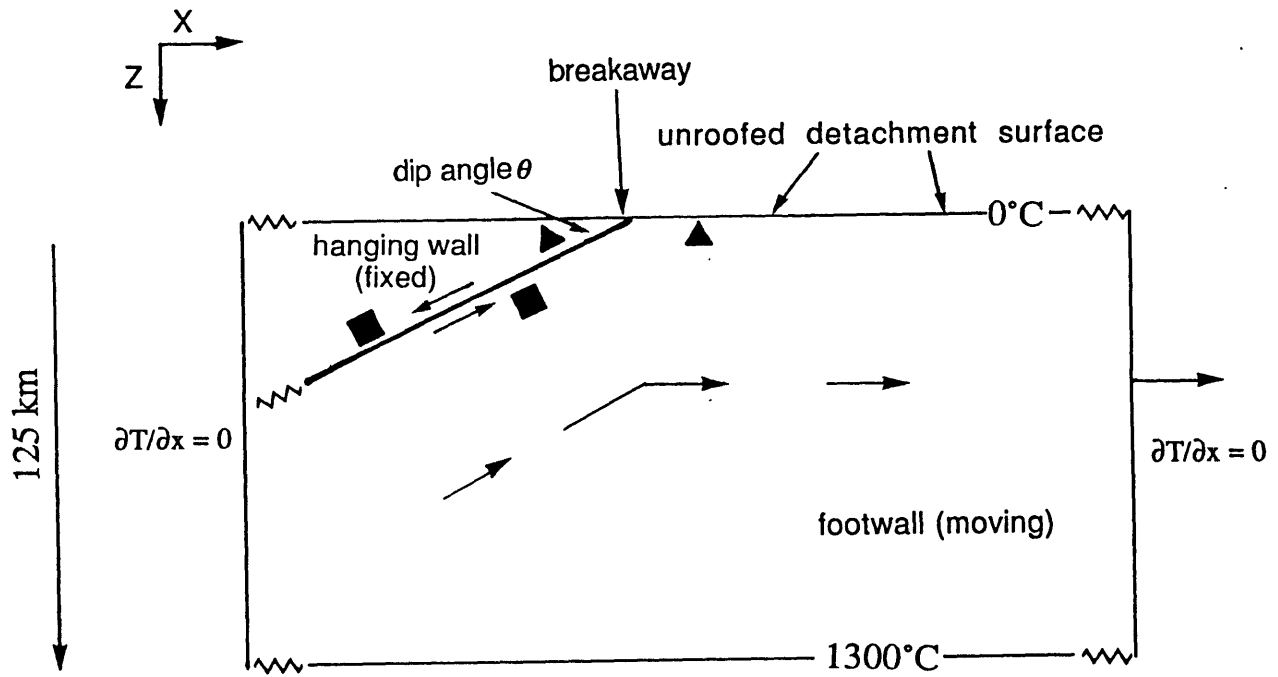


Figure 5.1

Figure 5.2



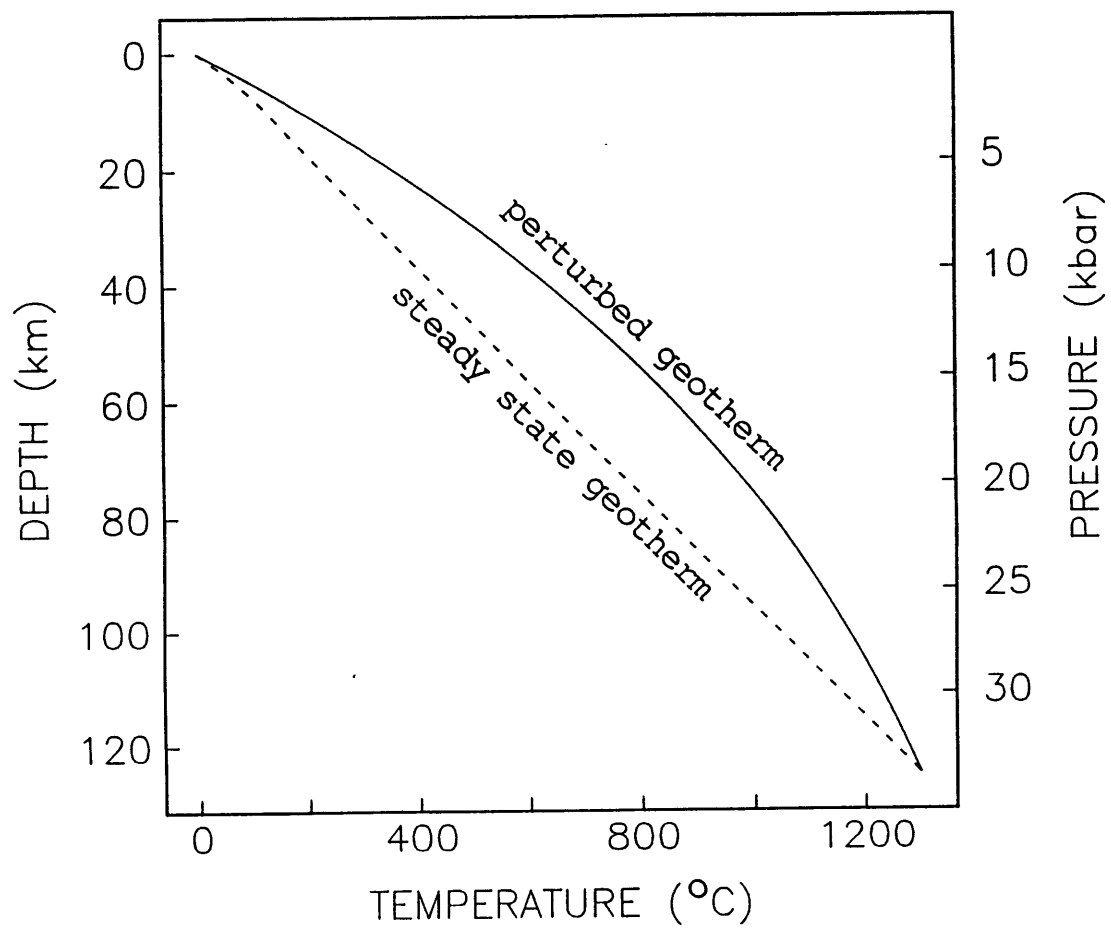


Figure 5.3

Figure 5.4

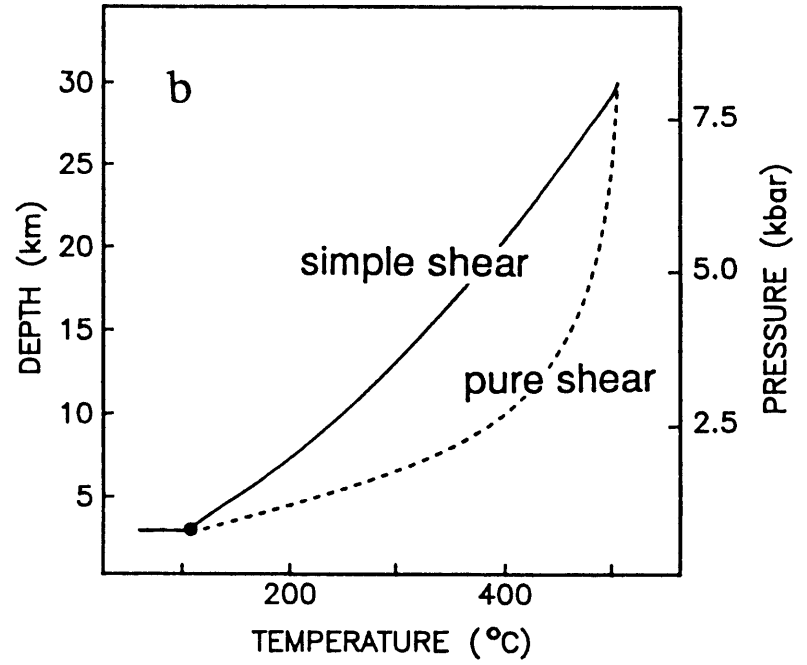
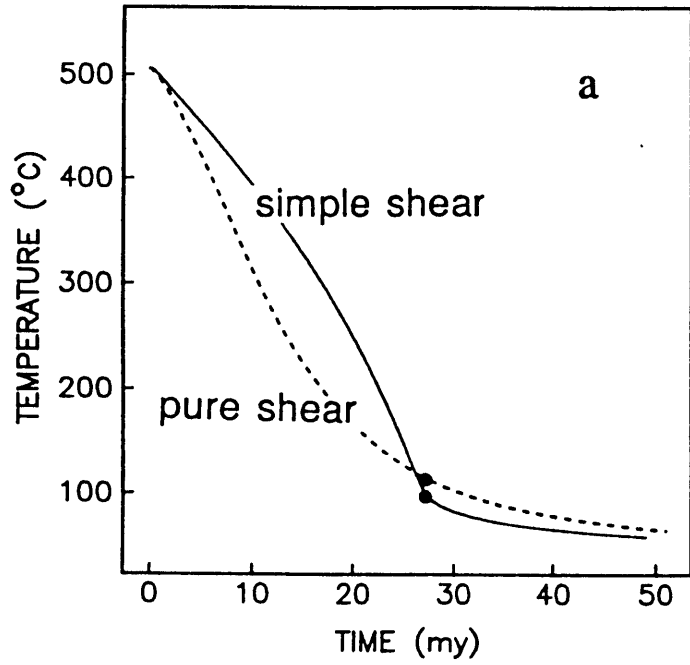


Figure 5.5

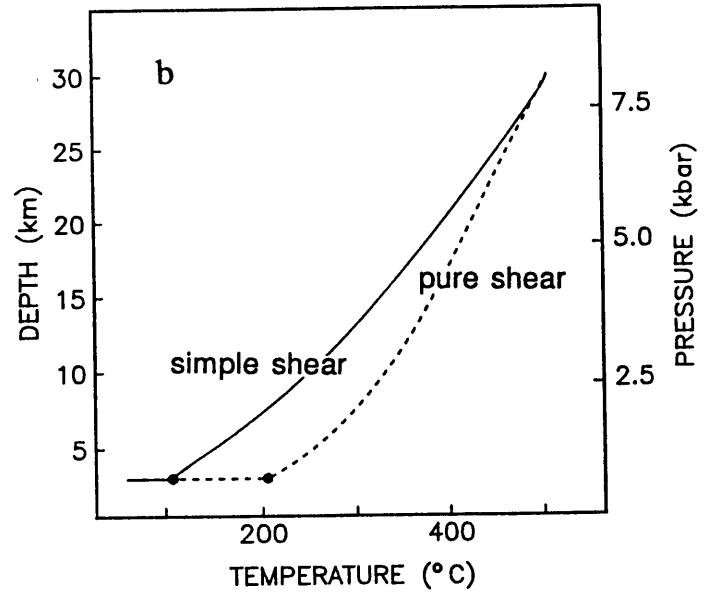
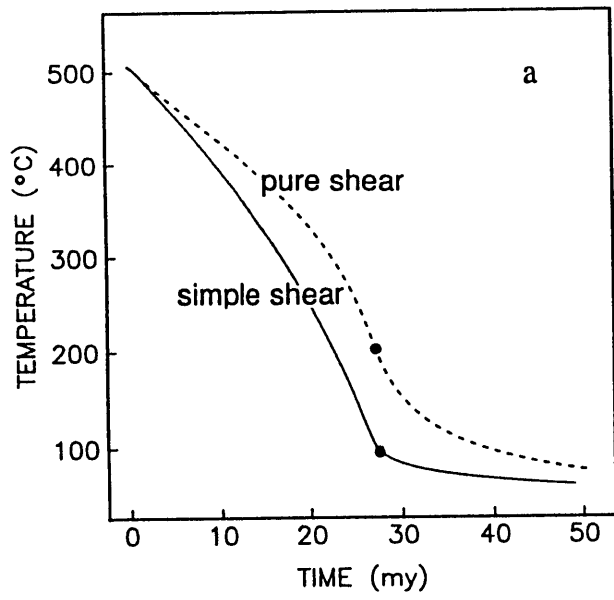


Figure 5.6

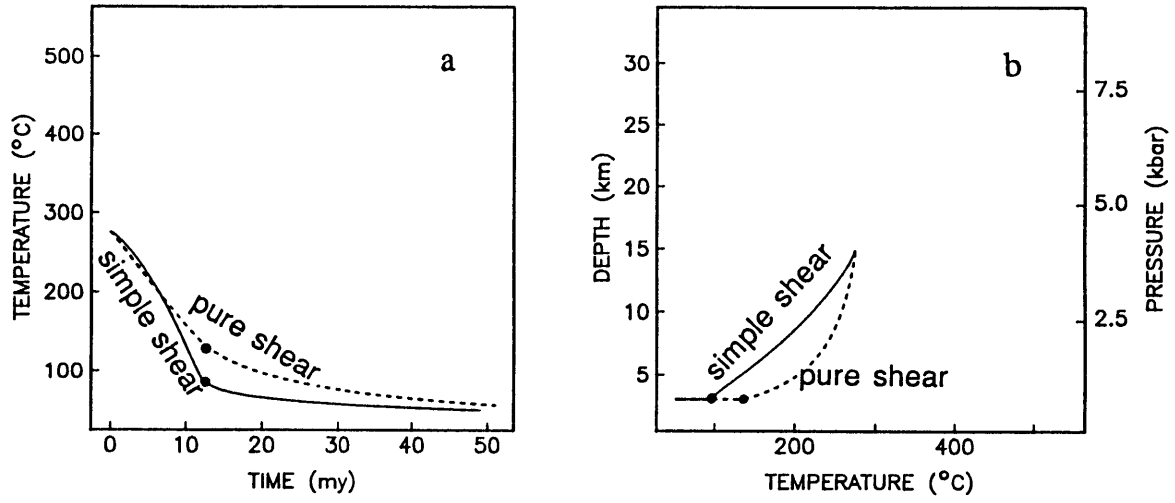


Figure 5.7

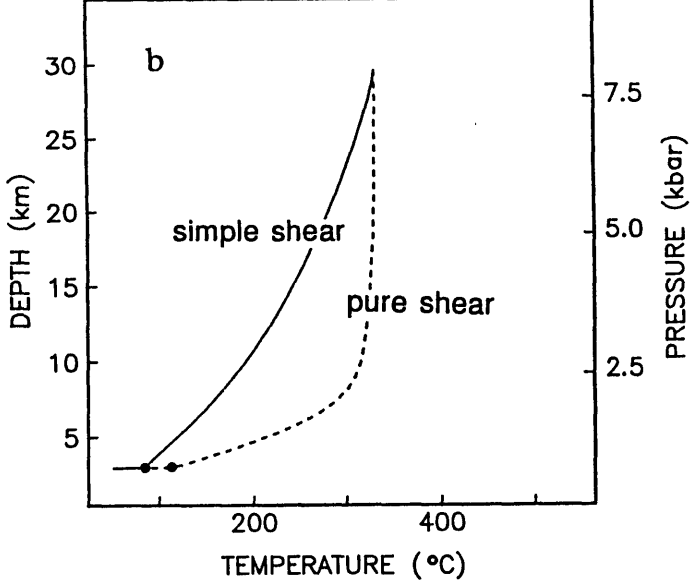
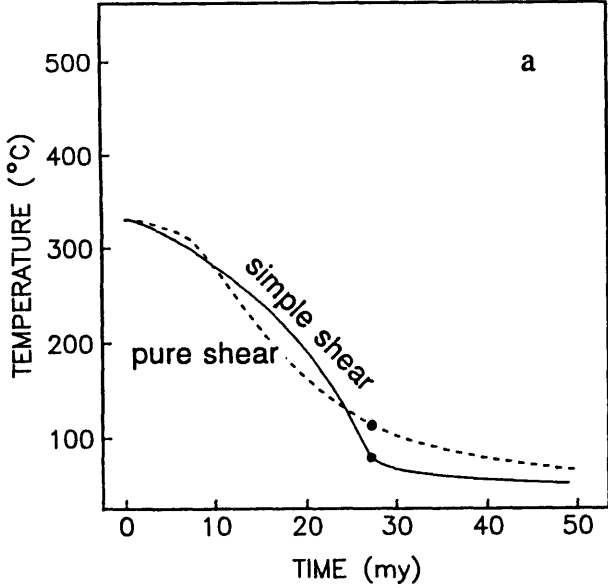


Figure 5.8

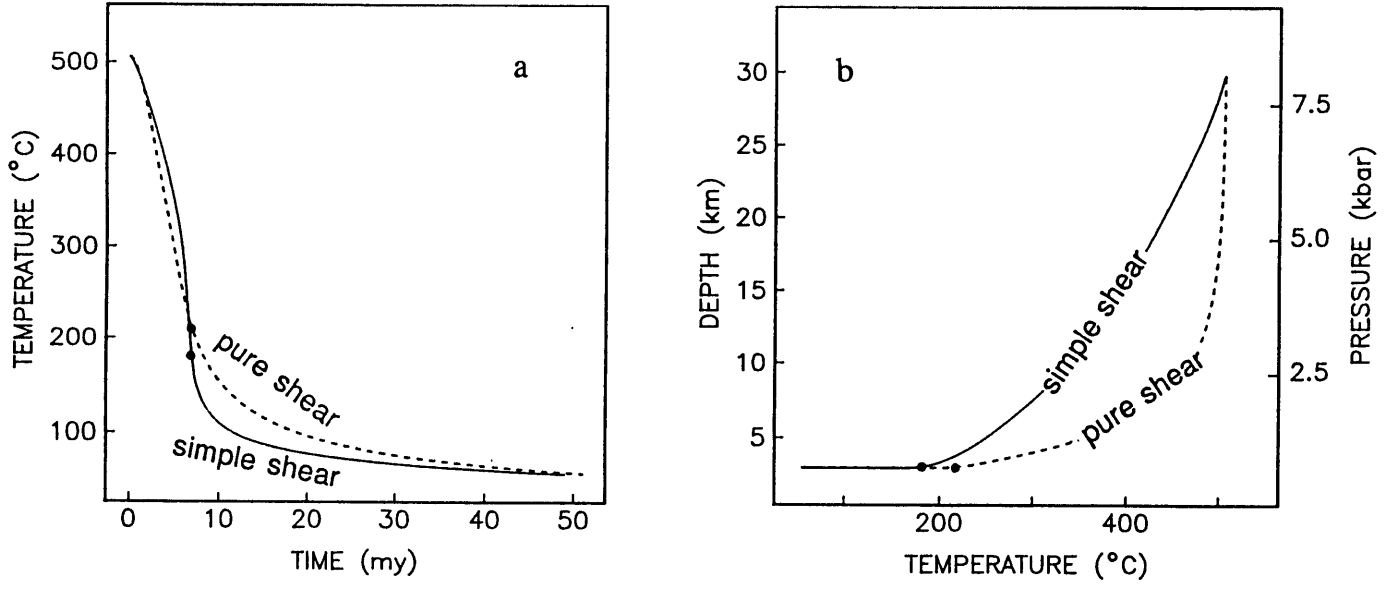


Figure 5.9

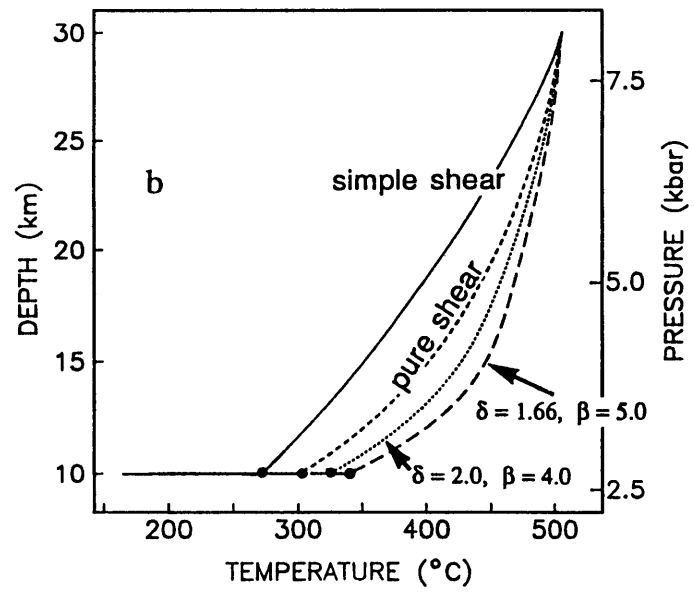
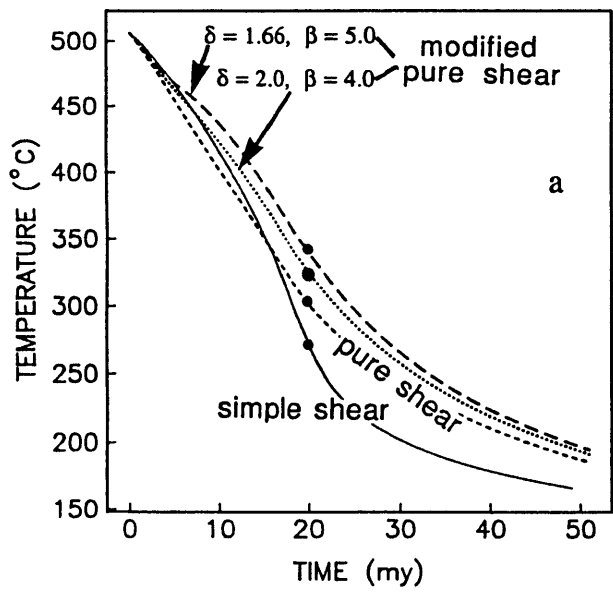


Figure 5.10

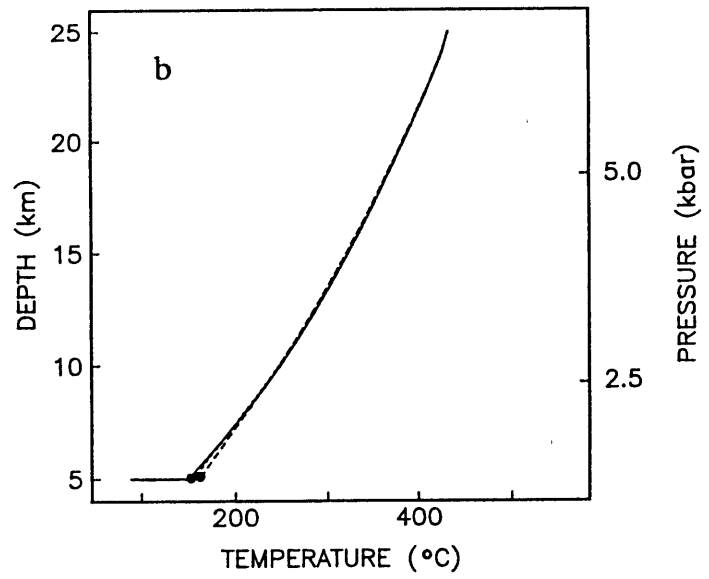
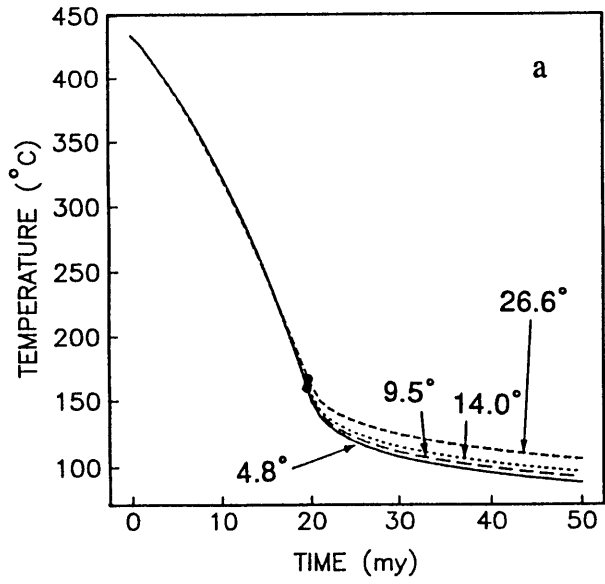
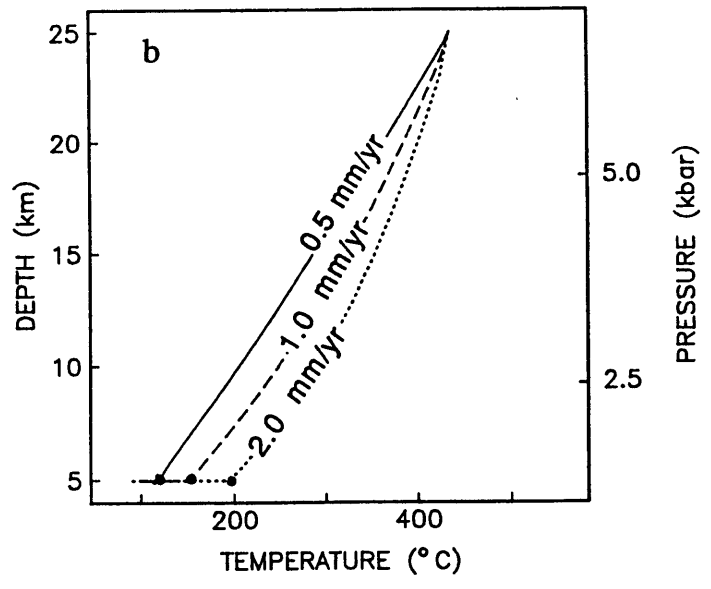
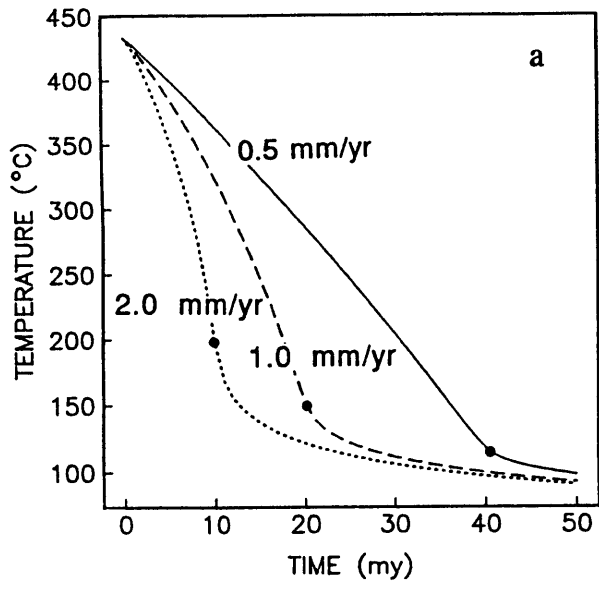


Figure 5.11



Chapter 6

Conclusions

This thesis has dealt with aspects of the thermal, mechanical, dynamic, and tectonic structure of active zones within the continents and has relied on the use of a variety of data and techniques to constrain the processes responsible for tectonism. This chapter briefly summarizes the main conclusions of this thesis and links the continental processes studied here to their oceanic analogs through a series of qualitative comparisons. In addition, we detail ongoing efforts to resolve some of the remaining research problems associated with rifts and large-scale extensional overthrust terrains and outline suggestions for future work.

SUMMARY

The conclusions of this thesis relate to the nature of the crust and mantle lithosphere beneath continental rifts and large-scale overthrust and extensional terrains, with particular emphasis on the thermal state of the lithosphere in each of these settings. Studies in the Baikal Rift zone reveal that this young, very discrete, and laterally heterogeneous rift may develop over lithosphere colder than that associated with any other continental rift zone. We attribute nearly all of the gravity signature over the rift to shallow compensation by anomalous masses and flexure of a 30 km thick elastic plate and show that most of the geological and geophysical observations in the BRZ are consistent with only a small thermal anomaly at lower crustal or upper mantle lithospheric levels. The present datasets are insufficient to constrain the driving forces for rifting in the BRZ, but passive rifting related to stresses transmitted across Asia from the Himalayan collision zone is gradually

becoming a less viable mechanism in light of recent geophysical studies implying the presence of a weak, possibly convecting, layer beneath the Tibetan plateau. Forces responsible for passive rifting in the BRZ may arise elsewhere in the internally deforming Asian plate however, and recent models for passive rifting are loosely consistent with certain BRZ observations, including the deep, narrow axial basin [*Bassi*, in press] and the high rift flanks (which might be convectively [*Buck*, 1986] or flexurally [*Weissel and Karner*, 1989] supported).

Surface observations do not presently support the existence of thermal driving mechanism for rifting at the site of the BRZ although the long time scale of conduction in the crust or mantle lithosphere implies that surface observations may lag many millions of years behind initial heating and thermal weakening associated with plume emplacement at depth. Even in light of the delay between heating and the onset of extension, we still find it difficult to reconcile the paucity of rift-related volcanic rocks and the seismogenic nature of the middle and possibly lower crust with a thermal driving mechanism for rifting in the BRZ. The geophysical data do not, at present, provide enough constraints to evaluate the possibility of dynamic driving mechanisms in the BRZ, but an upwelling plume associated with large-scale convection could produce the observed BRZ topography without heating the overlying lithospheric lid. Small-scale convection within a low-viscosity layer at the base of the crust may also explain some of the geological and geophysical observations in the BRZ and could lead to the development of significant levels of extensional stress in the lithosphere. Thermal erosion of the lithospheric lid due to underlying small-scale convection elevates the conductive gradient in the lithosphere, and, if such a process were in its early stages beneath the BRZ, the amount of partial melting at depth may be relatively small but sufficient to account for the volume of extruded volcanic rock and the 1 sec PKP delay [*Slack*, pers. comm.].

Among the many peculiarities which distinguish the BRZ from other continental rift zones is its extraordinarily discrete nature, and we explore one possible scenario for opening of the rift in Chapter 3. Analysis of Landsat photos and other geological and geophysical data lead to the conclusion that a significant component of left-lateral strike-slip may be present in the BRZ. The overall sinistral shape of the rift and the presence of left-lateral strike-slip zones at the southern and northern ends of the rift's axis and cutting obliquely through its center imply that the BRZ may represent a feature analogous to an extensional crack, but at the lithospheric scale. The pull-apart scenario for parts of the BRZ is consistent with (1) the great depth of the axial basins (in excess of 7 km close to bounding faults and probably in excess of 4 km on average), (2) the young (4 Ma) age of the rift advocated by some workers, (3) the lack of a significant thermal anomaly, and (4) the relatively small amount (10-30 km) of measured extension. This analysis may imply that passive driving forces control the development of the BRZ, and our interpretation has interesting implications in light of experimental and numerical models which produce strike-slip deformation, but not extension, near the site of the BRZ as the result of the "indentation" of Asia by India.

We next switch from the study of extension in the BRZ to the analysis of crustal thermal evolution in compressional and extensional settings. A time-dependent thermal model which includes two-dimensional conduction and advection of heat is used to explore the effects of overthrusting, erosional and tectonic unroofing, and various fault characteristics on the pressure-temperature-time (PTt) paths of metamorphic rocks. Our results highlight the importance of including the time-transitive aspects of tectonism when analyzing the PTt data collected from actual rocks and demonstrate that the number of factors affecting the thermal evolution of metamorphic rocks is so large that distinguishing among them merely on the basis of PTt paths is a fruitless, if not naive, exercise. An important motivation for the PTt study has been the emergence of occasionally

contradictory thermal histories for the Greater Himalayas and results which imply the existence of a temperature inversion in the crust. The existence of such temperature inversions over time-scales sufficient for them to be “recorded” by metamorphic rocks represents a physically counter-intuitive situation since such small-scale inversions should relax quickly. By varying a number of parameters which might preferentially raise temperatures near the fault (*e.g.*, frictional heating), we demonstrate that the temperatures recorded by metamorphic rocks at various structural distances from the fault do not necessarily approximate a crustal geotherm. The complex trade-offs between various factors controlling the thermal evolution of the crust during overthrusting and unroofing, coupled with the large uncertainties associated with geothermobarometric data, lead us to conclude that the best hope for extracting useful information from PTt data lies in the development of robust inversion techniques.

OCEANIC ANALOGS FOR CONTINENTAL FEATURES

The studies in this thesis describe the relationships between surface deformation and lithospheric thermal, mechanical, and dynamic structure. Thus, they serve as a good starting point for the goal outlined in Chapter 1—namely, to work towards a synthesis of results from oceanic and continental settings in order to reach fundamental conclusions about the nature of Earth processes. In terms of the processes occurring at oceanic rifts, the analysis of the cold, continental BRZ may appear to have little relevance. However, many characteristics of the BRZ make it analogous to now marine Dead Sea Rift, and the relationship between the cold BRZ and the hotter Rio Grande and East African Rift systems may help to define that between the cold oceanic rift (Australia-Antarctic Discordance along the Southeast Indian Ridge) and more archetypal mid-ocean ridges. In both the oceanic and continental cold rift endmembers, geophysical evidence supports the interpretation that

convection may play an important role in controlling surface deformation. In addition, the evolution of the BRZ at a crustal discontinuity may have implications for the localization of deformation at new sites when ocean ridges jump or propagate, and the highly segmented nature of the BRZ, a laterally heterogeneous rift comprised of four fundamentally different tectonic provinces, may provide an analogy to oceanic ridges, whose segmentation characteristics are presently the focus of active research.

The results of the study of the thermal evolution of large-scale continent-continent collision zones have one important application to understanding processes in oceans, namely to metamorphism in subduction zone settings. Although our models do not include fluid migration, whole lithospheric underthrusting, or other complicated subduction effects, basic conclusions about the nonunique nature of PTt paths and the interplay between various fault parameters and pre-existing crustal thermal states are valid for subduction zones as well. The primary difference between subduction zones and large-scale overthrust terrains lies in the continuing nature of subduction processes; whereas compression in the Himalayas has produced a complicated cycle of overthrusting, unroofing, and even extensional faulting within a few tens of millions of years, subduction is a longer-lived and more continuous process. Thus, subduction is more likely to produce a steady-state temperature structure in the lithosphere, a fact which has important implications for PTt paths in Barrovian terrains.

Studies of the thermal evolution of large-scale extensional terrains can be applied to several different marine settings. Pure shear has been proposed as the mechanism by which some passive continental margins undergo thinning (*e.g.*, Royden and Keen [1983]). Far from these margins, at mid-ocean ridges and along some transform faults, normal faulting (simple shear) predominates as the mode of deformation and large scarps may expose several kilometers of oceanic upper crust. The obvious differences between passive margin and transform fault or mid-ocean ridge settings include such factors as

thermal regime and crustal thickness, both factors which greatly affect the morphology of PT and Tt paths of metamorphic rocks. Although there exists no possibility of obtaining samples of metamorphosed rocks from intermediate and deep crustal levels in these settings, the PTt work described here could be easily applied to such metamorphic rocks where they are exposed on continents. More importantly, however, is the applicability of the two-dimensional modeling techniques to the analysis of the thermal evolution of the crust in these settings. Further modification of the models to include the effects of such processes as isostasy and basin formation could lead to the development of a set of techniques for analyzing how marine extension affects the middle and lower oceanic crust and for determining the relative importance of surface structural processes and such factors as \sqrt{t} cooling of ocean basins in determining the thermal regime of the oceanic crust.

SUGGESTIONS FOR FUTURE RESEARCH

The studies presented in this thesis should be viewed not as conclusive analyses of specific regions or of specific geological and geophysical problems, but rather as a basis for further research. This statement has particular validity for studies of the Baikal Rift zone, a region which has become accessible to Western scientists only within the course of the work presented here. Among the most important research problems in the BRZ is characterization of the rift's deep thermal structure using various kinds of seismic data. Projects already underway will "map" seismic velocities at depth using three-dimensional block inversion methods. This tomographic experiment provides the best immediate hope for estimating the magnitude of thermal anomalies, assessing the possibility of small-scale convective thinning, and completing the continental rift dataset. Multichannel seismic studies within Lake Baikal are already yielding important results about shallow rift structure, including information about the thickness of sediments, the degree of tectonic

control on sedimentation, and the time-evolution of the basin. Drill cores from the lake and detailed mapping of young sediments along its periphery should soon lead to the development of a definitive stratigraphy for the region and to the resolution of the controversy over the rift's age. Even these shallow drill cores may bear on the deep structure beneath the rift however, since analysis of the amount of ash in sediments may lead to a re-assessment of the notion that the BRZ constitutes a "dry" rift system.

In addition to the ongoing experiments, several kinds of research are required if we are to understand the geological and geophysical characteristics of the BRZ. First, an integrated program of land-based geophysical work in at least one key basin outside Lake Baikal would lead to fundamental knowledge about the depth of sediments, the amount of volcanic fill, the style of extension (*e.g.*, low-angle vs. high-angle faulting), the degree of basement involvement (*i.e.*, thinned skinned vs. thick-skinned deformation), and the similarities and differences between the axial part of the rift zone and the off-axis basins. Secondly, two-dimensional gravity data provide the only independent check on the results of the large-scale seismic experiments already underway in the BRZ. With the techniques employed in Chapters 2, high-quality gravity data would not only reveal the true nature of shallow compensation and shallow density structure, but also provide clues about the degree of thermal or dynamic compensation of the rift swell. Third, the existing digital dataset for teleseismic arrivals passing through the BRZ may provide a good starting point for the analysis of S-SS delays. Shear waves have proved useful in constraining lateral temperature variations in the oceans [*Sheehan*, 1991], beneath localized ocean ridges and swells [*Woodward and Masters*, 1991], and in the Tibetan Plateau [*Molnar*, 1990]. Preliminary attempts to explore the feasibility of shear wave studies lead us to conclude that the BRZ area may be plagued by (a) a lack of bounce points, (b) poor location relative to WWSN stations, and (c) too narrow a zone of deformation. Finally, the most critical research required in the BRZ is large-scale structural mapping from the perspective of

workers familiar with features in both diffuse and discrete continental extensional settings. The present mapping efforts bring us no closer to understanding the regional stress field, the overall tectonic setting, or the sequence of rift initiation, uplift, and basin subsidence, and efforts should focus first on reconnaissance mapping at a large scale before narrowing to the level of more specific features and problems.

The areas of future research relevant to the thermal evolution of large-scale overthrust and extensional terrains have been discussed at length in Chapters 4 and 5. Clearly, the most important need is for an inversion technique which would permit metamorphic petrologists and structural geologists to constrain such variables as unroofing rate or burial rate uniquely. Given the present uncertainties associated with geothermobarometric data and the complex way in which different factors affect PTt path morphology, prospects for the development of an inversion method are poor at present. On a less ambitious scale, experimental and theoretical studies of the temperatures and pressures recorded by rocks during metamorphism would fill an immediate gap in our knowledge about what PT paths truly measure and which PT information is preserved as a rock horizon undergoes a complicated sequence of processes. Finally, PT data, when applied correctly, provide a direct measure of lateral temperature variations in the crust during orogenesis. Ideally we should seek to understand the thermal structure of stable continental lithosphere before taking on thermal problems in orogenic belts, but, in the absence of a means of directly measuring crustal temperatures, the PT data from orogenic belts may provide the only hope for characterizing the normal and perturbed thermal states of the continents. One possibility for future research is therefore to use PT data to characterize the thermal state of the lithosphere during and after orogenesis in a variety of settings.

Throughout the course of the studies in this thesis, a key frustration has been the lack of a simple, self-consistent model for the thermal structure of the continental

lithosphere. The classic studies of sea-floor bathymetry led to the development of a simple accretionary model for oceanic lithosphere, but mid-ocean ridges and subduction zones, the defining features of plate-tectonics in the oceans, do not carry over cleanly to the continents. Thus, we are left with only crude models for the vertical temperature structure of both stable and actively-deforming continental regions. Seismologists have spent the past decade characterizing the roots of continents and underscoring the fundamental differences between the deep chemical boundary layers of continents and oceans. For students of continental tectonics, the next research problem—that of describing the thermal state of the continental lithosphere—has implications even more far-reaching than these continental root studies. The mantle lithosphere effectively serves as the relay zone between deep mantle processes and the deforming crust, and, until we can constrain the thermal state at depth within the mantle lithosphere, our understanding of the forces which drive tectonism and of the relationship between surface deformation and fundamental Earth processes will remain seriously hampered.

References

- Anderson, J.L., A.P. Barth and E.D. Young, Mid-crustal Cretaceous roots of Cordilleran metamorphic core complexes, *Geology*, *16*, 366-369, 1988.
- Andreasson, P.G. and B. Lagerblad, Occurrence and significance of inverted metamorphic gradients in the western Scandinavian Caledonides, *J. Geol. Soc. Lond.*, *137*, 219-230, 1980.
- Armstrong, R.L., Cordilleran metamorphic core complexes—from Arizona to southern Canada, *Ann. Rev. Earth Planet. Sci.*, *10*, 129-154, 1982.
- Artemjev, M. and E. Artyushkov, Structure and isostasy of the Baikal rift and the mechanism of rifting, *J. Geophys. Res.*, *76*, 1197-1211, 1971.
- Artyushkov, E., F. Letnikov, and V. Ruzhich, The mechanism of formation of the Baikal basin, *J. Geodynamics*, *11*, 277-291, 1990.
- Atlas of Russian Earthquakes: Resultati nabloodeni seti seismicheskikh stantsi SSSR, 1911-1957 gg.*, Moscow: Izd. Akad. Nauk, 1962.
- Atwater, T., Implications of plate tectonics for the Cenozoic tectonic evolution of Western North America, *Geol. Soc. Amer. Bull.*, *81*, 3513-3536, 1970.
- Balla, Z., M. Kuzmin, and K. Levi, Kinematics of the Baikal opening: results of modeling, *Annales Tectonicae*, *5*, 18-31, 1991.
- Barr, T. and F.A. Dahlen, Brittle frictional mountain building 2. Thermal structure and heat budget, *J. Geophys. Res.*, *94*, 3923-3947, 1989.
- Bartley, J.M. and B.P. Wernicke, The Snake Range Décollement interpreted as a major extensional shear zone, *Tectonics*, *3*, 647-657, 1984.
- Bassi, G., Factors controlling the style of continental rifting: insights from numerical modelling, *Earth Planet. Sci. Lett.*, in press, 1991.

- Bechtel, T., D. Forsyth, V. Sharpton, and R. Grieve, Variations in effective elastic thickness of the North American lithosphere, *Nature*, *343*, 636-638, 1990.
- Behrendt, J., W. LeMasurier, A. Cooper, F. Tessensohn, A. Tréhu, and D. Damaske, Geophysical studies of the West Antarctic rift system, *Tectonics*, *10*, 1257-1273, 1991.
- Brace, W. and D. Kohlstedt, Limits on lithospheric stress imposed by laboratory experiments, *J. Geophys. Res.*, *85*, 6248-6252, 1980.
- Buck, W.R., Small-scale convection induced by passive rifting: the cause for uplift of rift shoulders, *Earth Planet. Sci. Lett.*, *77*, 362-372, 1986.
- Buck, W.R., F. Martinez, M.S. Steckler, and J.R. Cochran, Thermal consequences of lithospheric extension: pure and simple, *Tectonics*, *7*, 213-234, 1988.
- Byerlee, J.D., Friction of rocks, *Pure and Appl. Phys.*, *116*, 615-626, 1978.
- Carslaw, H.S. and J.C. Jaeger, *Conduction of Heat in Solids*, Oxford University Press, New York, 2nd edition, 510 pp., 1959.
- Chen, W-P. and P. Molnar, Focal depths of intracontinental and intraplate earthquakes and their implications for the thermal and mechanical properties of the lithosphere, *J. Geophys. Res.*, *88*, 4183-4214, 1983.
- Chorowicz, J. and C. Sorlien, Oblique extensional tectonics in the Malawi Rift, *Geol. Soc. Amer. Bull.*, in review.
- Coney, P.J., Tertiary evolution of Cordilleran metamorphic core complexes, in *Cenozoic Paleogeography of the Western United States*, edited by J.M. Armentrout, M.R. Cole, and H. Terbest, SEPM, 15-28, 1979.
- Copeland, P., T.M. Harrison, K.V. Hodges, P. Maruéjol, P. LeFort and A. Pêcher, An Early Pliocene thermal disturbance of the Main Central Thrust, central Nepal: Implications for Himalayan tectonics, *J. Geophys. Res.*, 1991.

- Cowie, P. and G. Karner, Gravity effect of sediment compaction: examples from the North Sea and the Rhine graben, in prep., 1990.
- Crane, K. and S. O'Connell, The distribution and implications of heat flow from the Gregory Rift in Kenya, *Tectonophysics*, *94*, 253-275, 1983.
- Crane, K., B. Hecker, and V. Golubev, Heat flow and hydrothermal vents in Lake Baikal, USSR, *EOS*, *72*, 585-589, 1991.
- Das, S. and J. Filson, On the tectonics of Asia, *Earth Planet. Sci. Lett.*, *28*, 241-253, 1988.
- DeMets, C., R. Gordon, D. Argus, and S. Stein, Current plate motions, *Geophys. Jour. Int.*, *101*, 425-478, 1990.
- Déverchère, J., F. Houdry, M. Diament, N. Solonenko, and A. Solonenko, Evidence for a seismogenic upper mantle and lower crust in the Baikal Rift, *Geophys. Res. Lett.*, *18*, 1099-1102, 1991.
- Dewey, J. and J. Bird, Mountain belts and the new global tectonics, *J. Geophys. Res.*, *75*, 2625-2647, 1970.
- Diament, M. and M. Kogan, Long wavelength gravity anomalies and the deep thermal structure of the Baikal rift, *Geophys. Res. Lett.*, *17*, 1977-1980, 1990.
- Dodson, M.H., Closure temperatures in cooling geochronological and petrological systems, *Contrib. Mineral. Petrol.*, *40*, 259-274, 1973.
- Dorman, L. and B. Lewis, Experimental isostasy 1. Theory of the determination of the Earth's isostatic response to a concentrated load, *J. Geophys. Res.*, *75*, 3357-3365, 1970.
- Doser, D., Faulting within the western Baikal rift as characterized by earthquake studies, *Tectonophysics*, *196*, 87-107, 1991a.
- Doser, D., Faulting within the eastern Baikal rift as characterized by earthquake studies, *Tectonophysics*, *196*, 108-139, 1991b.

- Dushkov, A., editor, *Katalog dannikh po teplovomu potoku Sibiri (1966-1984 g.)*, Novosibirsk: Izd. IGiG CO AN CCCP, 1985.
- Ebinger, C., T. Bechtel, D. Forsyth, and C. Bowin, Effective elastic plate thickness beneath the East African and Afar plateaus and dynamic compensation of the uplifts, *J. Geophys. Res.*, *94*, 2883-2901, 1989.
- Edginton, D., J. Klump, J. Robbins, and Y. Kusner, Pb-210, Cs-137, and sedimentation in Lake Baikal, *EOS*, *71*, 1338, 1990.
- England, P. and G. Houseman, The mechanics of the Tibetan plateau, *Phil. Trans. R. Soc. Lond.*, *326*, 301-320, 1988.
- England, P. and J. Jackson, Migration of the seismic-aseismic transition during uniform and nonuniform extension of the continental lithosphere, *Geology*, *15*, 291-294, 1987.
- England, P., P. LeFort, P. Molnar, A. Pêcher, Heat sources for Tertiary metamorphism and anatexis in the Annapurna-Manaslu region, Central Nepal, *J. of Geophys. Res.*, in review 1991.
- England, P. and D. McKenzie, A thin viscous sheet model for continental deformation, *Geophys. J. R. astr. Soc.*, *70*, 295-321, 1982.
- England, P. and D. McKenzie, Correction to: a thin viscous sheet model for continental deformation, *Geophys. J. R. astr. Soc.*, *73*, 523-532, 1983.
- England, P.C. and S.W. Richardson, The influence of erosion upon mineral facies of rocks from different metamorphic environments., *J. Geol. Soc. Lond.*, *134*, 201-213, 1977.
- England, P.C. and A.B. Thompson, Pressure-temperature-time paths of regional metamorphism I. Heat transfer during the evolution of regions of thickened continental crust, *J. of Petrol.*, *25(4)*, 894-928, 1984.
- Essene, E.J., Geologic thermometry and barometry, *Reviews in Mineralogy*, *10*, 153-206, 1982.

- Fischer, K., T. Jordan, and K. Creager, Seismic constraints on the morphology of deep slabs, *J. Geophys. Res.*, *93*, 4773-4783, 1988.
- Fleitout, L. and C. Froidevaux, Tectonics and topography for a lithosphere containing density heterogeneities, *Tectonics*, *1*, 21-56, 1982.
- Forsyth, D., Subsurface loading and estimates of the flexural rigidity of continental lithosphere, *J. Geophys. Res.*, *90*, 12,623-12,632, 1985.
- Frost, B.R. and T. Chacko, The granulite uncertainty principle: limitations on thermobarometry in granulites, *J. Geology*, *97*, 435-450, 1989.
- Furlong, K.P. and M.D. Londe, Thermal-mechanical consequences of Basin and Range extension, in *Extensional Tectonics of the Southwestern United States; a perspective on processes and kinematics*, edited by Larry Mayer, Special Paper 208, Geol. Soc. of Amer., 23-30, 1986.
- Gans, P.B., An open-system, two-layer crustal stretching model for the eastern Great Basin, *Tectonics*, *6*, 1-12, 1987.
- Gansser, A., *Geology of the Himalayas*, 289 pp., Wiley Interscience, London, 1964.
- Garfunkel, Z., I. Zak, and R. Freund, Active faulting in the Dead Sea rift, *Tectonophysics*, *80*, 1-26, 1981.
- Golonetsky, S. and L. Misharina, Seismicity and earthquake focal mechanisms in the Baikal rift zone, *Tectonophysics*, *45*, 71-85, 1978.
- Gornostayev, V., V. Mikhalevskii, and V. Pospeev, Deep magnetotelluric sounding in the south of the Siberian platform and in the Baikal rift valley, *Geol. i geofiz.*, *4*, 111-118, 1970.
- Hamilton, W. and W.B. Myers, Cenozoic tectonics of the western United States, *Rev. Geophysics*, *4*, 509-549, 1966.

- Haugerud, R.A., 1DT - An interactive, screen-oriented microcomputer program for simulation of geothermal histories, *U.S. Geol. Surv. Open-File Report*, 86-511, 1-19, 1986.
- Hodges, K.V., Pressure-Temperature-Time Paths, *Ann. Rev. Earth Planet. Sci.*, 19, 207-236, 1991.
- Hodges, K.V. and P. Crowley, Error estimation and empirical geothermobarometry for pelitic systems, *Amer. Mineralogist*, 70, 702-709, 1985.
- Hodges, K.V., D. Lux, B.C. Burchfiel, L.H. Royden, Z. Chen, C. Deng, Y. Liu and J. Xu, Tectonic denudation and the unroofing history of the central Himalayas, *Geol. Soc. Amer. Abs. w. Prog.*, 21, A182, 1989.
- Hodges, K.V. and L.W. McKenna, Realistic propagation of uncertainties in geologic thermobarometry, *Amer. Mineral.*, 72, 673-682, 1987.
- Hodges, K.V. and L.H. Royden, Geologic thermobarometry of retrograded metamorphic rocks: an indication of the uplift trajectory of a portion of the northern Scandinavian Caledonides, *J. Geophys. Res.*, 89, 7077-7090, 1984.
- Hodges, K.V. and J.D. Walker, Thermobarometric constraints on the unroofing history of a metamorphic core complex, Funeral Mountains, SE California, *J. Geophys. Res.*, 95, 8437-8445, 1990.
- Hollister, L.S., R.C. Burruss, D.L. Henry and E.M. Hendel, Physical conditions during uplift of metamorphic terranes as recorded by fluid inclusions, *Bulletin de Minéralogie*, 102, 555-561, 1979.
- Hubbard, M., L. Royden, and K. Hodges, Constraints on unroofing rates in the High Himalaya, Eastern Nepal, *Tectonics*, 10, 247-298, 1991.
- Hutchinson, D., A. Golmshtok, L. Zonenshain, T. Moore, C. Scholz, and K. Klitgord, Depositional and tectonic framework of the rift basins of Lake Baikal from multichannel seismic data, in internal USGS review, 1991.

- Jackson, J., Active normal faulting and crustal extension, in: *Continental Extensional Tectonics*, ed., M. Coward, J. Dewey, and P. Hancock), Spec. Publ. geol. Soc. Lond 28, 3-18, 1987.
- Jessop, A., M. Hobart, and J. Sclater, *The world heat flow data collection—1975*, Geothermal Series 6, Energy, Mines, and Resources Canada.
- Jordan, T.H., Composition and development of the continental tectosphere, *Nature*, 274, 544-548, 1978.
- Khrenov, P., Z. Anismova, V. Belichenko, and V. Novikov, *Geological map of the Baikal region, 1:1,000,000*, Akad. Nauk and Sov. Ministry of Geology, 1983.
- Kiselev, A., H. Golovko, and M. Medvedev, Petrochemistry of Cenozoic basalts and associated rocks in the Baikal Rift zone, *Tectonophysics*, 45, 49-59, 1978.
- Kogan, M. and M. McNutt, Isostasy in the USSR I: Admittance data, in *Composition, Structure, and Dynamics of the Lithosphere-Asthenosphere System*, ed. K. Fuchs and C. Froidevaux, Geodyn. Series 16, Washington D.C.: Amer. Geophys. Union, 301-307, 1987.
- Kozhevnikov, V., Dispersia poverkhnostnix seismisheskikh voln Ryelyea i stroyenie litosferi Sibiriskoi platformi, *Fiziki Zemli*, 6, 48-56, 1987.
- Krylov, S., B. Mishenkin, Z. Mishenkina, G. Petrik, and V. Seleznev, Seismic section through the lithosphere in the region of the Baikal Rift, *Sov. Geology and Geophysics*, 16, 53-61, 1975.
- Lachenbruch, A.H. and J.H. Sass, Thermo-mechanical aspects of the San Andreas fault system, *Proc. of Conf. on Tectonic Problems of the San Andreas Fault Sytem*, ed. R.L. Kovach and A. Nur, Stanford Univ. Publ. Geol. Sci., 11, 192-205, 1973.
- Lalonde, A.E., Hepburn intrusive suite: Peraluminous plutonism within a closing back-arc basin, Wopmay orogen, Canada, *Geology*, 17, 261-264, 1989.

- LeFort, P., A. Pêcher and B.N. Upreti, A section through the Tibetan slab in central Nepal (Kali Gandaki Valley): mineral chemistry and thermobarometry of the Main Central Thrust zone, in *Orogenic Evolution of Southern Asia (from Turkey to Indonesia)*, edited by P. LeFort et al., pp. 211-228, Sciences de la Terre, Nancy, France, 1987.
- Logan, J.M. and K.A. Rauenzahn, Frictional dependence of gouge mixtures of quartz and montmorillonites on velocity, composition, and fabric, *Tectonophysics*, 144, 87-108, 1987.
- Logatchev, N. and N. Florensov, The Baikal system of rift valleys, *Tectonophysics*, 45, 1-13, 1978.
- Logatchev, N., Yu. Zorin, and V. Rogozhina, Baikal Rift: active or passive?—comparison of the Baikal and Kenya Rift zones, *Tectonophysics*, 94, 223-240, 1983.
- Logatchev, N. and Yu. Zorin, Evidence and causes of the two-stage evolution of the Baikal rift, *Tectonophysics*, 143, 225-234, 1987.
- Lubimova, E., Heat flow patterns in Baikal and other rift zones, *Tectonophysics*, 8, 457-467, 1969.
- Lysak, S., The Baikal rift heat flow, *Tectonophysics*, 45, 87-93, 1978.
- McKenna, L.W. and K.V. Hodges, Accuracy versus precision in locating reaction boundaries: Implications for the garnet-plagioclase-aluminum silicate-quartz geobarometer., *Am. Mineral.*, 73, 1205-1208, 1988.
- McNutt, M., M. Diament, and M. Kogan, Variations of elastic plate thickness at continental thrust belts, *J. Geophys. Res.*, 93, 8825-8838, 1988.
- McNutt, M. and L. Royden, Extremal bounds on geotherms in eroding mountain belts from metamorphic pressure-temperature conditions, *Geophys. J. R. astr. Soc.*, 88, 81-95, 1987.
- Meissner, R. and J. Strehlau, Limits of stresses in continental crusts and their relation to the depth-frequency distribution of shallow earthquakes, *Tectonics*, 1, 73-89, 1982.

- Miller, E.L., P.B. Gans, and J. Garing, The Snake Range décollement—an exhumed ductile-brittle transition, *Tectonics*, 2, 239-263, 1983.
- Minster, J. B. and T. Jordan, Present-day plate motions, *J. Geophys. Res.*, 83, 5331-5354, 1978.
- Misharina, L., Stresses in earthquake foci of the Mongolia-Baikal folded zone, in *Fields of Elastic Stresses of the Earth and Focal Mechanisms of Earthquakes*, 161-171, 1972.
- Misharina, L. and N. Solonenko, O napryazheneyax b oshagax slabikh zemletryaceni pribaikala, *Fiziki Zemli*, 24-36, 1972.
- Misharina, L., A. Solonenko, V. Melnikova, and N. Solonenko, Stresses and faulting in earthquake foci, in *Geology and Seismicity of the BAM zone*, 74-120, 1985.
- Mishenkina, Z., Intracrustal seismic waveguide in the Baikal rift zone, *Sov. Geol. and Geophys.*, 21, 73-80, 1980.
- Molnar, P., Structure and tectonics of the Himalaya: constraints and implications of geophysical data, *Ann. Rev. Earth Planet. Sci.*, 12, 489-518, 1984.
- Molnar, P., A review of geophysical constraints on the deep structure of the Tibetan plateau, the Himalaya, and the Karakoram, and their tectonic implications, *Phil. Trans. R. Soc. Lond.*, 326, 33-88, 1988.
- Molnar, P., S-wave residuals from earthquakes in the Tibetan region and lateral variations in the upper mantle, *Earth Planet. Sci. Letters*, 101, 68-77, 1990.
- Molnar, P. and P. England, Temperatures, heat flux, and frictional stress near major thrust faults, *J. Geophys. Res.*, 95, 4833-4856, 1990.
- Molnar, P. and H. Lyon-Caen, Some simple physical aspects of the support, structure, and evolution of mountain belts, in: *Processes in continental lithospheric deformation*, ed. S. Clark, B. Burchfiel, and J. Suppe, *Geol. Soc. Amer. Spec. Paper 218*, 179-207, 1988.

- Molnar, P. and P. Tapponnier, Cenozoic tectonics of Asia: effects of a continental collision, *Science*, 189, 419-426, 1975.
- Molnar, P. and P. Tapponnier, Active tectonics of Tibet, *J. of Geophys. Res.*, 83, 5361-5375, 1978.
- Morrow, C.A., L.Q. Shi, and J.D. Byerlee, Strain hardening and strength of clay-rich fault gouges, *J. Geophys. Res.*, 87, 6771-6780, 1982.
- Neugebauer, H., Mechanical aspects of continental rifting, *Tectonophysics*, 94, 91-108, 1983.
- Nikolayev, V., L. Vanyakin, V. Kalinin, and V. Milanovskiy, The sedimentary section beneath Lake Baykal, *Int. Geol. Rev.*, 27, 449-459, 1985.
- Oxburgh, E.R. and D.L. Turcotte, Thermal gradients and regional metamorphism in overthrust terrains with special reference to the Eastern Alps, *Schweiz. Min. Petr. Mitt.*, 54, 641-622, 1974.
- Parker, R., The rapid calculation of potential anomalies, *Geophys. J. R. Astron. Soc.*, 51, 447-455, 1973.
- Parrish, R.R., U-Pb systematics of monazite and a preliminary estimate of its closure temperature based on natural examples, *Geol. Assoc. Canada Prog. w. Abstracts*, 13, A94, 1988.
- Parsons, B. and J.G. Sclater, An analysis of the variation of ocean floor bathymetry and heat flow with age, *J. Geophys. Res.*, 82, 803-827, 1977.
- Peacock, S., Creation and preservation of subduction-related inverted metamorphic gradients, *J. Geophys. Res.*, 92, 12763-12781, 1987.
- Peacock, S., Numerical simulations of metamorphic P-T-t paths of fluid production in subducting slabs, *Tectonics*, 9, 1197-1211, 1990.

- Pitman, W.C. III and J.A. Andrews, Subsidence and thermal history of small pull-apart basins, in *Strike-slip deformation, basin formation, and sedimentation*, ed. by K.T. Biddle and N. Christie-Blick, SEPM Spec. Publ. 37, pp. 45-49, 1985.
- Pleshanov, S. and A. Romazina, Some problems of fault development in the central Baikal rift, in *Problemy razlnoi tektoniki*, ed. N. Florensov and N. Logatchev, Novosibirsk: Izd. Akad. Nauk, 34-35, 1975.
- Press, W.H., B.P. Flannery, S.A. Teukolsky, and W.T. Vetterling, *Numerical Recipes: The Art of Scientific Computing*, New York: Cambridge University Press, 818 pp., 1986.
- Puzyrev, N., editor, *Nedra Baikal po seismicheskim dannim*, Novosibirsk: Izd. Nauk Sib. Otd., 1981.
- Puzyrev, N. and S. Krylov, Principal results of regional seismic researches in Siberia, *Siberian Sci. Res. Inst.*, 249, 17-29, 1977.
- Reiter, M., C. Edwards, H. Hartman, and C. Weidman, Terrestrial heat flow along the Rio Grande rift, New Mexico and southern Colorado, *Geol. Soc. Amer. Bull.*, 86, 811-818, 1975.
- Royden, L., The Vienna basin: a thin-skinned pull-apart basin, in *Strike-Slip Deformation, Basin Formation, and Sedimentation*, eds. K. Biddle and N. Christie-Blick, SEPM Spec. Pub. 37, 319-338, 1985.
- Royden, L. and B.C. Burchfiel, Thin-skinned N-S extension within the convergent Himalayan region: gravitational collapse of a Miocene topographic front, in: *Continental Extensional Tectonics*, eds. M. Coward, J. Dewey, and P. Hancock, Geol. Soc. Spec. Publ. 28, 611-619, 1987.
- Royden, L. and K.V. Hodges, A technique for analyzing the thermal and uplift histories of eroding orogenic belts: A Scandinavian example, *J. Geophys. Res.*, 89, 7077-7090, 1984.

- Royden, L., F. Horváth, and B.C. Burchfiel, Transform faulting, extension, and subduction in the Carpathian Pannonian region, *Geol. Soc. Amer. Bull.*, *93*, 717-725, 1982.
- Royden, L. and C. Keen, Rifting process and thermal evolution of the continental margin of eastern Canada determined from subsidence curves, *Earth Planet. Sci. Lett.*, *51*, 343-361, 1980.
- Ruppel, C., L. Royden, and K.V. Hodges, Two-dimensional thermal models of compressional and extensional tectonics: theoretical pressure-temperature-time paths of metamorphic rocks, *EOS*, *69*, 1513, 1988.
- Sanford, A., K. Olsen, and L. Jaksha, Seismicity of the Rio Grande rift, in: *Rio Grande Rift: tectonics and magmatism*, ed. R. Riecker, Washington D.C.: Amer. Geophys. Union, 145-168, 1979.
- Scholz, C., Shear heating and the state of stress on faults, *J. Geophys. Res.*, *85*, 6174-6184, 1980.
- Sclater, J.G., C. Jaupart, and D. Galson, The heat flow through oceanic and continental crust and the heat loss of the earth, *Rev. Geophys. and Space Physics*, *18*, 269-311, 1980.
- Sengör, A.M.C., *The Cimmeride orogenic system and the tectonics of Eurasia*, Geol. Soc. Amer. Spec. Paper 195, 1984.
- Sheehan, A., Lateral variations in upper mantle temperature and composition beneath mid-ocean ridges inferred from shear-wave propagation, geoid, and bathymetry, Ph.D. thesis, Mass. Inst. of Tech., 1991.
- Sherman, S., Faults of the Baikal rift zone, *Tectonophysics*, *45*, 31-39, 1978.
- Sherman, S. and K. Levi, Transform faults of the Baikal Rift zone, *Dokl. Akad. Nauk SSSR*, *233*, 461-464, 1977.

- Sherman, S., M. Medvedev, V. Ruzhich, A. Kisselov, and A. Shmotov, *Tektonika i vulcanizm ugo-zapadnoy shasti Baikalskoy riftovoy zoni*, ed. N. Florensov, Novosibirsk: Izd. Nauka, 1973.
- Shi, Y. and C.-Y. Wang, Two-dimensional modeling of the P-T-t paths of regional metamorphism in simple overthrust terrains, *Geology*, 15, 1048-1051, 1987.
- Solonenko, N. and A. Solonenko, Aftershock sequences and earthquakes of the Baikal Rift Zone, Novosibirsk: Nauka, 302 pp., 1987.
- Solonenko, V., Seismotectonics of the Baikal rift zone, *Tectonophysics*, 45, 61-69, 1978.
- Spanier, J., Alternating direction methods applied to heat conduction problems, in *Mathematical Methods for Digital Computers II*, ed. A. Ralston and H. Wilf, 1967.
- Spear, F.S., Relative thermobarometry and metamorphic P-T paths, in *Evolution of Metamorphic Belts*, edited by J.S. Daly et al., pp. 63-81, Geological Society Special Publication, London, 1989.
- Spear, F.S. and F. Florence, On the interpretation of peak metamorphic temperatures in light of garnet diffusion during cooling, *V.M. Goldschmidt Conference Program and Abstracts*, 83, 1990.
- Spear, F.S. and S.M. Peacock, *Metamorphic Pressure-Temperature-Time Paths*, 102 pp., American Geophysical Union, Washington, 1989.
- Spear, F.S. and J. Selverstone, Quantitative P-T paths from zoned minerals: theory and tectonic applications, *Contrib. Mineral. Petrol.*, 83, 348-357, 1983.
- Spear, F.S., J. Selverstone, D. Hickmott, P. Crowley, and K.V. Hodges, P-T paths from garnet zoning: a new technique for deciphering tectonic processes in crystalline terranes, *Geology*, 12, 87-90, 1984.

- St-Onge, M.R., Zoned poikiloblastic garnets: P-T paths and synmetamorphic uplift through 30km of structural depth, Wopmay Orogen, Canada, *J. Petrol.*, 28, 1-27, 1987.
- Steckler, M. and A. Watts, Subsidence history and tectonic evolution of Atlantic-type continental margins, in *Dynamics of Passive Margins*, ed. R. Scrutton, Amer. Geophys. Union Geod. Ser., 6, 184-196, 1982.
- Stewart, J.H., Basin and Range structure — a system of horsts and grabens produced by deep-seated extension, *Geol. Soc. Am. Bull.*, 82, 1019-1044, 1971.
- Tapponnier, P., G. Peltzer, A. Le Dain, R. Armijo, and P. Cobbold, Propagating extrusion tectonics in Asia: New insights from simple experiments with plasticine, *Geology*, 10, 611-616, 1982.
- Tapponnier, P. and P. Molnar, Active faulting and Cenozoic tectonics of the Tien Shan, Mongolia, and Baykal regions, *J. Geophys. Res.*, 84, 3425-3459, 1979.
- Thompson, A.B. and P.C. England, Pressure-temperature-time paths of regional metamorphism II: their inference and interpretation using mineral assemblages in metamorphic rocks, *J. of Petrology*, 25, 929-955, 1984.
- Turcotte, D.L. and G. Schubert, Frictional heating of the descending lithosphere, *J. Geophys. Res.*, 78, 5876-5886, 1973.
- Wagner, G.A., G.M. Reimer and E. Jäger, Cooling ages derived by apatite fission track, mica Rb-Sr, and K-Ar dating: the uplift and cooling history of the Central Alps, *Mem. Univ. Padova*, 30, 1-27, 1977.
- Weissel, J. and G. Karner, Flexural uplift of rift flanks due to mechanical unloading of the lithosphere during extension, *J. Geophys. Res.*, 94, 13,919-13,950, 1989.
- Wendlandt, R. and P. Morgan, Lithospheric thinning associated with rifting in East Africa, *Nature*, 298, 734-736, 1982.

- Wernicke, B., Low-angle normal faults in the Basin and Range Province—nappe tectonics in an extending orogen, *Nature*, 291, 645-648, 1981.
- Wernicke, B., Uniform-sense normal simple shear of the continental lithosphere, *Can. Jour. Earth Sci.*, 22, 108-125, 1985.
- Woodward, R. and G. Masters, Global upper mantle structure from long-period differential travel times, *J. Geophys. Res.*, 96, 6351-6378, 1991.
- Wyllie, P.J., W-L Huang, C.R. Stern, and S. Maaløe, Granitic magmas: possible and impossible sources, water contents, and crystallization sequences, *Can. Jour. of Earth Sci.*, 13 (8), 1007-1019, 1976.
- Yanshin, A., V. Arsenyev, and P. Khrenov, chief compilers, *Geologicheskaya Karta Yuga vostochnoi Sibiri i severnoi shasti MNR*, 1:1,500,000, Ministry of Geology of the USSR, 1980.
- Yuen, D. and L. Fleitout, Thinning of the lithosphere by small-scale convective destabilization, *Nature*, 313, 125-128, 1985.
- Zamarayev, S. and V. Ruzhich, On relationships between the Baikal rift and ancient structures, *Tectonophysics*, 45, 41-47, 1978.
- Zoback, M.D. and J.H. Healy, Friction, faulting, and "in situ" stress, *Ann. Geophys.*, 2, 689-698, 1984.
- Zonenshain, L. and L. Savostin, Geodynamics of the Baikal rift zone and plate tectonics of Asia, *Tectonophysics*, 76, 1-45, 1981.
- Zorin, Yu., On the deep structure of the Baikal depression based on geophysical data, *Izd. Akad. Nauk. SSSR, Geol. Ser.*, 76-85, 1966.
- Zorin, Yu., *Recent structure and isostasy of the Baikal Rift zone and adjoining territories*, Moscow: Nauk, 168 pp., 1971.
- Zorin, Yu., Isostasy and gravimetric model of the Earth's crust and upper mantle, in *Essays on deep structure of the Baikal Rift*, Novosibirsk: Izd. Nauk., 83-98, 1977.

- Zorin, Yu., The Baikal rift: an example of the intrusion of asthenospheric material into the lithosphere as the cause of disruption of lithospheric plates, *Tectonophysics*, 73, 91-104, 1981.
- Zorin, Yu., V. Mordvinova, M. Novoselova, and Ye. Turutanov, Density inhomogeneities in the mantle under the Baikal Rift, *Izv. Earth Physics*, 22, 373-381, 1986.
- Zorin, Yu. and V. Rogozhina, Mechanism of rifting and some features of the deep-seated structure of the Baikal rift zone, *Tectonophysics*, 45, 23-30, 1978.
- Zuber, M.T., E.M. Parmentier, and R.C. Fletcher, Extension of continental lithosphere: a model for two scales of Basin and Range deformation, *J. Geophys. Res.*, 91, 4826-4838, 1986.

4523-48